

Weak Gravitational Lensing by Large-Scale Structures: A Tool for Constraining Cosmology

THÈSE N° 5732 (2013)

PRÉSENTÉE LE 28 JUIN 2013

À LA FACULTÉ DES SCIENCES DE BASE
INSTITUT DE PHYSIQUE DE L'ÉNERGIE ET DES PARTICULES
PROGRAMME DOCTORAL EN PHYSIQUE

ÉCOLE POLYTECHNIQUE FÉDÉRALE DE LAUSANNE

POUR L'OBTENTION DU GRADE DE DOCTEUR ÈS SCIENCES

PAR

Marc GENTILE

acceptée sur proposition du jury:

Prof. R. Schaller, président du jury
Prof. G. Meylan, Dr F. Courbin, directeurs de thèse
Prof. H. Hoekstra, rapporteur
Dr J. D. Rhodes, rapporteur
Prof. M. Unser, rapporteur



ÉCOLE POLYTECHNIQUE
FÉDÉRALE DE LAUSANNE

Suisse
2013

The most incomprehensible thing about the world is that it is comprehensible

— Albert Einstein (“Physics and Reality”, 1936)

To my parents

Acknowledgements

First and foremost, I want to express my gratitude to Professor Georges Meylan for his trust and for giving me the opportunity to complete this thesis at Laboratory of Astrophysics (LASTRO) of EPFL despite the limited time I had available. I am also grateful to him for all the efforts he made to render my studies as smooth as possible.

I would also like to address a special thank to Doctor Frederic Courbin for the constant guidance and availability he provided during my thesis. His many advice and fruitful discussions have without doubt greatly improved my results, especially on the GREAT08 and GREAT10 Challenges. I also greatly appreciated his help in improving my papers and this thesis report. I also wish to thank the other members of the jury, Professor Robert Schaller, Professor Michaël Unser, Professor Henk Hoekstra and Doctor Jason Rhodes for accepting to attend my thesis defense and taking the time to evaluate this work.

It is also a pleasure to thank Malte Tewes for his help and always useful advice, Carol Maury for the assistance she provided throughout this thesis and Olivier Genevay and Yves Revaz for their precious assistance in computing.

A special thank also to Pedro Figueira, Monika Lendl, Greg Lambert, Maxime Marmier, Dominique Naef, Damien Ségransan, Malte Tewes, Amaury Triaud and Luc Weber for the training and help they provided before and during the time I spent observing at the Swiss Euler telescope in La Silla.

Outside of LASTRO and the Geneva Observatory, I thank Sarah Bridle, Tom Kitching and the other members of the GREAT08 and GREAT10 organizing teams for launching these wonderful and fascinating challenges from which my thesis has benefited.

I am also deeply indebted to my parents who took care of my education and always made sure I could study under the best possible conditions. A thought to you, my father, who could not live long enough to see the completion of this thesis. Finally a warm thank you to my family for their encouragements, help and patience during these years of hard work.

Lausanne, February 2013

M. G.

Abstract

There is now very strong evidence that our Universe is undergoing an accelerated expansion period as if it were under the influence of a gravitationally repulsive “dark energy” component. Furthermore, most of the mass of the Universe seems to be in the form of non-luminous matter, the so-called “dark matter”. Together, these “dark” components, whose nature remains unknown today, represent around 96 % of the matter-energy budget of the Universe. Unraveling the true nature of the dark energy and dark matter has thus, obviously, become one of the primary goals of present-day cosmology.

Weak gravitational lensing, or weak lensing for short, is the effect whereby light emitted by distant galaxies is slightly deflected by the tidal gravitational fields of intervening foreground structures. Because it only relies on the physics of gravity, weak lensing has the unique ability to probe the distribution of mass in a direct and unbiased way. This technique is at present routinely used to study the dark matter, typical applications being the mass reconstruction of galaxy clusters and the study of the properties of dark halos surrounding galaxies. Another and more recent application of weak lensing, on which we focus in this thesis, is the analysis of the cosmological lensing signal induced by large-scale structures, the so-called “cosmic shear”. This signal can be used to measure the growth of structures and the expansion history of the Universe, which makes it particularly relevant to the study of dark energy.

Of all weak lensing effects, the cosmic shear is the most subtle and its detection requires the accurate analysis of the shapes of millions of distant, faint galaxies in the near infrared. So far, the main factor limiting cosmic shear measurement accuracy has been the relatively small sky areas covered. Next-generation of wide-field, multicolor surveys will, however, overcome this hurdle by covering a much larger portion of the sky with improved image quality. The resulting statistical errors will then become subdominant compared to systematic errors, the latter becoming instead the main source of uncertainty. In fact, uncovering key properties of dark energy will only be achievable if these systematics are well understood and reduced to the required level.

The major sources of uncertainty resides in the shape measurement algorithm used, the convolution of the original image by the instrumental and possibly atmospheric point spread function (PSF), the pixelation effect caused by the integration of light falling on the detector pixels and the degradation caused by various sources of noise. Measuring the Cosmic shear thus entails solving the difficult inverse problem of recovering the shear signal from blurred, pixelated and noisy galaxy images while keeping errors within the limits demanded by future weak lensing surveys.

Reaching this goal is not without challenges. In fact, the best available shear measurement methods would need a tenfold improvement in accuracy to match the requirements of a space mission like Euclid from ESA, scheduled at the end of this decade. Significant progress has nevertheless been made in the last few years, with substantial contributions from initiatives

Abstract

such as GREAT (GRavitational lEnsing Accuracy Testing) challenges. The main objective of these open competitions is to foster the development of new and more accurate shear measurement methods.

We start this work with a quick overview of modern cosmology: its fundamental tenets, achievements and the challenges it faces today. We then review the theory of weak gravitational lensing and explains how it can make use of cosmic shear observations to place constraints on cosmology. The last part of this thesis focuses on the practical challenges associated with the accurate measurement of the cosmic shear. After a review of the subject we present the main contributions we have brought in this area: the development of the *gfit* shear measurement method, new algorithms for point spread function (PSF) interpolation and image denoising. The *gfit* method emerged as one of the top performers in the GREAT10 Galaxy Challenge. It essentially consists in fitting two-dimensional elliptical Sérsic light profiles to observed galaxy image in order to produce estimates for the shear power spectrum. PSF correction is automatic and an efficient shape-preserving denoising algorithm can be optionally applied prior to fitting the data.

PSF interpolation is also an important issue in shear measurement because the PSF is only known at star positions while PSF correction has to be performed at any position on the sky. We have developed innovative PSF interpolation algorithms on the occasion of the GREAT10 Star Challenge, a competition dedicated to the PSF interpolation problem. Our participation was very successful since one of our interpolation method won the Star Challenge while the remaining four achieved the next highest scores of the competition.

Finally we have participated in the development of a wavelet-based, shape-preserving denoising method particularly well suited to weak lensing analysis.

Keywords: astrophysics, cosmology, cosmological parameter, gravitational lensing, weak lensing, cosmic shear, shape measurement, shear measurement, point spread function, PSF, deconvolution, denoising, GREAT08, GREAT10.

Résumé

De très concordantes observations suggèrent que notre Univers subit une phase d'accélération de son expansion sous l'influence d'une forme d'énergie gravitationnellement répulsive baptisée "énergie noire". De plus, l'essentiel de la masse de l'Univers semble se trouver sous la forme d'une matière non-lumineuse, appelée pour cette raison "matière noire". Ensemble, ces deux composants "sombre", dont la nature reste inconnue aujourd'hui, représentent environ 96% du total de la quantité de matière et d'énergie de l'Univers. Découvrir la véritable nature de l'énergie et de la matière noires est donc devenu l'un des principaux enjeux de la cosmologie moderne.

Le phénomène de lentille gravitationnelle dit "faible", est l'effet par lequel la lumière émise par les galaxies lointaines est très légèrement défléchie par l'effet de marée gravitationnelle des structures se trouvant en avant-plan. Parce qu'il ne dépend que de la physique de la gravitation, cet effet offre l'opportunité unique de pouvoir sonder la distribution de masse de façon directe et sans biais. Cette technique est maintenant devenue routine pour étudier la matière noire, des exemples bien connus d'application étant la reconstruction de la masse des amas de galaxies et l'étude des propriétés des halos de matière noire amassés autour des galaxies. Une autre application plus récente de l'effet gravitationnel faible est l'analyse du signal cosmologique induit par les structures à grande échelle, appelé "cisaillement cosmologique". Ce signal peut être exploité pour retracer la croissance des structures cosmiques et celle de l'Univers dans son ensemble, ce qui le rend particulièrement attrayant pour l'étude de l'énergie noire.

De tous les effets de lentilles gravitationnelles, celui dû au cisaillement cosmologique est le plus subtil et sa détection requiert une analyse très précise des formes de millions de galaxies lointaines et très peu lumineuses dans le spectre infrarouge proche. Le facteur qui a le plus limité la précision des mesures de cisaillement cosmologique a été jusqu'à présent le degré de couverture relativement réduit du ciel par les campagnes d'observation. Les campagnes de prochaine génération s'affranchiront de cette limitation en explorant une portion bien plus grande du ciel avec une meilleure qualité d'image. Les erreurs statistiques consécutives à ces nouvelles études deviendront alors négligeables au regard des erreurs de mesure à caractère systématique. Ces dernières proviennent en majeure partie des algorithmes de mesure de forme des galaxies, de la convolution des images par la fonction d'étalement du point (PSF) instrumentale et éventuellement atmosphérique, auxquels s'ajoutent l'effet de pixellisation engendré par l'intégration des rayons lumineux sur les détecteurs et les dégradations dues à diverses sources de bruit. Mesurer le cisaillement cosmologique impose donc de résoudre le problème inverse consistant à recouvrer le signal de cisaillement originel à partir d'images de galaxies brouillées par la PSF, pixellisées et altérées par le bruit, tout en maintenant le niveau d'erreur dans les limites exigées par les futures campagnes de mesure de lentille gravitationnelle faibles.

Le chemin pour y parvenir n'est pas exempt d'obstacles. En fait, l'on a estimé qu'un gain de l'ordre de 10% est encore nécessaire pour atteindre les niveaux de précision exigés par une mission spatiale telle que la future sonde Euclid de l'ESA, dont le lancement est prévu à la fin de la décennie. Des progrès substantiels ont néanmoins été effectués ces quelques dernières années, grâce en particulier à des initiatives comme la série des "GREAT challenges" (GRavitational lEnsing Accuracy Testing). Le but de ces compétitions est essentiellement de promouvoir le développement de méthodes de mesures de cisaillement cosmologique plus précises. Les contributions de chercheurs travaillant dans des domaines non directement liés à l'astronomie, comme les sciences informatiques ou statistiques, sont également invités à participer.

Nous débutons ce rapport de thèse par une introduction à la cosmologie moderne : ses fondements, ses succès et les défis auxquels elle est aujourd'hui confrontée. Nous continuons avec un exposé de la théorie décrivant le phénomène de lentille gravitationnelle faible. Cela nous permet d'expliquer comment l'étude du cisaillement cosmologique permet de placer des contraintes précises sur les paramètres cosmologiques. La dernière partie de cette thèse est consacrée à la mesure du cisaillement cosmologique dans ces aspects pratiques. Après une revue du sujet, nous exposons les principales contributions que nous avons apportées dans ce domaine durant notre thèse : le développement d'une nouvelle méthode de mesure de ce cisaillement ainsi que de nouveaux algorithmes pour l'interpolation de la PSF et la réduction du bruit.

La méthode *gfit* de l'auteur s'est distinguée comme l'une des procédures de mesure du cisaillement les plus performantes dans la récente compétition "GREAT10 Galaxy Challenge". Cette méthode consiste essentiellement à ajuster les profils de lumière des galaxies sur les images observées afin d'estimer le spectre de cisaillement cosmologique. La correction des effets de la PSF est automatique et un algorithme de réduction du bruit auquel l'auteur a contribué, peut optionnellement être appliqué au préalable.

Un autre problème important à résoudre dans le cadre de la mesure du cisaillement est celui de l'interpolation de la PSF. Cette dernière n'est vraiment connue qu'aux positions occupées par les étoiles alors que la correction de la PSF est en fait requise à n'importe quelle autre position dans le ciel. Nous avons développé de nouvelles techniques d'interpolation de PSF à l'occasion de la compétition "GREAT10 Star Challenge", dédiée à la résolution de ce problème. Notre participation s'est avérée être un grand succès car l'une de nos méthodes d'interpolation a remporté la première place de cette compétition, et quatre autres, les places suivantes.

Enfin, nous avons contribué au développement d'une méthode de réduction du bruit basée sur l'utilisation des ondelettes. Cette technique est particulièrement bien adaptée au domaine des lentilles gravitationnelles faibles car n'altérant pas les formes des galaxies.

Mots-clés : astrophysique, cosmologie, paramètre cosmologique, lentille gravitationnelle, effet de lentille gravitationnelle faible, cisaillement cosmologique, mesure de forme, measurement de cisaillement cosmologique, fonction d'étalement du point, PSF, deconvolution, réduction du bruit, GREAT08, GREAT10.

Contents

Acknowledgements	v
Abstract (English/Français)	vii
List of figures	xiii
List of tables	xix
1 Introduction	1
1.1 Concordance cosmology	1
1.2 The dark Universe	1
1.3 Gravitational lensing	2
1.4 Weak gravitational lensing and the cosmic shear	3
1.5 Measuring the cosmic shear	4
1.6 Outline of this thesis	4
2 Quick overview of modern cosmology	5
2.1 Early cosmological models and fundamental assumptions	5
2.1.1 The “Cosmological Principle”	6
2.1.2 Modeling the content of the Universe	7
2.1.3 Einstein’s static Universe and the cosmological constant	7
2.1.4 An expanding Universe	8
2.2 Modeling the expansion of the Universe	9
2.2.1 The Friedmann–Lemaître–Robertson–Walker metric	9
2.2.2 Rate of expansion	10
2.2.3 Cosmological redshift	11
2.2.4 Dynamical equations	12
2.2.5 Scaling of matter and energy components	12
2.2.6 Critical density and density parameters	13
2.2.7 Extreme scenarios of evolution	14
2.2.8 Cosmological distances	15
2.3 Formation of cosmic structures	18
2.3.1 Newtonian fluid equations of a collisional fluid	19
2.3.2 Newtonian linear perturbation equations in comoving coordinates	19
2.3.3 Density perturbations of a non-relativistic fluid with zero pressure	20
2.3.4 Density perturbations in a non-relativistic fluid with non-zero pressure	21
2.3.5 Density perturbations in a relativistic fluid with non-zero pressure	22

Contents

2.3.6	Density perturbations in a Λ -dominated Universe	23
2.3.7	Evolution of the density perturbations of baryonic matter	24
2.3.8	Evolution of the density perturbations of non-baryonic dark matter	24
2.3.9	Linear structure growth on super-horizon scales	24
2.3.10	Statistical properties of the matter density field	26
2.4	“Concordance” cosmology	30
2.4.1	The “Big Bang”	30
2.4.2	The Cosmic Microwave background	31
2.4.3	Dark matter and the “cold” dark matter paradigm	32
2.4.4	Accelerated expansion and the Λ CDM cosmological model	35
2.4.5	Latest constraints on cosmological parameter	40
2.4.6	Timeline	41
2.5	Unsolved problems	41
2.5.1	The “Horizon” and “Flatness” problem	42
2.5.2	The physical nature of dark matter	42
2.5.3	The physical nature of dark energy	43
3	Constraining cosmology with weak gravitational lensing	49
3.1	Fundamentals of gravitational lensing	49
3.1.1	Deflection of light and the weak field approximation	49
3.1.2	“Thin lens” approximation and the lens equation	51
3.1.3	Deflection potential	52
3.1.4	Image magnification and distortion	52
3.1.5	Geometrical interpretation	54
3.1.6	Representation in polar coordinates	56
3.1.7	Reduced shear	57
3.1.8	“Strong” versus “weak” lensing	58
3.2	Main applications of gravitational lensing	58
3.2.1	Strong gravitational lensing	58
3.2.2	Weak gravitational lensing	60
3.3	The “cosmic shear”, weak lensing by large-scale structures	61
3.3.1	Propagation of light in an inhomogeneous Universe	61
3.3.2	Effective convergence	63
3.3.3	Effective convergence power spectrum	64
3.3.4	E-modes and B-modes	65
3.3.5	Second-order measures of cosmic shear	66
3.4	Constraining cosmology with cosmic shear	68
3.4.1	Cosmic shear and cosmology	68
3.4.2	Determination of cosmological parameters from cosmic shear data	70
3.4.3	Cosmological constraints from cosmic shear observations	71
3.4.4	Probing dark energy with cosmic shear	74
3.4.5	Tomography and 3D lensing	75
3.4.6	Breaking the (Ω_m, σ_8) degeneracy	76
3.4.7	Future prospects	76

4	Cosmic shear measurement	79
4.1	Principles and challenges	79
4.1.1	Cosmic shear from galaxy shapes	79
4.1.2	Observational challenges	80
4.1.3	Methodological challenges	84
4.1.4	Computational challenges	85
4.2	The STEP and GREAT initiatives	86
4.2.1	The STEP programs	86
4.2.2	The GREAT08/10 challenges	86
4.3	Main approaches to shear measurement	88
4.3.1	Shear estimation from second-order brightness moments (KSB, KSB+)	88
4.3.2	“Forward model fitting” methods (DeepZot, gfit)	89
4.3.3	Analytical image decomposition (Shapelets, Reglens)	90
4.3.4	Bayesian analysis of galaxy shapes (lensfit, Im2Shape)	90
4.3.5	Image stacking	90
4.3.6	Application of machine learning techniques (DeepZot, MegaLUT, TVNN)	91
4.4	A closer look at some shear measurement methods	91
4.4.1	Moment-based shear measurement: idealized case	91
4.4.2	Moment-based shear measurement with KSB/KSB+	95
4.4.3	Galaxy model fitting with <i>gfit</i>	98
4.4.4	Image decomposition with Shapelets	114
4.4.5	Bayesian shear estimation with lensfit	120
4.5	PSF interpolation for weak lensing analysis	123
4.6	A denoising scheme for weak lensing	145
5	Conclusion	155
A	Appendix	157
A.1	Gravitational lensing magnification and shear	157
A.1.1	Inverse magnification transformation $\partial\boldsymbol{\beta}/\partial\boldsymbol{\theta}$	157
A.1.2	Magnification transformation $\partial\boldsymbol{\theta}/\partial\boldsymbol{\beta}$	162
A.2	Complex ellipticity χ	167
A.2.1	Expression for χ_1	169
A.2.2	Expression for χ_2	170
A.3	Explicit expression of the image (Q_{ij}) matrix	172
A.4	Eigenvalues of the image (Q_{ij}) matrix	174
A.4.1	First Derivation	174
A.4.2	Second Derivation	175
A.4.3	Expression in terms of the “shape parameters” Σ and $\Delta\Sigma$	177
A.5	Representation of the image (Q_{ij}) matrix in Polar coordinates	177
	Bibliography	194
	Curriculum Vitae	195

List of Figures

2.1	The final results of the 2dF Galaxy Redshift Survey (Colless et al. 2003). Galaxies are not distributed randomly, but are clumped together in groups and clusters connected by large filaments that enclose regions largely devoid of galaxies. . .	6
2.2	In Hubble (1929a), E. Hubble showed that almost all galaxies receded from ours with radial velocities proportional to their distances, implying the Universe was in expansion.	8
2.3	A small-size and a larger-size perturbations entering the horizon.	25
2.4	<i>Left:</i> Evolution of perturbations entering during the radiation domination era. Cold Dark matter is represented in black and baryons in blue. <i>Right:</i> Evolution of perturbations entering during the matter domination era.	25
2.5	Adiabatic transfer functions corresponding to baryons, hot dark matter (HDM), cold dark matter (CDM) and other possible forms of matter (Peacock 1998). . .	28
2.6	Matter power spectrum computed using the WMAP + SDSS cosmological parameters estimated in (Tegmark et al. 2004b). The solid and dashed curves respectively show the non-linear and linear power spectra. The linear power spectrum asymptotically falls off as $\sim k^{-3}$, whereas the non-linear spectrum deviates from the linear curve due to the enhanced contributions of non-linear effects on small-scale perturbations. The non-linear effects were computed using the fitting functions from Peacock & Dodds (1996).	29
2.7	<i>Left:</i> The CMB temperature fluctuations from the Planck probe data seen over the full sky (Ade et al. 2013a). <i>Right:</i> the angular power spectrum of the temperature anisotropies measured by the Planck probe (Ade et al. 2013a). This plot shows the temperature fluctuations as a function of angular size. The Planck data are in red color, with error bars, the best fit model is the blue curve, and the smoothed binned cosmic variance curve is the shaded region.	32
2.8	<i>Left:</i> Big Bang Nucleosynthesis predictions and observations. The boxes indicate the observational estimates for the primordial abundances of helium 4 (observed in galactic HII regions), deuterium (inferred from the absorption spectra of high-redshift quasars) and Lithium 7 (deduced from the surface of the oldest stars in our Galaxy). The horizontal arrow points to the upper limit of the abundance of helium 3, relative to hydrogen (Charbonnel 2002). <i>Right:</i> Several rotation curves of spiral galaxies, as determined by Vera Rubin and collaborators (Rubin et al. 1978). Predictions based on the mass of visible matter and gas would have resulted in curves that would decrease at large distances rather than remaining approximately constant.	33

List of Figures

2.9 *Left*: The telescope image of the “Bullet” cluster with the white bar indicating 200 kpc at the distance of the cluster. *Right*: Chandra image of the cluster. Shown in green contours in both panels are the weak-lensing reconstructions. The white contours correspond to 68.3%, 95.5%, and 99.7% confidence levels (Clowe et al. 2006). 34

2.10 *Left*: First evidence for cosmic acceleration from the Supernova Cosmology Project (SCP): the Hubble diagram shows the evolution of the apparent luminosity m_B with the redshift z for 42 high-redshift SNe Ia from the SCP (Perlmutter et al. 1999) and 18 low-redshift SNe Ia from the Calan/Tololo Supernova Survey (Hamuy et al. 1996). *Right*: The cover of Science Magazine in December 1998, celebrating the breakthrough of the year: the discovery of cosmic acceleration from supernovae. 36

2.11 *Left*: joint constraints on Ω_m and Ω_Λ from the SNe Union2.1 compilation, WMAP 7-years CMB and BAO from SDSS DR 7, at 68.3%, 95.4%, and 99.7% confidence level (assuming $w = -1$) Suzuki et al. (2012). The Union2.1 compilation combines multiple SNe data sets based on a scheme described by Kowalski et al. (2008). *Top right*: Joint constraints on the dark energy equation of state parameter $w(z) = w_0 + w_a[1 - a(z)] = w_0 + w_a(z/(1+z))$ (Linder 2003; Chevallier & Polarski 2001) from the Planck data (Ade et al. 2013a,b), the WMAP 9-year data (Hinshaw et al. 2012) (denoted by WP), BAO from SDSS DR7 and SNe data (Union2.1) (Suzuki et al. 2012) and SNLS (Conley et al. 2011), consistent with a cosmological constant with $w = -1$. *Bottom right*: Similar joint constraints on the dark energy equation of state from the combined Planck, WMAP 9-year (WP) and BAO SDSS DR7 data, showing the dependency on the value of H_0 (Ade et al. 2013b). 39

2.12 The respective contributions of the constituents of the Universe at present time (left) and at the epoch of recombination (about 380,000 years after the Big Bang), right. The WMAP data revealed that the universe is made of about 5% atoms (baryons), whereas dark matter and dark energy comprise respectively about 23% and 72% (source: WMAP 7-year data). The more recent results from the Planck CMB satellite (Ade et al. 2013a,b) suggest a weaker cosmological constant (by $\sim 2\%$), more baryons (by $\sim 3\%$) and more cold dark matter (by $\sim 5\%$). 40

2.13 *Left*: The history of the Universe as we understand it today. *Right*: Thermal history of the Universe (source: NASA/WMAP Science Team). 41

3.1 A light ray intersects the lens plane at \mathbf{x}_i and is deflected by an angle $\hat{\alpha}$ 50

3.2 Geometry of a typical gravitational lensing system. A light ray travels from the source S at transverse distance η from the optic axis to the observer at O , passing the lens at transverse distance ξ . As a result, that light ray is deflected by an angle $\hat{\alpha}$. The observer at O measures the respective angular separation of the source and the image as $\boldsymbol{\beta}$ and $\boldsymbol{\theta}$. The distances between the observer and the source, the observer and the lens, and the lens and the source are respectively D_s , D_d and D_{ds} . The angles $\hat{\alpha}$ and $\boldsymbol{\alpha}$ are related through $\boldsymbol{\alpha}D_s = \hat{\alpha}D_{ds}$ 51

3.3 Geometrical effects of the transformation $\boldsymbol{\theta} \rightarrow \boldsymbol{\beta}$ described by the \mathcal{A} matrix. . . 54

3.4 Geometrical effects of the transformation $\boldsymbol{\beta} \rightarrow \boldsymbol{\theta}$ described by the \mathcal{M} matrix. . . 55

3.5 Geometrical effects of convergence and shear: convergence magnifies the source without altering its shape, while shear only changes the shape. The case of the magnification transformation $\beta \rightarrow \theta$ is shown.	56
3.6 <i>Up-left</i> : the two images (A & B) of the quasar Q 0957+561 (Fischer et al. 1997). <i>Up-right</i> : the quadruple images of the “cloverleaf” quasar H1413+117 (Turnshek et al. 1997) as observed with the Hubble Space Telescope. <i>Bottom-left</i> : a 8GHz VLA map of the radio ring MG1131+0456. <i>Bottom-right</i> : giant arcs in the lensed galaxy cluster Abell 2218.	59
3.7 Mapping of a lens with four sources: three sources A, B, C on caustics and one on-axis source (square). Adapted from Peacock (1998).	59
3.8 Simulation of the propagation of three light rays through the large-scale structures of the Universe. The rays are deflected and distorted in numerous ways and both the location and shape of the original light sources are altered as seen by an observer on Earth. Credit: S. Colombi (IAP), CFHT Team.	62
3.9 <i>Upper row</i> : a mass overdensity (left) or underdensity (right) generates curl-free patterns called E-modes where the shear is respectively tangentially aligned (left) or radially aligned (right); <i>Lower row</i> : divergence-free B-mode pattern, obtained from the E-mode pattern by rotating all shears by 45° . B-modes cannot be produced by gravitational lensing (Van Waerbeke & Mellier 2003).	65
3.10 <i>Left</i> : the tangential and cross components of the shear as defined in (3.38) and (3.39); <i>Right</i> : illustration of the aperture mass statistics.	67
3.11 Constraints on the matter power spectrum obtained from the Sloan Digital Sky Survey (SDSS) by various probes, including cosmic shear. A Λ CDM cosmological model with $\Omega_m = 0.28$, $h = 0.72$, $\Omega_b/\Omega_m = 0.16$ was used. Picture from Tegmark et al. (2004a).	69
3.12 The effective convergence power spectrum P_k (left) and its dimensionless form (right) plotted for different cosmological models. The figure illustrates the sensitivity of P_k on cosmology. A mean source distribution $z_s = 1.5$ was assumed. The thin curves were calculated taking into account linear evolution only whereas the thick curves were derived using the full, non-linear evolution according to (Peacock & Dodds 1996). Plots from (Schneider et al. 1998).	70
3.13 Illustration of the dependence of the effective convergence on cosmology. The Terms in green color fixes H_0 and Ω_m . The terms terms highlighted in red and blue depend on cosmological distances and yield constraints on cosmological parameters. The term in blue is determined by the amplitude and shape of the matter power spectrum and can be used to probe the growth function (see Sect. 3.4.4).	71

3.14	Shear dispersion of several early cosmic shear surveys (CFHT vW+: Van Waerbeke et al. (2000); CFHT K+: Kaiser et al. (2000); CTIO: Wittman et al. (2000); VLT: Maoli et al. (2001); CFHT vW++ Van Waerbeke et al. (2001)). The inner and outer error bars respectively correspond to statistical and total uncertainties. The expected shear dispersion for a Λ CDM cosmological model with $\Omega_m = 0.3$ and $\Gamma = 0.21$ are also shown for a range of values for the median source redshift z_s , corresponding approximately to the uncertainty in this parameter. The models are shown both for $\sigma_8 = 1$ (solid lines) and $\sigma_8 = 0.7$ (dashed) cluster normalization. All results are broadly consistent with each other as well as with Λ CDM with $\sigma_8 = 1$. Source Bacon et al. (2003).	72
3.15	<i>Top left:</i> Joint (Ω_m, σ_8) constraints obtained by Contaldi et al. (2003) from the combination of the red-sequence cluster weak lensing survey (RCS) (Hoekstra et al. 2004) and the WMAP 1st year CMB data (Bennett et al. 2003b). <i>Top right:</i> Joint (Ω_m, σ_8) constraints (68.3, 95.5, and 99.7 %) found by Benjamin et al. (2012) from the CFHTLenS survey (5 years of CFHTLS data) (blue), combined with the WMAP 7th year CMB results (black), SDSS-III Baryon Oscillation Spectroscopic Survey (BOSS) (Anderson et al. 2012) and the R11 HST constrains on H_0 (Riess et al. 2011) (pink). A flat Λ CDM cosmological model is assumed. <i>Bottom left:</i> Contour plots computed by Jarvis et al. (2006), showing the combined (Ω_m, σ_8) constraints between the weak lensing CTIO survey (Jarvis et al. 2003), WMAP 1st year (Bennett et al. 2003b) and Type Ia supernovae, assuming a variable dark energy equation of state. <i>Bottom right:</i> Constraints obtained by Jarvis et al. (2006), on the dark energy equation of state (w_0, w_a) in the parametrization (3.71).	73
3.16	Planned survey with a weak lensing component.	77
4.1	<i>Upper panel:</i> schematic view of the different intervening processes, from the formation of the galaxy image to its restitution by the detector. (1) The original image (shape unknown) is changed with an unknown amount of shear to be estimated (2). The effect is exaggerated ~ 10 times here. The sheared image is then (3) convolved with the PSF resulting e.g. from the telescope and atmosphere. The resulting blurred image is further altered by a nearly constant sky background noise and pixelated (4). Finally (5), Poisson and Gaussian noise are generated during the image acquisition and restitution. <i>Lower panel:</i> star image experiences a similar sequence of transformation, except that the shear effect is negligible. Picture adapted from the GREAT08 handbook (Bridle et al. 2009). . .	85
4.2	Illustration of the complex ellipticity $\chi = \chi_1 + i \chi_2$. Circular images have both $\chi_1 = 0$ and $\chi_2 = 0$	94
4.3	<i>Left:</i> the GREAT08 leaderboard of the low-noise dataset at the close of the challenge (<i>gfit</i> is in third position). <i>Right:</i> the corresponding leaderboard for the high-noise dataset. The CVN Fourier and KK99 entries are stacking methods (see Sect 4.3.5). <i>gfit</i> is in fifth position. Source: GREAT08 results paper (Bridle et al. 2010).	97
4.4	The results of the 12 top-ranking methods of the GREAT10 Galaxy challenge out of 95 submissions. The bias metrics \mathcal{A} and \mathcal{M} , along with the quality Q , Q_{dn} and $Q_{dn\&trained}$ have been specified in Kitching et al. (2012a).	99

4.5	<i>Left plot</i> : multiplicative and additive biases of the ten leading shear measurement methods. <i>Right plot</i> : the biases of the four best performing methods. . .	99
4.6	The basis functions, up to order $n_{max} = 6$, parametrized by two integers n_1, n_2 (Massey & Refregier 2005).	115
4.7	The first few polar Shapelets basis functions $\chi_{n,m}$. The real components of the Shapelet basis functions are plotted in the top panel and the imaginary components in the bottom panel (Massey & Refregier 2005).	116
4.8	The final leaderboard of the Star Challenge, as displayed on the GREAT10 web site just after the deadline. The six methods, B-Splines, IDW, RBF, RBF-thin, Kriging and IDW-Stk were developed by the author and are described in Gentile et al. (2013). See also Kitching et al. (2012c).	123
A.1	Geometrical effects of the transformation $\boldsymbol{\theta} \rightarrow \boldsymbol{\beta}$ described by the \mathcal{A} matrix. . .	160
A.2	Geometrical effects of the transformation $\boldsymbol{\beta} \rightarrow \boldsymbol{\theta}$ described by the \mathcal{M} matrix. . .	165



List of Tables

2.1	Idealized constituents of the Universe and their scaling	13
3.1	Ongoing and planned surveys.	77
4.1	Approximate targeted bias of current and future cosmic shear surveys	88

1 Introduction

1.1 Concordance cosmology

How did the Universe happen to be? How did it evolve? What is it made of? Will it last forever? Such simple, yet fundamental questions have haunted mankind since the edge of time.

Modern cosmology attempts to provide quantitative answers through the application of the scientific method. Physical cosmology, as it is also called, was essentially born in the early twentieth century with the formulation of Albert Einstein's theory of general relativity (Einstein 1915, 1917). Einstein realized that the application of his field equations produced valid solutions when applied to a Universe modeled as a homogeneous and isotropic distribution of matter and energy. Since then, increasingly accurate astronomical observations combined with constant progress in the mathematical and physical sciences have succeeded in producing today's standard model of cosmology. This theoretical framework is very successful in reproducing all observations we have accumulated about our Universe, which is in itself an extraordinary achievement. Particularly remarkable is the fact that each of the key cosmological parameters governing the model has been corroborated by at least two very different observational methods, which is why the theory is often referred to as "concordance cosmology".

1.2 The dark Universe

Two of the key parameters of the standard model are the mass and energy densities of the Universe. The latest measured values of these parameters reveal that ordinary baryonic matter represents only a most 5% of the total mass of the Universe. The greatest challenge of cosmology today is perhaps to explain the physical nature of the "missing" matter and energy components, the so-called "dark matter" and "dark energy". Unfortunately, although concordance cosmology agrees very closely with the measured amount of these "dark" components — around 27% attributed to dark matter and about 68% to dark energy — it does not provide definitive answers about their true physical nature.

Dark matter does not mediate the electromagnetic force and its presence can only be indirectly detected through its gravitational effect on massive structures. This explains why it has taken so long to discover its existence. Indeed, until the first evidence of dark matter were discovered in 1933 by Fritz Zwicky (Zwicky 1933), astronomers had firmly believed they could faithfully rely on light or other types of electromagnetic radiation to infer knowledge about the Universe.

Although Zwicky's observations were initially received with great skepticism, the existence of a non-luminous matter was subsequently confirmed in the 1970s (e.g., Rubin & Ford 1970; Ostriker & Peebles 1973; Einasto et al. 1974; Ostriker et al. 1974; Mathews 1978; Faber & Gallagher 1979). It further became clear in the 1980s and 1990s that only a small fraction of the missing mass could be in baryonic form and that dark matter might be "cold", that is, in the form of some as yet unknown species of non-relativistic elementary particles (e.g., Rees & Ostriker 1977; White & Rees 1978; Doroshkevich et al. 1981; Zeldovich et al. 1982; Bond & Szalay 1983; White et al. 1993; Dekel 1994; Bahcall et al. 1995; Copi et al. 1995; Navarro et al. 1997). If this is indeed the case, we can then hope to discover dark matter candidates in high-energy particle accelerator experiments.

The situation is much less optimistic as regards dark energy. Like dark matter, this elusive quantity does not seem to interact with ordinary matter either. For decades, astronomers and cosmologists had believed the evolution of the Universe was solely governed by its matter content and geometry. But at the turn of the millenium, the analysis of the light curves of type Ia supernovae and the temperature anisotropies of the relic background radiation of the Universe revealed a very different — and perplexing — picture. The first surprise was that the geometry of the Universe was found to be flat to a high precision even though the combined densities of visible and dark matter alone are not sufficient to close the Universe (Smoot et al. 1992; Bennett et al. 2003b; Spergel et al. 2003; Tegmark et al. 2004b). Secondly, cosmic expansion appeared to be speeding up and not slowing down as expected (Perlmutter et al. 1997; Riess et al. 1998; Schmidt et al. 1998; Perlmutter et al. 1999; Knop et al. 2003; Riess et al. 2004). The immediate response was to reintroduce Einstein's cosmological constant Λ in the cosmological model, now acting as a new energy-momentum source originating from the vacuum (Zeldovich 1967; Zeldovich & Novikov 1983). The resulting model, which has become the concordance model, is able to reproduce the kinematics of acceleration very well. But despite this success, fundamental physics is proving unable to explain the smallness of Λ , which casts doubts on the validity of that interpretation. In desperation, cosmologists have invoked a new, as yet unknown, exotic form of energy with negative pressure — the dark energy — which has the virtue of simultaneously making up for the missing energy density and explaining accelerated expansion. There are quite a few possible alternative models of dark energy, notably in the form of time-evolving scalar fields and modified gravity, but current observational constraints are not tight enough to discriminate between them. In any case, the extremely low density of dark energy — less than $10^{-29} \text{ g cm}^{-3}$ — means it is hopeless to measure it from particle physics experiments as may be possible for dark matter. Answers can only come from extremely accurate astronomical observations.

1.3 Gravitational lensing

Light rays emitted by distant sources are deflected in different ways as they cross the gravitational field of intervening matter along their path to the observer. This phenomenon is commonly referred to as "gravitational lensing". The fact that gravity could bend light was hypothesized by Isaac Newton in his *Opticks* treatise and theoretically predicted by the theory of general relativity. This phenomenon was experimentally verified for the first time by Frank Dyson and Arthur Eddington when they measured the deflection of star light by the gravitational field of the Sun on the occasion of the 1919 solar eclipse (Dyson et al. 1920). In fact, Albert Einstein remained skeptical about projects of detecting such small deflections

on more distant astronomical objects (Einstein 1936). In 1937, Fritz Zwicky contradicted this point of view, predicting some of the effects of gravitational lensing and suggesting practical astrophysical applications (Zwicky 1937a). But despite this, one had to wait until the discovery in 1979 of the first gravitationally lensed system (QSO 0957+561 A & B) (Walsh et al. 1979) for the potential of gravitational lensing for astronomy and cosmology to be rediscovered. That event triggered an enormous amount of publications and has now become a very active field of research.

In the case of QSO 0957+561 A & B) the gravitational field of the lens, a giant elliptical galaxy, is so strong that two images of the same distant quasar QSO 0957+561 are observed. This is a particular example of “strong” lensing, which manifests itself by the observation of multiple or distorted images. Sometimes, the distortion is so extreme that the source objects are barely recognizable. Gravitational lensing in that regime is very useful to probe the source objects or the lensing system itself. Another important application is the measurement of the Hubble constant (Refsdal 1964a,b), which is only known with an accuracy of the order of 5% today.

1.4 Weak gravitational lensing and the cosmic shear

In most cases, however, the lensing effect is much more subtle, where intervening foreground structures induce weaker gravitational fields. Such “weak lensing” occurs around every massive object, like galaxies, galaxy clusters or strand of dark matter, but contrary to strong lensing, the weak lensing effect is far too small to be measurable from a single source. Instead, an integrated lensing signal can be reconstructed by performing a statistical analysis of the distortion of the apparent shapes of a large number of source galaxies. Because it only relies on the physics of gravity, gravitational lensing is sensitive to any form of energy and matter, whatever its physical state. So, in principle, key information about dark matter and dark energy can be extracted from the weak lensing signal.

In fact, since the first evidence of weak lensing effect around foreground clusters were detected by Anthony J. Tyson and collaborators (Tyson et al. 1990), weak lensing has become a well-established tool for estimating the total mass of galaxy clusters (e.g., Kochanek 1990; Miralda-Escude 1991a), mapping the distribution of their luminous and dark matter mass content (e.g., Dahle et al. 2002; Gray et al. 2002; Clowe & Schneider 2002; Wittman et al. 2003; Margoniner et al. 2005; Umetsu 2010; Pires et al. 2010), constraining the properties of galaxy dark matter halos (e.g., Hoekstra et al. 2004; Sheldon et al. 2004) and recently, detecting dark matter filaments (e.g., Jauzac et al. 2012).

Weak gravitational lensing has also emerged as a powerful technique that can potentially place very tight constraints on cosmological parameters and dark energy. The idea that this technique could constrain cosmology was postulated as early as 1966 (Kristian & Sachs 1966; Gunn 1967) but only theoretically investigated in the 1990s by a number of authors (e.g., Jaroszynski et al. 1990; Babul & Lee 1991; Blandford et al. 1991; Miralda-Escude 1991b; Kaiser 1992; Villumsen 1996; van Waerbeke et al. 1997; Mellier & Fort 1997; Jain & Seljak 1997; Kaiser 1998; Hu & Tegmark 1999; van Waerbeke et al. 1999). It was found that the lensing of distant background galaxies due to surrounding foreground large-scale structures should be detectable as a faint, but statistically correlated signal, now called the “cosmic shear”. The cosmic shear is directly related to the matter power spectrum and can thus be used to probe the recent expansion history of the Universe and the growth of cosmic structures. This makes it

a very promising technique for investigating the properties of dark energy and the distribution of dark matter on cosmological scales. In 2000, the cosmic shear was eventually detected in random patches of sky by four research groups (Bacon et al. 2000; Kaiser et al. 2000; Van Waerbeke et al. 2000; Wittman et al. 2000).

1.5 Measuring the cosmic shear

Accurately and reliably measuring the cosmic shear poses a number of challenges. The signal itself is subtle and its extraction requires the careful analysis of a great number of small, faint and noisy galaxy images. A first difficulty is thus to study a large enough sky area in order to reduce statistical errors as much as possible. Obtaining accurate redshift information is also very important. Future wide-field surveys such as those envisaged for LSST on the ground and ESA Euclid from space will likely overcome these hurdles. The main challenges will rather lie in reduction of systematic errors so that these do not overwhelm the subtle lensing signal. The most critical sources of uncertainty reside in the insufficient inaccuracy of the existing galaxy shape measurement algorithms and the convolution of the original image by the point spread function due to the optics and atmosphere. Successfully resolving these issues is critical for reaching a better understanding of the nature of dark energy and dark matter through gravitational lensing.

1.6 Outline of this thesis

Weak gravitational lensing and its applications to cosmology constitute the primary topic of this thesis. Our main objective is to describe how weak gravitational lensing by large-scale structures, the “cosmic shear”, can be used to probe dark matter and dark energy, with an emphasis on the latter.

This thesis is structured as follows. We provide in Chapter 2 a critical view of the concordance cosmological model and take the opportunity to present the latests observational results. We also highlight possible extensions to the Λ CDM cosmological model. We are then in position in Chapter 3 to introduce the theory of weak lensing and to explain how it can be used to constrain cosmological parameters and shed light on the dark Universe. In Chapter 4, we cover the practical aspects of weak lensing, describing in particular two very active fields of research: galaxy shape measurement and point spread function (PSF) correction and interpolation. After a review of the latest developments, we introduce the research we have performed in these areas and published in Gentile et al. (2012) and Gentile et al. (2013).

2 Quick overview of modern cosmology

We introduce in this chapter the main physical principles, concepts and theory underlying modern cosmology. We also take the opportunity to give an account of the most recent cosmological observations.

Throughout the text we adopt Einstein's notation, natural units with $c = 1$ and metric signature $(-, +, +, +)$, unless stated otherwise.

2.1 Early cosmological models and fundamental assumptions

After the development of general relativity, Albert Einstein turned his attention to potential cosmological applications of his theory. At that time, our knowledge about the structure, matter distribution and dynamics of the Universe was still at the stage of conjectures. The most advanced telescopes were barely powerful enough to image what looked like nebulae and astronomers were still debating whether these objects were just gas clouds inside the Milky Way or more distant galaxies (e.g., Smith 1982). To build his cosmological model, Einstein could only rely on the equations of general relativity and on philosophical considerations on the nature of the Universe, especially from physicist and philosopher Ernst Mach. He was also influenced by discussions and correspondence with Dutch astronomer Willem de Sitter (de Sitter 1916a,b). The result is the cosmological model he published in 1917 (Einstein 1917).

The starting point of that model is the postulate that the theory of general relativity is a correct description of gravity and can be applied to the Universe as a whole. The original form of the field equations used by Einstein was

$$R_{\mu\nu} - \frac{1}{2} g_{\mu\nu} R = 8\pi G T_{\mu\nu} \quad (2.1)$$

These equations relate the geometry of the Universe (left-hand part) to its content (the right-hand part). The geometry is mathematically described as a four-dimensional manifold with space-time metric $g_{\mu\nu}$ and the two successive contractions of the Riemann curvature tensor, the Ricci tensor $R_{\mu\nu} = R^{\alpha}_{\mu\alpha\nu}$ and the Ricci scalar R . The matter and radiation constituting the Universe are modeled by the energy-momentum tensor $T_{\mu\nu}$. With these equations at hand, the problem is then to find the $g_{\mu\nu}$ and the $T_{\mu\nu}$ that correspond to an adequate description of our Universe.

To tackle this daunting task, Einstein did not have other choice than to make a series of bold

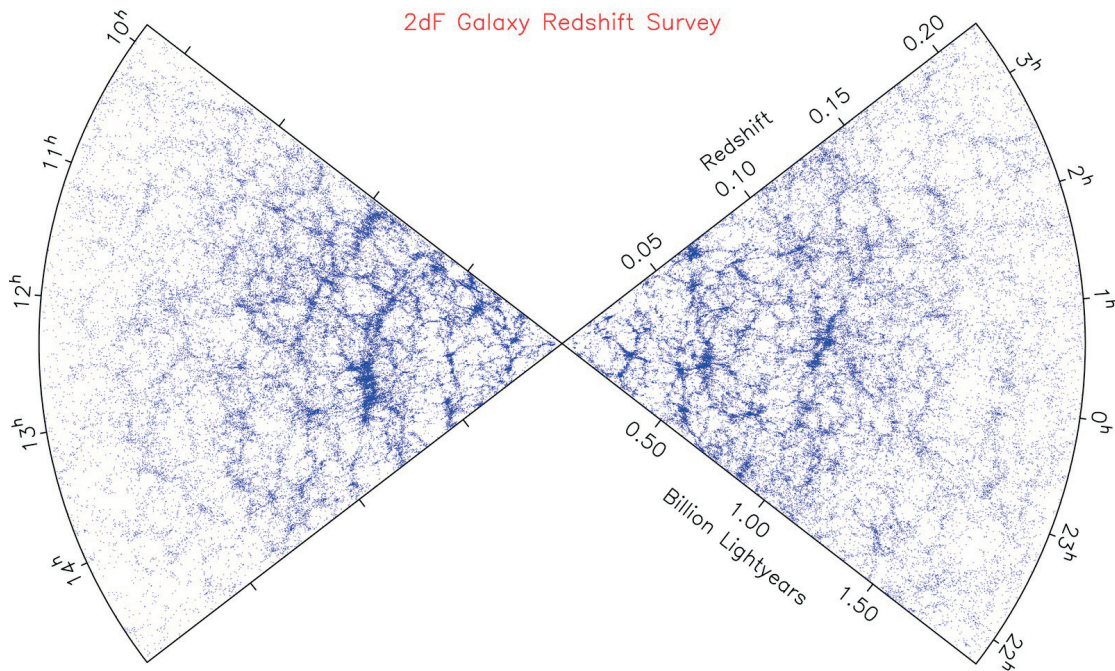


Figure 2.1: The final results of the 2dF Galaxy Redshift Survey (Colless et al. 2003). Galaxies are not distributed randomly, but are clumped together in groups and clusters connected by large filaments that enclose regions largely devoid of galaxies.

and simplifying assumptions about the Universe, which remain valid today.

1. The Universe is, on a sufficiently large scale, homogeneous and isotropic
2. The constituents of the Universe can be well modeled as a perfect fluid

2.1.1 The “Cosmological Principle”

The first assumption is known as the "Cosmological principle", as later coined by Milne (1935), which states that at a given point in time and on a sufficiently large scale, the Universe is homogeneous and isotropic. Isotropy means that at some specific space-time location in the Universe, the space appears the same no matter in what direction one looks (invariance under rotation). Homogeneity is the statement that the properties of the Universe do not depend on location (invariance under translation). There is no necessary relationship between homogeneity and isotropy, as a manifold can be homogeneous without being isotropic (like a torus) or isotropic around a point without being homogeneous (such as a cone around its vertex). However, a manifold that is symmetric everywhere is also homogeneous. Likewise, if a manifold is isotropic around one point and also homogeneous, it will be isotropic around every point.

The cosmological principle was truly a remarkable assumption as it is obvious that, on the small scale, the Universe is clearly not homogeneous, nor it is isotropic. However, the most recent observations show that the cosmological principle appears valid on scales larger than about 100 Megaparsecs (Mpc), where 1 Mpc is a distance of 3.26 million light-years or 3.08×10^{22} meters. This corresponds to the scale of the largest single structures of the

2.1. Early cosmological models and fundamental assumptions

Universe: the superclusters (clusters of clusters) of galaxies, and the vast non-luminous regions that separate them, known as giant voids. These structures form a sponge-like network, where superclusters occupy about 10% of the total volume and the voids, the remaining 90%. Beyond that characteristic scale, the Universe appears truly homogeneous and isotropic. An illustration of these structures is given in Fig. 2.1.

2.1.2 Modeling the content of the Universe

Einstein further simplified the problem by supposing the Universe was uniformly filled with an idealized form of ordinary matter, which he modeled as a perfect fluid. In such fluids, the energy momentum tensor $T_{\mu\nu}$ on the right-hand side of (2.1) is of the form

$$T_{\mu\nu} = (p + \rho) U_\mu U_\nu - p g_{\mu\nu} \quad (2.2)$$

where $U_\mu = g_{\mu\nu} U^\nu = g_{\mu\nu} \frac{dx^\mu}{ds}$ is the fluid four-velocity. The quantities p and ρ are respectively the pressure and density of the fluid, while x^k denotes the trajectory in space-time of a particle in the fluid. Such idealized fluids have no shear stress, viscosity, or heat conduction.

In fact, as shown in the remaining sections, the perfect fluid approximation is still retained in the present-day standard cosmological model for the representation of radiation, matter and various possible forms of dark energy.

2.1.3 Einstein's static Universe and the cosmological constant

Einstein found an exact solution given by a metric with line element

$$ds^2 = -dt^2 + dl^2 = -dt^2 + R^2 \left[\frac{dr^2}{1-r^2} + r^2(d\theta^2 + \sin^2\theta d\phi^2) \right] \quad (2.3)$$

where dl represents the spacelike part in spherical coordinates $\{r, \theta, \phi\}$ and dt is the timelike coordinate. That metric describes a Universe with flat cylindrical geometry, where the spatial sections of the cylinder are 3-spheres of radius R . Such a Universe was stationary, neither expanding nor collapsing.

He realized, however that in such a Universe would have a mean negative pressure and hence not physically viable. Instead of looking for a better model, he chose to adjust the left-hand side of the field equations of general relativity, introducing a small positive Λ term known as the ‘‘cosmological constant’’. The cosmological term had to be positive, curving space-time so as to counteract the attractive gravitation of matter and reach equilibrium. The Λ term also had to be small relative to $4\pi G\rho$ in order to satisfy Poisson's equation $\nabla^2\Phi = 4\pi G\rho$ in the Newtonian approximation, since in this case the Newtonian potential is approximated by $\Phi \approx g_{00} = 4\pi G\rho - \Lambda$. After such modification the field equations became

$$R_{\mu\nu} - \frac{1}{2}g_{\mu\nu}R + \Lambda g_{\mu\nu} = 8\pi G T_{\mu\nu} \quad (2.4)$$

Skeptical about the idea of a stationary Universe, de Sitter soon found another valid solution of an empty but expanding Universe (de Sitter 1917). In 1922, the Russian mathematician Alexander Friedmann had noticed that the Einstein and de Sitter cosmological models were just but

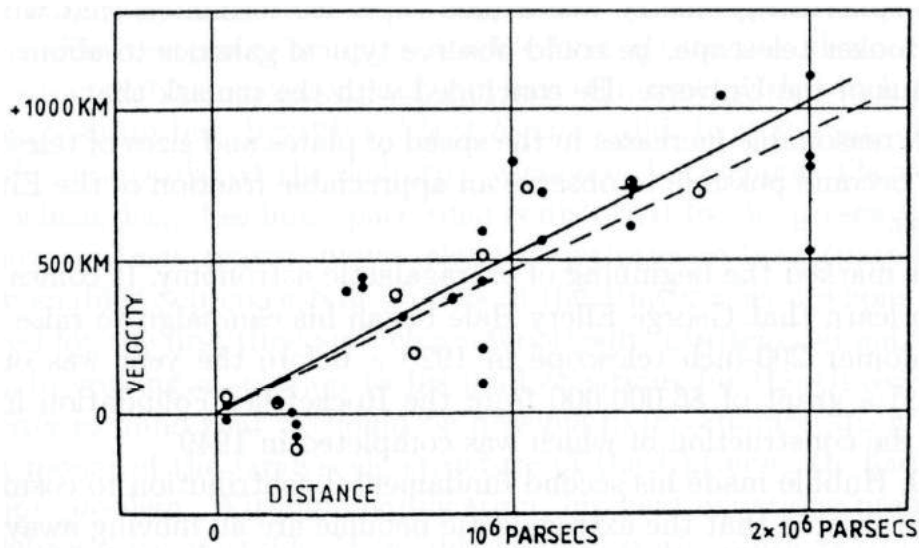


Figure 2.2: In Hubble (1929a), E. Hubble showed that almost all galaxies receded from ours with radial velocities proportional to their distances, implying the Universe was in expansion.

special cases of a broader class of solutions (Friedmann 1922, 1924, 1999a,b). The Belgian priest Georges Lemaître had also independently explored similar solutions between 1925 and 1927 (Lemaître 1925, 1927). Despite being well aware of the work of de Sitter and Friedmann (Einstein 1922, 1923), Einstein persisted in his view until incontestable observational evidence for an expanding Universe were found by Edwin Hubble and his assistant Milton L. Humason between 1929 and 1931 (Hubble 1929a,b; Humason 1931; Hubble & Humason 1931).

2.1.4 An expanding Universe

In his 1929 paper (Hubble 1929a), Edwin Hubble observed that almost all galaxies receded from ours with radial velocities proportional to their distances. He postulated the so-called “Hubble law”

$$v = H_0 D \tag{2.5}$$

In the above expression, v is the radial velocity of the galaxy, D its distance and H_0 is called the “Hubble constant”, in honor of E. Hubble. More details are provided in Sect. 2.2.2.

It became apparent that neither Einstein’s model nor de Sitter’s could provide a realistic approximation of the observed Universe. On one hand, Einstein’s stationary model could not explain the observations of redshift in the spectra of extragalactic sources. On the other hand, de Sitter’s Universe had too low a density as regards the observed density of matter (de Sitter 1930). Moreover, Eddington showed Einstein’s solution was unstable (Eddington 1930). At the same time, the papers from Friedmann and Lemaître were rediscovered and translated (Robertson 1929; Lemaître 1931b; de Sitter 1931).

In 1931, after visiting Edwin Hubble and discussing with Richard C. Tolman, Einstein finally recognized the shortcomings of his cosmological model (Einstein 1931). The next year, Einstein

and de Sitter wrote a paper that laid the foundation to the so-called “Einstein–de Sitter” cosmological model (Einstein & de Sitter 1932), a simple model with flat geometry and without cosmological constant. The Einstein–de Sitter model would prevail as the standard model of cosmology until the 1980s.

2.2 Modeling the expansion of the Universe

2.2.1 The Friedmann–Lemaître–Robertson–Walker metric

Postulating the cosmological principle as valid severely constrains the geometry of possible cosmological models of the Universe. The models of de Sitter, Friedmann and Lemaître featured a spatially symmetrical Universe evolving in time. This can be mathematically decomposed as a $\mathbf{R} \times \Sigma$ space-time where \mathbf{R} represents the time direction and Σ a maximally-symmetric three-dimensional manifold (e.g., Hawking & Ellis 1975). Such a space has a constant spatial curvature and a space-time metric with line element of the form

$$ds^2 = -dt^2 + S^2(t) [A(r)dr^2 + B(r)d\Omega^2]$$

The exact form was independently derived between 1935 and 1936 by the two mathematicians Howard P. Robertson and Arthur G. Walker (Robertson 1935; Walker 1935; Robertson 1936a,b). The resulting metric is called the Friedman–Lemaître–Robertson–Walker (FLRW) metric to honor these two mathematicians and acknowledge earlier contributions from A. Friedmann and G. Lemaître. The FLRW metric is of the form

$$ds^2 = g_{\mu\nu}dx^\mu dx^\nu = -dt^2 + R^2(t) \left[\frac{dr^2}{1 - kr^2} + r^2(d\theta^2 + \sin^2\theta d\phi^2) \right] \quad (2.6)$$

This metric assumes one can associate a timelike coordinate t , called the “cosmic time”, to every spacelike event (r, θ, ϕ) . The cosmic time is the proper time measured by a special class of observers, called fundamental observers who always perceive the Universe around them as isotropic even though the Universe expands. These notions form the basis of Hermann Weyl’s postulate (Weyl 1923). The timelike geodesics of these observers are assumed to never cross except at some single point (past or future), used to define the origin of cosmic time. Weyl’s postulate implies in particular the choice of $g_{00} = -1$ and the absence of cross terms $g_{0\nu}$ in the line element of Robertson–Walker metric.

The (r, θ, ϕ) coordinates are known as “comoving coordinates”, defined so as to always keep the same value even though proper distances increase because of the general expansion flow. In the FLRW metric, the relation between comoving and proper distance is explicit through the presence of the $R(t)$ term, called the “scale factor”, where the physics of the expansion has been absorbed. A proper distance $D_p(t)$ should have a unit of length, so it is conventional to treat comoving coordinates as dimensionless and to assign a dimension of length to $R(t)$. Proper distances $D_p(t)$ and comoving distances h are then related by $D_p(t) = R(t)h$.

The constant k , known as the “curvature parameter”, describes the spatial curvature ascribed to the model Universe. The radial coordinate r is often rescaled so that k takes the values 0 or ± 1 in the FLRW metric. A metric with $k = 0$ describes a spatially flat, open, euclidean space. A space with $k = -1$ is also open, but resembles a saddle and is negatively curved, whereas a space with $k = +1$ has the geometry of a 3-sphere, hence closed and positively curved. This

Chapter 2. Quick overview of modern cosmology

geometrical interpretation is more explicitly seen by introducing a new radial coordinate χ such that $dr = \sqrt{1 - kr^2} d\chi$, which when integrated, gives $r(\chi) = S_k(\chi)$, with

$$S_k(\chi) = \begin{cases} \sin(\chi) & k = +1 \\ \chi & k = 0 \\ \sinh(\chi) & k = -1 \end{cases} \quad (2.7)$$

The metric (2.6) can then be expressed as

$$ds^2 = -dt^2 + R^2(t) [d\chi^2 + S_k(\chi)^2 (d\theta^2 + \sin^2 \theta d\phi^2)] \quad (2.8)$$

It is conventional to normalize $r \rightarrow r/R_0$, define $\kappa = k/R_0$ and use a dimensionless form of the scale factor, replacing $R(t)$ with

$$a(t) = \frac{R(t)}{R_0} \quad (2.9)$$

In (2.9), R_0 is the present-time value of the scale factor, so that $a(0) = a_0 = 1$. The FLRW metric (2.6) then becomes

$$ds^2 = -dt^2 + a^2(t) \left[\frac{dr^2}{1 - \kappa r^2} + r^2 (d\theta^2 + \sin^2 \theta d\phi^2) \right] \quad (2.10)$$

2.2.2 Rate of expansion

The rate of expansion of the Universe with respect to time is defined by the ‘‘Hubble parameter’’

$$H(t) = \left(\frac{\dot{a}}{a} \right) = \frac{d}{dt} \ln(a(t)) \quad (2.11)$$

As its name suggests, the present-time value of this parameter yields the Hubble constant H_0 . Indeed, the Hubble law (2.5) between the observed radial velocities v_r of nearby galaxies and their physical distances D_p can be derived from the FLRW metric. Writing (2.8) as

$$ds^2 = -dt^2 + a^2(t) R_0^2 [d\chi^2 + S_k(\chi)^2 (d\theta^2 + \sin^2 \theta d\phi^2)] \quad (2.12)$$

the instantaneous physical (proper) distance $D_p(t)$ between a comoving observer at $\chi = 0$ and a source at comoving radial coordinate χ is given by¹ $D_p(t) \approx a(t) R_0 \chi$. Then,

$$v_r \approx \frac{dD_p}{dt} = \dot{D}_p(t) = \dot{a}(t) R_0 \chi = \frac{\dot{a}(t)}{a(t)} D_p(t) = H(t) D_p(t).$$

Hence $v_r \approx H_0 D_p(t_0) = H_0 D$ when evaluated today, which is the Hubble law (2.5). In fact, G. Lemaître used a similar reasoning to theoretically derive the Hubble law two years before E. Hubble’s discovery (Lemaître 1927).

Current observations yield a value of H_0 is of the order of $70 \text{ km s}^{-1} \text{ Mpc}^{-1}$ (e.g., Freedman et al. 2001; Paraficz & Hjorth 2010). The value of H_0 remains imprecise today and it is conventional to parametrize it as $H_0 = 100 h \text{ km s}^{-1} \text{ Mpc}^{-1}$. The inverse of H_0 , $H_0^{-1} \approx 10 h^{-1} \text{ Gyr}$, is called

¹This derivation assumes peculiar velocities are ignored, i.e. $\chi \approx \text{constant}$

the ‘‘Hubble time’’ and would be equal to the age of the Universe if the expansion rate would have been constant. The ‘‘Hubble radius’’, $R_H = c/H_0 \approx 3h^{-1}$ Gpc, is the distance a photon would have traveled without interacting during the Hubble time.

A second-order measure of the rate of expansion is provided by the ‘‘deceleration parameter’’, a dimensionless quantity defined by

$$q(t) = -\frac{a(t)\ddot{a}(t)}{\dot{a}^2(t)} = -\frac{\ddot{a}(t)}{a(t)H^2(t)} \quad (2.13)$$

This parameter was defined to be positive upon deceleration of the rate of the expansion. It turns out that the current value of this parameter is negative, signaling a Universe in accelerated expansion. This will be discussed further in Sect. 2.5.3.

2.2.3 Cosmological redshift

A light ray follows a null geodesic $ds^2 = 0$ in the metric (2.10). It follows that the radial trajectory of a light ray emitted by a distant comoving source r_1 at time t_1 and towards a comoving observer at $r = 0$ at time t_0 is determined by the relation

$$\int_{t_0}^{t_1} \frac{dt}{a(t)} = \int_0^{r_1} \frac{dr}{\sqrt{1-\kappa r^2}} \quad (2.14)$$

Differentiating both sides of this expression and noting that r_1 is time-independent, yields

$$\frac{\delta_1}{a(t_1)} = \frac{\delta_0}{a(t_0)} \quad (2.15)$$

where δ_1 represents the time interval between two light signals departing from the source and correspondingly, δ_0 is the time interval separating the signals upon reaching the observer. The respective wavelengths, λ_1 and λ_0 are then related by

$$\frac{\lambda_0}{\lambda_1} = \frac{a(t_0)}{a(t_1)}. \quad (2.16)$$

The observer at $r = 0$ will see λ_0 as shifted relative to λ_1 by a factor conventionally denoted by z with

$$z = \frac{\lambda_0 - \lambda_1}{\lambda_1} = \frac{a(t_0)}{a(t_1)} - 1 \quad (2.17)$$

Letting $a(t_0) = a_0 = 1$, $a(t)$ and z are then related at any time t by

$$a(t) = \frac{1}{1+z} \quad (2.18)$$

In an expanding Universe, $a(t)$ is increasing and the observed wavelengths will be redshifted relative to the emitted wavelengths.

The cosmological redshift z is caused by the stretching of space itself between the observer and the source, which creates the illusion that they move away from each other. It should not be confused with the Doppler redshift, which arises as a consequence of observer and source

moving away *through* space.

The cosmological redshift was first observed by Walter S. Adams in 1912 (Adams 1908) and further observed by Vesto Slipher (Slipher 1913, 1915) and Edwin Hubble (Hubble 1929a,b). It was again G. Lemaître who first proposed the observed redshift of galaxies as arising from the expansion of the Universe (Lemaître 1927).

2.2.4 Dynamical equations

Substituting $g_{\mu\nu}$ components of the FLRW metric (2.8) and the energy–momentum tensor $T_{\mu\nu}$ of the perfect fluid (2.2) in the field equations (2.4) yields a set of two independent equations that together govern the dynamics of the expansion.

The first equation was derived by A. Friedmann in 1922 (Friedmann 1922) and is for this reason commonly referred to as the “Friedmann equation”:

$$H^2 = \left(\frac{\dot{a}}{a}\right)^2 = \frac{8\pi G}{3}\rho - \frac{1}{a^2}\kappa + \frac{1}{3}\Lambda \quad \text{Friedmann equation} \quad (2.19)$$

The Friedmann equation relates the rate of increase of the scale factor, as encoded by the Hubble parameter (2.11), to the total energy density of all matter in the universe.

The second equation is usually called the “acceleration equation” because of its aspect and describes of the expansion accelerates or decelerates as the energy and matter content of the Universe evolves.

$$\frac{\ddot{a}}{a} = -\frac{4\pi G}{3}(\rho + 3p) + \frac{1}{3}\Lambda \quad \text{Acceleration equation} \quad (2.20)$$

A third “conservation”² equation can be derived by combining equations (2.19) and (2.20) or directly from the conservation of energy-momentum, $\nabla_{\mu}T^{\mu\nu} = 0$, where ∇ denotes the covariant derivative associated with the metric $g_{\mu\nu}$.

$$\dot{\rho} + 3H(\rho + p) = 0 \quad \text{Conservation equation} \quad (2.21)$$

2.2.5 Scaling of matter and energy components

The field equations of general relativity produce the two independent equations (2.19) and (2.20) with three unknown a , ρ and p . A third equation relating pressure and energy density, i.e. an equation of state (EOS), is therefore required to determine the evolution of the mean energy density and pressure with the scale factor.

As explained in Sect. 2.1.2, one fundamental assumption of the cosmological model is that each of the constituents of the Universe can be modeled as a perfect fluid. For such fluids, the EOS takes the simple form

$$p = p(\rho) = w\rho \quad (2.22)$$

where w is a dimensionless constant. Substituting (2.22) in (2.21) gives $d\rho/\rho = -3(1+w)\dot{a}/a$,

²Also referred to as the “adiabatic” or “energy” equation

Table 2.1: Idealized constituents of the Universe and their scaling

Component	w_i	ρ	$a(t)$
Pressureless Matter	0	a^{-3}	$t^{2/3}$
Radiation	1/3	a^{-4}	$t^{1/2}$
Cosmological constant (Λ)	-1	a^0	$\exp(H(t))$

which, integrated, tells how components with different EOS evolve with the scale factor

$$\rho(a) = \rho_0 a^{-3(1+w)} \propto a^{-3(1+w)}, \quad \rho_0 = \rho(t_0) \quad (2.23)$$

The Friedmann equation (2.19) also yield the time evolution of the scale factor

$$a(t) \propto t^{\frac{2}{3(1+w)-1}} \quad (2.24)$$

The content of the Universe is idealized into:

- A component with density ρ_m and pressure p_m , that represents homogeneously distributed matter, assumed to be non-relativistic, with velocity v much smaller than c . The pressure of such matter, of the order of $(v/c)^2$, is thus considered negligible, leading to $w = 0$ in (2.22).
- A component with density ρ_r and pressure p_r , that models the behavior of radiation, neutrinos or other relativistic species, with $w = 1/3$ in (2.23).
- A component identified with a non-zero cosmological constant Λ , interpreted as an energy density ρ_Λ arising from the vacuum (Zeldovich 1967; Zeldovich & Novikov 1983) and with negative pressure $p_\Lambda = -\rho_\Lambda$, i.e. with $w = -1$ in (2.23). We will discuss this topic in more details in Sect. 2.5.3.

The EOS and scaling of these components are summarized in Table 2.1.

It is customary to express ρ as $\rho = \sum_i \rho_i$ and p as $p = \sum_i p_i$, where $i = \{m, r, \Lambda\}$ represents the individual component of the Universe. The dynamical equations are then rewritten as

$$H^2 = \left(\frac{\dot{a}}{a}\right)^2 = \frac{8\pi G}{3} \sum_i \rho_i - \frac{1}{a^2} \kappa + \frac{1}{3} \Lambda \quad \text{Friedmann equation} \quad (2.25)$$

$$\frac{\ddot{a}}{a} = -\frac{4\pi G}{3} \left(\sum_i \rho_i + 3 \sum_i p_i \right) + \frac{1}{3} \Lambda \quad \text{Acceleration equation} \quad (2.26)$$

2.2.6 Critical density and density parameters

The Friedmann equation relates the rate of increase of the scale factor, as encoded by the Hubble parameter, to the total energy density of all matter in the Universe. It is useful to define a time-dependent critical energy density for which the spatial curvature is exactly flat ($k = 0$).

$$\rho_c = \rho_c(t) = \frac{3H^2(t)}{8\pi G} \quad (2.27)$$

Chapter 2. Quick overview of modern cosmology

and then define for each specie a dimensionless density parameter at time t by

$$\Omega_i(t) = \frac{\rho_i(t)}{\rho_c(t)} = \frac{8\pi G}{3H^2(t)} \rho_i(t) \quad (2.28)$$

where

$$\Omega_r = \frac{8\pi G}{3H(t)^2} \rho_r(t) \quad \Omega_m = \frac{8\pi G}{3H(t)^2} \rho_m(t) \quad \Omega_{DE} = \Omega_\Lambda = \frac{8\pi G}{3H(t)^2} \rho_\Lambda \quad (2.29)$$

We denote the current value of $\Omega_i(t)$ by

$$\Omega_{i,0} = \frac{\rho_{i,0}}{\rho_{c,0}} = \frac{8\pi G}{3H_0^2} \rho_{i,0} \quad (2.30)$$

It is also conventional to ascribe a fictitious density to curvature, use $\rho_k = -3k/(8\pi GR_0^2 a^2)$ and define

$$\Omega_k(t) = \frac{\rho_k(t)}{\rho_c(t)} = \frac{-\kappa}{H^2(t)a^2(t)} = \frac{-k}{R_0^2 H^2(t)a^2(t)} \quad (2.31)$$

The Friedmann equation (2.25) can then be simplified into

$$1 = \Omega_m + \Omega_r + \Omega_\Lambda + \Omega_k \quad (2.32)$$

It can also be written as

$$H^2(a) = H_0^2 \left(\Omega_r a^{-4} + \Omega_m a^{-3} + \Omega_k a^{-2} + \Omega_\Lambda \right) \quad (2.33)$$

The corresponding equation in terms of the redshift $z = (1/a - 1)$ is

$$H^2(a) = H_0^2 E^2(z) \quad (2.34)$$

where

$$E(z) = \left(\Omega_\Lambda + \Omega_k(1+z)^2 + \Omega_m(1+z)^3 + \Omega_r(1+z)^4 \right)^{1/2} \quad (2.35)$$

2.2.7 Extreme scenarios of evolution

Radiation-dominated Universe

A small value of the scale factor in (2.33) implies the early Universe was dominated by radiation. In this limit, the equation reduces to

$$H^2(a) = H_0^2 \left(\Omega_r a^{-4} \right) \quad (2.36)$$

with solution

$$a(t) = H_0^{1/2} \Omega_r^{1/4} t^{1/2} \propto t^{1/2} \quad (2.37)$$

The transition between a radiation-dominated and a matter-dominated Universe roughly

occurs when $\Omega_r a_{eq}^{-4} = \Omega_m a_{eq}^{-3} = \Omega_r / \Omega_m$. The exact value of a_{eq} depends on the cosmological model, especially on the presence of a cosmological constant. In any case, a_{eq} occurs before a_{rec} , the scale factor at the time of recombination (see Sect. 2.4.2).

Matter-dominated Universe

The scaling of a matter-dominated Universe is obtained by neglecting the curvature and cosmological constant terms in (2.33), which gives

$$H^2(a) = H_0^2 (\Omega_r a^{-3}) \quad (2.38)$$

The scale factor evolution is then of the form

$$a(t) = \left(\frac{3}{2} H_0\right)^{2/3} \Omega_m^{1/3} t^{2/3} \propto t^{2/3} \quad (2.39)$$

The evolution at later times will be first determined by the curvature terms and later on, by the cosmological term.

Universe dominated by a cosmological constant

For $a \gg a_{eq}$, the radiation and matter related terms in the acceleration equation (2.20) can be neglected, yielding

$$\frac{\ddot{a}}{a} = \frac{1}{3} \Lambda = H_\Lambda^2 \Rightarrow a(t) = A \exp H_\Lambda t + B \exp H_{-\Lambda} t \quad (2.40)$$

The range of solutions depend on the curvature parameter k

$$a(t) \propto \begin{cases} \cosh(H_\Lambda t) & k = +1 \\ \exp(H_\Lambda t) & k = 0 \\ \sinh(H_\Lambda t) & k = -1 \end{cases} \quad (2.41)$$

We note that a flat Universe dominated by a cosmological constant has an exponentially growing scale factor at later times.

2.2.8 Cosmological distances

The Robertson–Walker metric (2.10) provides the rules for assigning coordinates to astronomical objects and for turning such coordinates into physical cosmological distances. Two ways of measuring distances are possible. One possibility is to rely on comoving coordinates that remain fixed as the Universe expands; the other is to convert comoving coordinates into physical ones, taking into account the physics underlying the expansion.

Comoving distances

Setting $dt = 0$ in the FLRW metric yields the proper distance, at constant proper time, between a comoving observer at $\chi = 0$ (us) and a source at comoving radial coordinate χ .

$$D_P(t) = R(t) \int_0^{\chi} \frac{dr}{\sqrt{1 - kr^2}} = R(t)\chi = a(t)R_0\chi \quad (2.42)$$

This expression assumes that χ remains constant, the observer being located at $\chi = 0$, and that the source are perfectly comoving. The present-time distance is usually called the “comoving distance” and denoted by

$$D_C = D_P(t_0) = R_0\chi \quad (2.43)$$

This instantaneous distance, although conceptually useful, cannot be used in practice. One can only rely on light or other radiation to observe astronomical objects. But light takes a finite time to reach us and, in the interval, the scale factor will have changed. More practical comoving distances are those who involve the past light cone.

One such comoving distance is the distance light would have traveled in the absence of interaction since time $t = 0$

$$\eta = \int_0^t \frac{dt}{a(t)} \quad (2.44)$$

No information can propagate faster than light, so this distance delimits regions of space-time that are causally connected and can be thought as a “causal horizon”. Since η increases monotonically, it is often used as a time variable, called the “conformal time”. The proper distance associated to η is obtained by multiplying by the scale factor and is called the “particle horizon”.

$$R_p = a(t) \int_0^t \frac{dt}{a(t)} = a(\eta)\eta(t) \quad (2.45)$$

The particle horizon corresponds to the maximum physical distance over which causal processes can ever have had an effect *up to* time t . The particle horizon should be distinguished from the “Hubble radius”

$$R_H(t) = \frac{1}{H(t)} \quad (2.46)$$

also called “Hubble horizon”, which is approximately the maximum distance over which causal processes can operate *at* a given time t . The Hubble radius is usually preferred when studying the formation of structures.

Another related comoving distance is the so-called “lookback distance”, defined as the distance between us (at present time t_0) and a distant comoving source at time $t(a)$

$$D_{Lookback} = \int_{t(a)}^{t_0} \frac{dt}{a(t)} = \int_a^1 \frac{da}{a^2(t)H(a)} \quad (2.47)$$

Physical distances

When it comes to measuring physical distances at large redshifts, two distances are classically used: the “luminosity distance” and the “angular diameter distance”.

The luminosity distance relies on the known luminosity of an observed object, a “standard candle” to infer its distance. Neglecting the expansion flow, the observed flux at a distance d from a source of known luminosity L is

$$F = \frac{L}{4\pi d^2} \quad (2.48)$$

In an expanding Universe, equation (2.48) must be modified to account for a number of effects:

- The area A of a spherical object centered at comoving distance χ will become, according to the FLRW metric (2.8), $A = 4\pi R_0^2 S_k^2(\chi)$
- The rate of arrival of individual photons is lower than the rate at which they were emitted by the redshift factor $1/(1+z)$
- The energy of the individual photons received by an observer on earth is reduced by the same redshift factor $1/(1+z)$

The correct expression for F is therefore

$$F = \frac{L}{(1+z)^2 A} \quad (2.49)$$

Comparing (2.48) and (2.49) yields the expression for the luminosity distance d_L

$$d_L = (1+z)R_0 S_k(\chi) \quad (2.50)$$

One problem with this formula is that the quantity χ is not an observable. It can however be converted into the more useful form by using (2.18) and the expression of χ on a null radial geodesic

$$\chi = \frac{1}{R_0} \int_t^{t_0} \frac{dt}{a(t)} = \frac{1}{R_0} \int_a^1 \frac{da}{a^2 H(a)} = \frac{1}{R_0} \int_0^z \frac{dz}{H(z)} \quad (2.51)$$

The resulting distance is then

$$d_L = (1+z)R_0 S_k \left[\frac{1}{R_0} \int_0^z \frac{dz}{H(z)} \right] \quad (2.52)$$

The luminosity distance can also be obtained by expressing R_0 in terms of the present-time density parameter $\Omega_{k,0} = -k/(R_0^2 H_0^2)$ (see 2.31), leading to

$$d_L = (1+z) \frac{1}{H_0} \frac{1}{\sqrt{|\Omega_{k,0}|}} S_k \left[H_0 \sqrt{|\Omega_{k,0}|} \int_0^z \frac{dz}{H(z)} \right] \quad (2.53)$$

The angular diameter distance is based on the measurement of the angle $\delta\theta$ subtended by a

object of known physical size l , a “standard ruler”, and is defined as

$$d_A = \frac{l}{\delta\theta} \quad (2.54)$$

where $\delta\theta$ is small.

Assuming the observed object was at redshift z at comoving coordinate χ and the Universe the scale factor $a(t)$, then the angular part of the metric. The expression (2.8) gives $l = a(t)R_0 S_k(\chi)\delta\theta$ and

$$d_A = \frac{R_0 S_k(\chi)}{1+z} \quad (2.55)$$

Reusing the expression of χ in 2.51 and expressing in terms of $\Omega_{k,0}$, leads to

$$d_L = (1+z)^2 d_A \quad (2.56)$$

2.3 Formation of cosmic structures

The cosmological framework described in the last section models a Universe obeying the cosmological principle: isotropic and homogeneous on a large scale, as discussed in Sect. 2.1.1. On smaller scales, however, the Universe is obviously far from meeting these criteria and indeed, we can observe today massive structures such as galaxies, isolated or in clusters, that have a mean density up to several hundred times larger than the average density of the Universe.

As we will see later in Sect. 2.4.2, The average amplitude of the temperature anisotropies in the Universe at the time of recombination ($z \sim 1000$) was of the order $\Delta T/T \sim 10^{-5}$. This suggests the density of inhomogeneities at that epoch were indeed of very small amplitude. So what is still missing in the cosmological framework we have described so far is an understanding of how these tiny density fluctuations were able to grow to form the structures we see today.

The origin of the initial inhomogeneities themselves is still controversial. One possibility is that they arose from quantum fluctuations in the very early Universe ($\sim 10^{-43}$ s) that grew enormously during a phase of exponentially accelerated expansion called “inflation” (e.g. Guth 1997; Liddle & Lyth 2000; Mukhanov 2005).

The conventional approach to the problem consists in investigating the effect of a small perturbation $\Delta(r, t) = \rho(r, t) - \bar{\rho}(t)$ in the gravitational field on top of the average gravitational field of the average matter density $\bar{\rho}(t)$. It is then convenient to introduce the “relative density contrast”, defined as

$$\delta = \delta(\mathbf{r}, t) = \frac{\Delta(\mathbf{r}, t)}{\bar{\rho}(t)} = \frac{\rho(\mathbf{r}, t) - \bar{\rho}(t)}{\bar{\rho}(t)} \quad (2.57)$$

where $\bar{\rho}(t)$ denotes the mean cosmic matter density in the Universe at time t .

A full treatment of the formation of cosmic structures would involve the use of general relativity (e.g., Amendola & Tsujikawa 2010; Mo et al. 2010). We will only provide a limited treatment here, centering the discussion around weak gravitational perturbations $\delta(r, t) \ll 1$ for which the Newtonian description of gravity can be applied.

We first consider structures that are much smaller than the Hubble radius R_H given by (2.46), so that so that causality can be considered instantaneous.

2.3.1 Newtonian fluid equations of a collisional fluid

$$\frac{\partial \rho}{\partial t} + \nabla_{\mathbf{r}} \cdot (\rho \mathbf{u}) = 0 \quad \text{Continuity equation} \quad (2.58)$$

$$\frac{\partial \mathbf{u}}{\partial t} + (\mathbf{u} \cdot \nabla_{\mathbf{r}}) \mathbf{u} = -\frac{\nabla_{\mathbf{r}} p}{\rho} - \nabla_{\mathbf{r}} \Phi \quad \text{Euler equation} \quad (2.59)$$

$$\nabla_{\mathbf{r}}^2 \Phi = 4\pi G \rho \quad \text{Poisson equation} \quad (2.60)$$

Equations (2.58)–(2.60) respectively represent the continuity equation (conservation of mass), Euler equation (conservation of momentum), and Poisson equation (gravitational field). The quantities ρ , p and \mathbf{u} denote respectively the mass density, pressure and velocity of the fluid. Dissipative terms arising from viscosity or thermal conductivity are neglected. It is also assumed the fluid is isentropic.

2.3.2 Newtonian linear perturbation equations in comoving coordinates

For studying cosmological perturbations in the context of an expanding Universe, it is more appropriate to use comoving coordinates \mathbf{x} instead of the proper coordinates \mathbf{r} . Both coordinates are related through $\mathbf{r} = a(t)\mathbf{x}$. With (\mathbf{x}, t) replacing (\mathbf{r}, t) as the space-time coordinates and using $\partial \mathbf{x} / \partial t = -(\dot{a}/a)\mathbf{x}$, the time and spatial derivatives transform as

$$\nabla_{\mathbf{r}} \rightarrow \frac{1}{a} \nabla_{\mathbf{x}} \quad \frac{\partial}{\partial t} \rightarrow \frac{\partial}{\partial t} - \frac{\dot{a}}{a} \cdot \nabla_{\mathbf{x}} \quad (2.61)$$

From (2.57), the perturbed density can also be expressed as $\rho = \bar{\rho}(t)[1 + \delta]$. The pressure, velocity and gravitational can be perturbed the same way, so that

$$\rho \rightarrow \bar{\rho}(t)[1 + \delta] \quad (2.62)$$

$$p \rightarrow \bar{p}(t) + \delta p \quad (2.63)$$

$$\mathbf{u} \rightarrow \dot{a} \mathbf{x} + \mathbf{v} \quad (2.64)$$

$$\Phi \rightarrow \bar{\Phi} + \phi \quad \bar{\Phi} = \frac{a\ddot{a}}{2} |\mathbf{x}^2| \quad (2.65)$$

where \mathbf{v} is the peculiar velocity describing the motion of the fluid element relative to the fundamental comoving observer at \mathbf{x} . Noting that $\bar{\rho} \propto a^{-3}$, applying the transformation rules (2.61) and substituting in equations (2.58)–(2.60), lead to perturbed equations in comoving

coordinates

$$\frac{\partial \delta}{\partial t} + \frac{1}{a} \nabla_{\mathbf{x}} \cdot [(1 + \delta) \mathbf{v}] = 0 \quad \text{Perturbed continuity equation} \quad (2.66)$$

$$\frac{\partial \mathbf{v}}{\partial t} + \frac{\dot{a}}{a} \mathbf{v} + \frac{1}{a} (\mathbf{v} \cdot \nabla_{\mathbf{x}}) \mathbf{v} = -\frac{1}{a} \frac{\nabla_{\mathbf{x}} \delta p}{\bar{\rho}(1 + \delta)} - \frac{1}{a} \nabla_{\mathbf{x}} \phi \quad \text{Perturbed Euler equation} \quad (2.67)$$

$$\nabla_{\mathbf{x}}^2 \phi = 4\pi G \bar{\rho} a^2 \delta = \frac{3H_0^2 \Omega_m}{2a} \delta \quad \text{Perturbed Poisson equation} \quad (2.68)$$

The assumption that the perturbations are small, that is, $\delta(r, t) \ll 1$ and $v \ll Hr$, means that only first-order terms can be kept in equations (2.66)–(2.68), so that

$$\frac{\partial \delta}{\partial t} + \frac{1}{a} \nabla_{\mathbf{x}} \cdot [(1 + \delta) \mathbf{v}] = 0 \quad (2.69)$$

$$\frac{\partial \mathbf{v}}{\partial t} + \frac{\dot{a}}{a} \mathbf{v} = -\frac{1}{a} \frac{\nabla_{\mathbf{x}} \delta p}{\bar{\rho}} - \frac{1}{a} \nabla_{\mathbf{x}} \phi \quad (2.70)$$

$$\nabla_{\mathbf{x}}^2 \phi = 4\pi G \bar{\rho} a^2 \delta \quad (2.71)$$

These equations can be combined as one single equation, which is the linear perturbation equation for δ in the Newtonian approximation ³

$$\frac{\partial^2 \delta}{\partial t^2} + 2 \frac{\dot{a}}{a} \frac{\partial \delta}{\partial t} = \frac{\nabla_{\mathbf{x}}^2 \delta p}{a^2 \bar{\rho}} + 4\pi G \bar{\rho} \delta \quad (2.72)$$

The different terms have the following physical interpretations:

- $2 \frac{\dot{a}}{a} \frac{\partial \delta}{\partial t}$ represents the “Hubble drag”, the direct effect of the expansion of the Universe. This term tends to suppress perturbation growth due to the expansion.
- $4\pi G \bar{\rho} \delta$ represents the effect of the self-gravity of the perturbation. This term causes perturbations to grow via gravitational instability.
- $\frac{\nabla_{\mathbf{x}}^2 \delta p}{a^2 \bar{\rho}}$ describes the effect of pressure due to the spatial variations in density.

The evolution of the density perturbations is therefore the result of the competition between the Hubble drag on the left-hand side and the self gravity and pressure on the right-hand side of (2.72).

2.3.3 Density perturbations of a non-relativistic fluid with zero pressure

Setting $\nabla^2 p = 0$ in (2.72) gives

$$\frac{\partial^2 \delta}{\partial t^2} + 2H(t) \frac{\partial \delta}{\partial t} - 4\pi G \bar{\rho} \delta = 0, \quad H = \frac{\dot{a}}{a} \quad (2.73)$$

This equation admits solutions of the form

$$\delta(\mathbf{x}, t) = A(\mathbf{x})D_+(t) + B(\mathbf{x})D_-(t) \quad (2.74)$$

³The effect of relativistic pressure as an additional energy source is not included.

where $D(t)$ is called the “linear growth factor” and the two $A(\mathbf{x})$ and $B(\mathbf{x})$ functions are arbitrary. The notation highlights the fact that D_+ is growing or constant in time, a *growing mode*, whereas D_- is decreasing with time, a *decaying mode*.

The equations can be solved explicitly in the case of the Einstein–de Sitter Universe (EdS) (Einstein & de Sitter 1932), matter-dominated, with flat geometry ($k = 0$) and without cosmological constant ($\Lambda = 0$). This model is a good approximation of the Universe after the period of matter–radiation equality but well before Λ starts to dominate. In this simplified case, $a \propto t^{2/3}$, so that $H = 2/(3t)$ and $\bar{\rho} = 1/(6\pi G t^2)$, which yields

$$D_+ \propto t^{2/3} \quad D_- \propto t^{-1} \quad (2.75)$$

The D_- decaying with time, the only relevant solution is therefore

$$\delta(\mathbf{x}, t) \sim A(\mathbf{x})D_+(t) = A(\mathbf{x})t^{2/3} \quad (2.76)$$

In a EdS Universe, the density perturbation would therefore be allowed to grow as a power-law $\delta \propto a \propto t^{2/3}$ after the radiation-matter equality. But the real Universe is not EdS and, as shown in the next sections, incorporating the effects of a non-zero pressure leads to a different result for ordinary matter, whereby the perturbations is only allowed to grow after recombination. On the other hand, dark matter is able to grow just after a_{eq} at a rate $D_+ \propto t^{2/3}$.

2.3.4 Density perturbations in a non-relativistic fluid with non-zero pressure

Assuming a barotropic fluid with $p = p(\rho)$, $\delta p = (\partial p / \partial \rho) \bar{\rho} \delta = c_s^2 \bar{\rho} \delta$, where $c_s = (\partial p / \partial \rho)^{1/2}$ is the adiabatic sound speed, equation (2.72) can then be rewritten as

$$\frac{\partial^2 \delta}{\partial t^2} + 2H(t) \frac{\partial \delta}{\partial t} = \frac{c_s^2}{a^2} \nabla_{\mathbf{x}}^2 \delta + 4\pi G \bar{\rho} \delta \quad (2.77)$$

This equation is that of a damped oscillator where the Hubble drag term $2H(\partial \delta / \partial t)$ tends to damp any growing or oscillatory solution. Considering plane wave solutions of the form $D(t)e^{i\mathbf{k}\cdot\mathbf{x}}$, (2.77) can be expressed as

$$\ddot{D} + 2H\dot{D} = -\omega^2(t)D, \quad \omega^2(t) = \frac{c_s^2 k^2}{a^2} - 4\pi G \bar{\rho} \quad (2.78)$$

where \mathbf{k} is the comoving wave vector, related to the comoving wavelength λ_c through

$$k = 2\pi / \lambda_c \quad (2.79)$$

the corresponding proper wave length being $\lambda = a(t)\lambda_c$.

The nature of the solutions to equation (2.78) depends on whether $\omega^2(t) > 0$ or $\omega^2(t) < 0$, which in turns depends on whether $k > k_J$ or $k < k_J$ where k_J is the comoving Jeans wave vector

$$k_J = \sqrt{4\pi G \bar{\rho}} \frac{a}{c_s} \quad (2.80)$$

Chapter 2. Quick overview of modern cosmology

The corresponding characteristic proper length is the Jeans wavelength λ_J is

$$\lambda_J = \frac{2\pi}{k_J} a = c_s \sqrt{\frac{\pi}{G\bar{\rho}}} \quad (2.81)$$

There are two families of solutions:

- For $\lambda < \lambda_J$, ($\omega^2 > 0$), the solution corresponds to a sound wave that propagates with the sound speed c_s .
- For $\lambda > \lambda_J$, ($\omega^2 < 0$), the pressure can no longer support gravity and the solution to (2.78) represents a non-propagating, stationary wave, with an amplitude that will either increase (growing mode) or decrease (decaying mode) with time. The Hubble drags has the effect of slowing down the growth of perturbations that would be exponential otherwise.

So it is clear that a perturbation cannot grow unless $\lambda > \lambda_J$. For $\lambda \gg \lambda_J$, the pressure term in (2.85) can be neglected and the solutions are of the form

$$\delta(\mathbf{x}, t) = A(\mathbf{x})D_+(t) + B(\mathbf{x})D_-(t) \quad (2.82)$$

with

$$D_+ \propto t^{2/3} \quad D_- \propto t^{-1} \quad (2.83)$$

so that $\delta(\mathbf{x}, t) \sim t^{2/3}$ at later times for $\lambda \gg \lambda_J$.

In Summary, in the $a > a_{eq}$ epoch:

- For $\lambda < \lambda_J$, the growth of perturbation is suppressed.
- For $\lambda > \lambda_J$, the perturbations grow as $D_+ \propto a \propto t^{2/3}$ during $a > a_{eq}$.

2.3.5 Density perturbations in a relativistic fluid with non-zero pressure

This case is relevant to approximate the behavior of perturbations in a radiation-dominated Universe, where $p = (1/3)\rho c^2$. It is still assumed that bulk velocities are non-relativistic. Such conditions can be approximately modeled by the so-called “modified” Newtonian fluid equations (e.g., Lima et al. 1997) where pressure constitutes an additional source of energy.

For a radiation-dominated Universe, the linearized perturbation equation is

$$\frac{\partial^2 \delta}{\partial t^2} + 2 \frac{\dot{a}}{a} \frac{\partial \delta}{\partial t} = \frac{\nabla_{\mathbf{x}}^2 \delta p}{a^2 \bar{\rho}} + \frac{32\pi G}{3} \bar{\rho} \delta, \quad \delta p = \frac{1}{3} \bar{\rho} \delta \quad (2.84)$$

The explicit equation then reads

$$\frac{\partial^2 \delta}{\partial t^2} + 2 \frac{\dot{a}}{a} \frac{\partial \delta}{\partial t} = \frac{1}{3} \frac{\nabla_{\mathbf{x}}^2 \delta}{a^2} + \frac{32\pi G}{3} \bar{\rho} \delta \quad (2.85)$$

The analysis is similar to that of Sect. 2.3.4. Considering plane waves $D(t)e^{i\mathbf{k}\cdot\mathbf{x}}$, the damped

oscillator equation is slightly modified as

$$\ddot{D} + 2H\dot{D} = -\omega^2(t)D, \quad \omega^2(t) = \frac{c_s^2 k^2}{3a^2} - \frac{32}{3}\pi G\bar{\rho} \quad (2.86)$$

The comoving wave vector k_J is

$$k_J = \sqrt{\frac{32}{3}\pi G\bar{\rho}} \frac{a}{c_s} \quad (2.87)$$

The corresponding characteristic proper Jeans wavelength λ_J is

$$\lambda_J = \frac{2\pi}{k_J} a = \sqrt{\frac{3\pi}{8}} \frac{c_s}{\sqrt{G\bar{\rho}}} \quad (2.88)$$

There are again two families of solutions:

- For $\lambda < \lambda_J$, ($\omega^2 > 0$), the solution corresponds to a sound wave that propagate with the sound speed $c_s^2 = 1/3$.
- For $\lambda > \lambda_J$, ($\omega^2 < 0$), the solution represents a non-propagating, stationary wave, with an amplitude that will either increase (growing mode) or decrease (decaying mode) with time.

Therefore, a perturbation cannot grow unless $\lambda > \lambda_J$, as for a non-relativistic fluid with pressure. For $\lambda \gg \lambda_J$, the pressure term in 2.85 can be neglected and the solutions are of the form

$$\delta(\mathbf{x}, t) = A(\mathbf{x})D_+(t) + B(\mathbf{x})D_-(t) \quad (2.89)$$

with

$$D_+ \propto t \quad D_- \propto t^{-1} \quad (2.90)$$

so that $\delta(\mathbf{x}, t) \sim t$ at later times. Therefore, the growing mode in the radiation-dominated era, $a < a_{eq}$ has $D_+ \propto a^2 \propto t$ compared to $D_+ \propto a \propto t^{2/3}$ during $a > a_{eq}$.

2.3.6 Density perturbations in a Λ -dominated Universe

As we will see in Sect. 2.4.4, there is now very strong evidence that the Universe is currently in a phase of accelerated expansion. One possibility is that Einstein's cosmological constant, interpreted as vacuum energy, is responsible for this effect (see Sect. 2.5.3). In this particular case, $\delta\rho_\Lambda = 0$ and $\delta\rho \approx \rho_m$. Equation (2.73) can then be rewritten as

$$\frac{\partial^2 \delta_m}{\partial t^2} + 2H(t) \frac{\partial \delta_m}{\partial t} - \frac{3}{2}\Omega_m(t)H^2(t)\delta_m = 0, \quad H = \frac{\dot{a}}{a} \quad (2.91)$$

which, because $\Omega_m \ll 1$ and $H = \text{constant}$, simplifies to

$$\frac{\partial^2 \delta_m}{\partial t^2} + 2H(t) \frac{\partial \delta_m}{\partial t} = 0 \quad (2.92)$$

The solutions are of the form

$$\delta(\mathbf{x}, t) = A(\mathbf{x}) + B(\mathbf{x}) e^{-2Ht} \quad (2.93)$$

The growth of perturbation during the Λ -dominated era is thus suppressed: the self-gravity of the matter is overwhelmed by the expansion driven by the vacuum energy.

2.3.7 Evolution of the density perturbations of baryonic matter

It is now possible, based on the results of Sects. 2.3.4 and 2.3.5, to retrace the evolution of perturbations for baryonic matter at different epochs (within the Hubble horizon).

- During the radiation domination era ($a < a_{eq}$), it is thought that matter was mostly in the form a non-baryonic, pressureless, collisionless, non-relativistic “cold” dark matter (CDM). Baryonic matter was thus subdominant. The fluid during that era was a mix of relativistic collisional radiation and CDM. Peter Mészáros has shown that, in that case, the perturbation in such a fluid were “frozen” until the epoch of radiation-matter equality, an effect known as the “Mészáros effect” (Meszaros 1974).
- During the matter domination era ($a > a_{eq}$), and before recombination (a_{rec}), photons and electrons were tightly coupled by Compton scattering and baryons and photons behaved as a single fluid. Just before recombination, the sound speed in such a fluid was about $1.3 \times 10^8 \text{ m s}^{-1}$ and the length scale corresponded to that of a supercluster (~ 2500 Mpc). Under such conditions, the scale of λ_J was much too high for perturbations to have a chance to grow. According to the results of Sect. 2.3.5, the growth of structures of baryons was thus effectively suppressed before recombination.
- Just after recombination ($a > a_{dec}$), the sound speed dropped by a factor of $\sim 10^4$, to $\sim 6 \times 10^3 \text{ m s}^{-1}$. the Jeans length then became much smaller (~ 10 kpc), enough for perturbations to start growing at a rate $D_+ \propto a \propto t^{2/3}$, according to (2.83).

2.3.8 Evolution of the density perturbations of non-baryonic dark matter

Based on the results of the last sections, the evolution of cold dark matter within the Hubble horizon can be summarized as follows:

- During the radiation domination era ($a < a_{eq}$), we saw in Sect. 2.3.7 that the CDM perturbations were “frozen” due to the “Mészáros effect” (Meszaros 1974).
- As soon as the radiation-matter equality was reached, ($a > a_{eq}$), the results obtained in Sect. 2.3.3 for pressureless matter applies. The CDM was then able to grow at a rate $D_+ \propto a \propto t^{2/3}$.

2.3.9 Linear structure growth on super-horizon scales

The description of the previous sections applies to density perturbations of scales much smaller than the size of the Hubble horizon. The description of larger scale perturbation would require a relativistic treatment which is beyond the ambitions of this thesis. We nevertheless outline some important results below.

2.3. Formation of cosmic structures

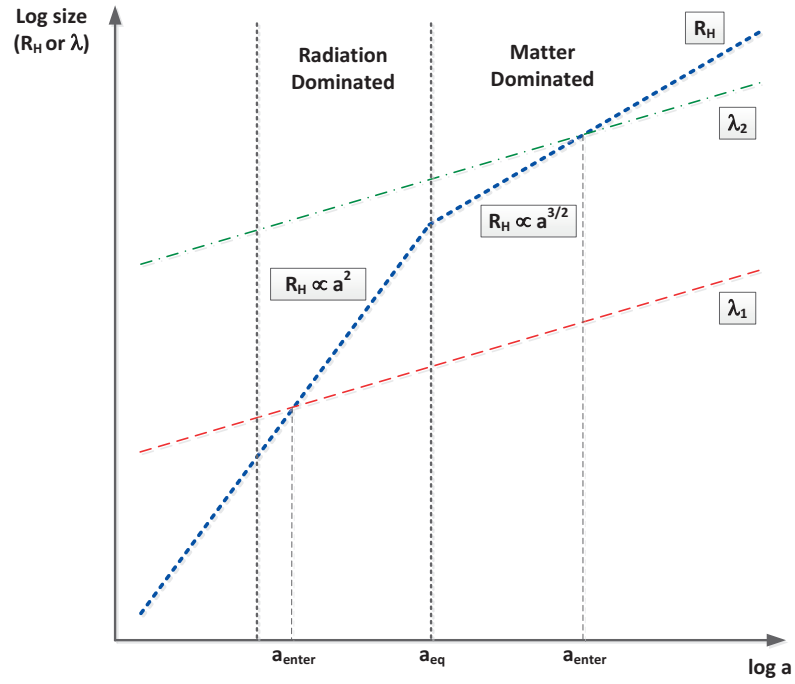


Figure 2.3: A small-size and a larger-size perturbations entering the horizon.

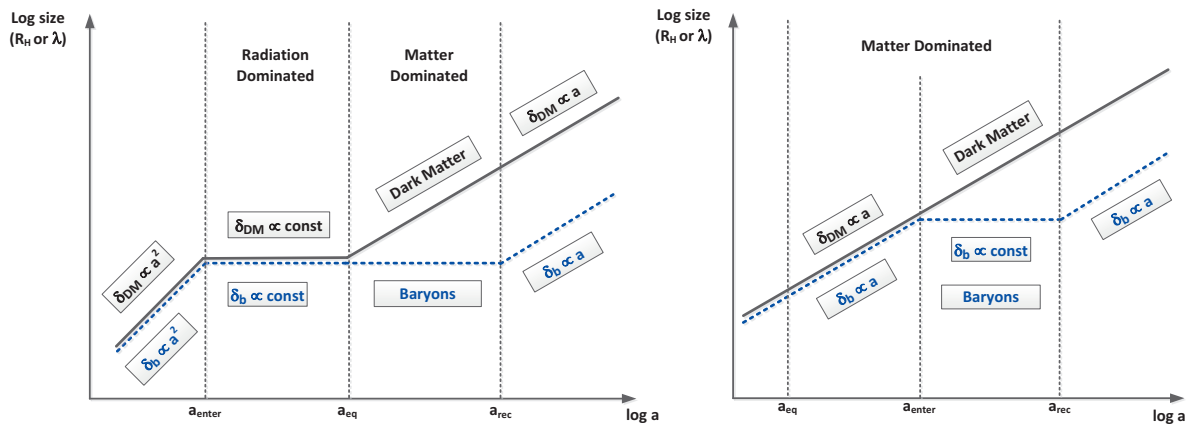


Figure 2.4: *Left*: Evolution of perturbations entering during the radiation domination era. Cold Dark matter is represented in black and baryons in blue. *Right*: Evolution of perturbations entering during the matter domination era.

Evolution of horizon size

The sizes of the Hubble horizon R_H in the different epochs are $2ct$ and $(3/2)ct$ during the radiation and matter dominated epochs, respectively. Therefore $R_H \propto t$.

$$R_H \propto \begin{cases} t \propto a^2 & \text{radiation-dominated epoch} \\ t \propto a^{3/2} & \text{matter-dominated epoch} \end{cases} \quad (2.94)$$

On the other hand, the proper lengths of perturbations λ scale as $\lambda = (2\pi)/ka \propto a$. Therefore:

- The perturbations are initially inside the horizon ($\lambda < R_H$) and then grow to a point where they leave the horizon ($\lambda > R_H$). The horizon exit time is defined by $t_{exit} = R_H(t_{exit})$.
- λ grows slower than R_H during the radiation and matter-dominated epochs, so, during these eras, perturbations are outside the horizon ($\lambda > R_H$) and then enter the horizon ($\lambda < R_H$). The horizon entry time is defined by $t_{enter} = R_H(t_{enter})$.

This is illustrated in Fig. 2.3.

Evolution of perturbations over different epochs

It can be shown that for $\lambda \gg R_H$, the perturbations grow in the same way as for $\lambda \ll R_H$, that is

$$D_+ \propto \begin{cases} a^2 \propto t & \text{radiation-dominated epoch} \\ a^{2/3} \propto t & \text{matter-dominated epoch} \end{cases} \quad (2.95)$$

The case of small perturbations that enter the horizon *before* matter–radiation equality ($a < a_{eq}$) is illustrated in Fig. 2.4, left. Outside the horizon, the perturbations evolve as $D_+ \propto a^2$ and all components, baryons (b), photons (γ), cold dark matter (DM) evolve in the same way, maintaining adiabatic ratios: $\delta_b \propto \delta_{DM} \propto (3/4)\delta_\gamma$. But as soon as they enter the horizon during $a < a_{eq}$, the perturbations cease to grow, as explained in Sect. 2.3.7, because of the Mészáros effect. Once matter–radiation equality is reached ($a > a_{eq}$), the CDM component is allowed to grow at a rate $D_+ \propto a \propto t^{2/3}$ as explained in Sect. 2.3.8. In contrast, the growth of baryonic matter is still suppressed until recombination, as described in Sect. 2.3.5. After recombination ($a > a_{rec}$) can start growing at a rate $D_+ \propto a \propto t^{2/3}$.

The case of larger-size perturbations enters the horizon *after* matter–radiation equality ($a > a_{eq}$) is illustrated in Fig. 2.4, right. All components remain outside the horizon during the radiation and matter domination eras $a < a_{eq}$ and grow without being affected at a rate $D_+ \propto a$. As soon as they reach a_{eq} , the baryons see their growth suppressed, as described in Sect. 2.3.5. In contrast, the CDM component continues to grow according to $D_+ \propto a$ (see Sect. 2.3.8). After recombination, the baryonic matter resumes its growth at a rate $D_+ \propto a \propto t^{2/3}$ (see Sect. 2.3.5).

2.3.10 Statistical properties of the matter density field

On large scales (i.e. $\delta \ll 1$), gravity competes with cosmic expansion and structures grow according to the linear theory of cosmic structures we have outlined in the previous sections. In this regime, the matter density field can be considered as a Gaussian random process whose

statistical properties that can be completely described by second-order (two-point) statistics such as a correlation function or a power spectrum. The power spectrum of the matter density perturbations is often referred to as the “matter power spectrum”.

On small scales, gravitational collapse is non-linear and much more difficult to model analytically, requiring the use of numerical simulations. Higher-order statistics are necessary to describe the full field on small scales and non-linear corrections have to be brought to the matter power spectrum.

Matter power spectrum in the linear regime

We first focus on statistical properties in the linear regime. The power spectrum of the density perturbations P_δ is defined by

$$\langle \hat{\delta}(\mathbf{k}, t) \hat{\delta}^*(\mathbf{k}', t) \rangle = (2\pi)^3 \delta_D(\mathbf{k} - \mathbf{k}') P_\delta(k, t) \quad (2.96)$$

where angle brackets denote ensemble averages. At a given time t , the power spectrum only depends on the wave vector \mathbf{k} . The power spectrum $P_\delta(k, t)$ at a given time t is related to the primordial power spectrum $P_\delta(k, t_i)$ at time t_i through

$$P_\delta(k, t) = T^2(k) P_\delta(k, t_i) \quad (2.97)$$

where $T(k)$ is called a “Transfer function”. This function describes how the shape of the initial power spectrum is modified by the different processes occurring during the growth of structures. The exact form of $T(k)$ depends on the matter content of the Universe and in particular, on the type of dark matter (see Sect. 2.4.3). The transfer function is for instance very different between cold (CDM) and hot (HDM), since HDM particles were relativistic at the time of radiation–matter equality, contrary to CDM particles. Several transfer functions corresponding to different kinds of matter are plotted in Fig. 2.5. In the linear regime, each Fourier mode evolves independently and the power spectra at times t and t_1 , ($t_1 < t$) are related by

$$P_\delta(k, t) = P_\delta(k, t_1) \frac{D_+^2(t)}{D_+^2(t_1)} = P_\delta(k, t_1) T^2(k) \frac{D_+^2(t)}{D_+^2(t_1)} \quad (2.98)$$

Standard cosmology assumes a primordial power spectrum in the form of a power law, i.e.

$$P_\delta(k, t_i) \propto A k^{n_s} \quad (2.99)$$

with “spectral index” n_s and normalization A . A primordial power spectrum with $n_s = 1$ is known as the “Harrison-Zeldovich” power spectrum (Harrison 1970; Zeldovich 1972), is in good agreement with the spectrum predicted by the theory of inflation (e.g., Dodelson 2003) and is favored by observations. In fact, the final results from WMAP (Hinshaw et al. 2012) and the latest findings from the Planck probe (Ade et al. 2013b), both suggest a value slightly lower than unity, around 0.96, favoring simple single-field “slow-roll” inflationary models (e.g., Mukhanov 2007).

In the case of a “Harrison-Zeldovich” power spectrum, the evolution of the overall power

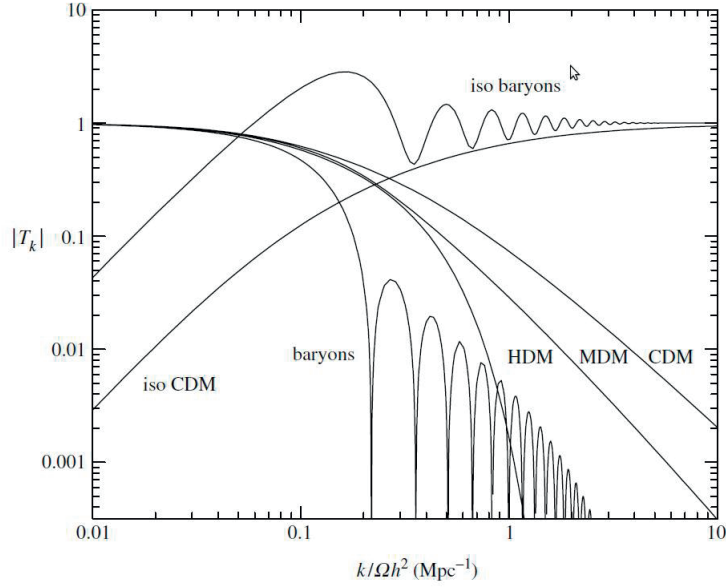


Figure 2.5: Adiabatic transfer functions corresponding to baryons, hot dark matter (HDM), cold dark matter (CDM) and other possible forms of matter (Peacock 1998).

spectrum evolution is approximated by

$$P_{\delta}(k) = \begin{cases} k & \text{for small } k \text{ (large scales)} \\ k^{-3} & \text{for large } k \text{ (small scales)} \end{cases} \quad (2.100)$$

The evolution of the matter power spectrum on different scales is depicted in Fig. 2.6. The large-scale perturbations (small k) remained outside the horizon and, not being impacted by physical processes inside R_H , were able to grow (i.e. their amplitude increased). This explains why the power spectrum curve increases in height on large scales. In contrast, small-scale perturbations were suppressed upon entering the horizon (R_H) before matter-radiation equality (a_{eq}), as described in Sects. 2.3.2 – 2.3.9. This is reflected in the steep decrease of the power spectrum curve toward high k . The bump in the curve is thus explained by the different growth rates between large and small-scale perturbations. After a_{eq} the Universe became pressureless (dominated by dark matter) and all scales were able to clump together more and more. The power spectrum thus essentially grew the same way on all scales and its shape became more or less frozen starting from that epoch. The turnover point in the processed power spectrum is therefore an indication of Jeans length at a_{eq} .

Completely specifying the power spectrum requires the determination of its overall amplitude. The theory of structure formation is not yet refined enough to predict this quantity, which is instead fixed by observations. The estimated value is used to normalize the power spectrum and enters the cosmological model via the σ_8 normalization parameter, defined as the variance of the density perturbations within a sphere of radius $8h^{-1}$ Mpc. This choice of scale was motivated observationally by the variance of galaxy counts, estimated to lie around unity. The $\sigma_8 \sim 1$ value identifies the transition from the linear to the non-linear scales.

As shown in the above discussion, the shape and amplitude of the power spectrum are a

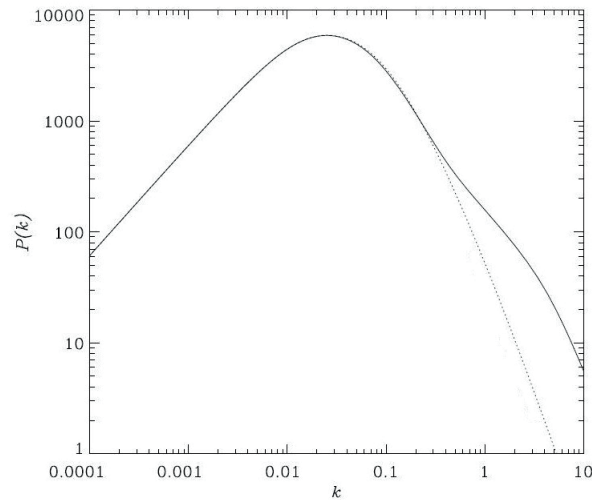


Figure 2.6: Matter power spectrum computed using the WMAP + SDSS cosmological parameters estimated in (Tegmark et al. 2004b). The solid and dashed curves respectively show the non-linear and linear power spectra. The linear power spectrum asymptotically falls off as $\sim k^{-3}$, whereas the non-linear spectrum deviates from the linear curve due to the enhanced contributions of non-linear effects on small-scale perturbations. The non-linear effects were computed using the fitting functions from Peacock & Dodds (1996).

sensitive probe of cosmology. The determination of σ_8 through observations is, however, very challenging. One approach is to combine cosmic shear measurements with galaxy number counts (Simon et al. 2004). Recent studies (e.g., Van Waerbeke et al. 2005; Hinshaw et al. 2012; Ade et al. 2013b) favor a value slightly smaller than unity, around 0.8. This topic will be covered in more details in Sect. 3.4.

Matter power spectrum in the non-linear regime

As mentioned earlier, the theory of linear structure formation ceases to be accurate for $\delta \gtrsim 1$. Gravitationally-bound low-redshift structures have a density contrast larger than unity and galaxy clusters have $\delta \sim 1000$. Unlike in the linear case, the Fourier k -modes are no longer independent but instead interacting with each other, introducing features in the matter density field that can no longer be fully described by random Gaussian processes, i.e. by two-point statistics (e.g., Munshi et al. 2008). The linear power spectrum described in the previous section is therefore no longer an adequate description of the statistical property of the density field and must be corrected.

Unfortunately, an analytical treatment that would account for all non-linear physical phenomena is still beyond reach. Such a treatment is only possible in special cases such as the spherical collapse model in EdS cosmology (e.g., Peacock 1998). Numerical calculations, such as the N-Body simulations of the Millennium project (Springel et al. 2001, 2005) are nevertheless able to reproduce the observed filamentary structures of the Universe at various scales. Relying on such simulations, the computation of the required corrections to the power spectrum in the non-linear regime have been estimated by several authors (Hamilton et al. 1991; Jain

et al. 1995; Peacock & Dodds 1996; Smith et al. 2003). One important parameter involved in the corresponding transfer functions is the shape parameter $\Gamma = \Omega_m h$ which determines the location of the peak in the power spectrum.

2.4 “Concordance” cosmology

2.4.1 The “Big Bang”

Georges Lemaître was the first to propose the observed redshift of galaxies could be interpreted as evidence for the expansion of the Universe (Lemaître 1927), and by 1933, the theory of the expanding universe was accepted by a majority of astronomers and the subject of detailed reviews by O. Heckmann, H. P. Robertson and R. C. Tolman (Heckmann 1932; Robertson 1933; Tolman 1934). One year earlier, A. Einstein and W. de Sitter had advocated a simple cosmological model, now known as the ‘Einstein–de Sitter’ cosmological model (EdS) (Einstein & de Sitter 1932), with a flat geometry ($k = 0$) and no cosmological constant ($\Lambda = 0$).

But other possible models were being explored, notably by G. Lemaître who envisaged cosmological models starting with a singularity and having a positive cosmological constant. In 1931, Lemaître went further, suggesting the Universe could have originated at a finite point in time from a “primeval atom” (Lemaître 1931a,c).

Indeed, the Friedmann, EdS and Lemaître models do allow such a possibility. The acceleration equation (2.20) can be expressed in terms of w as

$$\frac{\ddot{a}}{a} = -\frac{4\pi G}{3}\rho(1+3w) + \frac{1}{3}\Lambda \quad (2.101)$$

In the case of a zero cosmological constant, this equation implies that $\ddot{a} < 0$ for all time, provided $w > -1/3$, establishing that the expansion of the corresponding Universe is decelerating and that $a(t)$ must have been zero at some finite time in the past. Since $a(0) = 0$ at that point, the density ρ diverges, as does the Hubble parameter $H(t)$. In fact, this singularity cannot even be ruled out when $\Lambda > 0$, provided it does not dominate at early time, and indeed this scenario is precisely the one favored today by standard cosmology.

Lemaître’s idea was received with skepticism by the scientific community, notably Arthur Eddington (Eddington 1931). Sir James Jeans, in the 1920s, was the first to raise the possibility of a Universe with continuous creation of matter (Jeans 1928). But it was not until the end of the 1940s that the subject was revisited. Two competing theories that could explain the expansion of the Universe were proposed. The first one, in favor of an ever-lasting Universe was a “steady state” cosmological model put forward by Fred Hoyle (Hoyle 1948), Thomas Gold, Hermann Bondi and others. The second, advocated by Georges Gamov and his student Ralf A. Alpher (Alpher et al. 1948; Alpher & Herman 1949), was proposing a Universe born in a initial singularity, a “Big Bang”, as Fred Hoyle called it during a BBC Radio broadcast in 1949. The paper from Alpher et al. (1948) explained how light elements of the Universe could have been created during the first few minutes of the “Big Bang”, a process called “Big Bang Nucleosynthesis” (BBN), and predicted the expected abundance of hydrogen and helium. These calculations were further refined in 1953 by Alpher et al. (1953).

2.4.2 The Cosmic Microwave background

Equation (2.101) implies that the early Universe was radiation-dominated. Since radiation behaves as $\rho_r \propto T^4$, i.e. $T \propto t^{-1}$, the Universe was much denser and hotter than it is today, in the form of a plasma made of free nuclei and electrons, continuously interacting with each other through Thomson scattering. All these particles were in thermal equilibrium with photon energies described by the Planck distribution.

Eventually after about 380,000 years of expansion, the universe cooled to the point (around 3000K) where electrons could be captured into atomic orbits, a process known as “recombination”. This event had two important consequences. Firstly, matter and radiation were no longer in thermal equilibrium. As a result, perturbations in matter were no longer damped by interaction with radiation and could start to grow through gravitational instability, eventually forming the structures of the Universe. Secondly, the photons, no longer being scattered with electrons, were able to stream freely through the Universe. In 1948, Georges Gamov and separately, Ralf A. Alpher and Robert Herman (Alpher & Herman 1948), worked out this last process. Alpher and Herman predicted that the last scattering surface would be detectable in the form of a thermal radiation that would uniformly fill the observable Universe and would have a temperature around 5K. This relic radiation is known as the Cosmic Microwave Background (CMB).

Strangely, the paper of Alpher & Herman (1948) failed to attract the attention of the scientific community. Between 1948 and 1954, Alpher and Herman tried to convince astronomers to measure the CMB but without success. Georges Gamov and Robert Dicke also made various estimates of the CMB temperature. It was only in 1965 that Arnold Penzias and Robert W. Wilson fortuitly detected the CMB signal (Penzias & Wilson 1965). In the 1970s, further theoretical work from Edward R. Harrison (Harrison 1970), James E. Peebles (Peebles & Yu 1970), Yakov B. Zeldovich (Zeldovich 1972) and Rashid A. Sunyaev (Sunyaev 1978) estimated the observable imprint that these inhomogeneities would have on the CMB.

The definitive proof that the CMB was truly a remnant of the Big Bang came after the Cosmic Background Explorer (COBE) satellite confirmed their theoretical predictions in 1992 (Smoot et al. 1992). COBE’s measurement found in particular the expected level of anisotropies and showed that the spectrum of the CMB was that of a thermal black body to a high precision. COBE’s measurements were further confirmed and refined by NASA’s Wilkinson Microwave Anisotropy Probe (WMAP) (Bennett et al. 2003a,b, 2012; Hinshaw et al. 2012) and by ESA’s Planck satellite (Tauber et al. 2010a,b; Ade et al. 2013a), respectively launched in 2001 and 2009. The latest measurements from Planck (Ade et al. 2013a) give the CMB temperature to be 2.725K and temperature fluctuations of the order of $\Delta T/T \sim 10^{-5}$. The latest CMB temperature fluctuation map and power spectrum measured by the Planck satellite are shown in Fig. 2.7.

After the discovery of the CMB, the BBN abundance estimates were refined by Peebles (1966); Wagoner et al. (1967), and together with more recent calculations (e.g., Olive & Steigman 1995; Schramm & Turner 1998; Tytler et al. 2001; Charbonnel 2002; Mathews et al. 2005) fully confirmed the predictions of the Big Bang. Fig. 2.8, left, summarizes the current constraints on the baryon densities.

The expansion of the Universe, the CMB and the BBN constitute the three pillars of the Big Bang. Additional pieces of evidence have been found since, notably from the study of large scale structures, the age of stars and the formation and evolution of galaxies.

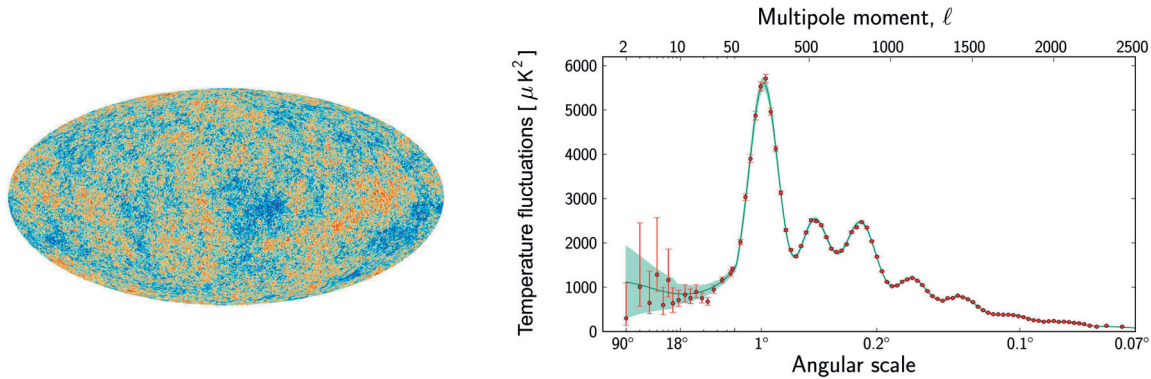


Figure 2.7: *Left*: The CMB temperature fluctuations from the Planck probe data seen over the full sky (Ade et al. 2013a). *Right*: the angular power spectrum of the temperature anisotropies measured by the Planck probe (Ade et al. 2013a). This plot shows the temperature fluctuations as a function of angular size. The Planck data are in red color, with error bars, the best fit model is the blue curve, and the smoothed binned cosmic variance curve is the shaded region.

2.4.3 Dark matter and the “cold” dark matter paradigm

Main evidence for dark matter

We outline in this section the main evidence for the existence of dark matter. Possible explanations on the actual nature of dark matter will be discussed in Sect. 2.5.2.

The presence of an unseen, yet real, material in the Universe was suspected as early as the 1920s and 1930s by astronomers such as Jacobus C. Kapteyn (Kapteyn 1922), Jan H. Oort (Oort 1932) and above all, Fritz Zwicky. To carry out his observations, Zwicky persuaded Caltech to build a 18-inch Schmidt telescope that would be able to capture large numbers of galaxies in a single wide-angle photograph. He used the instrument to make a survey of all the galaxies in the Coma cluster and used measurements of the Doppler shift of their spectra to determine their velocities. Applying the virial theorem, he obtained a mass estimate considerably greater than that expected from luminosity of the galaxies alone (Zwicky 1933, 1937b), suggesting the presence of unseen matter.

Zwicky’s findings were received with great skepticism and it was not until several decades later that further evidence was found. One way to explore the properties of dark matter is to measure the gravitational influence it exerts on nearby luminous matter. It is indeed by observing the motion of galaxies that the first pieces of evidence for dark matter were discovered. In 1970, Vera Rubin and Kent Ford measured the rotation velocities of spiral galaxy M31 using the 21cm line of neutral hydrogen. They were expecting velocities at a radius r around galaxies to decrease as $v(r) \propto 1/\sqrt{r}$ but instead found approximately “flat” rotation curves where $v(r) \approx \text{constant}$ (Rubin & Ford 1970). More observations of flat 21cm rotation curves subsequently followed (e.g., Rogstad & Shostak 1972; Roberts & Whitehurst 1975; Krumm & Salpeter 1976; Bosma 1978; Rubin et al. 1978, 1980), and reached general acceptance among the astronomers by the end of the 1970s. Fig. 2.8, right, shows the rotation curve of the NGC 3198 spiral galaxy along with the assumed respective dynamical contributions of the disk

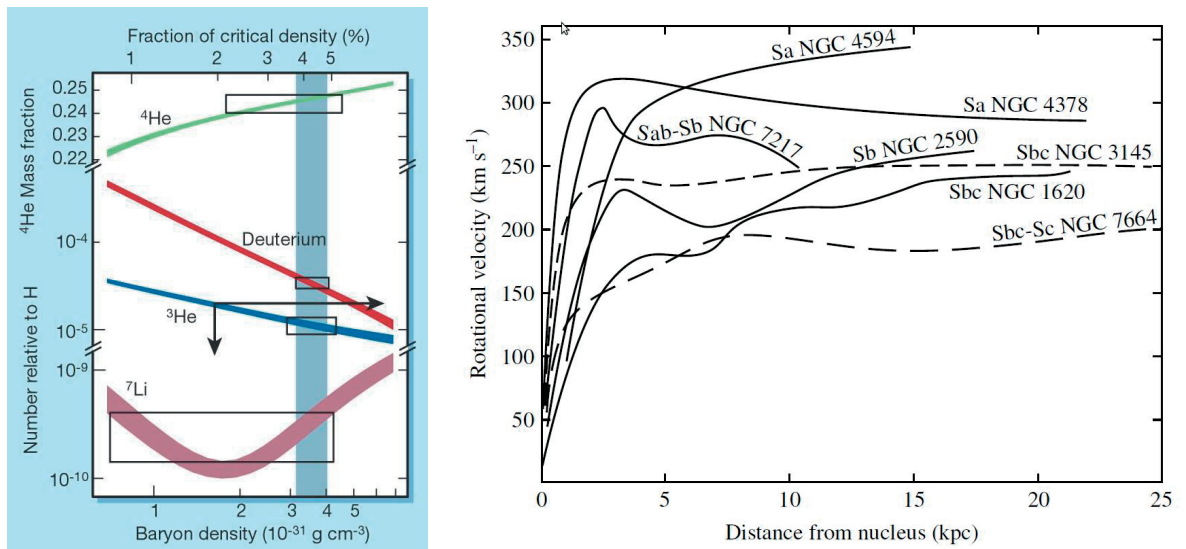


Figure 2.8: *Left*: Big Bang Nucleosynthesis predictions and observations. The boxes indicate the observational estimates for the primordial abundances of helium 4 (observed in galactic HII regions), deuterium (inferred from the absorption spectra of high-redshift quasars) and Lithium 7 (deduced from the surface of the oldest stars in our Galaxy). The horizontal arrow points to the upper limit of the abundance of helium 3, relative to hydrogen (Charbonnel 2002). *Right*: Several rotation curves of spiral galaxies, as determined by Vera Rubin and collaborators (Rubin et al. 1978). Predictions based on the mass of visible matter and gas would have resulted in curves that would decrease at large distances rather than remaining approximately constant.

and dark matter halo.

In the mean time, theorists found that the flat rotation curves were consistent with the presence of a massive “dark halo” of matter surrounding spiral galaxies but other types of galaxies as well (e.g., Ostriker & Peebles 1973; Einasto et al. 1974; Ostriker et al. 1974; Turner & Ostriker 1977; Faber & Gallagher 1979).

Around the same time, X-ray satellites detected strong thermal X-ray sources in clusters of galaxies. Detailed observations of the Virgo cluster, in particular, highlighted the fact that the cluster had to contain considerably more mass (other than the mass of the gas) in order prevent the hot X-ray-emitting gas from escaping via evaporation (e.g., Mathews 1978). In fact, the distribution of the gas can be used to map the distribution of the dark matter in the cluster. Subsequent concordant observations were made in the 1980s and 1990s (e.g., Forman & Jones 1982; Schindler et al. 1999) and are now considered as additional clues of the existence of dark matter. Mass-to-light ratios for large galaxy clusters are typically of 10 to 1.

Another way of study dark matter is to directly probe the gravitational field itself. As described by general relativity, light rays follow the curvature of space-time induced by the concentrations of matter or energy (luminous or not) that they cross. Careful measurements of the tidal deviations of light bundles along the line of sight, an affect known as “gravitational lensing”, can produce very useful information about the spatial distribution and other properties of

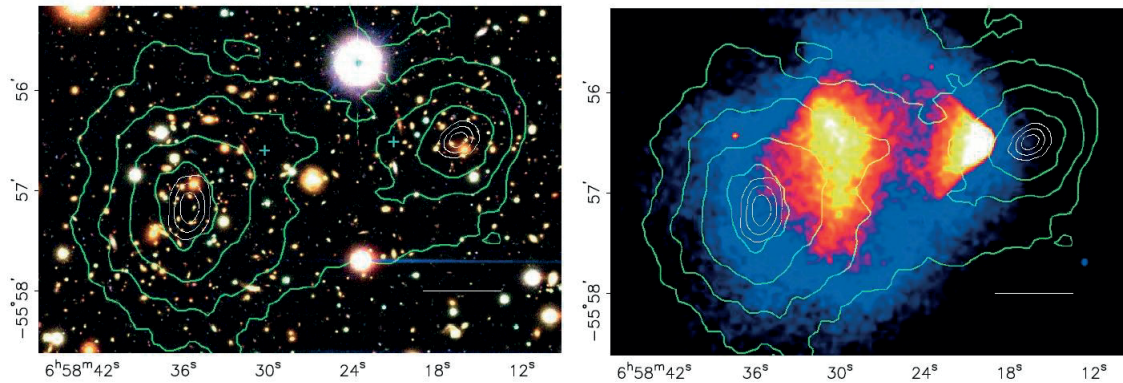


Figure 2.9: *Left*: The telescope image of the “Bullet” cluster with the white bar indicating 200 kpc at the distance of the cluster. *Right*: Chandra image of the cluster. Shown in green contours in both panels are the weak-lensing reconstructions. The white contours correspond to 68.3%, 95.5%, and 99.7% confidence levels (Clowe et al. 2006).

these structures. Fritz Zwicky had advocated in 1937 the use of gravitational lensing as an astrophysical tool (Zwicky 1937a), but as before was not taken seriously. But in 1979, interest in the use of gravitational lenses was revived after the discovery of the first strongly lensed system by Walsh et al. (1979). In the years that followed, this technique was used to measure the total mass of the clusters, confirming the estimates from X-ray studies.

The 1990s also saw the development of statistical techniques for analyzing weaker gravitational lensing effects (e.g., Tyson et al. 1990). Weak lensing has now become a powerful probe of dark matter. Examples of applications are the measurement of the total mass of galaxy clusters (e.g., Wittman et al. 2003; Margoniner et al. 2005), the mapping of the distribution of dark matter (e.g., Dahle et al. 2002; Gray et al. 2002; Clowe & Schneider 2002; Umetsu 2010; Pires et al. 2010) or the study of the properties of dark matter halos (e.g., Hoekstra et al. 2004; Sheldon et al. 2004).

The conjoint analysis of X-ray and weak gravitational lensing data is also particularly useful. A striking evidence for dark matter has been recently obtained by Clowe et al. (2006) from the combined analysis of X-ray and weak lensing data of the so-called “Bullet” cluster (1E 0657-558), which in fact consist of two colliding clusters of galaxies (see Fig. 2.9). It is thought that after colliding, the collisional visible matter of each cluster remained at the center of the system, while the supposedly collisionless dark matter passed through. Weak gravitational lensing is a central topic of this thesis and is covered in detail in Chapter 3.

Cold dark matter

At the same time the evidence for dark matter was being confirmed in the 1970s, suggestions were made regarding its possible nature. Candidates made of ordinary baryonic matter were considered first, but it became clear in the 1980s and 1990s that only a small fraction of the missing mass could be in baryonic form. Measurements from entirely different origins now all agree that baryonic matter can only represent a small fraction of the total amount of dark matter in the Universe. As we will see in Sect. 2.4.5, the density parameter for all baryons is estimated to be $\Omega_m \approx 0.3$, whereas that solely due to baryons is $\Omega_b \approx 0.05$. The

main constraints are provided by Big Bang nucleosynthesis (see Sect. 2.4.1) (e.g., Steigman 2006), measurements of the CMB (see Sect. 2.4.2), the theory of galaxy formation (e.g., Rees & Ostriker 1977; White & Rees 1978; Fall & Efstathiou 1980) and the estimated population of massive astrophysical compact halo object (“MACHOs”) (e.g., Hewitt et al. 1987; Alcock et al. 1993; Afonso et al. 2003).

Once it was established that most of dark matter is not made of baryons, two competing theories were put forward regarding the properties of that matter. The first one, led by Iakov B. Zel'dovich and his group, advocated that dark matter was mostly in the form of light neutrinos (e.g., Doroshkevich et al. 1981; Zel'dovich et al. 1982). That theory predicted a top-down model of structure formation where massive objects would have formed first, smaller structures subsequently created by fragmentation and instabilities. That approach was nick-named “hot dark matter” (HDM), since it involved fast, relativistic particles. The second scenario assumed dark matter is made of massive, non-relativistic particles (e.g., Efstathiou & Silk 1983; Blumenthal et al. 1984) and was, for this reason, dubbed “cold dark matter” (CDM) by Phillip J. E Peebles in 1982. That model predicted smaller structures would form early after recombination (see Sect. 2.3) and more massive ones later, through coalescence and clustering of from larger-scale density perturbations.

The CDM model has since then proved very successful in reproducing the observed late formation of galaxies, the level of anisotropies in the CMB, the power spectrum of the spatial distribution of galaxies and the results of numerical simulations (e.g., Bond & Szalay 1983; White et al. 1993; Dekel 1994; Bahcall et al. 1995; Copi et al. 1995; Navarro et al. 1997; Somerville & Primack 1999; Katz & Gunn 1991; Navarro & White 1994). Starting from the publication of White et al. (1983), the HDM scenario was progressively rules out.

With the emergence of the CDM paradigm in the 1980s, the then standard Einstein–de Sitter (EdS) cosmological model (Einstein & de Sitter 1932) began to be refined to incorporate cold dark matter. In the 1990s, the favored model was the so-called “standard cold dark matter model” or SCDM with $\Omega_\Lambda = 0$ and $\Omega_m = 1$. But cosmologists were also considering more “lightweight models”, in particular, the Λ CDM models with $\Omega_\Lambda = 0.7$ and $\Omega_m = 0.3$.

The possible composition of cold dark matter according to particle physics along with potential issues with the CDM model will be outlined in Sect. 2.5.2.

2.4.4 Accelerated expansion and the Λ CDM cosmological model

First evidence from type Ia supernova data

The observation of fainter than expected type Ia supernovae (SNe Ia) in the years 1997–98, which strongly suggested a Universe in accelerated expansion, has revolutionized the entire field of cosmology.

In principle, supernovae can be used to measure the luminosity distance as a function of redshift. The idea of using type Ia supernovae as standard candles for measuring the history of cosmic expansion dates back to the 1970s, the first serious attempt having been made with the pioneering work of Norgaard-Nielsen et al. (1989). But the systematic search and analysis of such objects on a large scale only became possible in the mid-1990s, which saw the constitution of two large international projects, the Supernova Cosmology Project (SCP), joined later by the High- z Supernova Search Team (HSZT). Supernovae as cosmological tools

Chapter 2. Quick overview of modern cosmology

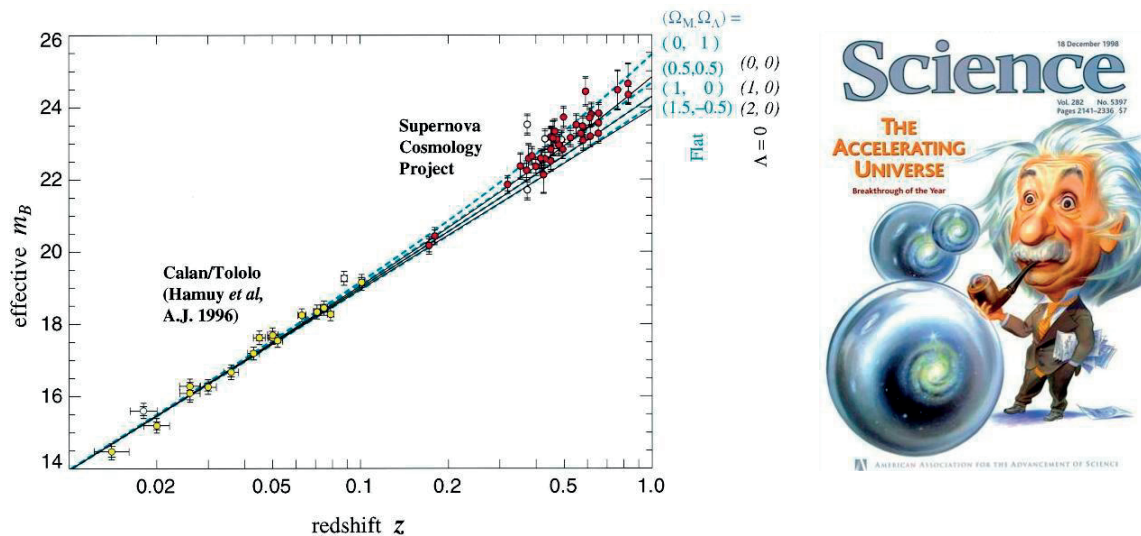


Figure 2.10: *Left*: First evidence for cosmic acceleration from the Supernova Cosmology Project (SCP): the Hubble diagram shows the evolution of the apparent luminosity m_B with the redshift z for 42 high-redshift SNe Ia from the SCP (Perlmutter et al. 1999) and 18 low-redshift SNe Ia from the Calan/Tololo Supernova Survey (Hamuy et al. 1996). *Right*: The cover of Science Magazine in December 1998, celebrating the breakthrough of the year: the discovery of cosmic acceleration from supernovae.

have been described in many papers and reviews, e.g. (Astier et al. 2006).

The first results obtained by the SCP team initially showed the expansion of the Universe was slowing down, in accordance with SCDM ($\Omega_m = 1$, $\Omega_\Lambda = 0$), the standard Robertson–Walker cosmology at that time (Perlmutter et al. 1997). But when they later included the high redshift type Ia supernova SN 1997ap to their sample, they found, to their astonishment, evidence for an accelerating Universe (Perlmutter et al. 1998). The discovery of 33 new supernovae in 1998 and the re-analysis of their previous sample allowed the SCP team to confirm their early results (Perlmutter et al. 1999), as shown in Fig. 2.10, left. At the end of 1998, working independently and with a different supernova sample, the HZT team reached a similar conclusion (Riess et al. 1998; Schmidt et al. 1998). The cover of Science magazine celebrating the discovery of the accelerating Universe from supernovae is reproduced in Fig 2.10, right.

Further confirmations from supernova data and other sources

Although both the HZT and SCP teams had independently reached the same conclusion, uncertainties were large, raising the possibility that acceleration was a side-effect of some systematic phenomenon such as dust extinction (Drell et al. 2000; Filippenko 2001; Leibundgut 2002).

Between 2000 and 2002, various balloon experiments designed to measure the CMB fluctuations found evidence for a flat Universe (i.e. $\Omega_0 \approx 1$) (e.g., de Bernardis et al. 2000, 2002; Pryke et al. 2002; Rubiño-Martín et al. 2003). Moreover, the outcome from various deep galaxy redshifts surveys, in particular the 2dF Galaxy Redshift Survey (2dGRS), favoured a value of

$\Omega_m \approx 0.3$ (Peacock et al. 2001; Efstathiou et al. 2002). These results seemed inconsistent with a matter-only dominated Universe and gave additional credit to the findings obtained from supernovae.

In September 2003, Knop et al. (2003) found $\Omega_m \approx 0.25$ from a completely independent sample comprising 11 new high-redshift SNe Ia observed, not from telescopes on the ground, as before, but from space with the Hubble Space Telescope (HST). Later the same month, the HZT team reported on the observation of 8 newly-discovered SNe Ia at redshifts in the region $0.3 < z < 1.2$, finding $\Omega_m \approx 0.3$. As the HZT paper was near completion they heard about the results from observations of the fluctuations in the CMB spectrum from the WMAP (Wilkinson Microwave Anisotropy Probe) satellite. The data from WMAP established the Universe has a flat geometry to a high precision, finding $\Omega_0 \approx 1.02$. It also further confirmed the value of Ω_m , finding $\Omega_m \approx 0.27$ (Bennett et al. 2003b; Spergel et al. 2003). The data from WMAP combined with results from the Sloan Digital Sky Survey (SDSS) also agreed well (Tegmark et al. 2004b).

The confirmation from WMAP of a flat, low-density Universe, strongly suggested the existence of a third, as yet unknown, component in the Universe besides matter and radiation, driving the current period of accelerated expansion. Because it would have a similar effect on the rate of expansion, a non-zero cosmological constant appeared as the prime candidate for such a dark component. Actually, it had already been observed that Λ CDM, a model with a substantial cosmological constant, had the potential to reconcile a flat Universe, as predicted by inflation, with the apparent age of globular clusters (Turner 1991; Krauss & Turner 1995; Ostriker & Steinhardt 1995). If so, the cosmological constant would have just enough density to close the Universe with $\Omega_\Lambda \approx 1.0 - 0.3 = 0.7$.

The case for accelerating expansion was further strengthened when HZT published the results from 16 new high-redshift SNe Ia obtained with the HST in the course of the GOODS ACS Treasury program (Riess et al. 2004). This paper confirmed again $\Omega_m \approx 0.3$ for a flat Universe and saw compelling evidence for a transition from a decelerating towards an accelerating Universe around $z \approx 0.46$.

The confirmation of accelerated expansion promoted Λ CDM as the new standard cosmological model.

Latest evidence for accelerated expansion

As of 2013, that the expansion of the Universe is accelerating due to some “dark energy” component, whatever its real physical nature, is a well established fact. Since the pioneering work of the SCP and HSZT teams, further support in favor of dark energy has come mainly from more detailed analysis of the CMB spectrum, new Supernovae observations, baryonic acoustic oscillations (BAO) and, more recently, weak gravitational lensing.

New supernovae data are now available from the ESSENCE supernova survey (Miknaitis et al. 2007; Wood-Vasey et al. 2007), the Supernova Legacy Survey (SNLS) (Pritchett & SNLS Collaboration 2005; Sullivan & Supernova Legacy Survey Collaboration 2005; Astier et al. 2006; Conley et al. 2011; Sullivan et al. 2011), the Sloan Digital Sky Survey-II (SDSS-II) Supernova Survey (Frieman et al. 2008; Kessler et al. 2009), along with smaller samples from the HST that extend to higher redshifts (Riess et al. 2007).

These data have confirmed and sharpened the evidence for accelerated expansion. By them-

selves supernova data cannot constrain all cosmological parameters but they can be efficiently combined with CMB data. The latter complement the measurements of luminosity distances from supernovae with estimates of the position, relative amplitude and width of the peaks in the CMB power spectrum, as described by the CMB shift parameter (Bond et al. 1997; Ödman et al. 2003). The measurements of the CMB obtained by the Planck satellite, the European successor of WMAP, have just been published and are available in Ade et al. (2013a). These results confirm and further refine those obtained by WMAP, like the presence of several large scale anomalies in the CMB temperature distribution and the non-detection of non-Gaussian statistics.

Around 2005, a new independent dark energy test has become available in the form of baryonic acoustic oscillations (BAO), reinforcing the standard theory of formation of cosmic structures (see Sect. 2.3). Such structures are believed to have resulted from the competition between self-gravity and the expansion of the Universe. As described in Sect 2.3, perturbations were able to grow as the decreasing rate of expansion allowed self-gravity to dominate other time. The early universe was a mixture of baryonic gas (nuclei, electrons), neutrinos, photons and cold dark matter (CDM). In overdense regions, CDM clustered, whereas the gas which was ionized and extremely hot was locked with the photons in a single plasma fluid. Consequently, that plasma expanded as a spherical acoustic wave. Over time the Universe cooled down and the spherical shell of the gas perturbation imprinted itself in the dark matter, forming the baryon acoustic oscillations in the galaxy power spectrum. Structures formed around the center of the initial perturbations of gas and dark matter in a shell of about 150 Mpc in radius. Because of the small scale of the perturbations, such a signature could only be clearly detected by probing very large volumes of space of order $1 \text{ h}^{-3} \text{ Gpc}^3$. More detailed descriptions of the underlying physics can be found in (e.g., Peebles & Yu 1970; Bond & Efstathiou 1984; Hu & Sugiyama 1996; Eisenstein & Hu 1998).

Since its detection in 2000 (Bacon et al. 2000; Kaiser et al. 2000; Van Waerbeke et al. 2000; Wittman et al. 2000), weak lensing has emerged as a very promising probe of cosmological parameters and especially the dark sector. The lensing of distant background galaxies due to surrounding foreground large-scale structures generates a faint but coherent signal called the “cosmic shear”, which can be exploited to probe the growth of cosmic structures and the recent expansion history of the Universe (e.g., Bartelmann & Schneider 2001; Hoekstra & Jain 2008; Refregier 2003b; Munshi et al. 2008; Huterer 2010).

A considerable amount of work has been devoted during the last decade to the measurement of the cosmic shear. Several large weak lensing surveys were performed, among them the Red Cluster Sequence (RCS) (Hoekstra et al. 2002), VIRMOS-Descart (Van Waerbeke et al. 2002a, 2005), CFHTLS (Hoekstra et al. 2006; Fu et al. 2008), CTIO (Jarvis et al. 2006), GaBoDS (Hettterscheidt et al. 2007) and COSMOS (Massey et al. 2007b). The still limited area of sky covered, the lack of knowledge of source redshifts and the still high level of systematic errors remain significant sources of uncertainty in these studies. Nevertheless, all tend to confirm an accelerating expansion of the Universe. They also place independent constraints on the Ω_m and σ_8 parameters consistent with those found by other methods (see Fig. 2.11, top right). Next-generation lensing surveys will be capable of probing a larger set of cosmological parameters. Weak gravitational lensing and how it can be used to constrain cosmological parameters are the main subjects of this thesis and covered in detail in the next chapter.

2.4. “Concordance” cosmology

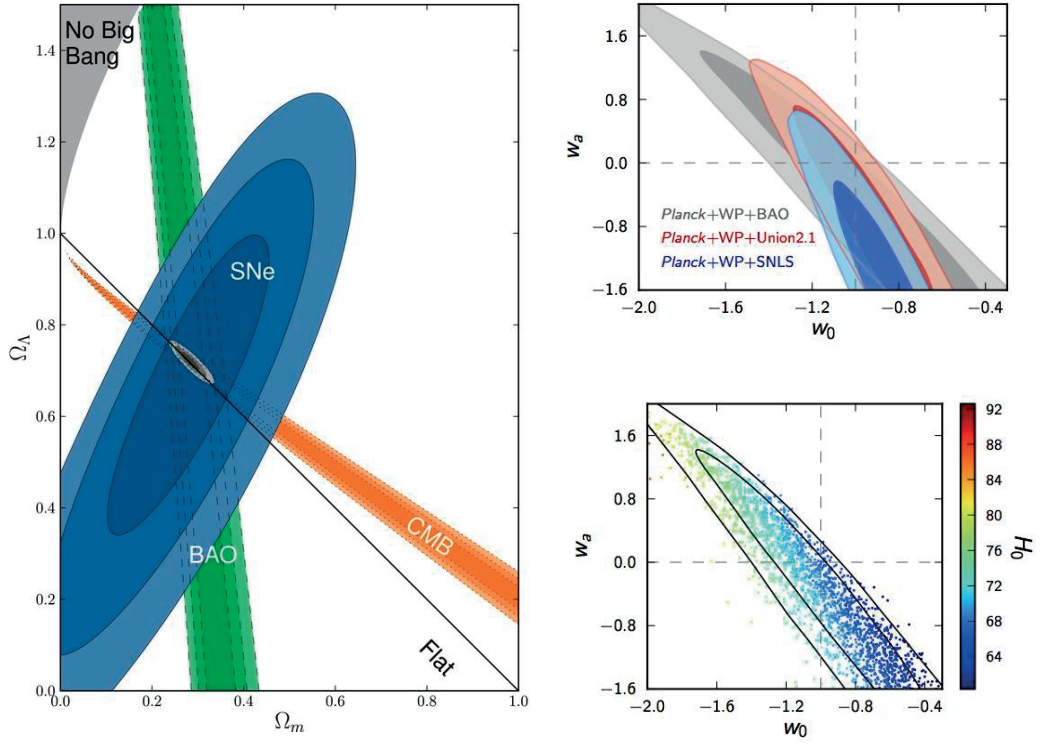


Figure 2.11: *Left*: joint constraints on Ω_m and Ω_Λ from the SNe Union2.1 compilation, WMAP 7-years CMB and BAO from SDSS DR 7, at 68.3%, 95.4%, and 99.7% confidence level (assuming $w = -1$) Suzuki et al. (2012). The Union2.1 compilation combines multiple SNe data sets based on a scheme described by Kowalski et al. (2008). *Top right*: Joint constraints on the dark energy equation of state parameter $w(z) = w_0 + w_a[1 - a(z)] = w_0 + w_a(z/(1+z))$ (Linder 2003; Chevallier & Polarski 2001) from the Planck data (Ade et al. 2013a,b), the WMAP 9-year data (Hinshaw et al. 2012) (denoted by WP), BAO from SDSS DR7 and SNe data (Union2.1) (Suzuki et al. 2012) and SNLS (Conley et al. 2011), consistent with a cosmological constant with $w = -1$. *Bottom right*: Similar joint constraints on the dark energy equation of state from the combined Planck, WMAP 9-year (WP) and BAO SDSS DR7 data, showing the dependency on the value of H_0 (Ade et al. 2013b).

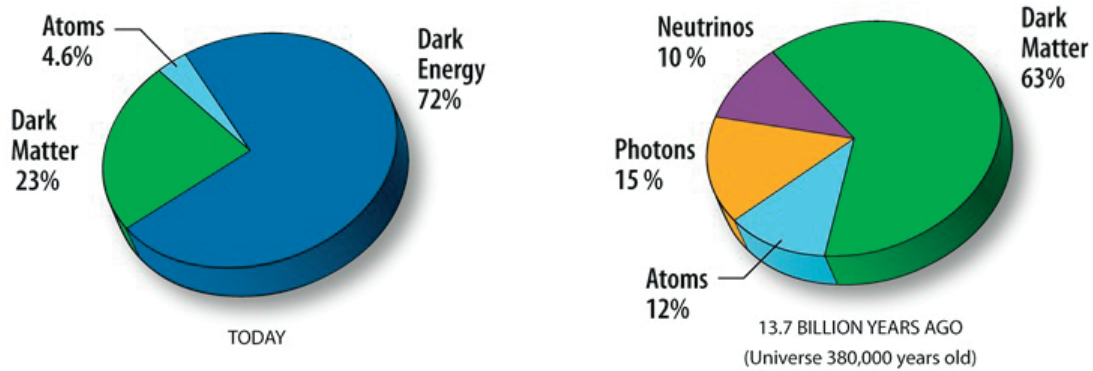


Figure 2.12: The respective contributions of the constituents of the Universe at present time (left) and at the epoch of recombination (about 380,000 years after the Big Bang), right. The WMAP data revealed that the universe is made of about 5% atoms (baryons), whereas dark matter and dark energy comprise respectively about 23% and 72% (source: WMAP 7-year data). The more recent results from the Planck CMB satellite (Ade et al. 2013a,b) suggest a weaker cosmological constant (by $\sim 2\%$), more baryons (by $\sim 3\%$) and more cold dark matter (by $\sim 5\%$).

2.4.5 Latest constraints on cosmological parameter

Remarkably, the observations from Supernovae, CMB power spectrum, BAO, weak lensing and other probes such as the integrated Sachs–Wolfe effect (e.g., Boughn & Crittenden 2004; Dupé et al. 2011) or the Lyman- α forest (e.g., Viel et al. 2010) converge to the predictions of the Λ CDM cosmological model.

All cosmological probes reach the conclusion that our Universe has a locally flat geometry ($\Omega_k \approx 0$), a low density $\Omega_m \approx 0.30$ with the remaining energy density being dominated by a cosmological constant, such that $\Omega_\Lambda \approx 0.70$. Recent constraints on the cosmological parameters from Supernova, the CMB (WMAP), BAO and lensing are illustrated in Fig. 2.11. The results published by the Planck Collaboration in March 2013 (Ade et al. 2013a), confirmed this picture and are in especially good agreement with those from BAO. There exists, however, tensions with the measurements obtained from SNe and weak lensing by large-scale structures. The respective contributions of baryonic matter, dark matter and dark energy are also slightly altered: a weaker cosmological constant (by $\sim 2\%$), more baryons (by $\sim 3\%$) and more cold dark matter (by $\sim 5\%$). The origin of these discrepancies is still unclear. They may originate from residual systematic errors or may in fact constitute hints of new physics beyond that of the standard model.

Another source of worry is the still high level of uncertainty in the determination of the Hubble constant H_0 . An illustration of this situation is the tension between the value of $H_0 = 72 \pm 8 \text{ km s}^{-1} \text{ Mpc}^{-1}$ determined by the HST Key Project (Freedman et al. 2001) and the recent measurement by the Planck CMB probe, $H_0 = 67.3 \pm 1.2 \text{ km s}^{-1} \text{ Mpc}^{-1}$ (Ade et al. 2013a). It is hoped that measurements of time delays from the study of strongly lensed QSO can reduce that uncertainty by a factor of 10 in the near future.

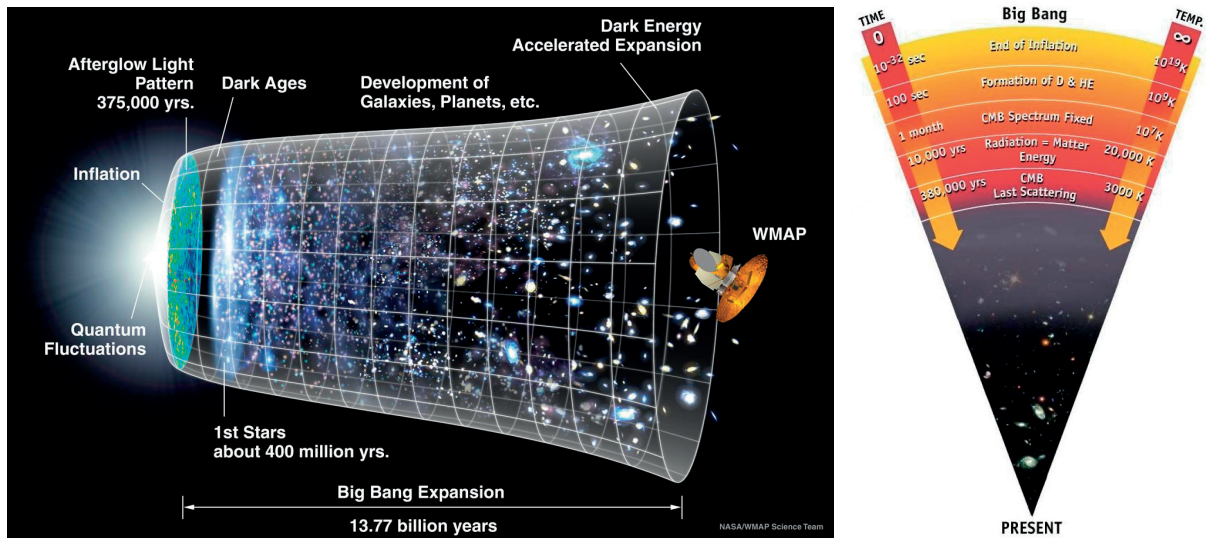


Figure 2.13: *Left*: The history of the Universe as we understand it today. *Right*: Thermal history of the Universe (source: NASA/WMAP Science Team).

2.4.6 Timeline

Fig. 2.13, created by the WMAP team, is a good illustration of what we think were the main events that took place in Universe history, up to the present time.

2.5 Unsolved problems

Standard cosmology in the form of the Λ CDM cosmological model has achieved remarkable successes:

- It accounts very well for the dynamics of expansion of the Universe (see Sect. 2.1.2)
- It predicts the observed abundance of light-elements produced during Big Bang nucleosynthesis (see Sect. 2.4.1).
- It explains the observation of the cosmic microwave background (see Sect. 2.4.2).
- It account correctly for the observed small and larger-scale structures of the Universe though the theory of structure formation (see Sect. 2.3).

Despite these successes, a number of fundamental questions remain unanswered, in particular:

1. Why is the Universe so homogeneous and why is its geometry flat to such a high precision?
2. What is dark matter? Is it some as yet unknown type of particle or something else? It is related to dark energy?
3. What is dark energy? Is it the cosmological constant or an evolving scalar field? If dark energy is the cosmological constant, why is its value precisely the value measured today and how can we explain that value? Is dark energy a manifestation of the failure of general relativity under some conditions? It is really by chance that we are able to witness the transition from a matter-dominated Universe to one dominated by dark

energy?

2.5.1 The “Horizon” and “Flatness” problem

The analysis of the CMB has shown that the average amplitude of the temperature anisotropies in the Universe at the time of recombination ($z \sim 1000$) was very small, of the order of $\Delta T/T \sim 10^{-5}$. Very distant regions in the Universe appear to share the same properties even though they could not have been causally connected in the past. This “cosmological Horizon problem” was pointed out by Charles Misner in the 1960s.

Another issue is the observation that the Universe is “flat” to a high degree, the so-called “Flatness problem”. Since the total density departs rapidly from the critical value over cosmic time, this means the Universe must have been even flatter in the past.

The “Horizon” and “Flatness” problems have found an elegant explanation in the 1980s, with the theory of “Inflation”, originally put forward by Alan Guth (Guth 1981) and later improved by Andrei Linde (Linde 1982a,b), Andreas Albrecht, Paul Steinhardt (Albrecht & Steinhardt 1982) and others. The Universe is supposed to have experienced a huge and extremely rapid phase of expansion soon after the Big Bang that rendered its curvature flat to such a degree that it is still flat today. Before inflation, the Universe is supposed to have been small enough, making it possible for all regions to be causally connected and reach thermal equilibrium, which provides an explanation for the observed homogeneity. Although hints of inflation have been found, e.g. in the CMB spectrum (Peiris et al. 2003), the evidence is still not strong enough for inflation to be included in the standard cosmological model. For a recent review see e.g. Baumann (2009).

2.5.2 The physical nature of dark matter

As of 2013, the physical nature of dark matter is still unknown. Most scientists think non-baryonic dark matter is composed of elementary particles created early in the history of the Universe. Dark matter candidates must meet a number of criteria: they must be stable on cosmological time scales in order to still exist at present time, they must interact very weakly with electromagnetic radiation and they must have the right range of mass. As we saw in (see Sect. 2.4.3), theory and observations also favor a “cold” form of dark matter made of particles that were already non-relativistic at the time of recombination. These considerations still allow a wide range of dark matter candidates and current observational constraints are too weak to discriminate between them. Favored dark matter candidates include axions, sterile neutrinos, gravitinos and weakly interacting massive particles (WIMPs). There are a dozen experiments planned or under way, but so far, none have detected dark matter candidates. For reviews, see e.g. Feng (2005); Trodden (2006); Bertone (2010).

Cold dark matter (CDM) is the preferred model and one of the pillar of the standard Λ CDM cosmological framework, which is indeed quite successful in reproducing the large-scale structure of the Universe. However, small-scale observations have proven harder to explain and there remains observations that seem to contradict the CDM model. In particular, simulations based on Λ CDM predict a larger number of dwarf galaxies that has been found in the Local Group (e.g., Kauffmann et al. 1993; Mateo 1998; Klypin et al. 1999; Moore et al. 1999) although new recent observations may provide solutions (e.g., Simon & Geha 2007; Vegetti et al. 2012). Other issues are related to the shape of the dark halo central density profiles. A CDM model

predicts cuspier density profiles than observed (e.g., Navarro et al. 1997; Swaters et al. 2003; Navarro et al. 2004; Diemand et al. 2005; Spano et al. 2008; Oh et al. 2011), although possible explanations have been put forward in e.g. Wechsler et al. (2002); Zentner & Bullock (2002).

For general reviews on dark matter, see e.g., Bahcall et al. (2004); Livio (2004); Drees & Gerbier (2012); Peter (2012).

2.5.3 The physical nature of dark energy

Dark energy as the “Cosmological constant”

To explain the current phase of cosmic expansion, the most obvious candidate is the old cosmological constant originally introduced by A. Einstein (Einstein 1917). And indeed, as shown in Fig. 2.11 bottom right, a Λ CDM cosmological model with $\Omega_m \approx 0.28$ and $\Omega_{DE} = \Omega_\Lambda \approx 0.72$ is still very much consistent with the latest observations.

A. Einstein originally introduced his cosmological constant on the left-hand side of the field equations (2.1) in order to curve space-time geometry just enough to obtain a static Universe (Sect. 2.1.3). The modern approach is to view the cosmological term as an additional source of gravity and move Λ to the right-hand side of (2.1), to obtain:

$$R_{\mu\nu} - \frac{1}{2}g_{\mu\nu}R = 8\pi G T_{\mu\nu} - \Lambda g_{\mu\nu} \quad (2.102)$$

Writing

$$T_{\mu\nu}^\Lambda = \Lambda g_{\mu\nu} \quad (2.103)$$

the energy-momentum tensor of the gravity source associated to Λ , one can rewrite (2.102) as

$$R_{\mu\nu} - \frac{1}{2}g_{\mu\nu}R = 8\pi G \tilde{T}_{\mu\nu} \quad (2.104)$$

with an effective energy-momentum tensor $\tilde{T}_{\mu\nu} = T_{\mu\nu} - 1/(8\pi G) T_{\mu\nu}^\Lambda$. A value $T_{\mu\nu} = 0$ can be physically interpreted as having empty space also filled with vacuum energy of mass density

$$\rho_\Lambda = \frac{\Lambda}{8\pi G} \quad (2.105)$$

and pressure

$$p_\Lambda = -\frac{\Lambda}{8\pi G} \quad (2.106)$$

Around 1967, Y. B. Zeldovich showed zero-point vacuum fluctuations would have the form (2.103) to respect Lorentz-invariance (Zeldovich 1967). In this sense, (2.105) and (2.106) can be considered as the density and pressure of the vacuum, with an equation of state

$$w_\Lambda = \frac{p_\Lambda}{\rho_\Lambda} = -1 \quad (2.107)$$

Within the Λ CDM framework, the negative pressure (2.106) is seen as responsible for the

Chapter 2. Quick overview of modern cosmology

current accelerated expansion of the Universe. Indeed, using $w_i = p_i/\rho_i$, the deceleration parameter (2.26) can be expressed as

$$q = -\frac{\ddot{a}}{aH^2} = \sum_i \left(\frac{4\pi G\rho_i}{3H^2} \right) (1 + 3w_i) \approx \frac{1}{2}\Omega_m - \Omega_\Lambda = \frac{1}{2}(1 + 3w_\Lambda\Omega_\Lambda) \quad (2.108)$$

With $\Omega_{m,0} \approx 0.30$ and $\Omega_{\Lambda,0} \approx 0.70$ as currently observed, (2.108) is negative, meaning accelerated expansion.

Even though the Λ CDM model predicts accelerated expansion as shown above, the physical nature of Λ is uncertain. There are essentially three problems affecting the cosmological constant, referred to in the literature as the “cosmological constant problem”, the “fine-tuning problem” and the “coincidence problem” (e.g., Weinberg 1989).

Considering $\Omega_0 \approx \Omega_\Lambda \approx 1$ at the present epoch, $\rho_\Lambda \approx 3H_0^2\Omega_0/(8\pi G)$ and so, from (2.105), $\Lambda \approx H_0^2$. According to current observations $\rho_\Lambda \approx 10^{-47}\text{GeV}^4$ and $\Lambda \approx (2.13\text{h} \times 10^{-42}\text{GeV}^2)$. On the other hand, assuming $\rho_\Lambda \equiv \rho_{vacuum}$, the quantum field theories predict $\rho_\Lambda \approx 10^{74}\text{GeV}^4$, some 123 orders of magnitude greater. The absence of a fundamental mechanism which sets Λ to its tiny observed value is the “cosmological constant problem”.

Moreover, Λ is not zero, so it seems its value is precisely fine-tuned for no apparent reason. If ρ_Λ had been a little larger, then the Universe would have expanded too fast for structures to form. This is also known as the “fine-tuning problem”.

The “coincidence problem” implies that we live at a special epoch: today, the dark energy density is approximately equal to the matter density. However, since matter and radiation evolved rapidly ($\rho_m \propto a^{-3}(t)$ and $\rho_r \propto a^{-4}(t)$) while ρ_Λ remained constant, it is difficult to understand why we are precisely living in an epoch where Ω_m and Ω_Λ are of the same order or magnitude.

Alternative models of Dark energy

Uncertainties related to the physical origin of the cosmological constant have motivated the search for alternative theories, broadly classified in three groups: “dynamical dark energy”, “unified dark energy” (UDE) and “modified gravity”.

In the first group of models, dark energy is modeled as an effective fluid whose origin lies in a scalar field ϕ , evolving in time under the action of some self-interacting potential $V(\phi)$. Different functional expressions for $V(\phi)$ have been investigated, from power laws to exponentials or a combination of both. Popular models are “quintessence”, “Phantom” (ghost) and “k-essence”. These models are able to correctly reproduce the observed data, but are affected by “fine-tuning” problems and the issue of the origin of the scalar field itself.

There is also the possibility that dark energy and dark matter be two different aspects of the same fluid and could thus be modeled by a single equation of state. Such a fluid would behave as dark matter at high densities and dark energy at low densities. Examples of unified dark energy models are the Chaplygin gas and the tachyonic fluid.

In both cases, dark energy is modeled as a new fluid within the framework of general relativity. However, Einstein’s theory of gravity, has not been experimentally verified on cosmological scales. This leaves open the option that dark energy may not have an existence of its own but

may just be the manifestation of a different behavior of gravity on such scales. Based on this idea, "modified gravity" theories are able to explain acceleration in a matter-only Universe without the need of any dark energy. Notable examples are the Dvali-Gabadadze-Porrati (DGP) model and fourth-order theories of gravity. Issues remain, however, such as their compatibility with the predictions of standard general relativity on small scales.

Dynamical models of dark energy

The main idea behind such models is to view dark energy as a new kind of energy arising from a time varying scalar field $\phi(t)$ whose evolution is governed by a potential $V(\phi)$. Such a field would contribute to the total energy density of the Universe, together with matter and radiation.

Mathematically, a scalar field can be regarded as a fluid with a time-dependent equation of state. By analogy, it is possible to find potentials such that dark energy would behave like as a cosmological fluid with negative effective pressure in order to reproduce acceleration within a FLRW framework. The desired potential $V(\phi)$ would also ensure that the huge energy density of the vacuum in the Planck era would decay to the currently observed tiny value of Λ . This would provide an answer to the "cosmological constant problem". Some models also attempt to address the "coincidence problem". Scalar fields naturally arise in particle physics where they are associated with spin-0 particles.

There are several dark energy models based on scalar fields. Their detailed description is beyond the scope of this thesis. For a review see e.g. Amendola & Tsujikawa (2010). We outline below three important models of this class: Quintessence, Phantom (ghost) and k-essence.

Quintessence is defined as "a time-dependent and spatially non-homogeneous component with negative pressure" (Steinhardt et al. 1999). It can be modeled as an ordinary scalar field with negative pressure and EOS such that $-1 < w_\phi = (p_\phi / \rho_\phi) < 0$. Phantom fields were first studied by Caldwell (2002), who called them "Phantom" because of their negative kinetic energy and "supernegative" EOS

$$w_\phi = \frac{p_\phi}{\rho_\phi} < -1 \tag{2.109}$$

which implies their energy density increases with cosmic expansion, unlike most cosmological models. Fundamental physics strongly suggests instabilities at the quantum level should rule-out their existence (Cline et al. 2004). Moreover, (2.109) means violation of the "dominant energy condition" (DEC)

$$\rho_\phi + p_\phi \geq 0 \tag{2.110}$$

believed to be required for stable cosmological solutions (Carroll et al. 2003). But despite this, Phantom cosmology is revealing itself surprisingly consistent with observations (Alam et al. 2004) and remains a possible option for dark energy.

Quintessence provides a mechanism for solving the "coincidence problem" thanks to the judicious choice of a suitably chosen potential. Potentials providing attractor-like solutions allow the Quintessence field to remain negligible until some value of the potential energy at $\phi = \bar{\phi}$ is reached. From that time, Quintessence overtakes the background matter density,

ϕ becomes frozen and cosmic acceleration begins. A weakness of the model is that the potential must be precisely adjusted so that $\bar{\phi}$ corresponds to the present epoch. So, despite the progress made, Quintessence does not allow a complete resolution of the “coincidence problem”. Moreover, the theory does not solve the “cosmological constant” and “fine tuning” problems. Instead of asking why the cosmological constant is so small, the same question can be asked about the initial value of the scalar field and the parameters of the potential. Another issue lies in the origin of the scalar field itself. There is hope that answers to these problems will come from advances in particle physics theories and experiments. Progress may come from further collaboration between the cosmology and particle physics communities.

Regarding Phantom fields, the fact that they are unstable at the quantum level, have negative kinetic energy, break the DEC and predict a Universe with a future singularity, suffice to make them very controversial, even if they seem to fit current observations. Phantom cosmology addresses the “cosmological” and “coincidence” problems no better than Quintessence, although (Scherrer 2005) pointed out that the coincidence problem is “significantly ameliorated” in Phantom cosmologies, as ρ_ϕ and ρ_m remain comparable during a significant portion of the Universe-life time. It was also claimed “Unified Phantom cosmology” models (González-Díaz 2003) could help solving these issues.

The “k-essence” model was introduced by Armendariz-Picon et al. (2000); Chiba et al. (2000) with the objective to provide better answers than Quintessence to the “coincidence” and the “cosmological constant” problems. Like Quintessence, k-essence relies on the dynamics of light scalar fields. But unlike Quintessence, k-essence features a non-canonical kinetic term and does not necessarily require any potential term. k-essence models can have “tracker-like” behaviour during the radiation era and “cosmological constant-like” behaviour after transition to the matter-dominated epoch. Unlike Quintessence, k-essence adjusts its behaviour automatically, for purely dynamical reasons, so there is no need to fine-tune any potential parameters as for Quintessence. In this regard, k-essence seems to provide a better answer to the coincidence problem. Additional details on k-essence can be found in e.g. Chiba (2006); Malquarti et al. (2003); Steinhardt (2003); Rendall (2006); Sen (2006); Copeland (2007).

Modified gravity

We found in previous sections that dynamical dark energy is still unable to provide satisfactory explanations for the origin and physical nature of dark energy. Despite the progress made, scalar field models still do not solve the coincidence problem in a compelling way nor do they answer the long-standing cosmological constant problem. Moreover, to many theorists, the introduction of a “dark energy” fluid seems artificial. Instead of supplementing the source terms of Einstein’s field equation with a cosmological constant or scalar field, another and possibly more “natural” way to obtain accelerated expansion is to introduce corrections to the geometrical part of the field equations. For a review of modified gravity see e.g. Amendola & Tsujikawa (2010).

Several families of models claim to obtain late-time cosmic acceleration in this way, without relying on dark energy. A popular family of models, known under the generic term “ $f(R)$ theories of gravity” (in metric or Palatini formulations), attempt to supplement the Einstein-Hilbert action with some function of the Ricci curvature scalar $f(R)$ which would only start dominating at very low curvature, i.e. at present time (e.g., Carroll et al. 2004; Capozziello et al.

2.5. Unsolved problems

2003; Vollick 2003; Wang & Meng 2004; Abdalla et al. 2005; Nojiri & Odintsov 2006; Sotiriou 2006). Another prominent model, initiated by Dvali, Gabadadze and Porrati (DGP), explains acceleration by the leakage of gravity into a large extra-dimension (the “bulk”) where our four-dimensional spacetime (“three-brane”) is assumed to be embedded (e.g., Randall & Sundrum 1999; Dvali et al. 2000; Lue 2006; Copeland 2007).

3 Constraining cosmology with weak gravitational lensing

According to the theory of general relativity, light rays follow null geodesic of the space-time metric associated with a gravitational field. In the astronomical context, the tidal deviation of these light bundles along the line of sight bears some resemblance with the lensing effect in optics and for this reason has been called “gravitational lensing”. This technique only relies on the physics of gravity and depends neither on the physical state of the matter generating the gravitational field nor on the underlying form of that matter. Gravitational lensing in its strong and weak regimes is thus very useful as an astrophysical tool.

The past decade has seen the rapid development of cosmological applications of gravitational lensing, on which we concentrate in this chapter. We start by introducing the theoretical foundation of gravitational lensing and then focus on gravitational lensing in its weak regime — weak gravitational lensing — as a tool to constrain cosmological parameters and probe the dark Universe.

Throughout the text we adopt Einstein’s notation and metric signature $(-, +, +, +)$, unless stated otherwise. Vectors are denoted by boldface letters. In some places we use the coma operator denote partial (non-covariant) differentiation.

3.1 Fundamentals of gravitational lensing

We provide in this section the fundamentals of gravitational lensing theory. The monograph from Schneider et al. (1992) contains probably the most detailed exposition of the theory. General review articles on the subject have also been provided in e.g. Wu (1996); Narayan & Bartelmann (1996); Courbin & Minniti (2002); Schneider et al. (2006).

3.1.1 Deflection of light and the weak field approximation

The propagation of light in curved space-time is governed by the non-linear field equations of general relativity, which are in general difficult to solve analytically. Fortunately, most astrophysical situations of interest in gravitational lensing only involve deflecting objects with weak gravitational potentials ($\|\Phi\| \ll c^2$) and small peculiar velocities ($v \ll c$). Within these limits, the space-time metric is well approximated by a metric of the form

$$ds^2 = -\left(1 + \frac{r_s}{r}\right) dt^2 + \left(1 - \frac{r_s}{r}\right) dl^2, \quad dl^2 = d\chi^2 + S_k(\chi)^2 (d\theta^2 + \sin^2 \theta d\Phi^2) \quad (3.1)$$

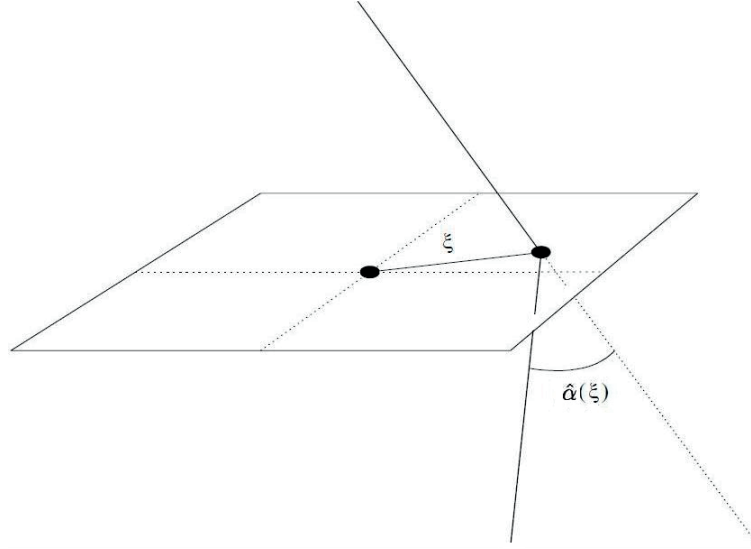


Figure 3.1: A light ray intersects the lens plane at \mathbf{x}_i and is deflected by an angle $\hat{\alpha}$.

where $r_s = 2GM/c^2$ is the Schwarzschild radius and we used the notations of Sect. 2.2. Since photons travel on null geodesics ($ds = 0$ in this metric), it can be shown (e.g., Schneider et al. 1992) that the bending of light rays can be modeled in terms of an effective index of refraction $n = 1 - 2\Phi/c^2 = 1 + 2|\Phi|/c^2$, where Φ is the Newtonian gravitational potential. So the gravitational field can indeed be seen as a refracting medium, distorting light rays as if they were going through a glass prism. The path of light rays is then determined by the application of the variational principle $\delta \int n dl$, where dl is an infinitesimal arc path length. The amount of deflection of light rays by a potential Φ is given by the line integral, along photons trajectory of the gradient of n taken perpendicular to the light path,

$$\hat{\alpha} = - \int \nabla_{\perp} n dl = \frac{2}{c^2} \int \nabla_{\perp} \Phi dl \quad \text{Deflection angle} \quad (3.2)$$

where $\hat{\alpha}$ denotes the deflection angle by a point mass. In general, the deflection angle is a two-component vector. Fig. 3.1 illustrates the situation where a light ray emitted from a source S gets deviated by a point mass M and reaches observer O . The distance of the unperturbed ray from M , orthogonal to the direction of propagation is the impact parameter, usually denoted by ξ . In practice, because the angle $\hat{\alpha}$ is so small, an additional simplification comes by integrating not along the actual photon path but along the unperturbed trajectory, keeping the same impact parameter. If one sets a coordinate system such that the source and the lens lie along the z -axis, and the origin is chosen at the position of the lens, the deflection angle by a point mass is then readily obtained from equation (3.2) as

$$\hat{\alpha} = - \int \nabla_{\perp} \Phi dz = \frac{4GM}{\xi c^2} \quad (3.3)$$

In this case, the lens is called a ‘‘Schwarzschild lens’’ or a ‘‘point-mass lens’’.

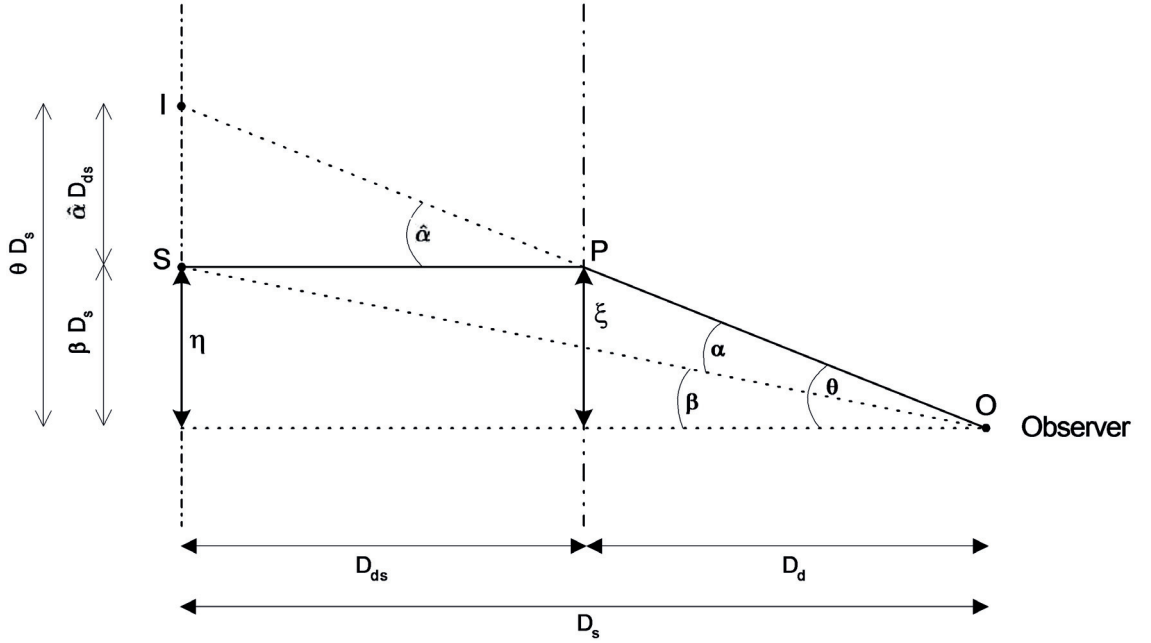


Figure 3.2: Geometry of a typical gravitational lensing system. A light ray travels from the source S at transverse distance η from the optic axis to the observer at O , passing the lens at transverse distance ξ . As a result, that light ray is deflected by an angle $\hat{\alpha}$. The observer at O measures the respective angular separation of the source and the image as β and θ . The distances between the observer and the source, the observer and the lens, and the lens and the source are respectively D_s , D_d and D_{ds} . The angles $\hat{\alpha}$ and α are related through $\alpha D_s = \hat{\alpha} D_{ds}$.

3.1.2 “Thin lens” approximation and the lens equation

Most of the deflection occurs within the distance of the point of closest $\|\xi\|$ approach. This distance is quite small compared to the distances from M to the source S or the observer O , so the actual thickness of the lens can be safely neglected. In the so-called “thin Lens approximation”, the lens is reduced to a plane perpendicular to the line of sight, the “lens plane”, onto which all the lens mass distribution gets projected. The mass distribution is then characterized by its surface density $\Sigma(\xi) = \int \rho(\xi, z) dz$ where ξ is a two-dimensional vector in the lens plane. The deflection angle is then

$$\hat{\alpha} = \frac{4G}{c^2} \iint \frac{\xi - \xi'}{\|\xi - \xi'\|^2} \Sigma(\xi') d^2 \xi' \quad (3.4)$$

Fig. 3.2 depicts the lensing geometry of a typical gravitational lensing system. The distances between observer and lens, lens and source and observer and source are D_d , D_{ds} and D_s respectively. A light ray emitted at S at a transverse distance η , passes the lens at a distance ξ and is deflected by an angle α . The angular separations of the source and image as observed at O are β and θ respectively.

It is clear from the figure that $\alpha D_s = \hat{\alpha} D_{ds}$ and $\theta D_s = \alpha D_{ds} + \beta$. Hence, the following relation,

called the “lens equation” holds

$$\boldsymbol{\beta} = \boldsymbol{\theta} - \boldsymbol{\alpha}(\boldsymbol{\theta}) = \boldsymbol{\theta} - \hat{\boldsymbol{\alpha}} \frac{D_{ds}}{D_s} \quad \text{Lens equation} \quad (3.5)$$

This equation is valid in curved space-time geometry because D_d , D_{ds} and D_s are actually angular-diameter distances (see Sect. 2.2.8). With such distances, $D_s \neq D_{ds} + D_d$. In general, the angles $\boldsymbol{\alpha}$, $\boldsymbol{\beta}$ and $\boldsymbol{\theta}$ are not coplanar and the Lens Equation is a vector equation. Depending on the mass distribution and the position of the source, it can have more than one solutions.

3.1.3 Deflection potential

Using the fact that $\boldsymbol{\xi} = D_d \boldsymbol{\theta}$, equation (3.4) gives

$$\hat{\boldsymbol{\alpha}} = \frac{4G}{c^2} \frac{D_d D_{ds}}{D_s} \int \int \frac{\boldsymbol{\theta} - \boldsymbol{\theta}'}{\|\boldsymbol{\theta} - \boldsymbol{\theta}'\|^2} \Sigma(\boldsymbol{\theta}') d^2 \theta' \quad (3.6)$$

Defining the “critical surface mass density”

$$\Sigma_{cr} = \frac{c^2}{4\pi G} \frac{D_s}{D_d D_{ds}} \quad \text{Critical surface mass density} \quad (3.7)$$

and the dimensionless quantity

$$\kappa(\boldsymbol{\theta}) = \frac{\Sigma(\boldsymbol{\theta})}{\Sigma_{cr}} \quad \text{Convergence} \quad (3.8)$$

known as the “convergence”, the deflection angle $\hat{\boldsymbol{\alpha}}$ becomes

$$\hat{\boldsymbol{\alpha}} = \frac{1}{\pi} \int \int \kappa(\boldsymbol{\theta}') \frac{\boldsymbol{\theta} - \boldsymbol{\theta}'}{\|\boldsymbol{\theta} - \boldsymbol{\theta}'\|^2} d^2 \theta' \quad (3.9)$$

The deflection angle in equation (3.4) can be also written as

$$\hat{\boldsymbol{\alpha}} = \nabla_{\boldsymbol{\theta}} \psi(\boldsymbol{\theta}) \quad (3.10)$$

where

$$\psi(\boldsymbol{\theta}) = \frac{1}{\pi} \int \int \kappa(\boldsymbol{\theta}') \ln \|\boldsymbol{\theta} - \boldsymbol{\theta}'\| d^2 \theta' \quad \text{Deflection potential} \quad (3.11)$$

is called the “deflection potential”. This quantity can be seen as the two-dimensional analogue of the Newtonian gravitational potential and obeys the Poisson equation

$$\nabla_{\boldsymbol{\theta}}^2 \psi(\boldsymbol{\theta}) = \nabla_{\boldsymbol{\theta}} \hat{\boldsymbol{\alpha}} = 2\kappa(\boldsymbol{\theta}) \quad (3.12)$$

3.1.4 Image magnification and distortion

An observer looking directly at the source plane would see the source as it is, without alteration. The various effects introduced by the lens can be mathematically formalized as a mapping

3.1. Fundamentals of gravitational lensing

$\boldsymbol{\beta} \longleftrightarrow \boldsymbol{\theta}$ between the source plane and the lens plane. So, in principle, some of the properties of the source can be deduced by analyzing its projected image onto the lens plane. More insight into the mapping transformation is obtained by locally linearizing the lens equation (3.5) in the vicinity of some angle $\boldsymbol{\theta} = \boldsymbol{\theta}_0$

$$\boldsymbol{\beta} \approx \boldsymbol{\theta}_0 + (\boldsymbol{\theta} - \boldsymbol{\theta}_0) \left[\frac{\partial \boldsymbol{\beta}}{\partial \boldsymbol{\theta}} \right]_{\boldsymbol{\theta}=\boldsymbol{\theta}_0} = \boldsymbol{\beta}_0 + A(\boldsymbol{\theta})(\boldsymbol{\theta} - \boldsymbol{\theta}_0) \quad (3.13)$$

Taking $\boldsymbol{\beta}_0$ and $\boldsymbol{\theta}_0$ to be the centers of light for the unlensed and lensed images respectively, the lensing transformation can simply be written as $\boldsymbol{\beta} = \mathcal{A}(\boldsymbol{\theta})\boldsymbol{\theta}$. The Jacobian matrix

$$\mathcal{A}(\boldsymbol{\theta}) = \partial \boldsymbol{\beta} / \partial \boldsymbol{\theta} \quad (3.14)$$

describes the local properties of the lens mapping and can be expressed as

$$\mathcal{A} = \left(\delta_{ij} - \frac{\partial}{\partial \theta_j} \alpha_i(\boldsymbol{\theta}) \right) = \left(\delta_{ij} - \frac{\partial^2}{\partial \theta_i \partial \theta_j} \psi(\boldsymbol{\theta}) \right) = \mathcal{M}^{-1} \quad (3.15)$$

\mathcal{M} is referred to as the ‘‘magnification matrix’’ and characterizes the magnification performed by the lens: gravitational lensing preserves the surface brightness of the source but alters the solid angle subtended by the image, so the end result is a magnification effect in proportion to the ratio

$$\mu = \frac{\text{image area}}{\text{source area}} = \det \mathcal{M} = \frac{1}{\det \mathcal{A}} \quad (3.16)$$

The distortion induced by the lens results from the combination of a ‘‘convergence’’ effect and a ‘‘shear’’ effect. They can be formalized in terms of the components of the Hessian matrix of ψ , $H(\boldsymbol{\theta}) = \partial^2(\psi) / (\partial \theta_i \partial \theta_j)$, which describes the deviation of the lens mapping from the identity mapping.

Convergence is defined as the scalar

$$\kappa = \kappa(\boldsymbol{\theta}) = \frac{1}{2} \nabla^2 \psi = \frac{1}{2} (\psi_{,11} + \psi_{,22}) \quad (\kappa \geq 0) \quad (3.17)$$

while shear is determined by the pseudo-vector $\boldsymbol{\gamma} = \boldsymbol{\gamma}(\boldsymbol{\theta})$ whose components are

$$\gamma_1 = \gamma_1(\boldsymbol{\theta}) = \frac{1}{2} (\psi_{,11} - \psi_{,22}), \quad \gamma_2 = \gamma_2(\boldsymbol{\theta}) = \psi_{,12} = \psi_{,21} \quad (3.18)$$

An expression of \mathcal{A} in terms of κ and $\boldsymbol{\gamma}$ is obtained by substituting (3.17) and (3.18) into (3.15):

$$\mathcal{A}(\boldsymbol{\theta}) = \delta_{ij} - \psi_{,ij} = \begin{pmatrix} 1 - \psi_{,11} & -\psi_{,12} \\ -\psi_{,21} & 1 - \psi_{,22} \end{pmatrix} = \begin{pmatrix} 1 - \kappa - \gamma_1 & -\gamma_2 \\ -\gamma_2 & 1 - \kappa + \gamma_1 \end{pmatrix} \quad (3.19)$$

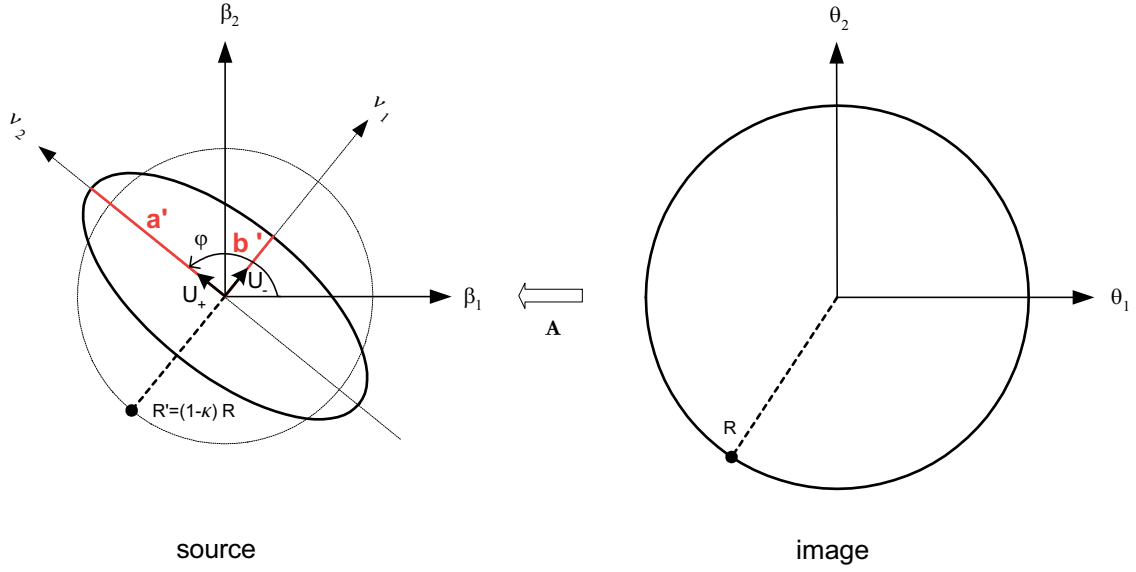


Figure 3.3: Geometrical effects of the transformation $\boldsymbol{\theta} \rightarrow \boldsymbol{\beta}$ described by the \mathcal{A} matrix.

3.1.5 Geometrical interpretation

The $\mathcal{A}(\boldsymbol{\theta})$ transformation $\boldsymbol{\theta} \rightarrow \boldsymbol{\beta}$

As shown in Appendix A.1.1, the geometrical effects of the transformation $\boldsymbol{\theta} \rightarrow \boldsymbol{\beta}$ described by the \mathcal{A} matrix are to compress by a factor λ_- in the \mathbf{U}_- direction and to stretch by a factor λ_+ in the \mathbf{U}_+ direction, where λ_{\pm} and \mathbf{U}_{\pm} are respectively the eigenvalues and eigenvectors of \mathcal{A} given by

$$\lambda_{\pm} = 1 - \kappa \pm |\boldsymbol{\gamma}|, \quad (\lambda_- < \lambda_+) \quad \mathbf{U}_{\pm} \propto \begin{pmatrix} \gamma_1 \mp |\boldsymbol{\gamma}| \\ \gamma_2 \end{pmatrix} \quad (3.20)$$

The area of the transformed object is reduced by a factor $(1 - \kappa)^2 - |\boldsymbol{\gamma}|^2 = \lambda_- \lambda_+$. Applied to a circular image of radius R , the $\boldsymbol{\theta} \rightarrow \boldsymbol{\beta}$ transformation will result in an ellipse with semi-major and semi-minor axis a' and b' respectively given by:

$$a' = R \lambda_+ = R(1 - \kappa + |\boldsymbol{\gamma}|) \quad (3.21)$$

$$b' = R \lambda_- = R(1 - \kappa - |\boldsymbol{\gamma}|) \quad (3.22)$$

This is illustrated in Figure 3.3.

The $\mathcal{M}(\boldsymbol{\beta})$ transformation $\boldsymbol{\beta} \rightarrow \boldsymbol{\theta}$

The magnification transformation matrix $\mathcal{M}(\boldsymbol{\beta})$, is given by (3.15) and reads

$$\mathcal{M}(\boldsymbol{\beta}) = \mu \begin{pmatrix} 1 - \kappa + \gamma_1 & \gamma_2 \\ \gamma_2 & 1 - \kappa - \gamma_1 \end{pmatrix} \quad (3.23)$$

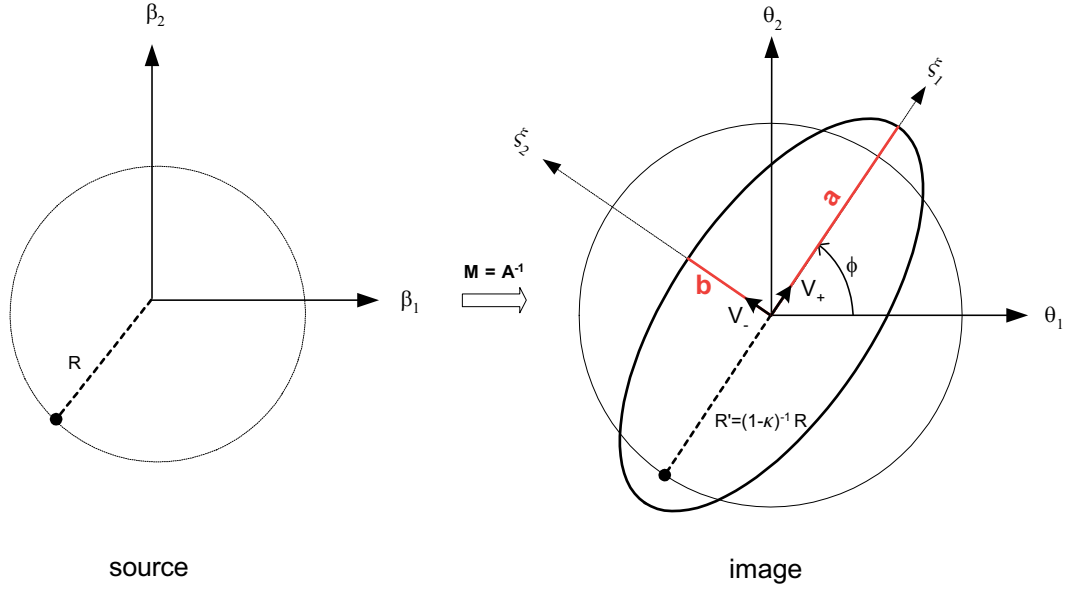


Figure 3.4: Geometrical effects of the transformation $\boldsymbol{\beta} \rightarrow \boldsymbol{\theta}$ described by the \mathcal{M} matrix.

According to (3.16) and as shown in Appendix A.1.2, the magnification factor μ is

$$\mu = \frac{1}{(1-\kappa)^2 - |\boldsymbol{\gamma}|^2} \quad (3.24)$$

As shown in Appendix A.1.2, the transformation $\boldsymbol{\beta} \rightarrow \boldsymbol{\theta}$ will tend to compress by a factor Λ_- in the \mathbf{V}_- direction and to stretch by a factor Λ_+ in the \mathbf{V}_+ direction, where λ_{\pm} and \mathbf{U}_{\pm} are respectively the eigenvalues and eigenvectors of the \mathcal{M} matrix given by

$$\Lambda_{\pm} = \frac{1}{\lambda_{\mp}}, \quad (\Lambda_- < \Lambda_+) \quad \mathbf{V}_{\pm} = \mathbf{U}_{\mp} \quad (3.25)$$

Overall, the area of the source is increased the factor $\mu = \Lambda_- \Lambda_+$. As illustrated in Figure 3.4, if applied to a circular source of radius R , these effects will result in an ellipse with semi-major and semi-minor axis a and b respectively given by:

$$a = R' \Lambda_+ = \mu R (1 - \kappa + |\boldsymbol{\gamma}|) = \frac{R'}{\lambda_-} = \frac{R}{1 - \kappa - |\boldsymbol{\gamma}|} = \mu a' \quad (3.26)$$

$$b = R' \Lambda_- = \mu R (1 - \kappa - |\boldsymbol{\gamma}|) = \frac{R'}{\lambda_+} = \frac{R}{1 - \kappa + |\boldsymbol{\gamma}|} = \mu b' \quad (3.27)$$

Convergence and shear

Decomposing the matrices \mathcal{A} and \mathcal{M} respectively as

$$\mathcal{A}(\boldsymbol{\theta}) = (1 - \kappa) \mathcal{I} - |\boldsymbol{\gamma}| \mathcal{S}_{\phi} \quad (3.28)$$

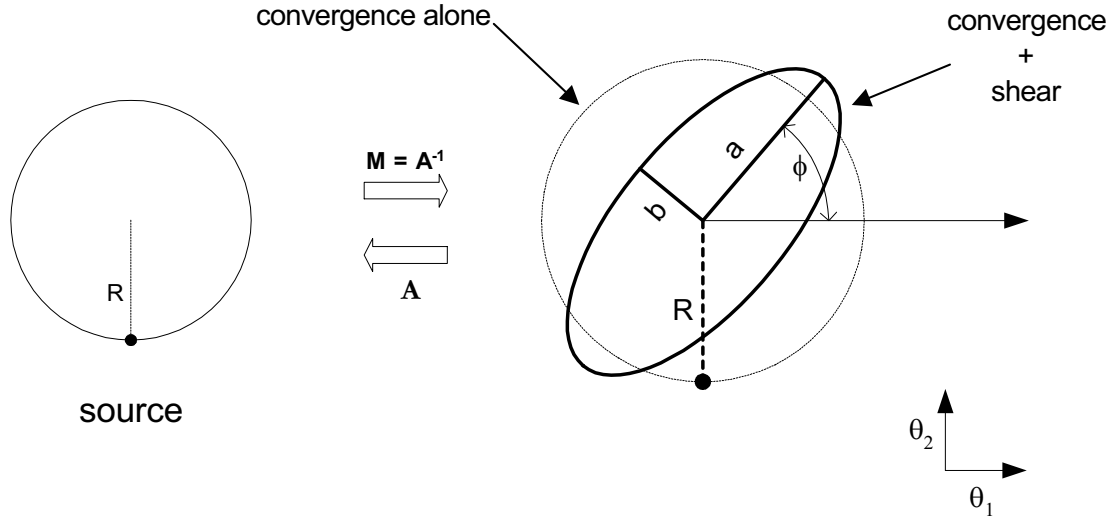


Figure 3.5: Geometrical effects of convergence and shear: convergence magnifies the source without altering its shape, while shear only changes the shape. The case of the magnification transformation $\boldsymbol{\beta} \rightarrow \boldsymbol{\theta}$ is shown.

and

$$\mathcal{M}(\boldsymbol{\theta}) = \mu(1 - \kappa)\mathcal{I} + \mu|\boldsymbol{\gamma}|\mathcal{S}_\phi \quad (3.29)$$

emphasizes the effect of the convergence and shear components. By acting only on the identity matrix \mathcal{I} , convergence acts to alter the size of the image but without introducing distortion. On the other hand, the remaining component involves the matrix

$$\mathcal{S}_\phi = \begin{pmatrix} \cos 2\phi & \sin 2\phi \\ \sin 2\phi & -\cos 2\phi \end{pmatrix} \quad (3.30)$$

which describes a reflection transformation about eigenvector \mathbf{U}_- for \mathcal{A} and \mathbf{V}_+ for \mathcal{M} . This results in an asymmetric shear along the directions \mathbf{U}_\pm and \mathbf{V}_\pm respectively. This is covered in more details in Appendix A.1.2.

3.1.6 Representation in polar coordinates

Comparing equations (3.28) with (3.15) one finds (see Appendix A.1.1, A.1.2) that the components of the shear in polar coordinates are

$$\gamma_1 = |\boldsymbol{\gamma}|\cos 2\varphi \quad (3.31)$$

$$\gamma_2 = |\boldsymbol{\gamma}|\sin 2\varphi \quad (3.32)$$

where φ is given by

$$\varphi = \arctan\left(-\frac{\gamma_1 + |\boldsymbol{\gamma}|}{\gamma_2}\right) + k\pi = \frac{1}{2}\arctan\left(\frac{\gamma_2}{\gamma_1}\right) + k\pi \quad (k \in \mathbb{Z}) \quad (3.33)$$

The corresponding relations for the magnification transformation are

$$\gamma_1 = |\boldsymbol{\gamma}| \cos 2\phi \quad (3.34)$$

$$\gamma_2 = |\boldsymbol{\gamma}| \sin 2\phi \quad (3.35)$$

with

$$\phi = \arctan\left(\frac{|\boldsymbol{\gamma}| - \gamma_1}{\gamma_2}\right) + k\pi = \frac{1}{2} \arctan\left(\frac{\gamma_2}{\gamma_1}\right) + k\pi \quad (k \in \mathbb{Z}) \quad (3.36)$$

In general, if a phase angle ϑ specifies the orientation of the semi-major axis of the ellipse with respect to the horizontal axis, then the shear will be oriented with twice that angle, i.e. 2ϑ . The shear is therefore invariant under a rotation of angle π radians.

The two components of shear γ_1 and γ_2 can be conveniently expressed in Complex space for form a complex shear with modulus $|\boldsymbol{\gamma}|$ and phase angle ϑ , i.e.

$$\boldsymbol{\gamma} = |\boldsymbol{\gamma}| e^{2i\vartheta} = |\boldsymbol{\gamma}| (\cos 2\vartheta + i \sin 2\vartheta) \quad (3.37)$$

One can also defines tangential and cross components of the shear as

$$\gamma_t = -\text{Re}\left(|\boldsymbol{\gamma}| e^{-2i\vartheta}\right) = -|\boldsymbol{\gamma}| \cos 2\vartheta \quad (3.38)$$

$$\gamma_\times = -\text{Im}\left(|\boldsymbol{\gamma}| e^{-2i\vartheta}\right) = +|\boldsymbol{\gamma}| \sin 2\vartheta \quad (3.39)$$

These two components are sketched in Fig. 3.10.

3.1.7 Reduced shear

In the literature, $\mathcal{A}(\boldsymbol{\theta})$ is often expressed as

$$\mathcal{A}(\boldsymbol{\theta}) = (1 - \kappa) \begin{pmatrix} 1 - g_1 & -g_2 \\ -g_2 & 1 - g_1 \end{pmatrix} \quad (3.40)$$

after introducing the "reduced shear"

$$\boldsymbol{g} = g_1 + i g_2 = \frac{|\boldsymbol{\gamma}|}{1 - \kappa} e^{2i\vartheta} \quad (3.41)$$

The corresponding expressions of the magnification tensor $\mathcal{M}(\boldsymbol{\theta})$ and magnification factor μ are

$$\mathcal{M}(\boldsymbol{\theta}) = \mu (1 - \kappa) \begin{pmatrix} 1 - g_1 & g_2 \\ g_2 & 1 - g_1 \end{pmatrix} \quad (3.42)$$

$$\mu = \frac{1}{(1 - \kappa)^2 (1 - |\boldsymbol{g}|^2)} \quad (3.43)$$

One should bear in mind that the shear $\boldsymbol{\gamma}$ is not directly observable. The only quantity that can be measured is the reduced shear \mathbf{g} . Existing shear measurement methods usually approximate $\boldsymbol{\gamma}$ with \mathbf{g} , neglecting the effect of the convergence κ . But, as shown by e.g. White (2005); Dodelson et al. (2006), such an approximation, if left uncorrected, will bias the determination of cosmological parameters by future cosmic shear surveys.

3.1.8 “Strong” versus “weak” lensing

When the deflection of the source light is strong enough to form multiple images, gravitational lensing enters the regime of “strong” lensing. In such a case, at least one point of the lens has $\Sigma \geq \Sigma_{cr}$, i.e. $\kappa(\boldsymbol{\theta}) \geq 1$ and the mapping between source and lens plane is not one-one. The lines joining the points in the source plane where the mapping diverges constitute closed curves called “caustics”. The caustics themselves appear as “critical” curves in the lens plane and whenever a ray from the source comes close to a caustic, its magnification increases. Also, the caustics separate images of different multiplicities, so that the number of images is multiplied by two whenever a source crosses a caustic. The production of multiple images is governed by the “odd number theorem” (Burke 1981). The first formally identified strong lensing system was a double image of the quasar Q0957+56 (Walsh et al. 1979) lensed by an intervening galaxy (see Fig. 3.6, upper left). Near the caustics magnification is maximum and images can take complicated shapes. For example, giant luminous arcs are produced by the lensing of rich galaxy clusters on extended sources like the optical image of a galaxy or the lobe of a radio galaxy, as illustrated in Fig. 3.6. When a source is almost perfectly aligned with a deflector along the line of sight, a ring-like shape called a “Einstein ring” forms. Fig. 3.7 illustrates some of these effects on a generic elliptical lens with four sources. Microlensing effects (Chang & Refsdal 1979; Alcock et al. 1993; Paczynski 1996; Schneider et al. 2006) can also occur where no distortion in shape can be seen but the amount of light received from a background object changes in time. We summarize some major applications of strong lensing in Sect. 3.2.1.

The “weak” lensing regime corresponds to lenses where $\Sigma \ll \Sigma_{cr}$, i.e. $\kappa(\boldsymbol{\theta}) \ll 1$ everywhere on the lens plane. Such lenses are unable to produce multiple images and the transformation matrix \mathcal{A} is very close to the unit matrix. Weak lensing is thus no longer detectable from a single source but only through the statistical analysis of a sufficiently large populations of objects. A typical shear distortion will be of the order of one percent on angular scales of a few arc minutes, which will cause the image of an intrinsically circular source to acquire a change in ellipticity of ~ 0.01 . The main, non-cosmological applications of weak lensing are summarized in Sect. 3.2.2.

3.2 Main applications of gravitational lensing

3.2.1 Strong gravitational lensing

Strong lensing not being a primary topic of this thesis, we only outline below some classical applications of strong gravitational lensing. For reviews, see e.g. Courbin & Minniti (2002); Schneider et al. (2006).

Strong lensing is typically used to probe the inner parts of galaxy clusters and massive elliptical galaxies. For instance, giant arcs can be exploited to model the gravitational potential of the lens and probe the dark and luminous matter distribution. Such arcs may also prove to be

3.2. Main applications of gravitational lensing

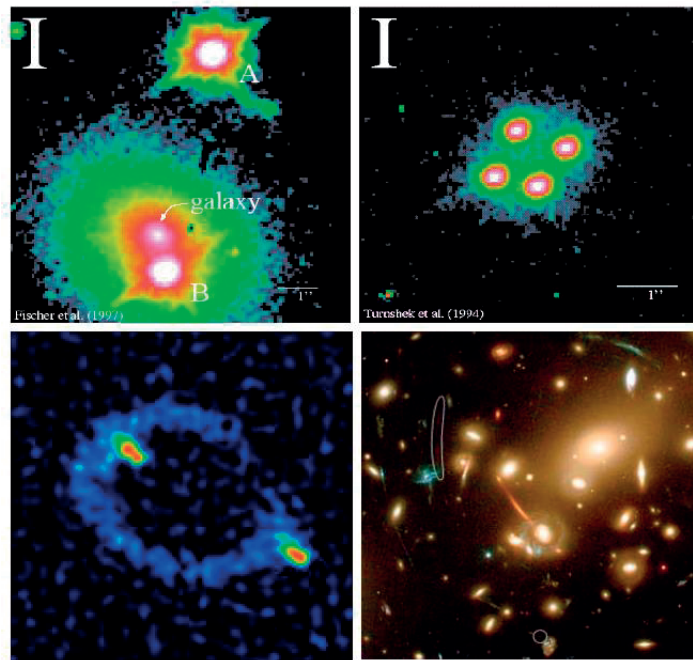


Figure 3.6: *Up-left*: the two images (A & B) of the quasar Q 0957+561 (Fischer et al. 1997). *Up-right*: the quadruple images of the “cloverleaf” quasar H1413+117 (Turnshek et al. 1997) as observed with the Hubble Space Telescope. *Bottom-left*: a 8GHz VLA map of the radio ring MG1131+0456. *Bottom-right*: giant arcs in the lensed galaxy cluster Abell 2218.

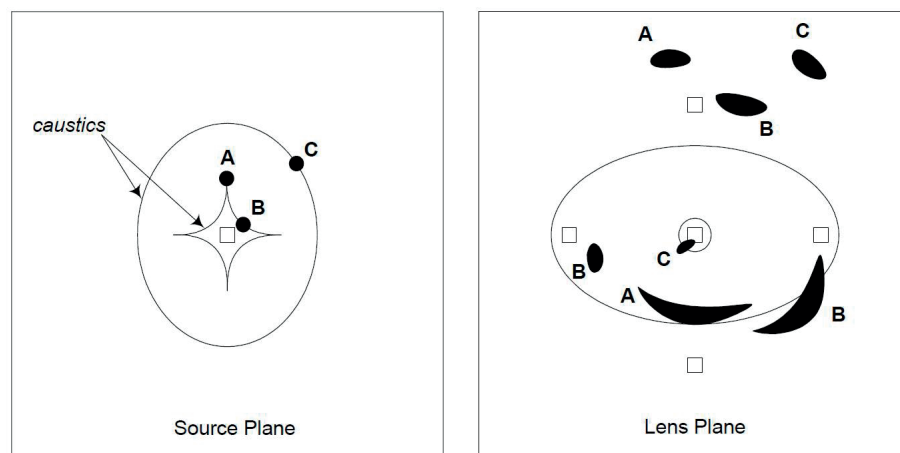


Figure 3.7: Mapping of a lens with four sources: three sources A, B, C on caustics and one on-axis source (square). Adapted from Peacock (1998).

highly magnified high-redshift galaxies that can be detected and studied this way (e.g., Fort & Mellier 1994).

Strong lensing statistics can also produce constraints on Ω_m and Ω_Λ : the number of multiplied-images quasars found in lens surveys increases dramatically with larger Ω_Λ (e.g., Turner et al. 1984; Turner 1990). This relation can be quantified by the “optical depth”, that is, the probability for a source to be imaged in a certain way by a population of lenses. A related statistic is the so-called lensing “cross section”, which is the area in the source plane where strong lensing events with a certain property are observed (e.g. observation of two images). The technique consists in setting up a model of lens population, calculating the cross sections of individual lenses for the desired properties using and comparing the results with observed image statistics. Cosmological parameters are then varied until agreement between the observations and the calculations is reached (e.g., Mitchell et al. 2005).

Another important application of strong lensing is the determination of the Hubble constant H_0 using the “time delay” method (Refsdal 1964a,b). The Lens Equation (3.5) which relates small displacements of a source to small displacement of its image is dimensionless and does not contain any cosmological information. The overall light travel time from the source to the observer is the only quantity that depends on the scale and the distance of a lens system: because of the lensing effect, light will take some extra-time, a time delay, to reach the observer. S. Refsdal realized H_0 could be determined by measuring the time delays of strongly lensed variable sources with multiple images. The time delay results from the competition between a geometrical time delay t_{geom} and a gravitational time delay t_{grav} . The delay t_{geom} reflects the additional travel time due the difference in length between the paths followed by deflected and undeflected photons while t_{grav} is the retardation caused by the gravitational potential of the lensing mass. One cannot directly measure the individual time delay of an image, but the relative time delays between pairs of images can be, by correlating their respective light curves. The total time delay is related to the term $(1 + z_d)D_d D_s / (c D_{ds})$, where z_d is the redshift of the lens, which yield an estimate of H_0 .

3.2.2 Weak gravitational lensing

Weak gravitational lensing has so far been primarily used to (1) study the distribution of dark and luminous matter on the scale of a galaxy cluster; (2) probe the Universe on even larger scale and place constraints on cosmology. The remainder of this thesis is dedicated to the use of weak lensing as a cosmological probe, starting from Sect. 3.3. In the mean time, we summarize here the most important aspects of (1).

Galaxy clusters are massive enough to induce detectable weak lensing effects in the form of distorted images of background galaxies called “arclets” (Fort et al. 1988). Several authors (Kochanek 1990; Tyson et al. 1990; Miralda-Escude 1991a) have shown that these structures exhibit a coherent pattern of distortion throughout the cluster that can be used to model the gravitational potential of the lens. Among the available techniques for reconstructing the projected mass distribution of the cluster are the so-called “direct” (Kaiser & Squires 1993; Broadhurst et al. 1995; Seitz & Schneider 1995) and “inverse” methods (Bartelmann et al. 1996; Squires & Kaiser 1996). Parameterized mass models are also often used to fit the observed data, for example using Navarro–Frenk–White (NFW) mass profiles (Navarro et al. 1997).

The chief advantage of weak lensing lies in its ability to directly probe the gravitational poten-

tial of the cluster regardless of the type of matter involved or the physical state of that matter. Weak lensing estimates can then be critically compared to those obtained from dynamical methods and the study of X-ray emissions from intra-cluster gas.

The reconstruction of cluster mass distribution is now primarily used to study dark matter (e.g., Dahle et al. 2002; Gray et al. 2002; Clowe & Schneider 2002; Wittman et al. 2003; Margoniner et al. 2005; Umetsu 2010; Pires et al. 2010), constrain the properties of galaxy dark matter halos (e.g., Hoekstra et al. 2004; Sheldon et al. 2004) and detect dark matter filaments (e.g., Jauzac et al. 2012). For review see e.g. (Bartelmann & Schneider 2001; Schneider et al. 2006; Hoekstra & Jain 2008).

3.3 The “cosmic shear”, weak lensing by large-scale structures

As explained in Sect. 2.1.1, the cosmological principle ceases to be valid on scales $\lesssim 100$ Mpc, which corresponds to superclusters and giant voids. The possibility that the propagation of light through such large-scale structures (LSS) could generate a weak but statistically detectable lensing signal was envisaged as early as 1966 (Kristian & Sachs 1966; Gunn 1967) and revived in the 1990s (e.g., Jaroszynski et al. 1990; Babul & Lee 1991; Blandford et al. 1991; Miralda-Escude 1991b; Kaiser 1992; Villumsen 1996; Bernardeau et al. 1997; van Waerbeke et al. 1997; Mellier & Fort 1997; Seljak 1995; Jain & Seljak 1997; Kaiser 1998; Hu & Tegmark 1999; van Waerbeke et al. 1999). The coherent shear distortion of distant background galaxy images by the foreground large-scale structures along the line of sight is referred to as the “cosmic shear” or “gravitational lensing by large-scale structures”.

As we explain in more details below, the cosmic shear signal reflects the statistical properties of the large-scale structures themselves and, as such, contains a wealth of cosmological information. Provided the cosmic shear signal can be recovered accurately enough (see Chapter 4), its study can help validate the models of structure growth and accurately retrace the recent expansion history ($z \lesssim 2$) of the Universe. Indeed, as shown by the results of recent surveys (e.g., Hoekstra et al. 2002; Van Waerbeke et al. 2002a, 2005; Hoekstra et al. 2006; Fu et al. 2008; Jarvis et al. 2006; Hettterscheidt et al. 2007; Massey et al. 2007b), weak lensing by large-scale structures is emerging as a powerful probe of dark matter and dark energy, despite still being limited by a still relatively-high level of statistical and systematic errors.

In this section we introduce the equations of propagation of light in an inhomogeneous Universe and present the statistical tools for describing the cosmic shear signal. The cosmological implications of the cosmic shear will be covered in Sect. 3.4.

3.3.1 Propagation of light in an inhomogeneous Universe

As illustrated in Fig. 3.8, the light emitted by background distant galaxies gets continuously deviated by foreground large-scale structures, resulting in distorted images of those galaxies as observed from Earth. Assuming a Universe with a geometry described by a weakly-perturbed Robertson–Walker metric, the propagation of light rays in a light bundle is governed, within the framework of general relativity, by the geodesic equation

$$\frac{d^2 \mathbf{x}}{d\chi^2} + k\mathbf{x} = -\frac{2}{c^2} \Delta \left[\nabla_{\perp} \Phi(\mathbf{x}(\boldsymbol{\theta}, \chi), \chi) \right] \quad (3.44)$$

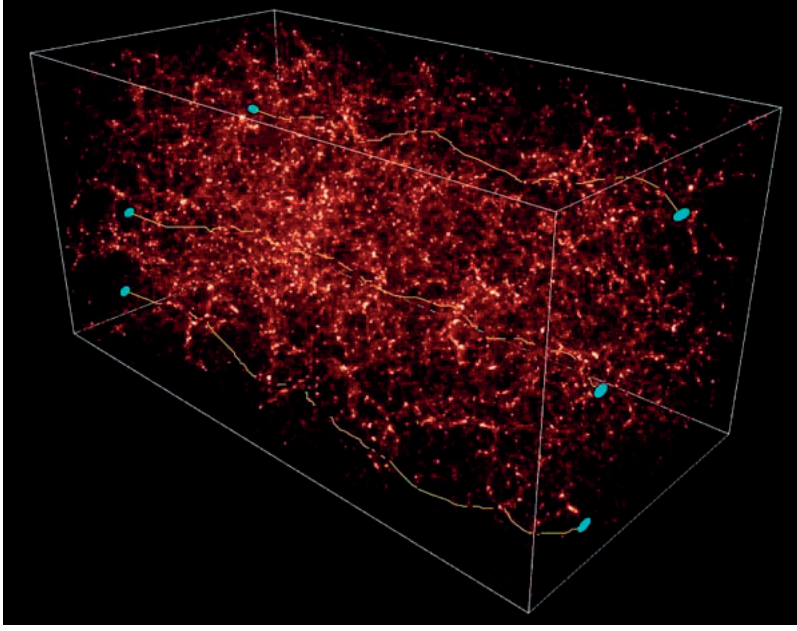


Figure 3.8: Simulation of the propagation of three light rays through the large-scale structures of the Universe. The rays are deflected and distorted in numerous ways and both the location and shape of the original light sources are altered as seen by an observer on Earth. Credit: S. Colombi (IAP), CFHT Team.

where k is the curvature parameter and χ is the comoving radial coordinate along the light ray defined by (2.7). All rays in the light bundle have a common intersection point which corresponds to the position of the observer at $\chi = 0$. The vector \mathbf{x} represents the comoving transverse separation vector between two neighboring light rays in the bundle and $\boldsymbol{\theta}$ is the angle between these rays as seen by the observer. In an homogeneous Universe, the right-hand side term in (3.44) would be zero. The non-zero term account for the perturbation effect of a weak comoving gravitational potential $|\Phi| \ll c^2$, where Φ is given by (2.65) and ∇_{\perp} denotes differentiation perpendicular to the path of the light ray. That extra term can be derived by applying the Fermat principle on the light rays (e.g., Blandford & Narayan 1986).

The solution can be found by the method of Green's function and reads

$$\mathbf{x}(\boldsymbol{\theta}, \chi) = S_k(\chi)\boldsymbol{\theta} - \frac{2}{c^2} \int_0^{\chi} S_k(\chi - \chi') \Delta \left[\nabla_{\perp} \Phi(\mathbf{x}(\boldsymbol{\theta}, \chi'), \chi') \right] d\chi' \quad (3.45)$$

where the radial coordinate $S_k(\chi)$ is defined by (2.7). By definition of the comoving angular diameter distance, the true position of a source at $\mathbf{x}(\boldsymbol{\theta}, \chi)$ is given by $\boldsymbol{\beta} = \mathbf{x}/S_k(\chi)$. The Jacobian matrix (3.14) becomes in this particular case

$$\mathcal{A}_{ij}(\boldsymbol{\theta}, \chi) = \frac{\partial \boldsymbol{\beta}}{\partial \boldsymbol{\theta}} = \frac{1}{S_k(\chi)} \frac{\partial \mathbf{x}}{\partial \boldsymbol{\theta}} \quad (3.46)$$

or

$$\mathcal{A}_{ij}(\boldsymbol{\theta}, \chi) = \delta_{ij} - \frac{2}{c^2} \int_0^\chi \frac{S_k(\chi - \chi') S_k(\chi')}{S_k(\chi)} \Phi_{,ik}(\mathbf{x}(\boldsymbol{\theta}, \chi'), \chi') \mathcal{A}_{kj}(\boldsymbol{\theta}, \chi') d\chi' \quad (3.47)$$

This equation is exact in a Universe with a geometry described by a metric of the form (3.1). It is conventional to simplify this expression by only keeping first-order terms in Φ , that is, by replacing $\Phi_{,ik}(\mathbf{x}(\boldsymbol{\theta}, \chi'), \chi')$ by $\Phi_{,ik}(S_k(\chi')\boldsymbol{\theta}, \chi')$ in (3.47). This is equivalent to integrating over the potential Φ along the unperturbed light ray (e.g., Schneider et al. 1998; Hilbert et al. 2009). This approximation is the analog of the “Born approximation” used in scattering theory. Equation (3.47) then becomes

$$\mathcal{A}_{ij}(\boldsymbol{\theta}, \chi) = \delta_{ij} - \frac{2}{c^2} \int_0^\chi \frac{S_k(\chi - \chi') S_k(\chi')}{S_k(\chi)} \Phi_{,ik}(S_k(\chi')\boldsymbol{\theta}, \chi') d\chi' \quad (3.48)$$

Defining the deflection potential $\psi(\boldsymbol{\theta}, \chi)$ as

$$\psi(\boldsymbol{\theta}, \chi) = \frac{2}{c^2} \int_0^\chi \frac{S_k(\chi - \chi') S_k(\chi')}{S_k(\chi)} \Phi_{,ik}(S_k(\chi')\boldsymbol{\theta}, \chi') d\chi' \quad (3.49)$$

the transformation matrix \mathcal{A} can be expressed as $\mathcal{A} = \delta_{ij} - \psi_{,ij}$ which is just the equation (3.19) of ordinary lens theory.

3.3.2 Effective convergence

The analog of the deflection angle (3.10) is given by the difference between the unperturbed and perturbed separations, divided by the angular diameter distance, so that

$$\hat{\boldsymbol{\alpha}}(\boldsymbol{\theta}, \chi) = \frac{S_k(\chi)\boldsymbol{\theta} - \mathbf{x}(\boldsymbol{\theta}, \chi)}{S_k(\chi)} = \frac{2}{c^2} \int_0^\chi \frac{S_k(\chi - \chi') S_k(\chi')}{S_k(\chi)} \nabla_\perp \Phi_{,ik}(S_k(\chi')\boldsymbol{\theta}, \chi') d\chi' \quad (3.50)$$

Similarly to ordinary lensing, an “effective convergence” (which this time also depends on χ) can be defined by

$$2\kappa(\boldsymbol{\theta}, \chi) = \nabla_\theta \hat{\boldsymbol{\alpha}}(\boldsymbol{\theta}, \chi) = \nabla_\theta^2 \psi(\boldsymbol{\theta}, \chi) \quad (3.51)$$

and the shear by

$$\gamma = \psi_{1,1} - \psi_{2,2} - i\psi_{1,2} \quad (3.52)$$

The effective convergence (3.51) can be further expressed in terms of the density contrast (2.57). Using the three-dimensional Poisson equation in comoving coordinates (2.68), (3.51) becomes

$$\kappa(\boldsymbol{\theta}, \chi) = \frac{3H_0^2 \Omega_m}{2c^2} \int_0^\chi \frac{S_k(\chi - \chi') S_k(\chi')}{S_k(\chi)} \frac{\delta(S_k(\chi')\boldsymbol{\theta}, \chi')}{a(\chi')} d\chi' \quad (3.53)$$

This quantity is the effective convergence for a source at comoving coordinate χ , observed at position $\boldsymbol{\theta}$ and taking into account all the intervening matter integrated along the line of sight.

Cosmic shear studies require the observations of a large number of sources (e.g. galaxies) along the line of sight. It is therefore of interest to obtain the integrated effective convergence for a population of sources spread over a range of distances (or redshifts z). Assuming the distribution of distance is well described by a probability density function $p_\chi d\chi = p_z dz$, one defines the total convergence by integration the effective convergence of each source along the line of sight, weighted by $p_\chi d\chi$ up to a maximum distance χ_h such that $p(\chi_h) \rightarrow 0$ (akin to a horizon).

$$\kappa(\boldsymbol{\theta}) = \int_0^{\chi_h} p(\chi) \kappa(\boldsymbol{\theta}, \chi) d\chi = \frac{3H_0^2 \Omega_m}{2c^2} \int_0^{\chi_h} g(\chi) S_k(\chi) \frac{\delta(S_k(\chi)\boldsymbol{\theta}, \chi)}{a(\chi)} d\chi \quad (3.54)$$

where $g(\chi)$ is called the “lensing efficiency”, defined as

$$g(\chi) = \int_\chi^{\chi_h} p_\chi(\chi') \frac{S_k(\chi' - \chi)}{S_k(\chi')} d\chi' \quad (3.55)$$

The lensing efficiency $g(\chi)$ can be interpreted as D_{ds}/D_s , weighted over the source population for a lens at comoving distance χ .

3.3.3 Effective convergence power spectrum

As shown in Sect. 3.3.5 below, effective convergence statistics can be derived by computing second-order or higher-order statistics on the observed shear field. It is therefore of great interest to relate the two-dimensional effective convergence power spectrum P_k to the three-dimensional matter power spectrum P_δ (2.98). P_k is defined as

$$\langle \hat{k}(\mathbf{l}) \hat{k}^*(\mathbf{l}') \rangle = (2\pi)^2 \delta_D(\mathbf{l} - \mathbf{l}') P_k(\mathbf{l}) \quad (3.56)$$

where \mathbf{l} is a two-dimensional wave vector, δ_D is the two-dimensional Dirac delta function and $\hat{k}(\mathbf{l})$ is the Fourier transform of the convergence defined by

$$\hat{k}(\mathbf{l}) = \int k(\boldsymbol{\theta}) e^{i\mathbf{l}\cdot\boldsymbol{\theta}} d\boldsymbol{\theta} \quad (3.57)$$

The respective power spectra $P_k(\mathbf{l})$ and $P_\delta(\mathbf{k})$ can be related through the use of the Limber equation (Limber 1953). The corresponding expression (e.g., Kaiser 1992, 1998) is

$$P_k(\mathbf{l}) = \frac{9H_0^4 \Omega_m^2}{4c^4} \int_0^{\chi_h} \frac{g^2(\chi)}{a^2(\chi)} P_\delta\left(\frac{l}{S_k(\chi)}, \chi\right) d\chi \quad (3.58)$$

where the lensing efficiency $g(\chi)$ was defined by (3.55).

It follows from (3.51) and (3.52) that the Fourier transform of the convergence and shear are related by

$$\hat{\gamma}(\mathbf{l}) = \left(\frac{l_1^2 - l_2^2 + 2il_1 l_2}{|\mathbf{l}|^2} \right) \hat{k}(\mathbf{l}) = e^{2i\phi} \hat{k}(\mathbf{l}) \quad (3.59)$$

where ϕ is the polar angle of the wave vector \mathbf{l} . This has the useful consequence that the

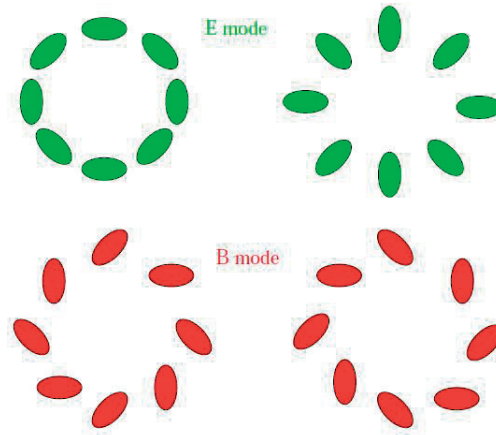


Figure 3.9: *Upper row:* a mass overdensity (left) or underdensity (right) generates curl-free patterns called E-modes where the shear is respectively tangentially aligned (left) or radially aligned (right); *Lower row:* divergence-free B-mode pattern, obtained from the E-mode pattern by rotating all shears by 45° . B-modes cannot be produced by gravitational lensing (Van Waerbeke & Mellier 2003).

two-point correlation functions (or power spectra) of convergence and shear are identical:

$$\langle \hat{\gamma}(\mathbf{l}) \hat{\gamma}^*(\mathbf{l}') \rangle = \langle \hat{\kappa}(\mathbf{l}) \hat{\kappa}^*(\mathbf{l}') \rangle \quad (3.60)$$

As shown later in Chapter 4, the shear power spectrum can be estimated from the observations of galaxy shapes. The equality relation (3.60) yields the corresponding effective convergence power spectrum which, in turn, can be used to constrain the matter power spectrum P_δ . This will be discussed in Sect. 3.4.

3.3.4 E-modes and B-modes

The shear field which can be described by a symmetric and traceless two-dimensional tensor field. Crittenden et al. (2002) have shown that such a field can be decomposed into a curl-free E-mode and a divergence-free B-mode component, in analogy with the decomposition of the electromagnetic field into a electric E-mode and a magnetic B-mode. The two-point statistics described in Sect. 3.3.5 can therefore also be expressed in terms of E-modes and B-modes.

In fact, it can be shown (Stebbins 1996; Kaiser 1992; Pen 2000) that gravitational lensing, deriving from a scalar potential, can only generate curl-free fields, i.e. pure E-modes. The B-mode components of the aforementioned two-point statistics must therefore vanish.

If non-zero B-modes are observed they can arise from essentially three kinds of sources: (1) systematic measurement errors such as inaccurate shear measurement or imperfect point spread function (PSF) correction; (2) errors related to lensing itself like source redshift clustering (Schneider et al. 2002b) and lens-lens coupling neglected when modeling the propagation of light (Schneider et al. 1998) (see Sect. 3.3.1); (3) the intrinsic correlation between galaxy orientations, also called “intrinsic alignments” (Crittenden et al. 2002).

3.3.5 Second-order measures of cosmic shear

The most commonly-used statistics are quadratic in the shear, that is, two-point statistics¹, namely:

- The shear correlation function
- The shear dispersion
- The aperture mass dispersion

All these statistics are linearly filtered versions of the effective convergence power spectrum P_k and constrain the matter power spectrum P_δ . We show in Sect. 3.4 how these second-order measures of the shear can be exploited to probe cosmology. For a review, see e.g. Schneider et al. (2002a, 2006).

Shear correlation function

One considers pairs of points (e.g. galaxy images) with separation θ and phase angle ϕ . The tangential and cross components of the shear, defined by (3.38) and (3.39), can be used to define the correlation functions for such pairs

$$\xi_{\pm}(\theta) = \langle \gamma_t \gamma_t \rangle(\theta) \pm \langle \gamma_{\times} \gamma_{\times} \rangle(\theta), \quad \xi_{\times}(\theta) = \langle \gamma_t \gamma_{\times} \rangle(\theta) \quad (3.61)$$

The cross-component γ_{\times} changes sign under parity transformations ($\gamma_t \rightarrow \gamma_t$, but $\gamma_{\times} \rightarrow -\gamma_{\times}$) and is expected to vanish for a sufficiently-large number of pairs.

It can be shown (e.g., Blandford et al. 1991; Miralda-Escude 1991b; Kaiser 1992), that the shear correlation functions are related to the effective convergence power spectrum P_k through

$$\xi_{+}(\theta) = \frac{1}{2\pi} \int_0^{\infty} l J_0(l\theta) P_k(l) dl, \quad \xi_{-}(\theta) = \frac{1}{2\pi} \int_0^{\infty} l J_4(l\theta) P_k(l) dl \quad (3.62)$$

where $J_n(x)$ is the n th order Bessel function of the first kind. These two-point correlation functions have, for instance, been used in recent weak lensing analyses, such as Hoekstra et al. (2006); Benjamin et al. (2007); Fu et al. (2008).

Shear dispersion

The shear dispersion² $\langle |\tilde{\gamma}|^2 \rangle(\theta)$ is a real-space two-point statistic, evaluated over a sufficiently large number of circular apertures or varying radii θ in order to reduce cosmic variance. Denoting the mean shear in an aperture as $\tilde{\gamma}$, it can be shown (e.g., Blandford et al. 1991; Miralda-Escude 1991b; Kaiser 1992) that the shear dispersion is related to the effective convergence power spectrum P_k through

$$\langle |\tilde{\gamma}|^2 \rangle(\theta) = \frac{1}{2\pi} \int l P_k(l) W_{TH}(l\theta) dl \quad (3.63)$$

where W_{TH} is the top-hat filter function defined by

$$W_{TH}(\eta) = \frac{4J_1^2}{\eta^2} \quad (3.64)$$

¹Also called “second-order” statistics

²Also called “shear top-hat variance”

3.3. The “cosmic shear”, weak lensing by large-scale structures

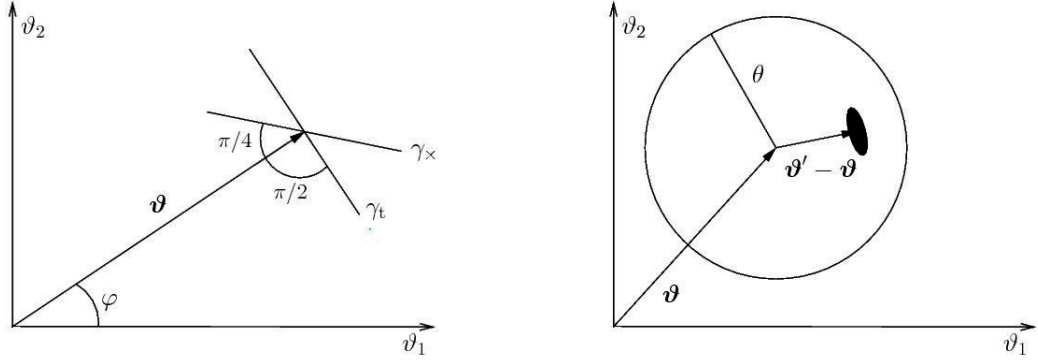


Figure 3.10: *Left*: the tangential and cross components of the shear as defined in (3.38) and (3.39); *Right*: illustration of the aperture mass statistics.

For examples of use in weak lensing surveys, see e.g. Maoli et al. (2001); Hoekstra et al. (2006); Fu et al. (2008).

Aperture mass dispersion

A two-point statistics similar to the shear dispersion (3.63) is the aperture mass in a circular aperture with radius θ centered at ϑ (Kaiser 1994; Schneider 1996; Schneider et al. 1998; Bartelmann & Schneider 1999), defined by

$$M_{ap}(\theta) = \int Q_{\theta}(\|\vartheta - \vartheta'\|) \gamma_t(\vartheta') d^2 \vartheta' \quad (3.65)$$

where Q_{θ} is the weight function in θ introduced by Schneider et al. (1998) of the form

$$Q_{\theta} = \frac{6}{\pi\theta^2} \left(\frac{\theta}{\vartheta}\right)^2 \left[1 - \left(\frac{\theta}{\vartheta}\right)^2\right] H(\vartheta - \theta) \quad (3.66)$$

where H is the Heaviside step function. The Aperture mass dispersion can be expressed in terms of the effective convergence power spectrum P_k as

$$\langle M_{ap}^2 \rangle = \frac{1}{2\pi} \int l P_k(l) W_{ap}(\theta l), \quad W_{ap} = \frac{576}{\eta^4} J_4^2(\eta) \quad (3.67)$$

The aperture mass statistic along with the tangential and cross components of the shear are illustrated in Fig. 3.10.

This statistic was used in e.g. Van Waerbeke et al. (2002a); Hoekstra et al. (2006); Semboloni et al. (2006); Fu et al. (2008).

Cosmic shear statistics compared

The shear correlation function has a number of advantages over shear dispersion and aperture mass dispersion:

- The shear correlation function ξ_{\pm} , as shown by (3.61) contains all second-order statistical information present the effective convergence power spectrum. Moreover, the other

two-point statistics can be derived from ξ_{\pm} .

- It is not always possible to use circular apertures on real data, for instance in the presence of CCD defects, fringes or bright stars. In contrast, it is always possible to find usable pairs of galaxies to calculate the correlation function.
- Calculating the correlation function is usually computationally faster.

On the negative side, the correlation functions do not yield an accurate separation between E-modes and B-modes. In contrast, this is easily achievable with the aperture mass M_{ap} (e.g., Crittenden et al. 2002; Schneider et al. 2002b).

All statistics are complementary in the sense that the filter functions they use probe different scales of the convergence power spectrum. The Bessel functions J_0 and J_4 in (3.62) and the W_{TH} used in (3.63) are quite broad filters, implying that these statistics depend on the power spectrum over a wide range of scales. Contrary to the correlation functions and shear dispersion, the aperture mass (W_{ap} filter) is more localized and more sensitive to the shape of the power spectrum. This makes M_{ap} a more suitable probe of cosmological parameters (e.g., Bartelmann & Schneider 1999).

3.4 Constraining cosmology with cosmic shear

3.4.1 Cosmic shear and cosmology

We saw in Sect. 2.3.10 how the evolution and properties of the three-dimensional matter power spectrum P_{δ} trace the evolution of the composition of the Universe and the growth rate of perturbations. Cosmology influences P_{δ} in many ways: it changes the observed shape of the power spectrum at $z = 0$ and its amplitude at any redshift z through the growth factor. It also affects the separation between galaxies, which is reflected by the wave number k . Finally, it determines the volume in which the matter power spectrum is calculated. Two properties in particular characterize the matter the power spectrum and are potential cosmological probes: Γ , the shape of the power spectrum and σ_8 , the normalization of its amplitude.

We also described in Sect. 3.3 how the two-dimensional effective convergence κ obtained from cosmic shear analysis can be related to the matter power spectrum through equation (3.58). The cosmic shear signal, in the form of the effective convergence κ , thus provides a way to directly probe the matter power spectrum P_{δ} and through it, the past expansion history of the Universe and the growth of cosmic structures. Fig. 3.13 shows how κ depends on cosmological parameters and the growth rate of perturbations through equation (3.53). Cosmic shear can therefore specifically constrain the density parameters Ω_m and Ω_{Λ} , the power spectrum normalization σ_8 , the shape of the power spectrum Γ and the characteristic redshift of the sources z_s .

The measurement of the matter power spectrum has been the primary target of several observational surveys, such as the 2dF Galaxy Redshift Survey (2dGRS) (Peacock et al. 2001; Efsthathiou et al. 2002) and Sloan Digital Sky Survey (SDSS) (Tegmark et al. 2004b,a). The corresponding data have been studied using various cosmological probes such as cluster abundance (e.g., Rozo et al. 2010), Lyman- α forest (e.g., Viel et al. 2010) and galaxy redshift distribution. Constraints have also been obtained from the WMAP and Planck measurements of the cosmic background radiations (CMB) (Bennett et al. 2012; Hinshaw et al. 2012; Ade et al. 2013a).

3.4. Constraining cosmology with cosmic shear

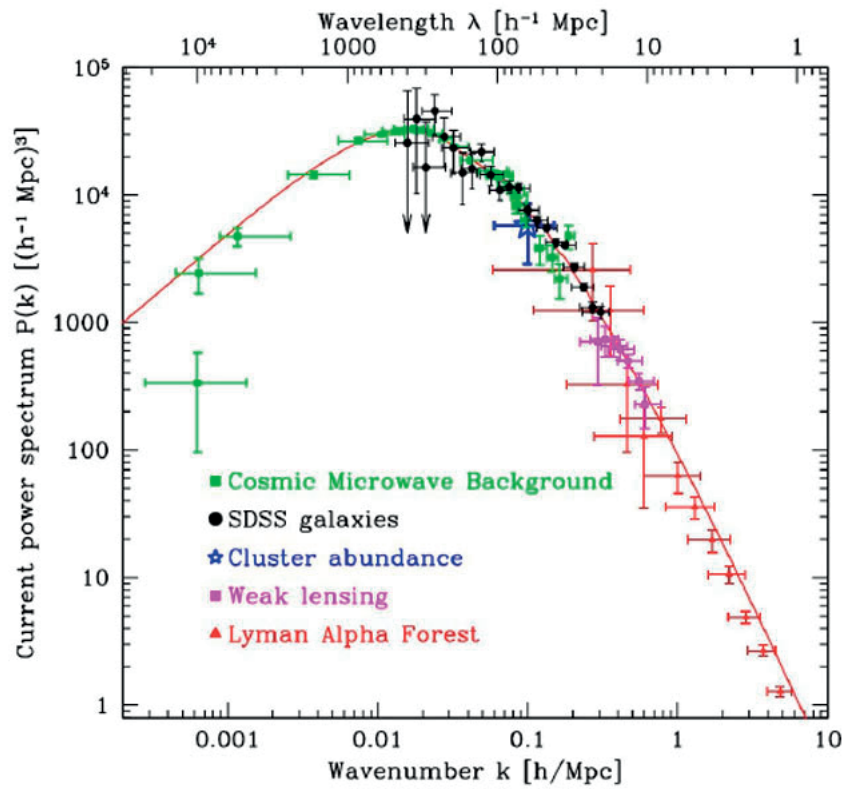


Figure 3.11: Constraints on the matter power spectrum obtained from the Sloan Digital Sky Survey (SDSS) by various probes, including cosmic shear. A Λ CDM cosmological model with $\Omega_m = 0.28$, $h = 0.72$, $\Omega_b/\Omega_m = 0.16$ was used. Picture from Tegmark et al. (2004a).

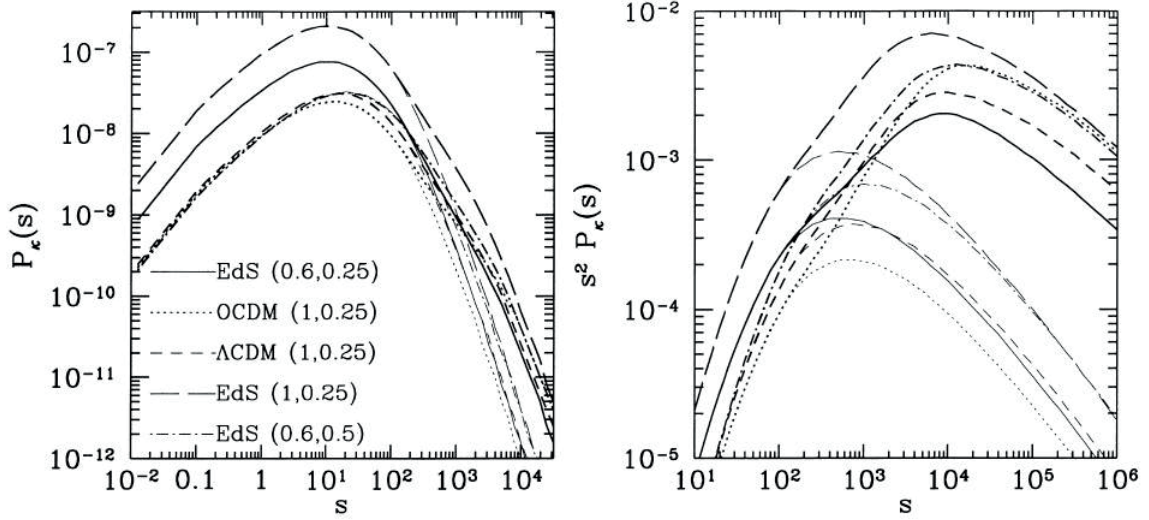


Figure 3.12: The effective convergence power spectrum P_k (left) and its dimensionless form (right) plotted for different cosmological models. The figure illustrates the sensitivity of P_k on cosmology. A mean source distribution $z_s = 1.5$ was assumed. The thin curves were calculated taking into account linear evolution only whereas the thick curves were derived using the full, non-linear evolution according to (Peacock & Dodds 1996). Plots from (Schneider et al. 1998).

Fig. 3.11, from Tegmark et al. (2004a), illustrates which region of the P_δ power spectrum these different methods were able to probe based on the SDSS data. This figure also shows that cosmic shear surveys can complement these surveys in very useful ways:

- Cosmic shear is the only method that can map out the dark matter distribution directly without any assumptions about the relation between dark and baryonic matter.
- Cosmic shear measures the mass distribution at redshifts $z \lesssim 2$ and therefore probes the non-linear portion of the matter power spectrum. This characteristic makes it a very promising tracer of dark energy. In contrast, the CMB measurements are relatively insensitive to the properties of the dark energy, as the latter was subdominant at the epoch of recombination. Cosmic shear measurement can also be confronted with those from type Ia supernovae (SNe Ia) which also probe the recent history of the Universe.
- The strongest constraints on cosmological parameters are obtained by combining measurements on large scales (e.g. from the CMB) and smaller scales (e.g. cosmic shear). It also permits to break degeneracies between parameters as shown by (e.g., Hu & Tegmark 1999; Spergel et al. 2003) and also illustrated in Fig. 3.15 in the case of the degeneracy between Ω_m and σ_8 .

3.4.2 Determination of cosmological parameters from cosmic shear data

We have described in 3.3.5 several two-point statistics that can be computed from the cosmic shear data. The correlation functions, shear dispersion and aperture mass, once measured, directly constrain the effective convergence power spectrum P_k and through it, the matter power spectrum P_δ . Moreover, the E-mode–B-mode decomposition scheme is a powerful test of the corruption of the signal by systematic errors and other spurious effects, given that

$$\kappa(\boldsymbol{\theta}, \chi) = \frac{3H_0^2\Omega_m}{2c^2} \int_0^\chi \frac{S_k(\chi - \chi')S_k(\chi')}{S_k(\chi)} \frac{\delta(S_k(\chi')\boldsymbol{\theta}, \chi')}{a(\chi')} d\chi'$$

Figure 3.13: Illustration of the dependence of the effective convergence on cosmology. The terms in green color fixes H_0 and Ω_m . The terms highlighted in red and blue depend on cosmological distances and yield constraints on cosmological parameters. The term in blue is determined by the amplitude and shape of the matter power spectrum and can be used to probe the growth function (see Sect. 3.4.4).

lensing can only generate a pure E-mode signal. The theoretical and derived power spectra can then be compared and exploited to extract cosmological information. These statistics are self-sufficient but it is often worth combining them, as explained in Sect. 3.3.5.

The next step is then to derive estimates and error bars on cosmological parameters. The conventional method for doing so is to calculate the Gaussian log-likelihood

$$\chi^2 = -\ln \mathcal{L}(\boldsymbol{p}) = \frac{1}{2} \sum_{ij} (d_i - m_i)(C^{-1})_{ij}(d_j - m_j) \quad (3.68)$$

on a grid of n -dimensional space, where n is the number of parameters, including e.g. $\{\sigma_8, \Omega_m, h, z_s\}$. An element d_i in (3.68) is one of the measured two-point statistics $\xi_{\pm}(\theta_i)$, $\langle |\bar{\gamma}|^2 \rangle(\theta_i)$ or $M_{ap}(\theta_i)$. The quantity m_i denotes the theoretical prediction of the shear statistics for the same angular separation θ_i and is a function of the cosmological parameters $\boldsymbol{p} = (p_1 \cdots p_n)$. C represents the covariance matrix of each of the estimators d_i (see e.g. Schneider et al. 2002a). The confidence contours are then calculated from the χ^2 values for each parameter.

The estimates obtained from the log-likelihood can be confronted to the best statistical errors achievable given by the Fisher matrix (Fisher 1935; Tegmark et al. 1997; Stuart et al. 2009)

$$\mathcal{F}_{ij} = \left\langle \frac{\partial^2 [-\ln \mathcal{L}(\boldsymbol{p})]}{\partial p_i \partial p_j} \right\rangle = \left(\frac{\partial^2 [-\ln \mathcal{L}(\boldsymbol{p})]}{\partial p_i \partial p_j} \right)_{\boldsymbol{p}=\boldsymbol{p}_0} \quad (3.69)$$

where \boldsymbol{p}_0 denotes the true parameters.

3.4.3 Cosmological constraints from cosmic shear observations

Instrumental developments (e.g. wide-field CCD cameras) and the availability of new image processing software in the 1990s greatly contributed to the first detections of cosmic shear at the turn of the millennium (Bacon et al. 2000; Kaiser et al. 2000; Van Waerbeke et al. 2000; Wittman et al. 2000). A first generation of cosmic shear surveys soon followed, initially covering small sky areas but rapidly increasing up to several tens of square degrees. A detailed description of these early surveys and the corresponding results can be found in e.g. Refregier (2003b); Schneider et al. (2006) and the shear dispersion of several of them are plotted in Fig. 3.14. Despite having used different instruments and image analysis software, all results are broadly consistent with each other and favor a Λ CDM with $\sigma_8 \approx 1$.

More recent “second generation” surveys include VIRMOS-Descart (Van Waerbeke et al. 2002a,

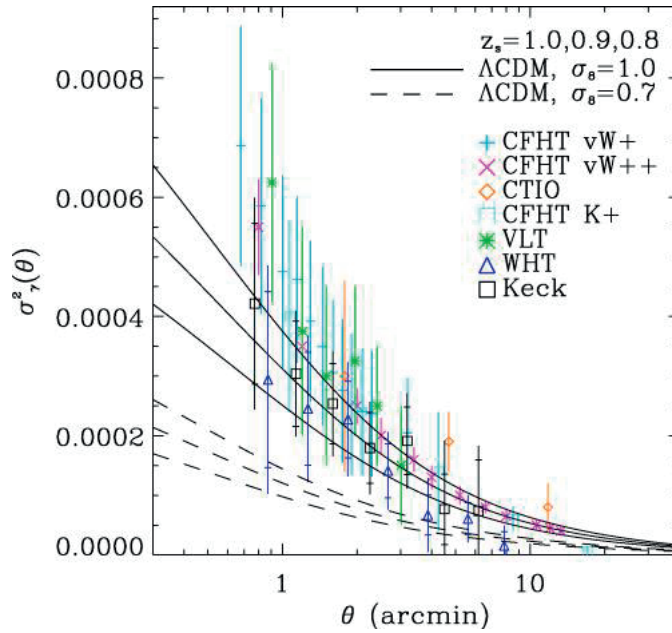


Figure 3.14: Shear dispersion of several early cosmic shear surveys (CFHT vW+: Van Waerbeke et al. (2000); CFHT K+: Kaiser et al. (2000); CTIO: Wittman et al. (2000); VLT: Maoli et al. (2001); CFHT vW++ Van Waerbeke et al. (2001)). The inner and outer error bars respectively correspond to statistical and total uncertainties. The expected shear dispersion for a Λ CDM cosmological model with $\Omega_m = 0.3$ and $\Gamma = 0.21$ are also shown for a range of values for the median source redshift z_s , corresponding approximately to the uncertainty in this parameter. The models are shown both for $\sigma_8 = 1$ (solid lines) and $\sigma_8 = 0.7$ (dashed) cluster normalization. All results are broadly consistent with each other as well as with Λ CDM with $\sigma_8 = 1$. Source Bacon et al. (2003).

3.4. Constraining cosmology with cosmic shear

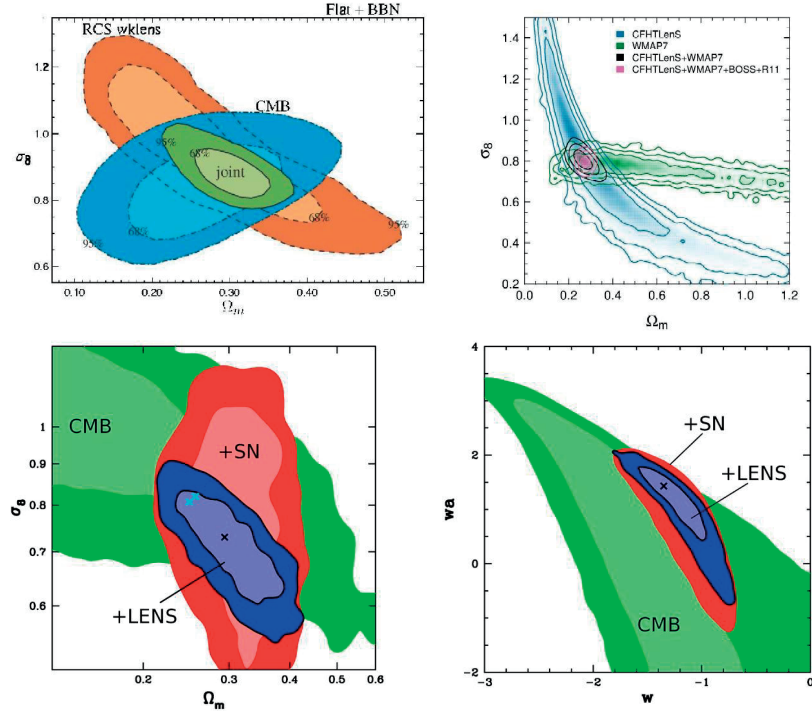


Figure 3.15: *Top left:* Joint (Ω_m, σ_8) constraints obtained by Contaldi et al. (2003) from the combination of the red-sequence cluster weak lensing survey (RCS) (Hoekstra et al. 2004) and the WMAP 1st year CMB data (Bennett et al. 2003b). *Top right:* Joint (Ω_m, σ_8) constraints (68.3, 95.5, and 99.7 %) found by Benjamin et al. (2012) from the CFHTLenS survey (5 years of CFHTLS data) (blue), combined with the WMAP 7th year CMB results (black), SDSS-III Baryon Oscillation Spectroscopic Survey (BOSS) (Anderson et al. 2012) and the R11 HST constrains on H_0 (Riess et al. 2011) (pink). A flat Λ CDM cosmological model is assumed. *Bottom left:* Contour plots computed by Jarvis et al. (2006), showing the combined (Ω_m, σ_8) constraints between the weak lensing CTIO survey (Jarvis et al. 2003), WMAP 1st year (Bennett et al. 2003b) and Type Ia supernovae, assuming a variable dark energy equation of state. *Bottom right:* Constraints obtained by Jarvis et al. (2006), on the dark energy equation of state (w_0, w_a) in the parametrization (3.71).

2005), CFHTLS (Hoekstra et al. 2006; Fu et al. 2008; Erben et al. 2012; Heymans et al. 2012), CTIO (Jarvis et al. 2006), GaBoDS (Hettterscheidt et al. 2007) and COSMOS (Massey et al. 2007b). A summary of the corresponding results can be found in Hoekstra & Jain (e.g., 2008); Munshi et al. (e.g., 2008). The main lessons as far as cosmology is concerned are summarized below.

- The recent weak lensing studies favor a value of $\sigma_8 \approx 0.8$ ($\Omega_m = 0.3$), which is competitive and in good agreement with the latest estimates from the Planck CMB probe $\sigma_8 = 0.828 \pm 0.012$ (Ade et al. 2013b) and the results from cluster abundance.
- Since the completion of early surveys, constraints on cosmological parameters have not greatly improved and the dispersion between σ_8 or Ω_m estimates is still relatively large, in the range $[0.7 - 0.9]$. One reason lies in lack of source redshift information. Another is the still high level of systematic errors due in particular to still imperfect PSF correction and shear measurement schemes, a topic we will cover in Chapter 4.
- The limited knowledge of the source redshifts also limits the accuracy with which one can measure the growth of structures, key to probing dark energy (e.g., Linder & Jenkins 2003; Hu & Jain 2004) (see also Sect. 3.4.4 below). The first attempt to probe dark energy with cosmic shear was made by Jarvis et al. (2006) (see Fig. 3.15, bottom), but with limited source redshift data. The most recent surveys (GaBoDS, COSMOS) have, however, started making use of photometric redshifts. The COSMOS survey (Massey et al. 2007b) in particular, was for the first time able to make a 3D cosmic shear analysis via redshift tomography. We outline some of the latest developments in this area in Sect. 3.4.5.
- Another issue is the degeneracy between σ_8 and Ω_m (e.g., Eke et al. 1996; Wang & Steinhardt 1998; Henry et al. 2009; Rozo et al. 2010). The obvious way to circumvent this problem is to combine the cosmic shear measurements with those from other complementary probes (e.g., CMB, SNe, BAO). In this regard, the combination of lensing and CMB studies is particularly powerful. Fig. 3.15 shows the joint Lensing – CMB constraints obtained by Contaldi et al. (2003) (RCS+WMAP), (Jarvis et al. 2003, 2006) (CTIO+WMAP+SNe) and Fu et al. (2008) (CFHTLS+WMAP). New promising lensing-specific techniques have also been recently developed, which we outline in Sect. 3.4.6.

3.4.4 Probing dark energy with cosmic shear

We saw in Sect. 3.4.1 how the last term under the integral sign of equation (3.53) relates the effective convergence κ and the growth of structures (see also Figs. 3.12, 3.13). That term depends on dark energy in two ways. Firstly, the radial comoving coordinate χ in (3.53) and given by (2.7) relates κ to the angular diameter distances D_s , D_d and D_{ds} (see Fig. 3.2). Secondly, the density contrast also depends on the amplitude of the power spectrum. Dark energy alters the expansion rate of the universe at redshifts $z \lesssim 2$, which in turns affects the growth of structures. Since the CMB fixes the amplitude of the power spectrum at $z \approx 1100$, the comparison with cosmic shear measurements of σ_8 place constraints on the growth function.

This topic has been explored in (e.g., Hu 1999, 2002a; Huterer 2002; Jain & Taylor 2003; Munshi & Wang 2003; Bernstein & Jain 2004; Hu & Jain 2004; Albrecht et al. 2006; Heavens et al. 2006; Jarvis et al. 2006; Huterer 2010).

Assuming a flat Universe, the dark energy modifies the expansion of the universe according to

the equation (e.g., Linder & Jenkins 2003; Hu & Jain 2004)

$$H^2(a) = H_0^2(a) \left[\Omega_m a^{-3} + \Omega_{DE} \exp \left(-3 \int_1^a \frac{da}{a} [1 + w(a)] \right) \right] \quad (3.70)$$

where the equation of state $w(a)$ is approximated by the parametrization (Linder 2003; Chevalier & Polarski 2001)

$$w(a) = w_0 + w_a [1 - a(z)] = w_0 + w_a [z/(1+z)], \quad w_0 = w(z=0) \quad (3.71)$$

and $\Omega_{DE} = 8\pi G \rho_{\Lambda} / [3H(t)^2]$ denotes the density parameter associated with dark energy (see Sects. 2.2.6 and 2.5.3).

The growth function G is related to the matter power spectrum through

$$P_{\delta}(k, z) = \left[\frac{1}{1+z} \frac{G(z)}{G_0} \right]^2 P_{\delta}(k, 0), \quad G_0 = G(z=0) \quad (3.72)$$

and $G(z)$ depends on dark energy through

$$\frac{d^2 G}{d \ln a^2} + \left[\frac{5}{2} - \frac{3}{2} w(a) \Omega_{DE}(a) \right] \frac{dG}{d \ln a} + \frac{3}{2} [1 - w(a)] \Omega_{DE}(a) G = 0 \quad (3.73)$$

The derivative of the growth function, the growth rate $f(z)$ can be simply related to the matter density as $f(z) = \Omega_m^{\gamma}$ and the growth index γ provides a way to discriminate between models of dark energy. In particular, the Λ CDM model is characterized by $\gamma \approx 0.55$ and any significant deviation from this value would favor a different model of dark energy.

3.4.5 Tomography and 3D lensing

The shear field depends on redshift and the imperfect knowledge of the source redshift distribution thus constitutes a significant source of uncertainty in cosmic shear surveys. As more accurate redshift data becomes available, it makes sense to exploit this information not only to improve the overall accuracy of a survey, but also, and most importantly, to tighten the constraints on dark energy, as outlined in Sect. 3.4.4. Indeed modern weak lensing surveys, such as GaBoDS (Hettterscheidt et al. 2007), COSMOS (Massey et al. 2007b), CFHTLenS (5 years of CFHTLS data) (Erben et al. 2012; Heymans et al. 2012) and the ongoing KIDS survey (de Jong et al. 2012), are designed to measure photometric redshifts (“photo- z ”) from multi-band photometry (e.g., Baum 1962; Puschell et al. 1982; Koo 1985, 1999; Benítez 2000; Ilbert et al. 2006; Hildebrandt et al. 2010; Bellagamba et al. 2012) at the same time as weak lensing data. In particular, next-generation surveys (see Sect. 3.4.7), which will probe large sky areas with a very low level of statistical errors, will require extremely accurate photo- z measurements to reduce systematic errors as much as possible. Other sources of systematics will be discussed in Chapter 4. We summarize below two technical approaches that have been discussed in the literature: “redshift tomography” and “3D lensing”.

Redshift tomography consists in dividing a survey into slices (bins) at different distances, study the shear field on each slice and integrate over all slices to obtain a three-dimensional view of that shear field. Cosmological information is extracted by computing cross- and

auto-correlation power spectra between slices and within each slice. The techniques behind tomography have been initially developed by Hu (1999, 2002b,a), while e.g. Taylor (2001); Huterer (2002); Heavens (2003) have estimated the accuracy with which cosmological parameters and the dark energy properties can be determined. The gains in accuracy are significant for a small number of bins but decrease rapidly with the number of slices. However, much tighter constraints are obtained on the equation of state of dark energy than with 2D lensing. Tomography has been applied to the COSMOS (Massey et al. 2007b; Schrabback et al. 2010) and the CFHTLenS survey data (Benjamin et al. 2012; Erben et al. 2012; Heymans et al. 2012).

Several authors (Heavens 2003; Heavens et al. 2006; Kitching et al. 2007, 2011) have considered using accurate photo- z data to reconstruct the 3D shear field in its entirety and developed the required formalism. The three-dimensional shear power spectrum is reconstructed using spherical harmonics and the cosmological signal is extracted from the covariance of the coefficients. 3D lensing has some advantages over tomography. In particular, no binning is required, avoiding its consequent loss of information and every galaxy contributes directly and individually to the signal (e.g., Kitching et al. 2011). Bacon et al. (2005); Kitching et al. (2007) applied 3D lensing to the COMBO17 survey data and found improvements in the determination of σ_8 compared to the 2D cosmic shear analysis of the same data (Brown et al. 2003).

3.4.6 Breaking the (Ω_m, σ_8) degeneracy

As highlighted in Sect. 3.4.3, the degenerate relation between Ω_m and σ_8 (e.g., Eke et al. 1996; Wang & Steinhardt 1998; Henry et al. 2009; Rozo et al. 2010) currently forces weak lensing to rely on other probes for breaking that degeneracy. Two alternatives have been suggested in the literature: the first is to reconstruct and exploit 3D shear information as outlined in Sect. 3.4.5. We focus here on the second alternatives, which relies on the use of higher-order statistics to extract the cosmological information associated with the non-linear region of the matter power spectrum (see Sect. 2.3.10 and Fig. 2.6). Significant non-Gaussian signatures were detected for the first time by Bernardeau et al. (2002) in the VIRMOS-DESCART survey data and later confirmed by Pen et al. (2003). Two-point statistics, such as the shear power spectrum are not sensitive to the non-Gaussian cosmic shear signal and must be supplemented by a new set of statistical tools. Breaking the $(\Omega_m$ and $\sigma_8)$ degeneracy can then be achieved by either combining two- and three-point statistics or by only relying on pure higher-order indicators (e.g., Bernardeau et al. 1997; Jain & Seljak 1997; Pen et al. 2003; Takada & Jain 2003; Jarvis et al. 2004; Kilbinger & Schneider 2005). For recent reviews, see e.g., Munshi et al. (2008); Pires et al. (2010).

3.4.7 Future prospects

A number of new-generation surveys with sky coverage greater than 1000 degree² are either ongoing or planned in the medium or longer term (~ 2020) (Fig. 3.16). Table 3.1 summarizes the main characteristics of these studies.

- The Kilo-Degree Survey (KIDS) (de Jong et al. 2012), complemented in the near-infrared with data from the VIKING survey, is studying a 1500 deg² area with weak lensing, as part of its dark energy science goal. It makes use of the 2.6m VLT Survey Telescope (VST) and the 4.1m VISTA (Visible and Infrared Survey Telescope for Astronomy) in ESO's

3.4. Constraining cosmology with cosmic shear



Figure 3.16: Planned survey with a weak lensing component.

Table 3.1: Ongoing and planned surveys.

Survey	Start	Telescope	Area (deg ²)	Space/Ground
KIDS	2011	VST & VISTA 2.6m, 4.1m	1500	Ground
HSC	~ 2012	Subaru 8.2m	~ 2000	Ground
DES	~ 2013	CTIO 4m	5000	Ground
PAN STARRS	> 2012	PS4 4x2m	30000	Ground
LSST	~ 2022	LSST 8.2m	20000	Ground
Euclid	~ 2019	1.2m	15000	Space
WFIRST	~ 2020	1.3m	2700/yr	Space

Chapter 3. Constraining cosmology with weak gravitational lensing

Paranal Observatory, Chile.

- The Hyper Suprime-Cam (HSC) camera achieved first light in 2012 on the 8.2m Subaru telescope, Hawaii, and will survey over 1500 deg² until around 2018 with weak lensing.
- The Dark Energy Survey (DES) (Frieman & Dark Energy Survey Collaboration 2013) is expected to start in 2013 and will perform a 5-year cosmic shear survey of a 5000 deg² area with the Cerro Tololo Inter-American Observatory (CTIO) 4m telescope in La Serena, Chile.
- The Panoramic Survey Telescope and Rapid Response System (Pan-STARRS) is a new four-mirror telescope, one of which is already operational in Hawaii. It will survey 30000 deg² with weak lensing (Heavens 2011).
- The Large Synoptic Survey Telescope (LSST) (e.g., LSST Science Collaboration et al. 2009; Chang et al. 2013) is a 8.4m telescope that will start observing 20000 deg² for weak lensing around 2022 from Cerro Pachon in Chile (Abell et al. 2009).
- Euclid (e.g., Laureijs et al. 2011) is a space mission from the European Space Agency (ESA) that will survey 15000 deg² from space with its weak lensing instruments once launched around 2019.
- The Wide-Field Infrared Survey Telescope (WFIRST) mission from NASA (e.g., Goullioud et al. 2012) aims to survey 2700 deg² per year from space with its weak lensing probe around 2020.

In order to achieve their science goals, these next-generation survey will have to probe cosmic shear field to sub-percent accuracy. For this purpose they will use state of the art imaging equipment and will target large sky areas to reduce statistical errors to a minimum. They will also collect themselves photometric redshift data and probe both second- and higher-order statistics to improve accuracy, break the (Ω_m, σ_8) degeneracy and tighten constraints on dark energy, as explained in Sect. 3.4.5.

The main challenge of these surveys will be to maintain the level of systematic errors to that of statistical errors. In fact, the main sources of systematic uncertainty will likely not reside in the determination of accurate redshifts or theoretical approximations, but rather in the insufficient accuracy of the existing galaxy shape measurement algorithms and the convolution of the original image by the point spread function due to the optics and atmosphere. Whether this challenge will be met within the time frame of the surveys or not is still uncertain. We will cover these two aspects in the next chapter.

4 Cosmic shear measurement

We showed in the last chapter that the cosmic shear contains a wealth of cosmological information whose statistical analysis can produce tight constraints on cosmological parameters, the growth of structures and the properties of dark energy. We also noted that the science goals of next-generation cosmic shear surveys will only be achieved provided the level of systematic uncertainties is kept below that of statistical ones.

Throughout Chapter 3, it was assumed the cosmic shear data were fully available and known to arbitrary accuracy, which in practice is obviously not the case. In this chapter, we investigate the practical aspects of cosmic shear measurement and in particular:

- How to observationally detect the cosmic shear and how to measure the cosmic shear field.
- What are the most challenging tasks and the main sources of uncertainty to tackle during the shear measurement process.
- What are the different approaches explored in the literature to address those issues and what are the prospect of success.

In the process, we also present the main research performed during this thesis:

- The development of a *gfit* shape measurement method (Gentile et al. 2012) and its experimentation in the GREAT08 (Bridle et al. 2009, 2010) and GREAT10 challenges (Kitching et al. 2010, 2012a).
- The application of novel spatial PSF interpolation techniques (Gentile et al. 2013) and their successful use in the GREAT10 Star challenge (Kitching et al. 2012c).
- The contribution to the development of *DWT-Wiener* an innovative, wavelet-based and shape-preserving denoising method (Nurbaeva et al. 2011).

Lastly, we have included in Appendix the derivations of results frequently quoted in the lensing literature without explicit proofs.

4.1 Principles and challenges

4.1.1 Cosmic shear from galaxy shapes

In order to apply the formalism described in chapter 3, a lensing survey will require measurements of the shear field γ over many areas in the sky. Second or higher-order statistics can then be computed which ultimately yield constraints on cosmology. And obviously, the

final error bars on cosmological parameters will largely depend on the accuracy of the shear measurement process.

The shear transformation slightly alters the apparent shape of galaxies and this effect is in principle measurable by observing a sufficiently large number of galaxies with the adequate technology. The weak lensing community has therefore concentrated its efforts toward developing the required shear measurement methods and image processing tools to extract the shear signal from the analysis of many galaxy shapes.

An accurate shear measurement process is however proving very challenging to implement:

1. The first challenge is observational. The shear effect is very subtle and requires the statistical analysis of millions of faint and noisy galaxy images in the near infrared. Moreover, several additional effects, unrelated to lensing, come into play to modify and degrade the original shear signal. The most critical of these effects are the convolution of the sheared source galaxy image by the instrumental and/or atmospheric point spread function (PSF), the degradation due to various sources of noise and the pixelation effect caused by the integration of light falling on the detector pixels. In other words, the challenge here is to deal with loss of information.
2. The next challenge relates to extraction of information. This entails developing a shear measurement method that can first, infer the shape a galaxy had just *after* being sheared but *before* being altered by the PSF and other effects and second, measure the amount of shear. This involves in particular, the definition of a practical “shear estimator” that can provide an estimate of the shear based on the photometric data of a galaxy.
3. Computation of information: lastly, having to measure large numbers of galaxies also implies very large amounts of data to process. The third challenge is thus computational because the shear measurement software must be capable of processing huge quantities of galaxy images (terabytes and even more) within a reasonable amount of time.

In the next sections, we describe these difficulties in more detail and outline the main approaches followed to address them.

4.1.2 Observational challenges

Weak lensing cosmological surveys rely on the shape measurement of galaxy images. A number of practical difficulties complicate the measurement process, which we review in this section.

Distortions by large scale structures are tiny

The change in ellipticity due to the shear is about 10 times smaller than the typical ellipticity of a galaxy. It is therefore hopeless to attempt measuring the shear effect from the observation of individual galaxies, which makes the analysis of sufficiently-large numbers of galaxies mandatory. Thus:

- One should first consider as many objects as possible, by observing a large number density of galaxy sources, or by considering a large solid angle on the sky (a few arcmin² or more), or both. This entails making use of large wide-field detectors at the best observing locations. Only the optical sky has a dense enough population of sources and weak lensing are therefore performed with optical or near-infrared (NIR) digital CCD cameras. Such device are able to capture large sky areas in reasonable amounts of

observation time and their numerical output is directly exploitable by computers. The advent of such wide-field cameras was decisive in making possible the first detection of cosmic shear in year 2000 by several groups (Bacon et al. 2000; Kaiser et al. 2000; Van Waerbeke et al. 2000; Wittman et al. 2000). In fact, the formalism for extracting cosmological information from the shear was ready several years before.

- Then employ statistical techniques to estimate the shear. The greater the number of sources subject to weak lensing analysis, the better the accuracy of the shear measurement will potentially be.

The study of faint, distant galaxies is required

- The study of faint, distant galaxies is required because the densest and more numerous populations available for weak lensing study are remote galaxies lying in the optical or NIR range, and also because the more distant the observed sources, the greater the shear signal contained in their image. In fact, when averaging over \mathcal{N} galaxies, the lensing signal to noise ratio $S/N \propto \sqrt{\mathcal{N}}/\sigma_\epsilon$, where σ_ϵ is the dispersion of intrinsic (i.e. unsheared) galaxy ellipticity. This is another justification for covering large sky areas.
- This also means that these galaxies are small and that they are likely to be strongly affected by sources of noise and spurious distortions (see remaining sections and Sect. 4.1.3).

The Intrinsic shape or orientation of source galaxies is poorly known

- Galaxies greatly vary in size, orientations and morphology but only their projected shapes are accessible.
- Moreover, individual projected shapes are not circular but elliptical, so one cannot just measure the shear as a mere deviation of circularity.
- The observed image of an individual galaxy does not give any information about the intrinsic shape or exact intrinsic orientation it had before being sheared. If it was the case then one would be able to directly use transformation (3.40) and related equations to estimate the shear (assuming being able to accurately quantify shapes through observation).
- It is not possible to tell from the observed shapes of two individual galaxies which one has been affected by the shear and which one has not.

The PSF distortion is comparable or larger than the shear signal one intend to measure

One can only observe astronomical objects through dedicated instruments, which introduce various types of distortion to the original image.

Light beams from an observed point source are not focused perfectly on a detector. Images observed from a telescope in space are dominated by diffraction and aberration phenomena originating from the optical system (system pupils, mirror struts and other incident light perturbation structures) and possibly pointing errors and other thermal or mechanical effects. For ground-based observations, turbulence, refraction and convection phenomena in the atmosphere (the “seeing”) constitute additional source of distortion. The Point Spread Function (PSF) describes how the image of a point source is modified by all these phenomena.

Chapter 4. Cosmic shear measurement

The surface brightness distribution $I(\boldsymbol{\theta})$ of an observed image resulting from the combination of a source image and a PSF kernel can be mathematically described by a convolution operation

$$I(\boldsymbol{\theta}) = O(\mathbf{v}) \star P(\boldsymbol{\theta}) = \int P(\boldsymbol{\theta} - \mathbf{v}) O(\mathbf{v}) d^2v \quad (4.1)$$

assuming the distortion process can be considered linear and shift-invariant. The quantities $O(\mathbf{v})$ and $P(\boldsymbol{\theta} - \mathbf{v})$ respectively represent the surface brightness of the source image and PSF kernel.

The PSF is one of the largest contributors of systematic errors in cosmic shear observations for the following reasons:

- The PSF kernel P is generally not circularly symmetric and is made of an isotropic and an anisotropic component. The effect of the isotropic part of the PSF kernel is to dilute the cosmic shear signal and to make the source image appear rounder, while the anisotropic part introduces an artificial shear effect which may be confused with the genuine shear lensing signal. That anisotropy is in fact comparable or larger than the shear signal one intend to measure. Moreover, in real ground-based data the size of the PSF is roughly comparable to the size of the observed galaxies. Clearly, both dilution and anisotropy phenomena, if left uncorrected, will ruin all attempts to determine the tiny change in galaxy shape due to lensing.
- Another difficulty arises because the PSF often varies in space and over time. The PSF-convolved shape of a galaxy at the given location will depend on the PSF kernel at the very same position. But the PSF is not known at galaxy positions because it can only be tracked at the positions of stars, assumed to be point sources. With a varying PSF, one can no longer assume the PSF kernel at the position of the galaxy is the same as that observed at the star position. The PSF kernel determined from the star must then be interpolated and reconstructed at the position of the target galaxy. The lack of stability of the PSF in time further complicates the process. Additional issues may also complicate the interpolation process. For instance, the PSF, instead of varying smoothly throughout the image, may experience more rapid variations near the corners or between chip boundaries in multi-chip cameras.

The above considerations imply accurate cosmic shear observations requires the best possible seeing:

- A PSF in good and stable atmospheric conditions from the best astronomical sites is of the order of 1 arcsec or less. This is a maximum for ground-based cosmic shear observations which ideally require $\lesssim 0.8''$. Exceptionally, images with $\sim 0.5''$ can be obtained.
- Observations from space can benefit from a much better seeing. A probe such as Euclid from ESA (see Sect. 3.4.7) will have a PSF resolution better than $0.2''$, with $0.1''$ pixels in one wide visible band (R+I+Z). PSF measured from space are also likely to be more stable. On the other hand, diffraction-limited PSFs are more complex to model, which complicates the task of PSF correction and interpolation schemes. It is thus essential during the design of a space mission with a weak-lensing science goal, to ensure the PSF is as simple and predictable as possible.

Approaches for interpolating the PSF are presented in Sect. 4.5, where we present our research in this area.

Various sources of noise degrade the shear signal in galaxy images

Correcting astronomical images from the effect of noise has always been a challenging task. This is particularly true for galaxy images captured for weak lensing analysis because noise not only degrades the overall quality of these images but also alters the shapes of the galaxies. Unfortunately the images with the strongest shear signal are also the faintest and often the noisiest ones, which makes the issue of denoising a prominent one. It is especially difficult to solve because the noise correction scheme must preserve the shape of the galaxy.

The noise in astronomical images comes from various sources,

- Nearly constant noise introduced by the sky background and the detector. In the optical and near infrared wavebands (wavelength $\lambda \lesssim 2\mu m$) emission from the sky is the primary source of background radiation. The main emission sources come from the Zodiacal light (sunlight scattered by dust particles in the Solar System interplanetary medium) air glow (photochemical reactions in the Earth's upper atmosphere) and diffuse galactic light. The average sky surface brightness is about 23 B-mag arcsec⁻² (measured in the B wavelength band) and greater than all but the inner core of a typical galaxy. The detector itself can be another strong source of thermal radiation in wavebands $\lambda \gtrsim 2\mu m$, particularly at wavelength $\lambda \approx 10\mu m$ at which a Planck function at 300K has maximum intensity.
- Combination of Gaussian and Poisson noise added to the image. In an ideal world, every photon striking a detector pixel would be converted into exactly one electron. The number of electrons would then be precisely counted and converted to a number, telling how much light struck each pixel. Unfortunately, the process of converting light to pixel values in the detecting device is governed by some fundamental physical laws and other factors that generate various types of noise. Some of this noise is introduced during the image integration, like the photon noise (shot noise) or dark current, or during the process of reading out the pixels.

A denoising scheme that gives good results in weak lensing applications and to which I have contributed during this thesis is described in Sect. 4.6.

Pixelization effect introduced by the detector

Detectors used for weak lensing are typically made of multiple CCD chips whose surface is divided into individual elements (pixels). Photons striking individual pixels are converted to electrons (also called "photoelectrons") which are stored in each pixel well. The count of electrons in each pixel is proportional to the count of photons that struck that pixel. After an exposure has been completed, the electrons in each pixel are read out of the detecting device and converted to a number, indicating how dark or light each particular pixel should be, and stored in a computer image file. Pixelation is equivalent to a convolution of the image with the pixel response function (PRF) $R(\theta)$ of each pixel

$$I(\theta) = O(\mathbf{v}) \star P(\theta) \star R(\theta)$$

The PRF may vary from pixel to pixel and with color. This effect is significant enough to distort the weak lensing signal from faint, distant galaxies. A recent study on the effects of pixelisation in weak lensing can be found in e.g. High et al. (2007).

4.1.3 Methodological challenges

The sequence of transformations a galaxy image undergoes, from its formation to its restitution by a detector, is shown in Fig. 4.1.

1. The process starts with the formation of the source galaxy image.
2. The image is then weakly gravitationally sheared through the transformation (3.23).
3. The quality of the image is degraded by the sky background noise.
4. That image can only be observed through the atmosphere (if from the ground) and the telescope. The lensing signal is diluted and distorted by the convolution with a PSF kernel.
5. That image is also contaminated by photon (shot) Poisson noise and by the Gaussian noise introduced by the detector itself.

The shear measurement problem consists in estimating the tiny change in the (unknown) shape of the source galaxy caused by the shear field. This is an example of an inverse problem. The only data available are the right-hand images of the observed galaxy and PSF. This illustrates how the different difficulties identified in Sect. 4.1.2 come together to render the resolution of the shear measurement problem very difficult indeed.

A shear measurement method must overcome the observation-related difficulties highlighted in Sect. 4.1.2 and summarized in Fig. 4.1. To this end, a satisfactory solution should be found to each of the following problems:

1. *PSF correction*: determine the shape or light profile a galaxy had before being convolved with the PSF. If the spatial variation of the PSF over the field of view is significant, this step also requires interpolating the PSF to the positions of the galaxies in the sky.
2. *Shape measurement*: determine the galaxy shape or light profile *after* it has been altered by the cosmic shear but *before* PSF convolution and other subsequent distortions. We refer to the corresponding shape as the *sheared* galaxy shape. The real galaxy shape prior to gravitational lensing (i.e. unsheared) is referred to as the intrinsic shape.
3. *Shear measurement*: extract the shear signal from the sheared galaxy shapes estimated in the previous step. The shear field can seldom be assumed constant. A spatially-varying shear field is commonly described by two-point statistics such as a power spectrum or a correlation function. A shear estimator that relates the shear to the shape or light profile of the observed galaxy image must be defined. Moreover, what is actually measured is not the lensing shear γ but the reduced shear \mathbf{g} , which includes the effects of the convergence κ . Correcting that approximation is required for the accurate determination of cosmological parameters and other cosmological constraints.
4. *Pixelation and noise*: additional steps can be incorporated to correct the images from these effects, prior or during the determination of the shear, to improve the overall accuracy of the measurement.

Prior to performing these steps, non-trivial tasks are to identify, stars and galaxies, separate them and select the objects suitable for shear measurement. We do not consider here that

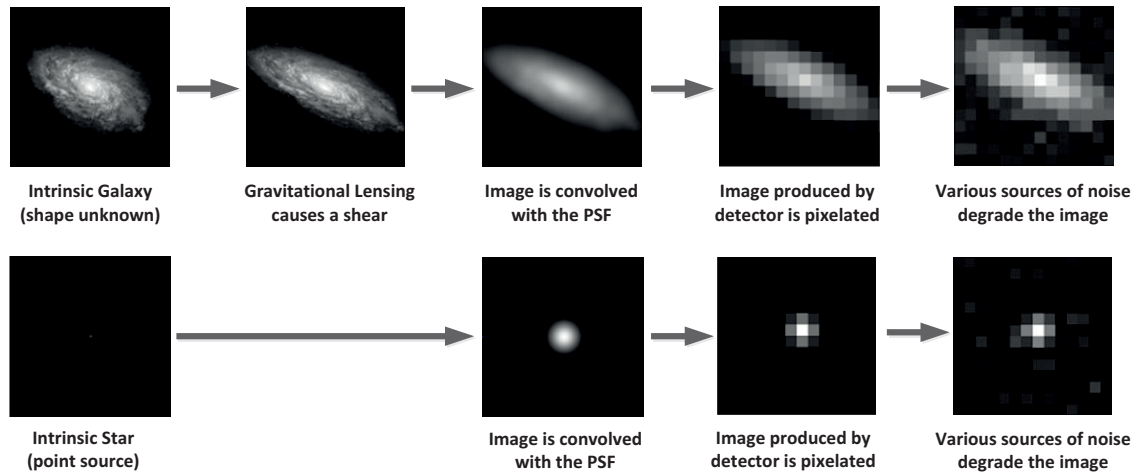


Figure 4.1: *Upper panel*: schematic view of the different intervening processes, from the formation of the galaxy image to its restitution by the detector. (1) The original image (shape unknown) is changed with an unknown amount of shear to be estimated (2). The effect is exaggerated ~ 10 times here. The sheared image is then (3) convolved with the PSF resulting e.g. from the telescope and atmosphere. The resulting blurred image is further altered by a nearly constant sky background noise and pixelated (4). Finally (5), Poisson and Gaussian noises are generated during the image acquisition and restitution. *Lower panel*: star image experiences a similar sequence of transformation, except that the shear effect is negligible. Picture adapted from the GREAT08 handbook (Bridle et al. 2009).

such tasks should be carried out by the shear measurement method itself.

How to approach the shear measurement problem and how to solve it are the focus of active research, which we review in Sect. 4.3.

4.1.4 Computational challenges

The cosmic shear signal is very small and its analysis requires the observations of millions of galaxies over large sky areas, as explained in Sect. 4.1.2. This represents huge quantities of data, mostly in the form of astronomical images. Such data cannot be efficiently compressed and typically occupy large volumes on computer discs.

Once the images are collected and stored, the next step is to process them. A typical shear measurement algorithm has to iterate over each galaxy image and perform some image processing operations to best determine its shape. Deconvolution, interpolation or denoising tasks also involve heavy processing tasks. In any case, even if the CPU time for such tasks may be reduced to a small amount by an efficient algorithm, the total number of objects to process is such that the overall processing time quickly explodes. Splitting the workload over a large number of processors executing concurrently is probably the only way out.

Euclid-like surveys will collect petabytes of data. Extracting and analyzing the cosmic shear signal in such a large amount of data will require the use of supercomputers or computer

clusters with hundreds or thousands of CPUs. In order to process the data within reasonable time scale, any serious shear measurement method will have to be able to take full advantage of such advanced distributed, multi-processor machines. One can hope that computer technology will progress at a fast enough pace to compensate for the relative slowness of software algorithms, whose efficiency typically improve more slowly.

4.2 The STEP and GREAT initiatives

4.2.1 The STEP programs

As highlighted in Sect. 3.4.3, first-generation cosmic shear surveys showed a relatively large dispersion in their cosmological σ_8 or Ω_m estimates. The TESting Programme (STEP) (Heymans et al. 2006; Kitching et al. 2012b), hereafter STEP 1, was launched in 2004 to assess whether the discrepancies found between the cosmic shear results were caused by variations in the accuracy of the different shear measurement pipelines used. A secondary goal was to improve the reliability and accuracy of available cosmic shear measurement methods, in preparation for next-generation wide-field surveys.

The STEP I data consisted of a large volume of images containing a mixture of simulated stars and galaxies. The participants were asked to run their shear measurement methods and determine the (constant) shear encoded in the images. The competition was blind, so that the answers were kept unknown to the participants during the competition and only revealed after the deadline. The estimates from each participants would then be compared to the answers and analyzed. The STEP 1 results pointed out large variations in accuracy between KSB+ variants, from 1 to 20%. The STEP 2 (Massey et al. 2007a), STEP 3 editions introduced more complicated Shapelet-based galaxy morphologies and larger amounts of data. Despite this added complexity, significant improvements were observed (Massey et al. 2007a) between STEP 1 and STEP 2. STEP 3 focused on space-based observations with very complicated PSFs. STEP 4, on the other hand, marked a return to less complexity and the desire to focus on the basic factors impacting the accuracy of shear measurement.

Overall, the main lessons from the STEP programs was that accurate shear measurement is far from trivial and that the shear measurements methods in frequent used at the time (such as KSB+) were sufficiently accurate compared to the level of statistical errors of that generation of cosmic shear surveys.

4.2.2 The GREAT08/10 challenges

The Gravitational LEnsing Accuracy Testing 2008 (GREAT08) Challenge (Bridle et al. 2009, 2010) continued the trend initiated by STEP 4, to “step back” and focus on the core problems to be solved for achieving the greater accuracy requirements of more ambitious cosmic shear surveys. Difficulties not purely related to the problem of shear measurement such as the presence of overlapping stars and galaxies or the necessity to separate stars and galaxies, were put aside. The simulated images therefore consisted of postage stamps of galaxy images with two levels of noise contamination: low and high. The shear field and PSF were set as constant. Training sets were also made available, but the challenge was blind, as in STEP.

It was also recognized that the shear measurement problem could also be formulated as a statistical problem and that experts from other disciplines may be in a position to participate

and bring original and innovative contributions. The challenge, which ran during 6 months, from October 2008 until the end of April 2009, was a success in this respect, since it turned out the winners were not astronomers (Bridle et al. 2010).

One of the outcomes of STEP and GREAT08 was the introduction of a split of the total bias into an shear-independent additive bias and a shear-dependent multiplicative bias between the measured and true shear, respectively denoted as c and m where $c = \langle c_i \rangle$ and $m = \langle m_i \rangle$, $i = (1, 2)$. The c_i and m_i are respectively the additive and multiplicative biases over the two component of shear γ_1 and γ_2 . The c_i and m_i coefficients are calculated by assuming the shear field is constant and that the error on the shear, $\gamma_i - \gamma_i^{true}$, and the true shear γ_i^{true} obeys a linear relationship of the form

$$\gamma_i - \gamma_i^{true} = m_i \gamma_i^{true} + c_i \quad (i = 1, 2) \quad (4.2)$$

The GREAT08 results confirmed the shear measurement method available at the time were able to match the accuracy requirements of CFHTLenS-like surveys, that is, an additive bias of $c \approx 0.001$ and a multiplicative bias of $m \approx 0.02$.

The continuation of GREAT08, the GREAT0 challenge (Kitching et al. 2010, 2012a), ran for 9 months, between December 2010 and September 2011. Unlike GREAT08, the cosmic shear and PSF were no longer kept constant but instead varied spatially across images. Indeed, the cosmic shear intrinsically variable whereas the PSF also varies spatially across images because of telescope optics and atmospheric effects, among others.

So GREAT10 was effectively two challenges in one: the ‘‘Galaxy challenge’’ was to reconstruct the cosmic shear field in the form of shear catalogs at requested positions or shear power spectra. The ‘‘Star Challenge’’, on the other hand, was to recreate the PSF field at non-star positions. The Star challenge is discussed in more details in Sect. 4.5.

The volume of data significantly increased compared to that of GREAT08 and reached approximately 1 Terabyte, with 50 millions galaxies. The challenge thus also became computational.

The introduction of variable shear and PSF fields also meant that the evaluation metrics for accuracy and bias used in STEP and GREAT08 had to be extended (see e.g. Kitching et al. (2012a); Gentile et al. (2012) for more details). According to these metrics, the GREAT10 Galaxy Challenge saw a factor of 3 improvement in the accuracy achieved by other shape measurement methods. A majority of methods also reached additive biases below 10^{-3} and a few methods (which included the author’s *gfit*), achieved sub-percent multiplicative biases. This is shown in Fig. 4.5 from the GREAT10 Galaxy challenge results paper (Kitching et al. 2012a).

This level of multiplicative and additive bias corresponds to the level expected by next-generation surveys like KIDS, HSC or DES, $c \approx 0.0006$ and $m \approx 0.004$. However, all methods fell short of meeting the Euclid requirements $c \approx 0.0003$ and $m \approx 0.001$ on images with $S/N < 20$. The approximate targeted bias values of current and future cosmic shear surveys are summarized in Table 4.1.

The third GRavitational lEnsing Accuracy Testing challenge, GREAT3 (Mandelbaum et al. 2013), is in preparation and will start in July 2013, running for a period of 6 months. Compared to GREAT10, GREAT3 will include more realistic simulated data. It will include in particular galaxies with realistic morphologies based on real images, realistic space- and ground-based

Table 4.1: Approximate targeted bias of current and future cosmic shear surveys

Targeted Bias	m	c
CFHTLens, etc.	$\sim 2 \times 10^{-2}$	$\sim 1 \times 10^{-3}$
KIDS, DES, HSC, etc.	$\sim 4 \times 10^{-3}$	$\sim 6 \times 10^{-4}$
Euclid, WFIRST, LSST	$\sim 1 \times 10^{-3}$	$\sim 3 \times 10^{-4}$

PSF and multi-epoch data, all combined.

4.3 Main approaches to shear measurement

Every shape measurement methods is unique in the way it tackles the problems of PSF correction, shape measurement, shear estimation, noise and pixelation described in the previous sections. The methods presented in this section illustrate different possible approaches to solving these problems:

4.3.1 Shear estimation from second-order brightness moments (KSB, KSB+)

In order to be measured the shape of a galaxy must be quantified. Real galaxies differ widely in morphology and elongation. They also have structure and their light profile is far from being smooth. Taking all these characteristics into account seems, at first sight, quite difficult.

In images used for weak lensing analysis, however, the combined effects of noise, PSF convolution and pixelation destroy most of these distinguishing features. For instance the distinction between elliptical and spiral galaxies disappears. What remains of the original galaxy images is a structureless, more or less elliptical distribution of light. The prominent characteristics that can be realistically measured with accuracy are the surface brightness profile and the deviation of the shape from circularity.

The most ancient and popular technique for measuring ellipticity is to use second-order geometrical moments calculated from the surface brightness of the galaxy as recorded in its image. Methods such as KSB (Kaiser et al. 1995) and its variants, referred to as “KSB+” (e.g., Luppino & Kaiser 1997; Hoekstra et al. 1998) rely on the observation that the average projected shape of observed galaxies is elliptical and that the orientation of galaxies is random. According to weak lensing theory, the shear is a very small perturbation on the galaxy ellipticity, which is largely intrinsic. The shear being independent of intrinsic ellipticity, averaging over the measured galaxy ellipticities yields an estimate of the reduced shear signal.

The main steps are: measure the surface brightness of individual galaxies taken from a large population (ideally tens of thousands or millions), quantify galaxy shapes by computing second order brightness moments and use these to construct a shear estimator χ , usually called “polarization” or “complex ellipticity”. Then deduce the reduced shear from χ .

An more detailed description along with an assessment of the KSB/KSB+ method can be found in Sect. 4.4.2.

4.3.2 “Forward model fitting” methods (DeepZot, gfit)

Instead of modeling the light profile and ellipticity of a galaxy with second brightness moments like in KSB/KSB+, one can also start from a more or less elaborate model of a typical galaxy and then fit the observed shape and profile to that model. A good galaxy model does not need to quantify as many features of a galaxy as possible. Rather, it should only capture the features that are considered essential to the current generation of shear measurement methods: information on the shape and light distribution of the galaxy.

The most popular model for the surface brightness profile of a galaxy is certainly that of Sérsic (Sérsic 1968). This profile describes a two-dimensional circularly-symmetric surface brightness distribution, with parameters for specifying the central intensity, the size and the degree of curvature of the light profile. The profile can be made elliptical to approximate the shape of a galaxy by the application of the shear transformation (3.42), where the convergence is considered as negligible ($\kappa \approx 0$). A galaxy can then be modeled using either a single Sérsic function or a combination of multiple Sérsics, for instance one describing the disk and the other its bulge. The *gfit* method from the author, described in Sect. 4.4.3 provides an example of the use of a single component Sérsic. Galaxy models based on bulge/disk Sérsics are used in e.g. the DeepZot (Kitching et al. 2012a), im3shape (Zuntz et al. 2013) and lensfit (Miller et al. 2007; Kitching et al. 2008; Miller et al. 2013) methods. Another rather successful model is that of a combination of Gaussian functions, explored by the *im2Shape* method (Bridle et al. 2002). See also Kuijken (1999).

A model-fitting method proceeds by iteratively modifying the parameters of the galaxy model until a satisfactory match is found between the modeled galaxy and its observed image. Shape information (e.g. ellipticity) is then derived from the fitted model parameters. An example of a simple shape measurement algorithm based on model fitting is the following: (1) Modify the parameters of the galaxy model; (2) convolve the resulting galaxy image with the PSF; (3) Estimate the fidelity of the match between the PSF-convolved model and the observed galaxy using e.g. the chi-squared statistics; (4) Stop if the match is satisfactory, otherwise continue iterating, moving back to step (1). The algorithm produces an estimate of the model parameters and an image of the best-fitted unconvolved source galaxy. This algorithm is referred to as ‘forward model fitting’. For a detailed description of the use of this kind of algorithm for galaxy shape measurement, see the Gentile et al. (2012) *gfit* paper reproduced in Sect. 4.4.3.

Methods based on model-fitting have performed well in the GREAT08 (Bridle et al. 2010) and GREAT10 challenges (Kitching et al. 2012a) (DeepZot was actually the GREAT10 winning method). The implementation of such methods is not as straightforward as it may seem. Firstly, model-fitting necessarily introduces a “model bias” arising from fitting an incorrect model to the data. Such a bias can be minimized, but at the price of additional complexity of the model, which in turn increases the difficulty and computational cost of the fitting process. Secondly, model-fitting methods critically rely on the accuracy and speed of their minimizer. Fitting galaxy models typically involve non-linearly varying parameters. Unlike linear minimizations schemes that only involve a matrix inversion, non-linear optimization requires iterating over the parameter space to find the minimum value of the objective function. As the number of parameter increases (such as with a combined bulge/disk Sérsic model), the CPU cost per galaxy increases rapidly as well as the risk of degeneracies between parameters. Moreover, a minimizer may find an excellent fit, but with a set of parameters that are totally unphysical.

These issues have been discussed in e.g. Gentile et al. (2012).

4.3.3 Analytical image decomposition (Shapelets, Reglens)

Images of galaxies are decomposed as truncated series of orthogonal basis functions. Essentially two techniques have been proposed: the first is the so-called "Shapelets" (Refregier 2003a; Refregier & Bacon 2003; Massey & Refregier 2005; Massey et al. 2005; Kuijken 2006) which adopted Gauss-Hermite or Gauss-Laguerre polynomials as basis functions, depending on the coordinate system chosen. The second uses elliptical Gauss-Laguerre polynomials as basis functions (Bernstein & Jarvis 2002; Hirata & Seljak 2003; Nakajima & Bernstein 2007).

In such methods, a two-dimensional image is represented as a linear combination of coefficients in the chosen specific basis function. The effect of a given operation (such as shear or convolution) on an image can then be analytically traced through its contribution on each coefficient in the basis function expansion. For example, the second-order $f_{2,2}$ coefficient of a Shapelet is the KSB ellipticity shear estimator.

As more detailed description of Shapelets is provided in Sect. 4.4.4.

4.3.4 Bayesian analysis of galaxy shapes (lensfit, Im2Shape)

Two examples of this approach are provided by the `im2shape` (Bridle et al. 2002) and `lensfit` (Miller et al. 2007; Kitching et al. 2008; Miller et al. 2013) methods. The idea behind these schemes is also to measure the shear through its effects on the shape of galaxies, quantified by their ellipticities. A Bayesian analysis of ellipticities is then performed, which leads to the definition of a Bayesian shear estimator.

In the case of `lensfit`, the galaxy model is chosen to be a sum of Sérsic functions for the galaxy bulge and disk, whereas it is a sum of two Gaussian functions in `im2shape`. This last representation was however found to have difficulties for describing galaxies with peaky profiles on real data. In `lensfit`, the likelihood can be directly computed through model fitting, whereas in `im2shape` the parameters of the galaxy model are estimated using Monte Carlo Markov Chain (MCMC) (e.g., Gregory 2005).

MCMC sampling has the advantage of dealing with complex models with more or less the same CPU cost (which can nevertheless be high). Running a minimizer on the same model may take a prohibitively high amount of processing time with no guarantee of a successful convergence. The case may arise, for example, when dealing with a sum of Sérsics, which requires the estimation of around 10 parameters. The `lensfit` method avoids this issue by marginalizing over some parameters and keeping others constant.

The principles and algorithms underlying `lensfit` are described in more details in Sect. 4.4.5.

4.3.5 Image stacking

The so-called "stacking" methods (Bridle et al. 2010) were the revelation of the GREAT08 Challenge. As the name indicates, such a method consists essentially in (1) accurately estimating the location of the centroid in images, (2) aligning the images so that they all share the same centroid and (3) averaging the pixel values over all the images. This can be done for galaxies and the PSF. The key assumption behind this technique is the constancy of the PSF and shear

fields, a condition which was indeed fulfilled in GREAT08 simulations. But it is questionable whether this kind of methods can be applied on real astronomical images where both the PSF and shear are spatially variable fields.

4.3.6 Application of machine learning techniques (DeepZot, MegaLUT, TVNN)

The latest GREAT10 Galaxy Challenge (Kitching et al. 2012a) has seen for the first time the application of machine learning techniques to the shear measurement problem. The GREAT10 winning method, DeepZot (Kitching et al. 2012a) makes use of a 13-input neural network to correct the ellipticities obtained from model-fitting.

The MegaLUT method (Tewes et al. 2012) performs a classification of galaxies and associated PSF kernels according to measured shape parameters, and builds a lookup table of ellipticity corrections by supervised learning.

Lastly, the TVNN method (Nurbaeva et al. 2013), applies a PSF deconvolution algorithm based on a Hopfield neural network (Hopfield 1982). The ellipticities of the galaxies are then estimated by computing the second brightness moments of the auto-correlation function (ACF) of the deconvolved images.

Neural networks and other supervised or unsupervised machine learning algorithms surely have a role to play in the next-generation of shear measurement methods. They may provide the performance leap to match the sub-percent accuracy level required by the next-generation of cosmic shear surveys.

4.4 A closer look at some shear measurement methods

We illustrate in this section several shear measurement approaches by providing an overview of KSB/KSB+, the authors method (*gfit*), Shapelets and lensfit.

4.4.1 Moment-based shear measurement: idealized case

Before introducing the underlying formalism of KSB/KSB+ methods, we first describe a idealized case, based on second brightness moments, but where the effects of noise and PSF convolution are ignored.

This approach is based on the observations that the average projected shape of observed galaxies is elliptical and that the orientation of galaxies seems random. According to weak lensing theory, ellipticity only depends on shear and is proportional (to first order) to the reduced shear g . The approach can be summarized as follows:

1. Measure surface brightness I of individual galaxies taken from a large galaxy population with size $\mathcal{N} \gg 10000$.
2. Construct a shear estimator, the so-called ‘‘complex ellipticity’’ or ‘‘Polarisation’’ χ , from observed images by computing second or higher moments from these values. The observed ellipticity χ is related to the ellipticity χ^{src} of sources and to the reduced shear (3.41), $\mathbf{g} = \mathbf{g}(\kappa, \boldsymbol{\gamma})$, $\kappa \ll 1$, $|\boldsymbol{\gamma}| \ll 1$.
3. Assume the intrinsic orientation of galaxies is random, so that $\langle \chi^{src} \rangle = 0$ and $\boldsymbol{\gamma} \approx \langle \chi \rangle$.

These steps are described in more details below.

Galaxy shape from surface brightness

One considers the second-order brightness moments

$$Q = (Q_{ij}) = \frac{\int w_I[I(\boldsymbol{\theta})] I(\boldsymbol{\theta}) (\theta_i - \bar{\theta}_i) (\theta_j - \bar{\theta}_j) d^2\theta}{\int w_I[I(\boldsymbol{\theta})] I(\boldsymbol{\theta}) d^2\theta} \quad i, j \in \{1, 2\} \quad (4.3)$$

based on the distribution of surface brightness $I = I(\boldsymbol{\theta})$, measured within a region around the centroid

$$\bar{\boldsymbol{\theta}} = \bar{\boldsymbol{\theta}}(\bar{\theta}_i, \bar{\theta}_j) = \frac{\int w_I[I(\boldsymbol{\theta})] I(\boldsymbol{\theta}) \boldsymbol{\theta} d^2\theta}{\int w_I[I(\boldsymbol{\theta})] I(\boldsymbol{\theta}) d^2\theta} \quad (4.4)$$

of the observed galaxy (usually several half-light radii away, the half-light radius r_h being defined as the effective radius within which half of the galaxy luminosity is contained, assuming a radially symmetric galaxy. The weight function w_I is arbitrarily chosen, provided the integrals converge. It can be, for instance, a function of the Heaviside step function.

Gravitational lensing conserves surface brightness, so if $I_{src}(\boldsymbol{\beta})$ is the surface brightness in the source plane, the observed surface brightness distribution $I(\boldsymbol{\theta})$ in the lens plane is

$$I(\boldsymbol{\theta}) = I_{src}[\boldsymbol{\beta}(\boldsymbol{\theta})] \quad (4.5)$$

It is then possible to define, in an equivalent way, the second brightness moments for the unlensed source

$$Q^{src} = (Q_{ij}^{src}) = \frac{\int w_I[I_{src}(\boldsymbol{\beta})] I_{src}(\boldsymbol{\beta}) (\beta_i - \bar{\beta}_i) (\beta_j - \bar{\beta}_j) d^2\beta}{\int w_I[I_{src}(\boldsymbol{\beta})] I_{src}(\boldsymbol{\beta}) d^2\beta} \quad i, j \in \{1, 2\} \quad (4.6)$$

and, using the linearised Lens equation (3.5), one obtains the transformation formula between Q^{src} and Q

$$Q^{src} = \mathcal{A} Q \mathcal{A}^T = A Q A \quad (4.7)$$

Ellipticity from surface brightness

A measure of the size of an observed image is given by

$$\omega = (Q_{11} Q_{22} - Q_{12}^2)^{1/2} \quad (4.8)$$

But, more importantly, the second moments characterize the elliptical area formed by distorting a circularly symmetric distribution of points along two orthogonal directions (while preserving the area). Second-order moments weighted by surface brightness thus provide a measure of the ellipticity and orientation, i.e. the “shape”, of a projected, two-dimensional galaxy light profile.

4.4. A closer look at some shear measurement methods

There are several possible parametrizations, but the following two are the most commonly used. The first, denoted by χ is given in complex space by

$$\chi = \chi_1 + i\chi_2 = \frac{Q_{11} - Q_{22}}{T} + i\frac{2Q_{12}}{T} \quad (4.9)$$

where T is the trace of the matrix (4.3)

$$T = Q_{11} + Q_{22} \quad (4.10)$$

The characterization of ellipticity using χ is illustrated in Figure 4.2. The second parametrization is

$$\epsilon = \epsilon_1 + i\epsilon_2 = \frac{Q_{11} - Q_{22}}{T + 2\omega} + i\frac{2Q_{12}}{T + 2\omega} \quad (4.11)$$

For an idealized galaxy image with elliptical isophotes, of semi-minor to semi-major axis ratio $q = b/a$, ($b < a$), these complex ellipticities have moduli

$$|\chi| = \frac{1 - q^2}{1 + q^2} = \frac{a^2 - b^2}{a^2 + b^2} \quad |\epsilon| = \frac{1 - q}{1 + q} = \frac{a - b}{a + b} \quad (4.12)$$

A derivation of χ is given in Appendix A.2. The ellipticities ϵ and χ transform into one another through the equations

$$\epsilon = \frac{\chi}{1 + (1 - |\chi|^2)^{1/2}}, \quad \chi = \frac{2\epsilon}{1 + |\epsilon|^2}$$

These two ellipticities have the advantage to be simply related to the reduced shear \mathbf{g} . If we define the ellipticities χ and ϵ of the source in analogy with (4.9) and (4.11), one can derive the transformation equations (e.g., Schneider & Seitz 1995; Seitz & Schneider 1997)

$$\chi^{src} = \frac{\chi - 2\mathbf{g} + |\mathbf{g}|^2\chi^*}{1 + |\mathbf{g}|^2 - 2\text{Re}(\mathbf{g}\chi^*)} \quad (4.13)$$

$$\epsilon^{src} = \begin{cases} \frac{\epsilon - \mathbf{g}}{1 - \mathbf{g}^*\epsilon} & \text{if } |\mathbf{g}| < 1 \\ \frac{\epsilon - \mathbf{g}\epsilon^*}{\epsilon^* - \mathbf{g}^*} & \text{if } |\mathbf{g}| > 1 \end{cases} \quad (4.14)$$

where the asterisk * denotes complex conjugation.

Interchanging source and image ellipticities and setting $\mathbf{g} \rightarrow (-\mathbf{g})$ yield the inverse transformations.

Shear from Ellipticity

Equations (4.13) and (4.14) show that the transformation of image ellipticities expressed as quadrupole moments depends only on the reduced shear \mathbf{g} and not on κ or γ . The reduced shear is therefore the only relevant observable when it comes to measuring the shear from

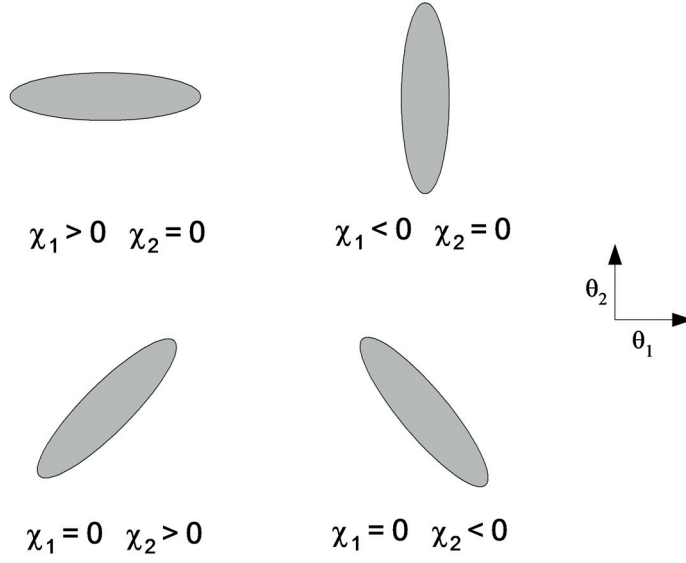


Figure 4.2: Illustration of the complex ellipticity $\chi = \chi_1 + i\chi_2$. Circular images have both $\chi_1 = 0$ and $\chi_2 = 0$.

ellipticities.

Cosmic Shear is weak, hence $\kappa \ll 1$, $|\gamma| \ll 1$ and to this limit, the aforementioned equations become

$$\chi^{src} \approx \chi - 2\mathbf{g} \approx \chi - 2\boldsymbol{\gamma} \quad \boldsymbol{\epsilon}^{src} \approx \boldsymbol{\epsilon} - \mathbf{g} \approx \boldsymbol{\epsilon} - \boldsymbol{\gamma} \quad (4.15)$$

Assuming the intrinsic orientation of galaxies is random,

$$\langle \chi^{src} \rangle = \langle \boldsymbol{\epsilon}^{src} \rangle = 0 \quad (4.16)$$

which gives the shear estimator

$$\boldsymbol{\gamma} = \mathbf{g} = \frac{1}{2} \langle \chi \rangle \quad \boldsymbol{\gamma} = \mathbf{g} = \langle \boldsymbol{\epsilon} \rangle \quad \text{Shear estimator} \quad (4.17)$$

Further, one can show that the lensing signal to noise ratio S/N , when averaging over \mathcal{N} galaxies, can be expressed in terms of $\langle \boldsymbol{\epsilon} \rangle$ as

$$S/N = \frac{|\langle \boldsymbol{\epsilon} \rangle| \sqrt{\mathcal{N}}}{\sigma_\epsilon}$$

where σ_ϵ is the dispersion of galaxy ellipticity. This expression shows the signal to noise ratio becomes stronger as the number of background sources increases.

The formalism just described forms an ideal theoretical construct that does not account for noise and PSF convolution. In fact, a weighting function w_I that directly depends on surface brightness leads to practical difficulties. Shear measurement methods (especially KSB/KSB+, see next section) usually use customized weighting schemes in order to prevent the noise in

the image from dominating the signal to be measured. This formalism nevertheless forms the underlying theoretical framework of measurement methods that aim to estimate the true shear from ellipticities.

4.4.2 Moment-based shear measurement with KSB/KSB+

The original method was developed by Nick Kaiser, Gordon Squires and Thomas Broadhurst in 1995 (Kaiser et al. 1995), hence its name. Its formalism was later corrected and improved by Luppino & Kaiser (1997), Hoekstra et al. (1998). The enhanced method is known under the generic name of “KSB+” and is described in more details below. KSB+ is the most ancient and still probably most widely-used shear measurement method.

The method is based on the following key assumptions

1. The intrinsic orientations of galaxies is random, that is

$$\langle \chi^{src} \rangle = 0 \quad (4.18)$$

2. The PSF is assumed to consist of a small, highly anisotropic kernel q , convolved with a large isotropic component P^{iso} and reads

$$P(\boldsymbol{\theta}) = \int q(\boldsymbol{\theta}) P^{iso}(\boldsymbol{\theta} - \mathbf{v}) d^2\mathbf{v} \quad (4.19)$$

Shape measurement

Cosmic shear introduces a coherent perturbation on top of the intrinsic ellipticities of galaxies. According to assumption (1), galaxies can be considered as randomly oriented and the average galaxy shape will be circular. By considering a large number of galaxies and measuring the statistical deviation of their average shapes from circularity, one can therefore, in principle, obtain an estimate of the shear. The shapes of individual galaxies are considered elliptical and a measure of their ellipticity is estimated based on the second brightness moments (4.3) & (4.6) and complex ellipticities (4.9) & (4.11) described in the previous section.

However, the second brightness moments are not normalized by the flux contrary to the standard definition:

$$Q^{KSB} = (Q_{ij}^{KSB}) = \int W_{\boldsymbol{\theta}}(|\boldsymbol{\theta} - \bar{\boldsymbol{\theta}}|) I(\boldsymbol{\theta}) (\theta_i - \bar{\theta}_i) (\theta_j - \bar{\theta}_j) d^2\boldsymbol{\theta} \quad i, j \in \{1, 2\} \quad (4.20)$$

The effect of the components of χ on the galaxy shape has been illustrated in Fig 4.2.

In expression (4.20), $\boldsymbol{\theta} = (\theta_1, \theta_2)$ is a position vector within the observed image plane, $I(\boldsymbol{\theta})$ is the surface brightness at position $\boldsymbol{\theta}$ and $W_{\boldsymbol{\theta}}$ is a weighting function that depends on position only and not on surface brightness. Central moments are very sensitive to noise and the role of the $W_{\boldsymbol{\theta}}$ function is to give more weight in the moment calculation to areas with high signal to noise ratios. If it were not so, the convergence of the Q integral would not be guaranteed.

The reason for choosing the polarisation χ as estimator of ellipticity is that, in the absence of noise, the reduced shear $\mathbf{g} = (g_1, g_2)$ is simply related to the source and image polarisations χ through (4.13) or (4.14) and, in the weak lensing regime applicable to cosmic shear by (4.15).

Chapter 4. Cosmic shear measurement

Unfortunately, in more realistic situations where noise levels are significant, equation (4.17) generally does not produce reliable enough results. In order to improve this, it is replaced by an equation that rely on a improved position-dependent weighting function W_{θ} , that attempts to filter out the effects of noise. This, however, comes at the price of an increased complexity: instead of equation (4.17), KSB/KSB+ thus makes use of the more complicated expression

$$\langle g_i \rangle = \left\langle \frac{\chi_i - P_{ij}^{sm} q_j}{P_{ij}^{g-1}} \right\rangle \quad (4.21)$$

with

$$P_{ij}^g = P_{ij}^{sh} - P_{ij}^{sm} P_{ij}^{sh*} \left(P_{ij}^{sm*} \right)^{-1} \quad (4.22)$$

The quantities $P_{ij}^{sh} = \frac{\partial \chi_i}{\partial g_j}$ and P^{sm} are respectively called the “shear polarisation tensor” and the “smear polarisation tensor”. The P^{sh} matrix encodes the lensing shear effect, whereas the P^{sm} matrix and the q vector describe the “smearing”, i.e. blurring effect of convolution with the PSF (the * symbol denotes the corresponding tensor is measured from a star).

In expression (4.22), $\left(P_{ij}^{sm*} \right)^{-1}$ is the inverse matrix of P_{ij}^{sm*} . To calculate P^{sh} , P^{sm} and P^g , the *getshape* program is available as part of the freely available Imcat set of tools, developed by Nick Kaiser (<http://www.ifa.hawaii.edu/~kaiser/>).

PSF modeling and correction

In KSB/KSB+, the PSF is inferred from carefully-selected stars: bright stars provide a way of measuring the PSF and its distribution across a field, because they are point-like object and the effect of shear on them negligible. A PSF is modeled as a small anisotropic kernel convolved with an isotropic larger component (assumption 2). In equation (4.21), the q vector describes the anisotropic PSF kernel, while the P^{sm} matrix represents the larger isotropic portion. The q vector for stars, denoted q^* is estimated from a set of stars selected within the field of view using equation

$$q_i^* = \chi_i \left(P_{ij}^{sm*} \right)^{-1} \quad (4.23)$$

while the P_{ij}^{sm*} is calculated by the *getshape* program. However, the values of q^* obtained in this way have to be measured at the positions of galaxies instead of stars: the values for the galaxy PSF kernels, q_i , are usually and typically found by polynomial interpolation or some finite-difference method, assuming a smooth enough variation of the PSF across the field. An critical review of such interpolators is available in the author’s paper on PSF interpolation (Gentile et al. 2013).

Noise reduction

To minimize the effects of noise on the quadrupole moment calculation, KSB/KSB+ typically employ as weighting function W_{θ} , the “Mexican Hat”, which is a circularly symmetric Gaussian

4.4. A closer look at some shear measurement methods

Rank	ID	Method	Q	Rank	Author	Method	Q
1	HHS1	Gauss	488	1	HB	CVN Fourier	211
2	AL	CLT KK99	375	2	AL	KK99	131
3	PG	gfit	136	3	TK	LENSFIT	119
4	TK	LENSFIT	33.7	4	CH	KSBf90	52.3
5	CH	KSBf90	32.4	5	PG	gfit	32.0
6	MV	KKshapelets with flexion	21.2	6	MV	KKshapelets with flexion	28.6
7	MJ	BJ02 deconvolved shapelets	20.2	7	KK	KKshapelets	23.0
8	KK	KKshapelets	19.7	8	HHS3	GaussStackForwardGaussCleaned	22.4
9	SB	IM2SHAPE	15.3	9	SB	IM2SHAPE	20.1
10	USQM	USQM	1.84	10	HHS2	GaussStackForwardGauss	19.9
				11	HHS1	Gauss	12.8
				12	MJ	BJ02 deconvolved shapelets	9.80
				13	USQM	USQM	1.22

Figure 4.3: *Left*: the GREAT08 leaderboard of the low-noise dataset at the close of the challenge (*gfit* is in third position). *Right*: the corresponding leaderboard for the high-noise dataset. The CVN Fourier and KK99 entries are stacking methods (see Sect 4.3.5). *gfit* is in fifth position. Source: GREAT08 results paper (Bridle et al. 2010).

with a scale demoted by σ and of the form

$$W_{\theta}(|\boldsymbol{\theta} - \bar{\boldsymbol{\theta}}|) = \frac{1}{2\pi\sigma^2} \exp\left(-\frac{|\boldsymbol{\theta} - \bar{\boldsymbol{\theta}}|^2}{2\sigma^2}\right) \quad (4.24)$$

The actual value of σ depend on KSB/KSB+ implementations, but is a function of the size of the object, like its half-light radius. The quadrupole moment (4.20) is calculated over a circle centered at the image centroid and of specific radius “window”, even though, isophotes are not generally of circular shape.

Strength

- The KSB method has been historically, the first method able to provide reliable and reasonably accurate shear estimates, and as such, has been extensively tested. KSB is actually the most widely-used shear measurement methods and astronomers have accumulated a significant experience as regards its behavior on real data. In particular, they have learned how to correct its bias or inaccuracy in certain situations.
- Implementations of the method has shown a good accuracy of the order of 5 – 10%, often working better than expected given is oversimplifying assumptions Nevertheless, the KSB method is not expected to improve enough to reach the level accuracy of $\sim 1\%$ expected for next-generation surveys such as Euclid (see Sect. 3.4.7).
- The method is fast.

Weaknesses

- Assumption (2) of a PSF distortion described as a small highly anisotropic kernel convolved with a large isotropic disk, is not realistic in most cases. It constitutes a reasonable approximation, for example, in the case of atmospheric seeing in the presence of small amplitude telescope guiding errors. But this approximation breaks down when the PSF strongly deviates from a Gaussian function, as it is likely to happen for space-based

imaging.

- The method for estimating the PSF distribution from individual stars is prone to errors, because the PSF often varies spatially across the image field, requiring the use of interpolation techniques. Moreover, possible temporal variations of the PSF are not accounted for. However, this problem is more general and not specific to KSB/KSB+ (see e.g. Gentile et al. (2013)).
- The convolution kernel q is assumed to only depend on the coordinates θ , but it was found that q_* and its interpolated value q , also vary according to object sizes. Indeed, the weighting function W_θ depends on object sizes through σ and also affects the calculation of the relevant polarizations and tensors χ , P^{sh} , P^{sm} , P^g as well as q through equation (4.23). To circumvent this, some KSB/KSB+ implementation group galaxies in a number of bins, each bin containing objects with a given range of sizes. When it comes to calculate the PSF correction and shear for a specific galaxy of size s , the polarization and tensor values calculated for the bin corresponding to size s are used. Nevertheless, it is not clear how many bins there should be and which range of object sizes should be used.
- The description of shapes using second surface brightness moments Q_{ij} may not be good enough: it is possible to have zero Q_{ij} but non-zero anisotropy (Kuijken 1999). Also, central moments are notoriously sensitive to noise and the use of the weighting function W_θ is only a crude way to address this. Moreover, KSB/KSB+ assumes circular isophotes when calculating the moments.
- Another issue lies with the presence of inverted matrices in equations (4.23) and (4.22). For some objects the matrices are not invertible and give rise to very high values which must be discarded. The high variance of q and P^g quantities makes it difficult to improve the accuracy of the calculations. In this respect, the stability of the KSB/KSB+ algorithm and its ability to reach high precision is thus questioned.
- No specific treatment is performed to correct for pixelation. It is assumed the image data have been depixelated during data reduction.
- The issues just listed certainly gives some clues about why it is that known implementations of KSB/KSB+, despite using the same framework, vary significantly in terms of accuracy of result. This is apparent, for example, when looking at the results of the STEP programs (Heymans et al. 2006; Massey et al. 2007a).

4.4.3 Galaxy model fitting with *gfit*

The *gfit* “Forward model fitting” shear measurement method was developed by the author, inspired by a prototype in IDL from Stéphane Paulin-Henrikson.

The method was first tested on the GREAT08 challenge, where it respectively finished third and fifth on low-noise and high-noise data, as shown in the leaderboard, Fig. 4.3, reproduced from the GREAT08 results paper (Bridle et al. 2010). *gfit* was then enhanced to compete in the GREAT10 Galaxy challenge, where it obtained good results: as highlighted in the Kitching et al. (2012a) paper and illustrated in Fig. 4.5, it obtained the lowest additive bias and the second lowest multiplicative bias on the shear power spectrum. *gfit* was therefore among the methods that could reach a sub-percent multiplicative bias.

The method and an analysis of the GREAT10 results are described in detail in the Gentile et al. (2012) paper, which we have also reproduced below for convenience.

4.4. A closer look at some shear measurement methods

Method	Q	Q_{dn}	$Q_{dn \& \text{trained}}$	m	$c/10^{-4}$	$\mathcal{M}/2$	$\sqrt{\mathcal{A}}/10^{-4}$
†ARES 50/50	105.80	163.44	277.01	-0.026 483	0.35	-0.018 566	0.0728
†cat7unfold2 (ps)	152.55		150.37			0.021 409	0.0707
DEIMOS C6	56.69	103.87	203.47	0.006 554	0.08	0.004 320	0.6329
fit2-unfold (ps)	229.99		240.11			0.040 767	0.0656
gfit	50.11	122.74	249.88	0.007 611	0.29	0.005 829	0.0573
*im3shape NBC0	82.33	114.25	167.53	-0.049 982	0.12	-0.053 837	0.0945
KSB	97.22	134.42	166.96	-0.059 520	0.86	-0.037 636	0.0872
*KSB f90	49.12	102.29	202.83	-0.008 352	0.19	0.020 803	0.0789
†MegaLUTsim2.1 b20	69.17	75.30	52.62	-0.265 354	-0.55	-0.183 078	0.1311
method04	83.52	92.66	116.02	-0.174 896	-0.12	-0.090 748	0.0969
†NN23 func	83.16	60.92	17.19	-0.239 057	0.47	-0.015 292	0.0982
shapefit	39.09	63.49	84.68	0.108 292	0.17	0.049 069	0.8686

Figure 4.4: The results of the 12 top-ranking methods of the GREAT10 Galaxy challenge out of 95 submissions. The bias metrics \mathcal{A} and \mathcal{M} , along with the quality Q , Q_{dn} and $Q_{dn \& \text{trained}}$ have been specified in Kitching et al. (2012a).

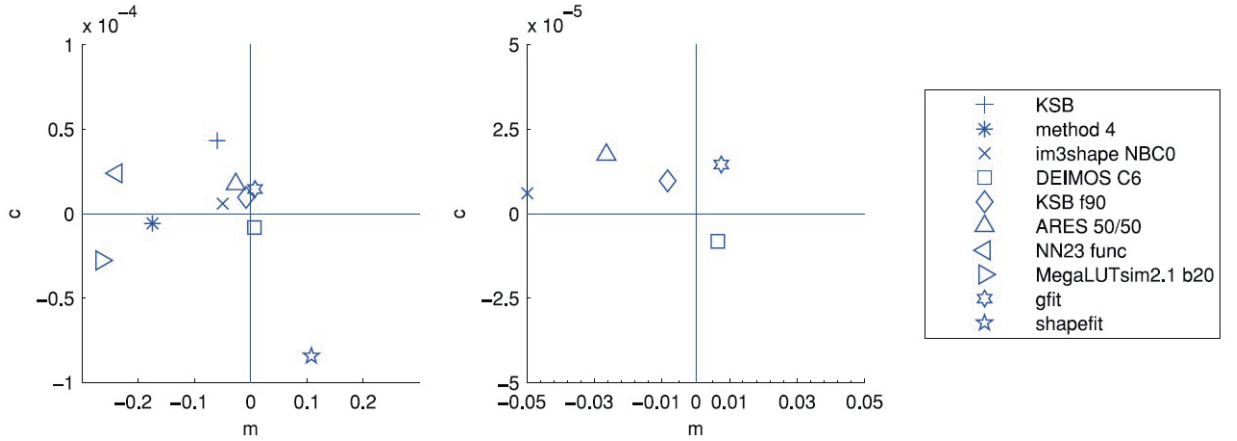


Figure 4.5: *Left plot*: multiplicative and additive biases of the ten leading shear measurement methods. *Right plot*: the biases of the four best performing methods.

A simple fitting method (*gfit*) for galaxy shape measurement in weak lensing surveys

M. Gentile¹, F. Courbin¹ and G. Meylan¹

Laboratoire d'astrophysique, Ecole Polytechnique Fédérale de Lausanne (EPFL), Observatoire de Sauverny, CH-1290 Versoix, Switzerland

Submitted to A&A

ABSTRACT

It is anticipated that the large sky areas covered by planned wide-field weak lensing surveys will reduce statistical errors to such an extent that systematic errors will instead become the dominant source of uncertainty. It is therefore crucial to devise numerical methods to measure galaxy shapes with the least possible systematic errors. We present a simple "forward deconvolution" method, *gfit*, to measure galaxy shapes given telescope and atmospheric smearings, in the presence of noise. The method consists in fitting a single 2D elliptical Sérsic profile to the data, convolved with the point spread function. We applied *gfit* to the data proposed in the GRavitational lEnsing Accuracy Testing 2010 (GREAT10) Galaxy Challenge. In spite of its simplicity, *gfit* obtained the lowest additive bias ($\sqrt{\mathcal{A}} = 0.057 \times 10^{-4}$) on the shear power spectrum among twelve different methods and the second lowest multiplicative bias ($M/2 = 0.583 \times 10^{-2}$). It remains that *gfit* is a fitting method and is therefore affected by noise bias. However, the simplicity of the underlying galaxy model combined with the use of an efficient customized minimization algorithm allow very competitive performances, at least on the GREAT10 data, for a relatively low computing time.

Key words. Gravitational lensing: weak – Methods: data analysis

1. Introduction

Weak gravitational lensing (e.g., Bartelmann & Schneider 2001; Hoekstra & Jain 2008), whereby the gravitational bending of light by structures in the Universe slightly distorts images of distant galaxies, is now recognized as a powerful means to study the history of the Universe and probe the mysterious nature of the dark matter and dark energy (Munshi et al. 2008; Huterer 2010).

Since the first detection of weak lensing (Maoli et al. 2001; Bacon et al. 2000; Kaiser et al. 2000; Van Waerbeke et al. 2000; Wittman et al. 2000), a number of methods have been devised and implemented to tackle the inverse problem of recovering the lensing signature from observed, distorted galaxy images (Kaiser et al. 1995; Luppino & Kaiser 1997; Hoekstra et al. 1998; Bernstein & Jarvis 2002; Hirata & Seljak 2003; Refregier & Bacon 2003; Heymans et al. 2006; Massey et al. 2007; Miller et al. 2007; Kitching et al. 2008; Bridle et al. 2010; Kitching et al. 2012).

We describe in this paper *gfit*, a simple shear measurement method that nevertheless obtained good results in the latest GRavitational lEnsing Accuracy Testing 2010 (GREAT10) Galaxy challenge (Kitching et al. 2011, 2012). Galaxies are assumed to be well modeled by a seven-parameter, single-component elliptical Sérsic profile. The shape measurement algorithm essentially consist in iteratively shearing and convolving the galaxy model until a sufficiently close match with the observed galaxy is reached. Instead of an out-the-box minimizer, we employ a custom-developed minimizer well suited to fitting faint and noisy images like those frequently found in weak lensing.

The paper is structured as follows. We provide in Sect. 2 a description of the underlying principles, galaxy model and shape measurement algorithm of *gfit*. We continue in Sect. 3 with a pre-

sentation of the pipeline we used to participate in the GREAT10 Galaxy challenge and follow with an analysis of the *gfit* results in Sect. 4. We conclude in Sect. 5.

2. The *gfit* shear measurement method

2.1. The shear measurement problem

According to the theory of weak gravitational lensing, the light emitted by a galaxy is slightly deviated by the foreground gravitational field, an effect that can be modeled to first order as the combination of two effects, the *convergence* κ and the *shear* γ , that describe how light bundles emitted by a source are distorted by a potential well. The convergence models the magnification effect whereby the galaxy image see its apparent size increased without altering its shape, whereas the shear describes a stretching effect where only ellipticity is altered, not size.

All so-called "shear measurement methods" attempt to reconstruct the reduced shear $g = \gamma/(1 - \kappa - \gamma)$ which is approximately equals to the shear γ in the weak gravitational limit, where $\kappa \ll 1$ and $\gamma \ll 1$.

The lensing effect is very subtle, however, and requires measuring the shapes of thousands of faint galaxies. Moreover, before they reach the observer, the apparent galaxy images undergo a number of additional distortions, unrelated to lensing, that further complicates that task, mainly:

- The convolution of the images by the instrumental and/or atmospheric point spread function (PSF) that flattens and circularizes the galaxy light profile.
- The Gaussian and Poisson noise introduced by the surrounding sky emissions and the detecting device.
- The pixelation effect caused by the integration of light falling on the detector pixels.

The traditional approach for estimating the shear is to measure the deviation from circularity of a large number of galaxy shapes. But this technique assumes the shear remains constant across the field of view, which is generally not the case. Moreover, accurate shear measurement must also account for a spatially varying PSF that must be interpolated at the positions of the galaxies.

A shear measurement pipeline must overcome all the above difficulties, typically going through the following steps:

1. *PSF correction*, whose goal is to restore the shape a galaxy had before being convolved with the PSF. If the spatial variation of the PSF over the field of view is significant, this step also requires interpolating the PSF to the position of the galaxies in the sky.
2. *Shape measurement*, that is, the estimation of the galaxy shape *after* it has been altered by the cosmic shear but *before* PSF convolution and other subsequent distortions. In this paper, we call the corresponding shape the *sheared* galaxy shape. The real galaxy ellipticity prior to gravitational lensing (i.e. unsheared) is referred to as the *intrinsic ellipticity*.
3. *Shear measurement*, that is, the task of extracting the shear signal from the sheared galaxy shapes estimated in the previous step. A spatially-varying shear field is commonly described as a power spectrum or a correlation function.

Additional steps may also be performed to correct the images from the effects of pixelation and noise.

2.2. Shear measurement with *gfit*

The *gfit* “galaxy fitting” method grew from a prototype initially developed by Stéphane Paulin-Henrikson on the occasion of the GREAT08 challenge (Bridle et al. 2008), where it obtained the third and fifth ranks on images with high and low signal to noise ratios respectively (Bridle et al. 2010).

The GREAT10 *gfit* code was subsequently made more generic in order to satisfy the more demanding requirements of the Galaxy challenge. It was also enhanced in several aspects that we describe in subsequent sections of this paper.

It is also worth mentioning that a wavelet-based denoising algorithm described in Nurbaeva et al. (2011) was also experimented in the Galaxy challenge and proved quite successful. This denoising scheme is presented in Sect. 2.7.

The overall shape measurement procedure is the following:

1. Application of the denoising algorithm on the galaxy and/or PSF images [optional]
2. Estimation of the galaxy and PSF centroids in all images
3. Application of the PSF correction and shape measurement algorithm
4. Generation of the ellipticity catalogs
5. Production of various statistics and plots for analysis [optional]

We detail in the next sections the shape measurement algorithm along with its underlying models and components.

2.3. Modeling the galaxies

gfit is fundamentally a model-fitting method. We describe here the model used to represent galaxies and cover the fitting-related

aspects in Sects. 2.4 and 2.5.

Galaxies are assumed to have a surface brightness distribution well described by an elliptical Sérsic function (Sérsic 1968), defined by:

$$I(\xi, n, r_e) = I_{sky} + I_0 \exp \left[-b_n \left(\frac{\xi}{r_e} \right)^{1/n} \right] \quad (1)$$

where:

- I_{sky} represents the sky brightness
- I_0 is the central surface brightness of the galaxy
- n denotes the Sérsic index that determines the degree of curvature of the profile. A small value of n leads to a less centrally concentrated profile and a shallower logarithmic slope at small radii.
- The scale radius parameter r_e is defined as the effective radius encircling half of the total light of the profile (e.g. Ciotti 1991; Trujillo et al. 2004; Graham & Driver 2005).
- The factor b_n (e.g. Ciotti & Bertin 1999) arises from the definition of r_e and is related to the Sérsic index n through the equation $\Gamma(2n) = 2\gamma(2n, b_n)$ where Γ and γ functions are respectively the complete and incomplete gamma functions (Abramowitz & Stegun 1965).
- The parameter ξ in Eq. (1) is defined as

$$\xi = \sqrt{(x' - x_c)^2 + \frac{(y' - y_c)^2}{q^2}} \quad (2)$$

and denotes the distance from the centroid (x_c, y_c) of the galaxy to a point on an elliptical isophote at spatial coordinate (x', y')

$$\begin{bmatrix} x' - x_c \\ y' - y_c \end{bmatrix} = \begin{bmatrix} \cos \phi & \sin \phi \\ -\sin \phi & \cos \phi \end{bmatrix} \begin{bmatrix} x - x_c \\ y - y_c \end{bmatrix},$$

obtained after counterclockwise rotation through an angle ϕ with respect to the $(0, x)$ axis.

- The quantity q in expression (2) of ξ is the ratio of the semi-minor axis b to the semi-major axis a of the isophote ellipse. It is related to the complex ellipticity $\mathbf{e} = (e_1, e_2)$ of the galaxy through $q = b/a = (1 - |\mathbf{e}|)/(1 + |\mathbf{e}|)$ with $|\mathbf{e}| = \sqrt{e_1^2 + e_2^2}$, $e_1 = |\mathbf{e}| \cos 2\phi$ and $e_2 = |\mathbf{e}| \sin 2\phi$.

This model was initially chosen for its simplicity and has the other merit of being relatively easy to fit. A galaxy represented as the sum of a bulge and a disc would be more realistic, but it is not clear whether such a model would prove more accurate on weak lensing images and worth the additional complexity and computational cost, given degeneracies between parameters. As regards *gfit*, the GREAT10 results does not provide a definitive answer (see Sect. 4).

2.4. Galaxy shape measurement and PSF correction

We describe in this section the shape measurement algorithm of *gfit*. It is based on iterative fitting of observed galaxies to the galaxy model described in Sect. 2.3. The basic assumptions of the algorithm are the following:

- All galaxy and PSF fields have been reduced and the objects they contained assumed available in the form of square postage stamps in FITS format. We denote by O a galaxy field image of the GREAT10 Challenge and by o any of its

10,000 galaxy postage stamps. The GREAT10 PSF field image corresponding to O is labeled as P and any of its individual PSF kernel as p .

- The O and P images have been denoised beforehand if requested. The denoising tool described in Sect. 2.7 is the default choice.
- The centroids of all galaxies and PSF to be processed have been estimated. A tool based on SExtractor (Bertin & Arnouts 1996) has been written for this purpose (see Sect. 2.6.)
- The PSF field at the position of each galaxy is known, so that we can always find the PSF p that matches galaxy o .

The fitting algorithm itself is summarized below:

- For each galaxy object o in observed galaxy field O
 - ◊ Extract a square stamp cutout of a given dimension $N_G \times N_G$ around the centroid (x_c, y_c) of o .
 - ◊ Remove the sky background from o after having estimated its variance σ_{sky}^2 .
 - ◊ Estimate the galaxy noise variance σ^2 of o .
 - ◊ Select guess parameters for the 7 model parameters $\{l_0, (x_c, y_c), (e_1, e_2), n, r_e\}$ described in Sect. 2.3.
 - ◊ Construct an initial galaxy postage stamp g based on the Sérsic profile having these parameters.
 - ◊ Select the PSF p that matches the spatial coordinates of o in O and extract a cutout of dimension $N_p \times N_p$ about the centroid. Make sure the PSF is normalized and has the sky background removed.
 - ◊ Iteratively vary the model parameters with the objective of minimizing the residuals between g and o .

At each step:

- ⇒ Convolve the model galaxy g with the observed PSF p and compute a new galaxy estimate $k = p \star g$
- ⇒ Compute the residuals between o and k using the chi-squared statistics

$$\chi^2 = \sum_n \sum_m \frac{(o_{n,m} - k_{n,m})^2}{\sigma_{n,m}^2}$$

where $o_{n,m}$ and $p_{n,m}$ represent the pixel value at position (n, m) in o and p respectively. Similarly, $\sigma_{n,m}$ denote the standard deviation of the noise associated with each pixel at (n, m) .

- ⇒ If the minimum χ^2 has not been reached, select a new set of parameters and construct the corresponding model galaxy g . Otherwise, exit the minimization loop.
- ◊ At the end of the iteration cycle, the algorithm yields:
 - ⇒ An estimate for all 7 model parameters and for the complex ellipticity (e_1, e_2) in particular.
 - ⇒ A postage stamp for the best-fitted intrinsic galaxy postage stamp g .
 - ⇒ A postage stamp for the best-fitted convolved galaxy k .
- ◊ The same procedure is followed for the next galaxy o in O , until all galaxies have been processed.

- Once the shape of all galaxies have been measured, produce a catalog containing the fitted parameters at the positions of the galaxies o in O and optionally, additional statistics and plots. Quantities such as the ellipticity modulus $|\mathbf{e}|$, the position angle ϕ and the minor-to-major axis ratio q can be respectively derived from (e_1, e_2) using $|\mathbf{e}| = \sqrt{e_1^2 + e_2^2}$, $\phi = \frac{1}{2} \arctan(e_2/e_1)$ and $q = (1 - |\mathbf{e}|)/(1 + |\mathbf{e}|)$.

The algorithm just described is not dependent on the galaxy or the PSF model. It would remain unchanged, for instance, if the centroid of the PSF itself was taken into account during fitting or if a bulge and a disc were incorporated in the galaxy model. The quality of the whole shape measurement procedure can thus be increased by improving the models.

The shape measurement algorithm has its own strengths and weaknesses, outlined below:

- Strengths:
 - ◊ Simplicity.
 - ◊ PSF deconvolution and galaxy model estimation are performed simultaneously.
 - ◊ The deconvolution process does not involve any matrix inversion and its side effects (numerical instabilities, presence of artifacts, noise amplification, etc.).
 - ◊ The intrinsic and best-fitted modeled galaxies are obtained as a by-product of the algorithm, in addition to the estimated model parameters.
- Weaknesses:
 - ◊ A bias is introduced through the choice of a galaxy model, which is necessarily imperfect.
 - ◊ The choice of the initial guess parameters of the galaxy model are more or less arbitrary and may also influence the final model parameter estimates:
 - ◊ The algorithm relies heavily on the accuracy and robustness of the minimizer.
 - ◊ The method is sensitive to noise bias
 - ◊ No estimate of errors is available

2.5. The *gfit* minimizer

The *gfit* galaxy model expressed by Eq. (1) varies linearly with the parameter l_0 , but non-linearly with the remaining parameters $\{(x_c, y_c), (e_1, e_2), n, r_e\}$. This requires the use of a non-linear minimization algorithm over a seven-dimensional parameter space.

Unlike linear minimizations schemes that only involve a matrix inversion, non-linear optimization requires iterating over the parameter space to find the minimum value of the objective function, which is in our case the χ^2 of the residuals between observed and estimated images. That minimum is not necessarily the absolute minimum of the χ^2 function but the most relevant from the point of view of the physics of the problem. In our case, the minimum should coincide with the Sérsic model parameters that best fit the galaxy shape.

A good minimizer is essential to any galaxy model fitting algorithm, but finding such a minimum in a reliable manner can prove tricky for a number of reasons:

- Parameter degeneracy, where different combinations of the parameters yield similar χ^2 values.
- Errors related to noise and undersampling may degrade the accuracy of the fit in several ways: (1) the distortion of the galaxy image may be such that the minimizer fits a wrong shape, even if it does it accurately. (2) The minimizer may be fooled by a “false” local minimum and converge toward wrong fitted parameter values. (3) The minimizer may fail to converge altogether if it cannot reconcile the model with the observed image.
- The choice of initial guess values for the parameters can influence the outcome of the minimization algorithm: depending on the starting location on the parameter hypersurface, the algorithm may tend to follow a different path and converge to a different minimum.

In this regards, the choice of the galaxy model used by *gfit* leads to a number of challenges:

- The total flux I_0 is degenerate with the n and r_e parameters, so that, for instance, in Eq. (1), a low I_0 flux may be compensated by a higher exponential function of n , r_e and (x_c, y_c) , modifying the shape of the fitted galaxy profile. Similarly, an error in the estimation of the sky brightness I_{sky} may “drive” the minimizer toward a wrong combination of the remaining parameters. This is why we estimate I_{sky} separately in the algorithm described in Sect. 2.4.
- *gfit* attempts to limit the effect of noise by applying the denoising method described in Sect. 2.7. As regards pixelization, *gfit* can optionally construct the galaxy model in higher resolution and rebin the pixels before fitting.
- To estimate the initial guess values for fitting a particular galaxy, *gfit* can be setup to either accept default values or use estimates from SExtractor.

Several families of optimization algorithms were experimented on GREAT08 and GREAT10 images: simplex (*Nelder-Mead downhill*), gradient descent (*Powell*), Newton & quasi-Newton (*Newton-CG*, *BFGS*) and *Levenberg-Marquardt* (LVM). Descriptions of these algorithms can be found in (e.g. Levenberg 1944; Marquardt 1963; Powell 1964; Nelder & Mead 1965; Zhu et al. 1997; Nocedal & Wright 1999; Bonnans et al. 2006).

None of these methods proved entirely satisfactory, either failing to converge or yielding insufficient accuracy, especially on low signal to noise ratio (S/N) images. The LVM implementation from the SciPy library (Jones et al. 2001–; Community 2010) that we used was the fastest and the most accurate. For these reasons we used it in the GREAT08 version of *gfit*, but that implementation of LVM:

- Failed to converge in about 5-10% of the time on GREAT08 “real noise blind” images.
- Was occasionally tricked by “false” local minima, producing the smallest residuals but with unphysical Sérsic parameters or ellipticities.
- Required good estimates of guess parameters in order to converge towards the right minimum.

We also experimented a parameter estimation scheme based on a Bayesian approach and implemented using the *pymc* Markov Chain Monte Carlo (MCMC) library of Patil et al. (2010), but that method produced less accurate estimates while being less computationally efficient.

In an attempt to overcome these issues, we eventually decided to implement a custom minimizer, better suited to fitting noisy, pixelized galaxy images than vanilla minimization algorithms. We found that a scheme based on an adaptive *cyclic coordinate descent* algorithm (CCD) was able to produce more accurate estimates while at the same time being more robust:

- Able to better cope with degenerate and correlated parameters: LVM has difficulties with the $\{I_0, n, r_e\}$ degeneracy and coupling and the steepest descent algorithm used in LVM occasionally jumps without precaution to a minimum value that may be the smallest but not the most appropriate one. To avoid this, the CCD algorithm ensures that these parameters are carefully varies in a “round-robin” manner at the beginning of the fitting process, where the amplitudes in variation are the greatest. This scheme is also much more tolerant with regards to initial guess values and converges reliably, making it more robust overall.

- More resilient to noise and on average more accurate than LVM, especially on low S/N images.

The CCD algorithm proved suitable for fitting without any single failure the huge number of GREAT10 galaxies. It nevertheless has a number of drawbacks, namely:

- The convergence rate is lower than that of LVM, resulting in a greater number of function evaluation. It is thus much slower than LVM.
- Its efficiency decreases rapidly with the number of parameters. The algorithm performance is also influenced by factors such as the specific stopping conditions chosen or the range of iteration step sizes specified for the parameters.

The current *gfit* implementation can be configured to use either the CCD, LVM or MCMC-based minimizer.

2.6. Centroid estimation

gfit does not assume objects to be correctly centered within their postage stamps and accurate estimates for galaxy and PSF objects are required for two main reasons:

- *gfit* does not necessarily use the whole postage stamps for the galaxy and the PSF to save computational time and reduce noise: the corresponding postage stamps are cut out to a smaller dimension (e.g. 24×24 instead of e.g., 48×48 around the estimated centroid).
- The coordinates of the galaxy and PSF centroids are provided to the minimizer as initial guess values before the fitting cycle can begin. Accurate centroids are especially important if the LVM minimization algorithm is used (CCD is much more tolerant in this respect).

gfit relies on centroid estimates obtained from the SExtractor tool (Bertin & Arnouts 1996). A catalog is generated with centroid information and additional data such as flux, ellipticities and position angles, that can be optionally used to set guess parameter values.

2.7. Denoising

Correcting astronomical images from the effect of noise has always been a challenging task. This is particularly true for galaxy images captured for weak lensing analysis because noise not only degrades the overall quality of these images but also alters the shapes of the galaxies. This causes serious difficulties to all existing shear measurement schemes that found their shear extraction algorithms on the accurate measurement of galaxy shapes.

The challenge is then to correct galaxy images from noise without compromising the shear signal they encode. Unfortunately, popular denoising algorithms based on median filtering (Arce 2005; Arias-Castro & Donoho 2009), Wiener filtering (Wiener 1949; Khireddine et al. 2007) or discrete wavelet transform (DWT) (Bruce et al. 1994; Vetterli & Kovacevic 1995) are not shape preserving and do not meet that requirement.

By default, *gfit* uses *DWT-Wiener*, a shape-preserving denoising technique combining DWT and Wiener filtering developed at the laboratory of astrophysics of EPFL by Nurbaeva et al. (2011). That algorithm has been experimented during the GREAT10 Galaxy challenge and was able to significantly improve the quality factors of all the shear measurement methods from EPFL that participated in the Galaxy challenge (Kitching

et al. 2012); that was the case for *gfit* but also for *MegaLUT* (Tewes et al. 2012) and *TVNN* (Nurbaeva et al. in prep.).

Interestingly, denoising improves the shape measurement of the three algorithms even though they are fundamentally different from each other.

Beyond shape-preservation, another advantage of the *DWT-Wiener* algorithm lies in its ability to denoise “in one go” images containing a great number of objects, without having to individually process each object in turn. In GREAT10, for instance, *DWT-Wiener* was directly applied to images containing 100×100 PSF or galaxy postage stamps.

3. Applying *gfit* to the GREAT10 data

3.1. The GREAT10 Galaxy challenge

We describe in this section the specific pipeline we used in the GREAT10 Galaxy Challenge competition that took place between December 2010 and September 2011. The aim, content and rules of the challenge have been described in the GREAT10 Handbook (Kitching et al. 2011, 2012). In a nutshell, the main goals of the GREAT Challenges are (i) to test existing weak lensing measurements methods and (ii) to promote the development of new, more accurate, shear measurement techniques.

The data consist of 24 datasets of 200 simulated galaxy images, each containing 10,000 noisy, PSF-convolved 48×48 pixel galaxy postage stamps, arranged on a 100×100 grid (see Fig. 1). The GREAT10 edition includes spatially-varying PSF and shear fields, contrary to its predecessor, the GREAT08 challenge (Bridle et al. 2008; Bridle et al. 2010), where these fields were set as constant.

Each of the 24 sets is designed to evaluate the ability of competing methods to deal with galaxy or PSF fields with different properties (e.g. size, signal to noise ratio). We have reproduced in Table 2 the main PSF and galaxy characteristic attached to each of the GREAT10 set, as specified in the Galaxy Challenge results paper (Kitching et al. 2012), Appendix D.

The sets were also classified into “Single epoch”, “Multi-epoch” and “Stable single epoch”, depending on whether the intrinsic ellipticities and PSF keep the same or change their spatial distribution between images in a set (see Table 1).

Participating methods were ranked according to the following metrics :

- A “Raw” quality factor Q according to which the live leader board was scored and that measures the difference, averaged over all sets, between the reconstructed and true shear power spectra.
- A quality factor Q_{dn} obtained after estimation and correction of pixel noise.
- A quality factor $Q_{dn \& \text{train}}$ after application of an additional training step on top of pixel-denoising. That step consists essentially in estimating the multiplicative and additive biases on high S/N galaxy images (set 7) and applying that calibration on the remaining sets.
- A split of the total bias into an shear-independent additive bias and a shear-dependent multiplicative bias between the measured and true shear, respectively denoted as c and m where $c = \langle c_i \rangle$ and $m = \langle m_i \rangle$, $i = (1, 2)$. The c_i and m_i are respectively the additive and multiplicative biases over the two component of shear γ_1 and γ_2 and are similar to those used in STEP I (Heymans et al. 2006) and GREAT08 (Bridle et al. 2010) for a constant shear field. They are calculated by

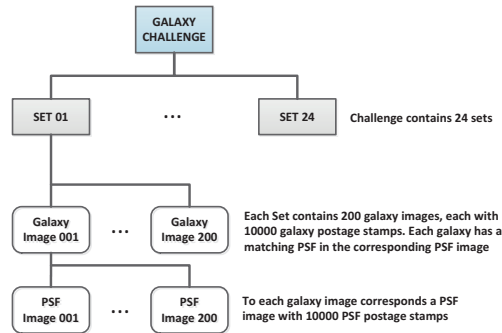


Fig. 1. The GREAT10 Galaxy challenge dataset structure. There are 24 galaxy sets, each containing 200 galaxy images with 10000 galaxy postage stamps each. To each galaxy postage stamp corresponds a matching PSF postage stamp at the same spatial position in the galaxy image.

assuming the error on the shear, $\gamma_i - \gamma_i^{true}$, and the true shear γ_i^{true} obeys a linear relationship of the form

$$\gamma_i - \gamma_i^{true} = m_i \gamma_i^{true} + c_i \quad (i = 1, 2) \quad (3)$$

More details are provided in Appendix B of (Kitching et al. 2012). See e.g. Huterer et al. (2006) for a discussion on the origin of additive and multiplicative errors in weak lensing studies.

- Additional bias metrics $\mathcal{A} \approx \sigma^2(c)$ and $\mathcal{M} \approx m^2 + 2m$, intended to measure the additive and multiplicative biases calculated at power spectrum level. Unlike c and m , these metrics account for spatial variability.

3.2. The GREAT10 *gfit* implementation

The GREAT10 version of *gfit* only implements the first two steps described in Sect. 2.1, that is, PSF correction and galaxy shape measurement.

In GREAT10, the estimation of the shear field (third step in Sect. 2.1) was not mandatory as participants were allowed to supply for each image a catalog of estimated galaxy ellipticities instead of a shear power spectrum (Kitching et al. 2011): an analysis program was written by the GREAT10 team to calculate a shear power spectrum from user-supplied ellipticity catalogs. Consequently, like most other competing methods, *gfit* only provided its estimates in the form of a catalog of estimated ellipticities at requested positions within the images. Future version of *gfit* will allow the extraction of a spatially varying shear.

The *gfit* implementation used in GREAT10 consisted of the following stages:

Table 1. Spatial variability of PSF and intrinsic ellipticities: images within a set may keep or not the same PSF or intrinsic ellipticity pattern of variation.

Type of variability within a set	PSF	Intrinsic ellipticity
Type 1: “Single epoch”	Variable	Variable
Type 2: “Multi-epoch”	Variable	Fixed
Type 3. “Stable single epoch”	Fixed	Variable

Table 2. Some of the PSF and galaxy properties characterizing the GREAT10 image sets. The second and third columns specify whether the PSF or intrinsic ellipticity field were kept constant for all images within a set. The parameters in the fourth column have been detailed in Kitching et al. (2012). The default signal to noise (S/N) ratio is 20, while low and high S/N ratios are 10 and 40 respectively. All sets, except the last four, have galaxies with co-centered bulges and disks with a 50/50 bulge-to-disk ratio.

Set	PSF	Intrinsic ellipticity	Property of images
1	Variable	Variable	Fiducial
2	Fixed	Variable	Fiducial
3	Variable	Fixed	Fiducial
4	Variable	Variable	Low S/N
5	Fixed	Variable	Low S/N
6	Variable	Fixed	Low S/N
7	Variable	Variable	High S/N
8	Fixed	Variable	High S/N
9	Variable	Fixed	High S/N
10	Variable	Variable	Smooth S/N
11	Fixed	Variable	Smooth S/N
12	Variable	Fixed	Smooth S/N
13	Variable	Variable	Small galaxy
14	Fixed	Variable	Small galaxy
15	Variable	Variable	Large galaxy
16	Fixed	Variable	Large galaxy
17	Variable	Variable	Smooth galaxy
18	Fixed	Variable	Smooth galaxy
19	Variable	Variable	Kolmogorov PSF
20	Fixed	Variable	Kolmogorov PSF
21	Variable	Variable	Uniform bulge/disc ratios
22	Fixed	Variable	Uniform bulge/disc ratios
23	Variable	Variable	50/50 bulge/disc offset
24	Fixed	Variable	50/50 bulge/disc offset

1. Optional denoising of the galaxy and PSF images with the DWT-Wiener method presented in Sect. 2.7.
2. Centroid estimation using SExtractor (Bertin & Arnouts 1996) as described in Sect. 2.6.
3. Galaxy shape measurement with the *gfit* program, configured to use the CCD minimization algorithm described in Sect. 2.5. We used 24×24 pixel cutouts instead of the full 48×48 pixel original galaxy postage stamps. Similarly, the size of PSF postage stamps was reduced to 12×12 pixels. That decision was made in order to keep the overall computation time within acceptable limits and avoid picking-up too much noise near the borders of the postage stamps.

Because of the large number of galaxies, running the pipeline on one single processor would not have allowed to meet the GREAT10 deadline. Even with a processing time per galaxy of 0.5 seconds, it would have taken about one month to complete process the full GREAT10 dataset. The ability to simultaneously run multiple program instances use of parallelism is thus imperative and all programs (denoising, SExtractor wrapper, *gfit*) are written to take advantage of parallel computers through the Message Passing Interface (MPI) (Forum 1995, 1998). When only a few processors are required, the same programs can also run on machines with symmetric multiprocessing (SMP) architecture. It took about 5 days to process the entire GREAT10 chal-

Table 3. Main metrics for “gfit den” and “gfit”.

Method	Q	Q_{dn}	$Q_{dn \& \text{train}}$	$M/2 \times 10^{-2}$	$\sqrt{\mathcal{A}} \times 10^{-4}$
gfit den	103.81	197.88	229.19	-2.067	+0.061
gfit	50.11	122.74	249.88	+0.583	+0.057

lenge images on a 64-processor machine, which corresponds to a processing time between 1 and 2 seconds per galaxy.

The pipeline is implemented in Python, a programming language known for its power, flexibility and short development cycle. The usual standard Python libraries are used, notably: NumPy, SciPy, PyFITS and matplotlib. SciPy is the standard scientific library for Python and most of its functions consist of thin Python wrappers on top of fortran, C and C++ functions. SciPy takes advantage of installed optimized libraries such as LAPACK (Linear Algebra PACKage) library (Anderson et al. 1990).

4. Analysis of the gfit GREAT10 results

We summarize and analyze in this section the main Galaxy Challenge results as far as *gfit* is concerned. An overview of the GREAT10 results for available participating shear measurement methods has already been performed in the GREAT10 Galaxy challenge paper (Kitching et al. 2012). Our objective here is to provide a more detailed analysis of the *gfit* results.

We do not, however, analyze the influence of the pixel-denoising and training calibration schemes applied in (Kitching et al. 2012), which we leave for future investigation.

4.1. Overall results

The results of the best 12 methods that participated in the GREAT10 Galaxy Challenge are listed in Table 3 of the Kitching et al. (2012) GREAT10 result paper. That list aggregates results submitted before the official challenge deadline as well as submissions made during the so-called “Post challenge”, a one-week extension to the competition following the deadline.

Two versions of *gfit* were submitted during the challenge, one named “gfit den cs” that included a denoising step using the DWT-Wiener algorithm described in Sect. 2.7 and the other, simply named “gfit”, that did not. The results obtained by both methods are shown in Table 3.

The *gfit* version presented in Kitching et al. (2012) is what we refer to here as “gfit”. In addition, we also present “gfit den cs”, described in Appendix E5 of Kitching et al. (2012) but whose results were not included in the analysis. The “gfit” version is identical except that no denoising was applied to the data before applying the shape measurement algorithm. To simplify, we shorten he name “gfit den cs” to “gfit den” in the remainder of this article.

It can be seen from Table 3 that “gfit den” reaches a raw quality factor Q twice as high as that of “gfit”. This illustrates the gain in accuracy provided by the DWT-Wiener denoising algorithm. This is further analyzed in Sect. 4.2.2. When the pixel-level denoising algorithm of Kitching et al. (2012) is applied, the Q_{dn} quality factors of both “gfit” and “gfit den” are improved by a factor ~ 2 , “gfit den” scoring the best Q_{dn} of all methods ($Q_{dn} = 197.88$). The training calibration further increases both

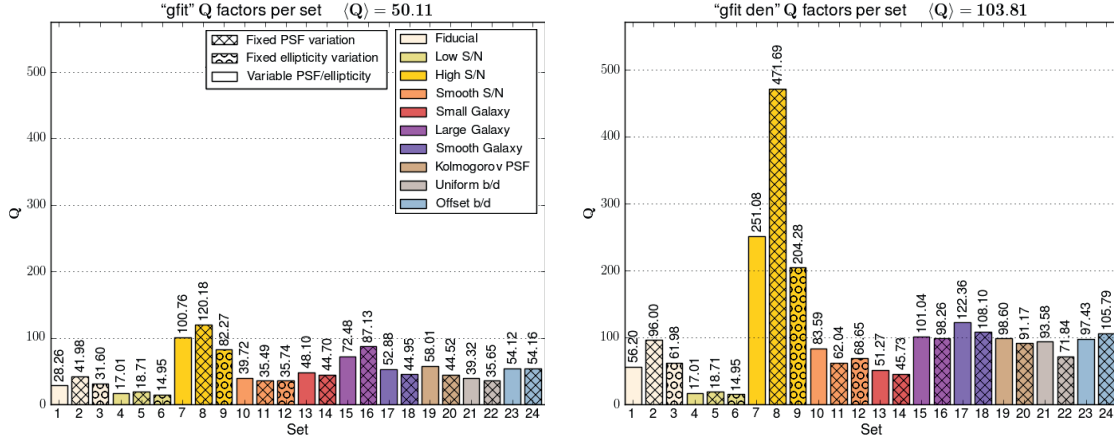


Fig. 2. Quality factors per set for “gfit” (left) and “gfit den” (right). The various colors and patterns in the legend indicate the types of features simulated in the sets. The acronyms S/N , b/d respectively refer to the signal to noise ratio and galaxy bulge/disc ratio or offset. The fiducial S/N was 20 whereas the low S/N and high S/N were respectively set to $S/N = 10$ and $S/N = 40$. The labels “Fixed PSF” and “Fixed intrinsic ellipticity” correspond to sets where the PSF and intrinsic galaxy ellipticities were spatially varying across the field but that variation did not change between images within a set. Further details on the structure of the Galaxy challenge dataset and the procedures for calculating the quality factor can be found in in the GREAT10 Galaxy challenge results paper Kitching et al. (2012).

$Q_{dn\&train}$ quality factors, especially that of “gfit” (two-fold increase).

We have also included in Table 3 the average additive and multiplicative biases \mathcal{A} and $M/2$ over all 24 sets. Comparing with Table 3 of the Kitching et al. (2012) result paper, we see that “gfit” reached the lowest average additive bias ($\sqrt{\mathcal{A}} = 0.057 \times 10^{-4}$) and the second lowest average multiplicative bias ($M/2 = 0.583 \times 10^{-2}$) of all twelve methods (see also the plot in Figure. 1, page 6 of that paper).

We stress that, contrary to what is suggested in Sect. 4.4 of Kitching et al. (2012), the low overall bias of “gfit” is intrinsic to the method and *does not* result from the application of a denoising step. The DWT-Wiener algorithm was only used in “gfit den”, not “gfit” and actually, the average multiplicative bias of “gfit den” ($M/2 = -2.067 \times 10^{-2}$) is higher than that of “gfit”. Moreover, both methods have similar additive biases. Drawing a more refined conclusion about these biases requires an analysis at individual set level, which we perform in Sect. 4.3.

4.2. Method accuracy

In this section we use the quality factor as a measure of accuracy and assess the influence of:

- Galaxy and PSF characteristics included in the images (size, signal-to-noise, etc.)
- Denoising with the DWT-Wiener algorithm

The quality factors scored for each individual image set are plotted on the left-hand side part of Fig. 2, for each *gfit* variant. They are also quoted in Tables A.1 and A.2.

Due to an editorial mistake, the shear power spectra attributed to “gfit” in the GREAT10 Galaxy Challenge paper, Figure E9, is that from the “fit2-unfold” method. The correct picture was made available at the time of publication and can be found here. We also provide the correct figure in Fig. B.1. We

include the “gfit den” power spectrum in Fig. B.2 as well.

We focus first on the influence of galaxy and PSF features on accuracy. We leave aside the effects of DWT-Wiener denoising for now and thus base our analysis on the results of the “gfit” variant which is devoid of built-in denoising scheme. The data of interest are summarized in Figs. 2 and B.1 and in Tables A.1, A.2.

4.2.1. Influence of Galaxy and PSF characteristics

– **Influence of signal-to-noise ratio:** this is best reflected on the results of the “gfit” variant, since it has no built-in noise correction scheme. All that was done regarding noise was to cut out galaxy and PSF postage stamps to lower dimensions: 12×12 pixels for the PSF and 24×24 pixels for galaxies. As expected, higher S/N yields higher Q factors: we observe a roughly linear progression with a \sim two-fold increase from low $S/N = 10$ to fiducial $S/N = 20$ and a \sim three-fold increase from low $S/N = 10$ to higher $S/N = 40$ (see sets 4 to 12 in Fig. 2).

– **Influence of galaxy size:** as seen from the results of sets 13 to 18 in in Fig. 2), “gfit” seems quite sensitive to galaxy size, the worst Q factors being obtained on smaller galaxies and the best on the larger ones, with a factor ~ 2 difference. The use of postage stamp cut-outs of identical dimensions, regardless of the actual FWHM of the galaxy they contain could be responsible for this effect, as cut-outs with smaller galaxies are likely to be more noise-dominated than those with larger objects. It may also be that the minimizer is less accurate on smaller objects. “Smooth” galaxies have sizes varying according to a Rayleigh distribution (Kitching et al. 2012), so it is not surprising that the Q factors of the corresponding sets 10, 11, 12 take values in between those

of small and large galaxies.

- **Influence of bulge/disc distribution and offset:** having varying b/d ratios (sets 21, 22) seems to decrease accuracy down to the level of small-size galaxies (sets 13, 14). On the other hand, introducing a non-zero 50/50 bulge-to-disc (b/d) offset (sets 21, 22) tends to yield slightly higher accuracy compared to “smooth” galaxies (sets 17, 18). So it seems the single-component galaxy model (see Sect. 2.3) of “gfit” is more sensitive to b/d ratio than to b/d separation. The use of a more sophisticated galaxy model would certainly yield a small gain for some types of galaxies but at the price of an additional computational time for model fitting. On real data, the importance of the b/d distribution and offset will probably depend on the available galaxy sample.
- **Influence of turbulence:** The raw Q factor plot in Fig. 2 does not show a strong impact from the inclusion of a Kolmogorov power spectrum in the PSF ellipticities. We note however a higher score on the fiducial turbulent set compared to the non-turbulent one for no obvious reason. This seems counter intuitive as PSF turbulence usually degrades accuracy and this phenomenon may actually not be related to turbulence.
- **Influence of spatial variability between images:** as described in Kitching et al. (2012), the Galaxy challenge data are divided into so-called “Single epoch”, “Multi-epoch” and “Stable single epoch” depending on whether the intrinsic ellipticities and PSF keep the same or change their spatial distribution between images in a set (see Table 1). It seems that having fixed instead of variable intrinsic ellipticities (“Multi-epoch” sets) slightly decreases accuracy. Apart from this, no clear trend really stands out from the results and it is not clear whether the difference in accuracy is due to the type of spatial variability used or to the specific sample of images chosen for a set. This topic nevertheless deserves to be investigated further in a separate work.

4.2.2. Effect of denoising on accuracy

We discuss in this section the effect on accuracy of the application of the DWT-Wiener denoising scheme described in Sect. 2.7. The influence of denoising can be clearly observed by comparing the plot of “gfit den” (left) with that of “gfit” in Fig. 2 (right). The corresponding scores are also listed in Tables A.1 and A.2.

We find an average two-fold increase in accuracy, the effect being stronger on high S/N images and larger galaxies. Sets with small galaxies are only slightly improved, however. We also notice that the plots of “gfit” and “gfit den” show identical quality factors for low S/N sets 4 to 6. Further investigation showed that denoising was, by mistake, not applied on those sets. This would probably have improved the overall Q factor of “gfit den”.

These results strongly suggest that the DWT-Wiener algorithm really improves the overall accuracy on galaxy shape measurement. We also note that denoising does not alter the quality factor hierarchy between sets: the sets with best scores in the “gfit” plots remain the same in the “gfit den” plot.

4.3. Bias analysis

We investigate in this section how multiplicative and additive biases are affected by galaxy properties and the use of denoising.

4.3.1. Influence of Galaxy and PSF characteristics

To complement the results of Table 3 relative to bias, we have plotted in Figs. 3 and 4 the multiplicative and additive biases of each set. As noted in Sec. 4.1, “gfit den” reached the lowest average additive bias and the second lowest average multiplicative bias of all 12 twelve competing methods.

Focusing on the multiplicative bias and leaving aside the effect of denoising for now, we can make a few observations from the left-hand side plot of Figs. 3.

- **Highest and lowest multiplicative bias:** all multiplicative bias values, except one (set 5), lie below $\mathcal{M}/2 = 3.5 \times 10^{-2}$ in absolute value. The largest biases are found on fiducial set 1 (fixed PSF & variable ellipticities), set 5 (low S/N, fixed PSF) and set 18 (smooth galaxies, fixed PSF). The smallest biases are obtained on set 4 (low S/N, fixed PSF & variable ellipticities), set 17 (smooth galaxies, fixed PSF) and sets 22 to 24 (galaxies with varying b/d ratios and fixed PSF, galaxies with non-zero b/d offset).
- **Influence of signal-to-noise ratio:** the results from sets 1 and 7 suggest, as expected, that multiplicative bias decreases with S/N. The low S/N set 4, however, shows a very small bias. It may be that the true bias is large and positive but that it was offset by e.g. a negative bias due to the contribution of large galaxies in that particular set. The relatively large bias of set 5 compared to sets 4 and 6 may also be an consequence of the PSF having a fixed variation pattern in that set.
- **Influence of galaxy size:** small galaxies (sets 13, 14) and large galaxies (sets 15, 16) have comparable biases in absolute value, smaller galaxies having a positive bias and larger ones a negative bias. A lower bias is reached on “Smooth” galaxy images (set 17), likely because the negative and positive biases of small and large galaxies respectively compensate each others. The bias in set 18 may also have been artificially amplified by the fixed variation pattern of the PSF in that set.
- **Influence of bulge/disc distribution and offset:** letting the b/d ratios of galaxy vary within a set tends to yield a multiplicative bias comparable to that of small-size galaxies, probably causing the decrease in accuracy mentioned in Sect. 4.2. In contrast, the biases associated with a non-zero 50/50 b/d offset are among the lowest. As noted earlier, the underlying single-component Sérsic-based galaxy model of “gfit” (see Sect. 2.3) seems handle quite well profiles with an off-centered bulge and disk.
- **Influence of turbulence:** the introduction of PSF with turbulent ellipticities (set 19) does not induce a particularly significant bias compared to the average.
- **Influence of spatial variability between images:** we note that having “Fixed PSF” and “Fixed intrinsic ellipticity” significantly alters the multiplicative bias, especially on low S/N and smooth galaxy sets. Because all images have the

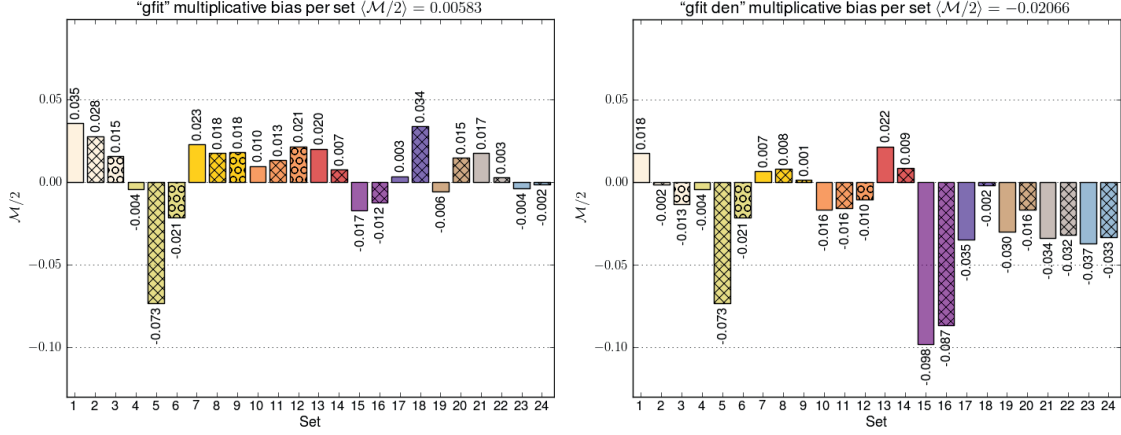


Fig. 3. Multiplicative bias $M/2$ per set. The legend patterns and colors are identical to those of Fig. 2

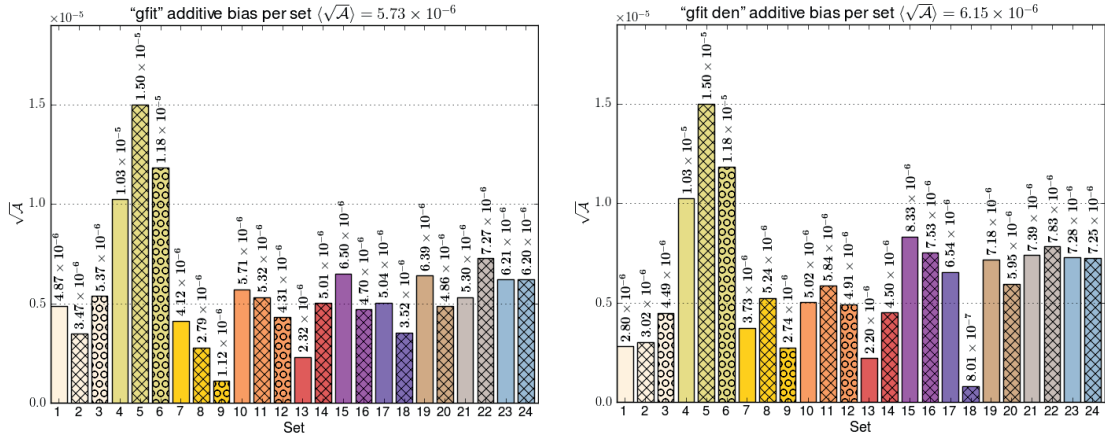


Fig. 4. Additive bias \sqrt{A} per set. The legend patterns and colors are identical to those of Fig. 2

same spatial variation within a set, it is likely that the bias of one image is just amplified as many times as there are images (i.e. 200 times). The effect is particularly strong on image with low S/N (set 5) and smooth galaxies (set 18).

As far as additive bias is concerned, we note the following trend:

- **Highest and lowest additive bias:** “gfit” obtains an additive bias $\sqrt{A} \lesssim 10^{-5}$ on all types of sets, except on the low S/N ones. All values are positive. The lowest bias is reached on small galaxies (sets 13, 14) and the largest on low S/N images (sets 4 to 6).
- **Influence of signal-to-noise ratio:** as for multiplicative bias, we find a trend toward higher biases for lower S/N (sets 1 to 9).
- **Influence of turbulence:** the introduction of a Kolmogorov power spectrum in PSF ellipticity induces a slightly greater additive bias than average (see set 19).

– **Influence of galaxy size:** as for multiplicative bias, we note a tendency of smaller galaxies to have a higher additive bias, as reflected by the values for sets 15 to 18.

– **Influence of bulge/disc distribution and offset:** the additive bias appears larger on galaxies with varying b/d ratios (sets 21, 22) and non-zero b/d offset (sets 23, 24).

4.3.2. Effect of denoising on bias

Comparing the plots for “gfit” and “gfit den” in Figs. 3 and 4, we find that the additive bias does not change significantly, keeping about the same bias values per set. In contrast, the structure of the multiplicative plots is significantly altered.

As seen on the “gfit den” plot, denoising tend to introduce some amount of negative multiplicative bias on all sets. Although the amount of bias on fiducial sets remains roughly the same in absolute value, the DWT-Wiener algorithm clearly impacts the multiplicative bias relative to galaxy size, b/d ratio and turbulence.

As regards galaxy size, even though the multiplicative bias on small galaxies is almost unchanged, that on large galaxies increases about six-fold. Because of that, the bias on “Smooth” galaxies, which also includes large galaxies, also increases.

DWT-Wiener denoising seems to also improve the resolution of the bulge and disk components, so that “*gfit*” has more difficulty fitting its underlying single-component Sérsic model to images with “uniform” and “offset” b/d. The effect is stronger on larger galaxies, causing a \gtrsim tenfold multiplicative bias increase.

Lastly, the introduction of PSF turbulence result in a \sim five-fold multiplicative bias degradation.

Despite the degradation of multiplicative bias on some sets, the accuracy of shape measurements increases two-fold as shown by the corresponding gain in Q factor. We also note that denoising improves the results on sets that already have a high S/N. All in all, the use of denoising is thus clearly beneficial.

5. Conclusions

We have described in this paper the *gfit* shape measurement method, a model-fitting based on a simple Sérsic galaxy model (Sect. 2). The method uses a custom-developed minimizer based on a “coordinate descent” algorithm that finds a local minimum with the lowest χ^2 of the residuals between true and modeled galaxy.

We have also performed an analysis of our results in the GREAT10 Galaxy Challenge (Sect. 3). We participated in the competition with two *gfit* variants: “*gfit* den”, which applied a denoising step before performing model-fitting, and “*gfit*”, which did not use denoising. The noise removal technique employed is DWT-Wiener, a wavelet-based, shape-preserving algorithm particularly suitable for shape measurement. (see Sect. 2.7).

We highlight below the main conclusions of your analysis.

- **Method accuracy:** accuracy improves significantly as S/N gets higher and galaxy size larger. The underlying simple Sérsic-based galaxy model of *gfit* has more difficulty handling galaxies with a non-zero 50/50 offset between bulge and disc. The inclusion of Kolomogorov turbulence in ellipticities is not seen to yield a significant change in accuracy.
- **Additive and multiplicative bias:** the non-denoised “*gfit*” variant reached the lowest average additive bias and second lowest average multiplicative bias of all twelve competing methods. Both additive and multiplicative bias tend to be larger on galaxies with high S/N, smaller size and galaxies with b/d ratio differing from 50/50.
- **Impact of denoising:** the application of the DWT-Wiener noise removal algorithm yields a two-fold improvement in accuracy (Q factor) despite significantly degrading the multiplicative bias on galaxies with a high S/N, small size and significant bulge/disk ratio and separation.

It is interesting to see that, despite the simplicity of the galaxy model used, its results in the Galaxy Challenge established *gfit* as one of the four top-performing methods, both in terms of accuracy and bias. Given that the results were obtained on simulated data, this raises the question of how important having a realistic galaxy model really matters when measuring

galaxy shapes from real data. Providing more clues on this question is one of the objectives of the forthcoming GREAT3 challenge.

Acknowledgements. This work is supported by the Swiss National Science Foundation (SNSF). Many thanks to Tom Kitching for his help and for sharing the shear analysis code. We also thank the GREAT10 Coordination Team for organizing this stimulating challenge. GREAT10 was sponsored by a EU FP7 PASCAL 2 challenge grant. We also acknowledge support from the International Space Science Institute (ISSI) in Bern, where some of this research has been discussed.

References

- Abramowitz, M. & Stegun, I. A. 1965, Handbook of Mathematical Functions, 1st edn., Dover books on mathematics (Dover Publications)
- Anderson, E., Bai, Z., Dongarra, J., et al. 1990, in Proceedings of the 1990 ACM/IEEE conference on Supercomputing, Supercomputing '90 (Los Alamitos, CA, USA: IEEE Computer Society Press), 2–11
- Arce, G. 2005, Nonlinear Signal Processing: A Statistical Approach, Wiley InterScience online books (Wiley-Interscience)
- Arias-Castro, E. & Donoho, D. L. 2009, The Annals of Statistics, 37, 1172
- Bacon, D. J., Refregier, A. R., & Ellis, R. S. 2000, ApJS, 318, 625
- Bartelmann, M. & Schneider, P. 2001, Phys. Rep., 340, 291
- Bernstein, G. M. & Jarvis, M. 2002, AJ, 123, 583
- Bertin, E. & Arnouts, S. 1996, A&AS, 117, 393
- Bonnans, J. F., Gilbert, Lemaréchal, C., & Sagastizábal, C. 2006, Numerical Optimization – Theoretical and Practical Aspects, Universitext (Springer Verlag, Berlin)
- Bridle, S., Balan, S. T., Bethge, M., et al. 2010, MNRAS, 405, 2044
- Bridle, S., Shawe-Taylor, J., Amara, A., et al. 2008, ArXiv eprints, 3, 11
- Bruce, A. G., Donoho, D. L., Gao, H.-y., & Martin, R. D. 1994, Denoising and Robust Non-Linear Wavelet Analysis, Vol. 2242, 325–36
- Ciotti, L. 1991, A&A, 249, 99
- Ciotti, L. & Bertin, G. 1999, Astronomy & Astrophysics, 3, 2
- Community, S. 2010, October, 1
- Forum, M. P. I. 1995, Message Passing Interface Forum
- Forum, M. P. I. 1998, International Journal of High Performance Computing Applications, 12, 1
- Graham, A. W. & Driver, S. P. 2005, Publications of the Astronomical Society of Australia, 22, 11
- Heymans, C., Van Waerbeke, L., Bacon, D., et al. 2006, MNRAS, 368, 1323
- Hirata, C. & Seljak, U. 2003, MNRAS, 343, 459
- Hoekstra, H., Franx, M., Kuijken, K., & Squires, G. 1998, ApJ, 504, 636
- Hoekstra, H. & Jain, B. 2008, Annual Review of Nuclear and Particle Science, 58, 99
- Huterer, D. 2010, General Relativity and Gravitation, 42, 2177
- Huterer, D., Takada, M., Bernstein, G., & Jain, B. 2006, MNRAS, 366, 101
- Jones, E., Oliphant, T., Peterson, P., et al. 2001–, SciPy: Open source scientific tools for Python
- Kaiser, N., Squires, G., & Broadhurst, T. 1995, ApJ, 449, 460
- Kaiser, N., Wilson, G., & Luppino, G. A. 2000, arXiv:astro-ph/0003338
- Khreedde, A., Benmahammed, K., & Puech, W. 2007, Adv. Eng. Softw., 38, 513
- Kitching, T., Amara, A., Gill, M., et al. 2011, Ann.Appl.Stat., 5, 2231
- Kitching, T. D., Balan, S. T., Bridle, S., et al. 2012, MNRAS, 423, 3163
- Kitching, T. D., Miller, L., Heymans, C. E., van Waerbeke, L., & Heavens, A. F. 2008, MNRAS, 390, 149
- Levenberg, K. 1944, The Quarterly of Applied Mathematics, 2, 164
- Luppino, G. A. & Kaiser, N. 1997, ApJ, 475, 20
- Maoli, R., Van Waerbeke, L., Mellier, Y., et al. 2001, A&A, 368, 766
- Marquardt, D. W. 1963, Journal of the Society for Industrial and Applied Mathematics, 11, 431
- Massey, R., Heymans, C., Bergé, J., et al. 2007, MNRAS, 376, 13
- Miller, L., Kitching, T. D., Heymans, C., Heavens, A. F., & van Waerbeke, L. 2007, MNRAS, 382, 315
- Munshi, D., Valageas, P., van Waerbeke, L., & Heavens, A. 2008, Phys. Rep., 462, 67
- Nelder, J. A. & Mead, R. 1965, The Computer Journal, 7, 308
- Nocedal, J. & Wright, S. 1999, Numerical Optimization, Springer Series in Operations Research (Springer)
- Nurbaeva, G., Courbin, F., Gentile, M., & Meylan, G. 2011, A&A, 531, 144
- Nurbaeva, G., Courbin, F., Gentile, M., & Meylan, G. in prep.
- Patil, A., Huard, D., & Fonnesbeck, C. J. 2010, Journal Of Statistical Software, 35, 1

M. Gentile, F. Courbin and G. Meylan: A simple fitting method (*gfir*) for galaxy shape measurement in weak lensing surveys

- Powell, M. 1964, *The Computer Journal*, 7, 155
- Refregier, A. & Bacon, D. 2003, *MNRAS*, 338, 48
- Sérsic, J. L. 1968, Cordoba
- Tewes, M., Cantale, N., Courbin, F., Kitching, T., & Meylan, G. 2012, *A&A*, 544, A8
- Trujillo, I., Erwin, P., Ramos, A. A., & Graham, A. W. 2004, *Camera*, 127, 1917
- Van Waerbeke, L., Mellier, Y., Erben, T., et al. 2000, *A&A*, 358, 30
- Vetterli, M. & Kovacevic, J. 1995, *Wavelets and Subband Coding* (Prentice Hall Signal Processing Series) (Prentice Hall PTR)
- Wiener, N. 1949, *Extrapolation, Interpolation, and Smoothing of Stationary Time Series* (MIT Press)
- Wittman, D. M., Tyson, J. A., Kirkman, D., Dell'Antonio, I., & Bernstein, G. 2000, *Nature*, 405, 143
- Zhu, C., Byrd, R. H., Lu, P., & Nocedal, J. 1997, *ACM Transactions on Mathematical Software*, 23, 550

Table A.1. “gfit”: results per set. Sets with S/N 10, 40 are respectively highlighted in orange and blue. Fiducial sets with S/N 20 are represented in green and all remaining sets also have a S/N of 20.

Set	Q	Q_{dn}	$Q_{dn\&train}$	$M/2 \times 10^{-2}$	$\sqrt{\mathcal{A}} \times 10^{-4}$
1	28.26	50.44	205.57	+3.542	+0.0487
2	41.98	78.50	352.54	+2.770	+0.0347
3	31.60	77.86	411.57	+1.539	+0.054
4	17.01	38.11	114.55	-0.432	+0.103
5	18.71	34.41	89.59	-7.345	+0.150
6	14.95	31.32	63.61	-2.136	+0.118
7	100.75	450.35	111.06	+2.270	+0.041
8	120.18	308.43	143.61	+0.176	+0.028
9	82.27	185.17	184.27	+1.780	+0.011
10	39.72	89.40	319.88	+0.964	+0.057
11	35.49	81.86	357.68	+1.327	+0.053
12	35.74	86.16	348.86	+2.141	+0.043
13	48.10	121.62	215.05	+2.010	+0.023
14	44.70	114.73	254.17	+0.740	+0.050
15	72.48	155.84	193.04	-1.732	+0.065
16	87.13	245.81	135.62	-1.238	+0.047
17	52.88	125.30	246.64	+0.334	+0.050
18	44.95	117.64	180.68	+3.366	+0.035
19	58.01	113.55	284.16	-0.593	+0.064
20	44.52	90.47	436.67	+1.465	+0.049
21	39.32	73.23	291.54	+1.732	+0.053
22	35.65	67.33	345.03	+0.271	+0.073
23	54.12	105.81	339.60	-0.382	+0.062
24	54.15	102.45	372.16	-0.164	+0.062
All	50.11	122.74	249.88	+0.583	+0.057

Table A.2. “gfit den”: results per set. Sets with S/N 10, 40 are respectively highlighted in orange and blue. Fiducial sets with S/N 20 are represented in green and all remaining sets also have a S/N of 20.

Set	Q	Q_{dn}	$Q_{dn\&train}$	$M/2 \times 10^{-2}$	$\sqrt{\mathcal{A}} \times 10^{-4}$
1	56.20	182.89	269.98	+1.761	+0.028
2	96.00	316.69	291.60	-0.154	+0.030
3	61.98	271.56	272.04	-1.321	+0.045
4	17.01	38.11	59.06	-0.432	+0.103
5	18.71	34.41	54.09	-7.345	+0.150
6	14.95	31.32	45.34	-2.136	+0.118
7	251.08	518.17	143.08	+0.671	+0.037
8	471.69	203.29	108.09	+0.821	+0.052
9	204.28	503.64	156.95	+0.137	+0.027
10	83.59	303.87	269.16	-1.647	+0.050
11	62.04	162.31	285.93	-1.556	+0.058
12	68.65	258.49	412.10	-1.022	+0.049
13	51.27	165.24	259.73	+2.166	+0.022
14	45.73	127.28	258.15	+0.863	+0.045
15	101.04	100.83	85.12	-9.790	+0.083
16	98.26	101.14	94.13	-8.678	+0.075
17	122.36	207.82	266.86	-3.468	+0.065
18	108.10	264.72	204.89	-0.202	+0.008
19	98.59	154.86	286.79	-0.301	+0.072
20	91.17	198.34	548.31	-1.640	+0.059
21	93.58	158.18	257.46	-3.363	+0.074
22	71.84	137.44	327.12	-3.189	+0.078
23	97.43	144.90	265.60	-0.037	+0.073
24	105.79	163.57	278.86	-3.339	+0.072
All	103.81	197.88	229.19	-2.067	+0.061

Appendix A: Accuracy and bias per set

Tables A.1 and A.2 respectively quote the actual quality factor and bias values reached by the non-denoised and denoised variants of the *gfit* shape measurement method.

Appendix B: Sear power spectra

Figs B.1 and B.2 respectively show the shear power spectra of the non-denoised and denoised variants of *gfit* submitted in the GREAT10 galaxy Challenge.

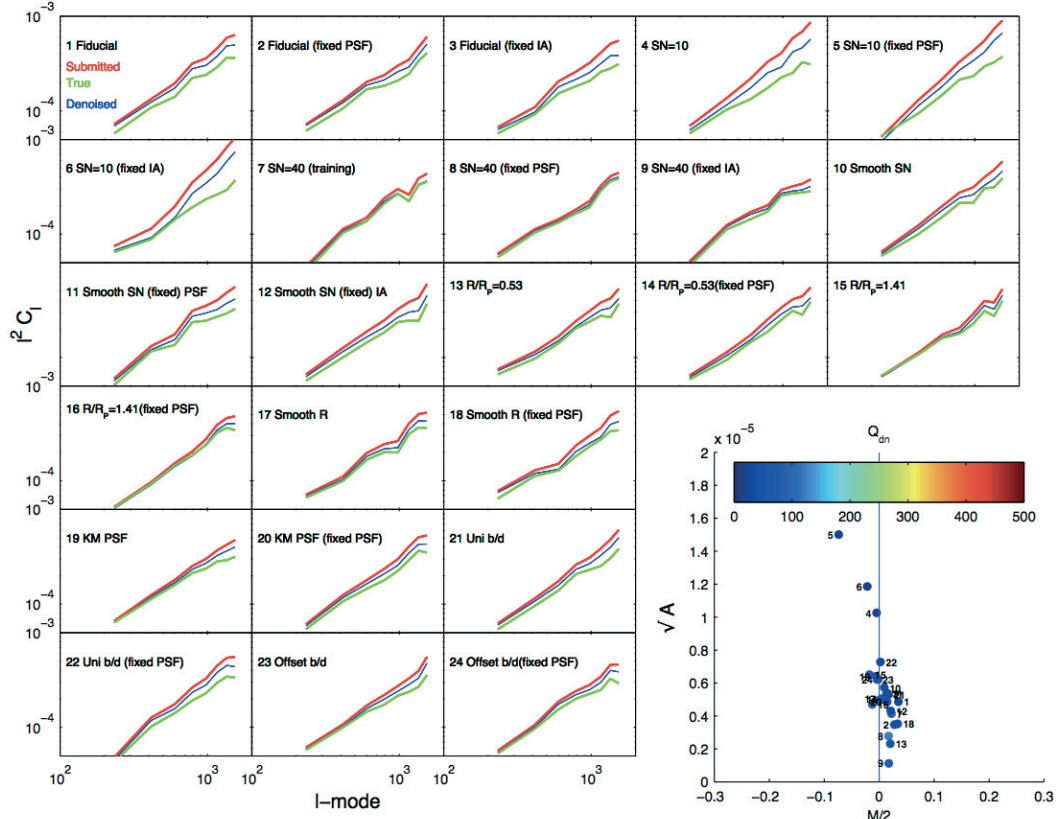


Fig. B.1. The shear power spectra of the “gfit” variant over the 24 sets of the Galaxy challenge. The red lines denote the estimated shear power spectra while the green lines represents the true shear power. The blue lines indicate the spectra after application of pixel-level denoising (not DWT-Wiener denoising). The code run to plot these power spectra is identical to that used in the (Kitching et al. 2012) paper. Note that the power spectra attributed to “gfit” in the Figure E9 of (Kitching et al. 2012) are actually those of the “fit2-unfold” method.

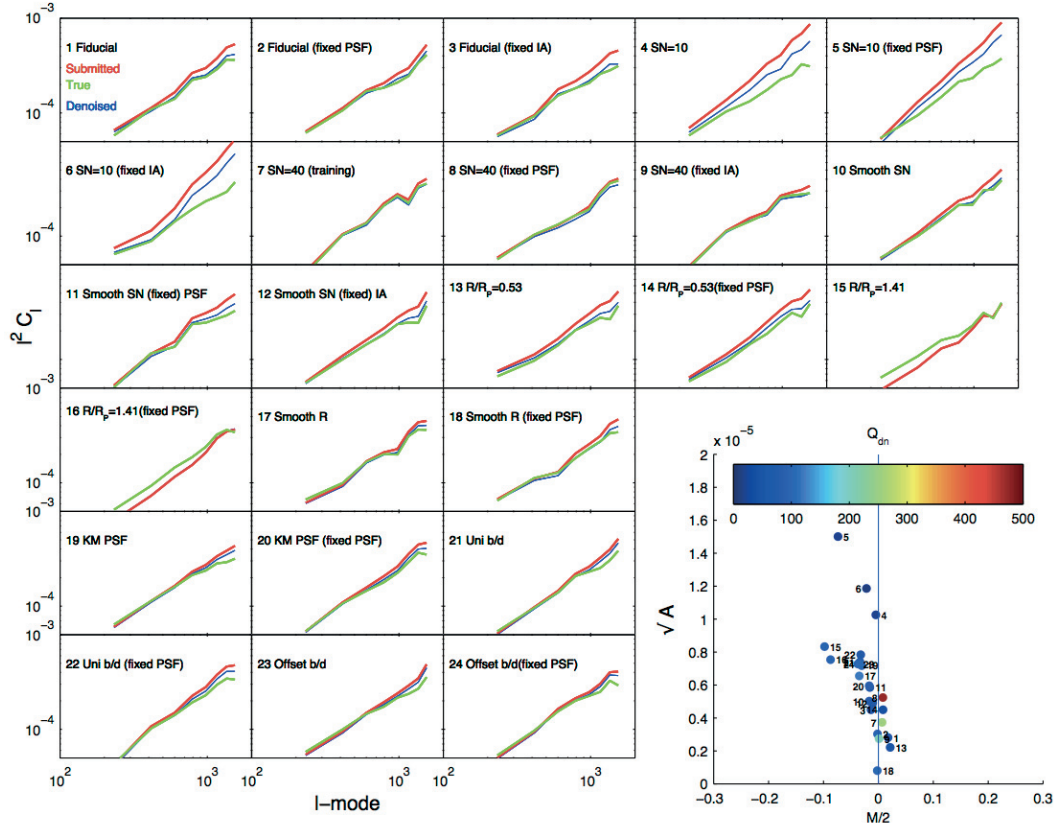


Fig. B.2. The shear power spectra of the “gfit den” variant over the 24 sets of the Galaxy challenge. This variant has a preliminary denoising step using the DWT-Wiener algorithm. The red lines denote the estimated shear power spectra while the green lines represents the true shear power. The blue lines indicate the spectra after application of pixel-level denoising (not DWT-Wiener denoising). The code run to plot these power spectra is identical to that used in the (Kitching et al. 2012) paper.

4.4.4 Image decomposition with Shapelets

“Shapelet” is the name given to the basis function used to decompose a 2D object (shape inferred from surface brightness distribution or whole image) in terms of Hermite or Laguerre polynomials (e.g., Abramowitz & Stegun 1965). The basis functions is also referred to as “Gaussian-Hermite” or “Gaussian-Laguerre” because they involve the Gaussian function $\exp(-x^2/2)$ and can be interpreted as perturbations around a circular Gaussian. They form a complete set of smooth, integrable, orthonormal basis functions of two variables (Refregier 2003a; Refregier & Bacon 2003; Massey & Refregier 2005; Massey et al. 2005; Kuijken 2006).

A method implementing the Shapelet formalism will analytically decompose the galaxy images into a truncated series of orthogonal polynomials. It then becomes possible to manipulate the image by altering the coefficients of each Shapelet polynomial basis. Useful applications are: PSF correction, depixelation, noise reduction and shear measurement. It is also possible, for instance, to derive the image flux and the various central moments from a Shapelet decomposition. One of the advantages of using an orthogonal basis is that each coefficient in a basis can be independently manipulated without altering the others.

Shapelets come in two variants, “cartesian” and “polar”, depending on the coordinate system chosen. The choice of one or another depends on the situation.

Cartesian Shapelets

In a 2D cartesian coordinate system, the dimensional basis functions are of the form

$$B_{\mathbf{n}}(\mathbf{x}; \beta) = \frac{1}{\beta} \phi_{\mathbf{n}}\left(\frac{\mathbf{x}}{\beta}\right) \quad (4.25)$$

with

$$\phi_{\mathbf{n}}(\mathbf{x}) = \phi_{n_1}(x_1) \phi_{n_2}(x_2) \quad \mathbf{x} = (x_1, x_2) \quad \mathbf{n} = (n_1, n_2) \quad (4.26)$$

and

$$\phi_n(x) = \left[2^n \pi^{\frac{1}{2}} n!\right]^{-\frac{1}{2}} H_n(x) e^{-\frac{x^2}{2}} \quad (4.27)$$

The quantity β represents the characteristic scale of the Shapelet, typically close to the size or radius of the object and $\phi_{\mathbf{n}}(x)$ is the dimensionless basis function. $H_n(x)$ is a Hermite polynomial of order n . The basis functions $B_{\mathbf{n}}(\mathbf{x}; \beta)$ are orthogonal, that is

$$\int_{\mathbb{R}} \int_{\mathbb{R}} B_{\mathbf{n}}(\mathbf{x}; \beta) B_{\mathbf{m}}(\mathbf{x}; \beta) d^2x = \delta_{n_1 m_1} \delta_{n_2 m_2} \quad (4.28)$$

where δ_{ij} denotes the Kronecker symbol.

A sufficiently well-behaved 2D object represented by a function $f(\mathbf{x})$ can then be expanded as

$$f(\mathbf{x}) = \sum_{n_1, n_2=0}^{\infty} f_{\mathbf{n}} B_{\mathbf{n}}(\mathbf{x}; \beta) \quad (4.29)$$

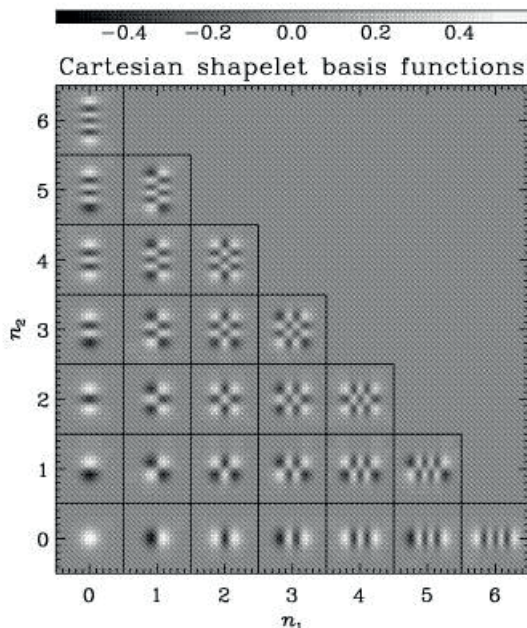


Figure 4.6: The basis functions, up to order $n_{max} = 6$, parametrized by two integers n_1, n_2 (Massey & Refregier 2005).

the coefficients f_n being given by

$$f_n = \int_{\mathbb{R}} \int_{\mathbb{R}} f(\mathbf{x}) B_n(\mathbf{x}; \beta) d^2 x \quad (4.30)$$

In practice the series expansion (4.29) will be truncated at a finite order $n_1 + n_2 \leq n_{max}$. The expansion will converge fast enough provided the object $f(\mathbf{x})$ is sufficiently localized and if the scale β and the origin of $\mathbf{x} = \mathbf{0}$ are not too different from the size and location of the object respectively. An appropriate choice for these values should then produce a faithful representation of an object with a minimum number of Shapelet coefficients. How to find the optimal values for objects of different shapes and size is one key issue to address when implementing a Shapelet-based method. The first 28 basis functions of a Cartesian SAhapelet are plotted in Fig. fig:cartesian shapelets.

Polar Shapelets

Polar Shapelets are the equivalents of cartesian Shapelets, but expressed in polar coordinates (r, θ) . A variant of the same formalism was also independently proposed by Bernstein & Jarvis (2002). The use of polar coordinates makes the basis function separable in r and θ , which may make them more intuitive and convenient to use in practice. Instead of Gaussian-Hermite polynomials H_{n_l, n_r} , polar Shapelets use Gauss-Laguerre polynomials $L_{n_l}^{n_r}$, but both polynomials are related by

$$H_{n_l, n_r}(x) = (-1)^{n_l} (n_l!) x^{n_r - n_l} L_{n_l}^{n_r - n_l}(x^2) \quad (n_r, n_l) \in \mathbb{N}^2, (n_r > n_l \geq 0) \quad (4.31)$$

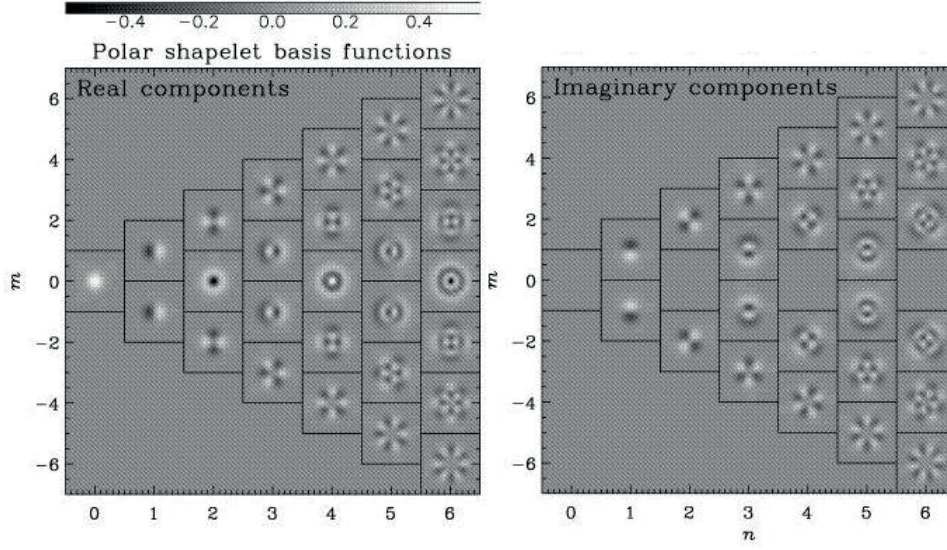


Figure 4.7: The first few polar Shapelets basis functions $\chi_{n,m}$. The real components of the Shapelet basis functions are plotted in the top panel and the imaginary components in the bottom panel (Massey & Refregier 2005).

Letting $n = n_r + n_l$ and $m = m_r - m_l$, the 2D polar Shapelet basis functions are

$$\chi_{n,m}(r, \theta; \beta) = \frac{(-1)^{\frac{n-m}{2}}}{\beta^{|m|+1}} \left[\frac{\left(\frac{n-|m|}{2}\right)!}{\pi \left(\frac{n+|m|}{2}\right)!} \right]^{1/2} r^{|m|} L_{(n-|m|)/2}^{|m|} \left(\frac{r^2}{\beta^2} \right) e^{-\frac{r^2}{2\beta^2}} e^{-im\theta} \quad (4.32)$$

The index n describes the total number of oscillations (spatial frequency) and also the radius of the basis function; the index m represents the degree of rotational symmetry of the basis function. m can be any integer between $-n$ and $+n$ in steps of 2.

Therefore the basis functions with $m = 0$ are rotationally invariant and their use would be sufficient to describe a circularly symmetric object. Basis functions with $|m| = 1$ are invariant only under rotation of a 2π radians angle.

The corresponding coefficients describe the location of the object centroid, the real and imaginary parts representing respectively relative displacements towards the x or y direction in complex space. At the next higher order, $|m| = 2$, the basis functions are invariant under angle rotation of π radians and become negative representations of themselves under rotations of $\pi/2$ radians; They represent ellipses. The first few polar Shapelets basis functions $\chi_{n,m}$ are shown in Fig. 4.7.

Expression (4.32) allows the decomposition of a well behaved function using the expression

$$f(r, \theta) = \sum_{n=0}^{\infty} \sum_{m=-n}^n f_{n,m} \chi_{n,m}(r, \theta; \beta) \quad (4.33)$$

The Polar Shapelet coefficients are then given by

$$f_{n,m} \int_{\mathbb{R}} \int_{\mathbb{R}} f(r, \theta) \chi_{n,m}(r, \theta; \beta) r dr d\theta \quad (4.34)$$

For practical reasons, as for cartesian Shapelets, the series expansion in terms of polar Shapelets is truncated at some order $n \leq n_{\max}$. An expansion using low m indice is already capable, in principle, of giving a good representation of a typical galaxy.

Shear measurement

The operation of convergence and shear take a simple form when expressed in terms of Shapelets. They allow to construct a more accurate shear estimator that supersedes the ellipticity shear estimator: the location of the centroid, flux and all the information about a shape can be parametrized using Shapelets, not only the second order ellipticity like in KSB variants. Moreover, various higher-level shear estimators can be formed from combinations of Shapelet estimators.

Assuming the unlensed surface brightness of a galaxy is described by the 2D function $f(\mathbf{x})$, it has been shown (Refregier 2003a) that the lensed surface brightness $f'(\mathbf{x})$ is given to first order after a weak shear $\boldsymbol{\gamma} = (\gamma_1, \gamma_2)$ by

$$f'(\mathbf{x}) \simeq (1 + \gamma_i \hat{S}_i) f(\mathbf{x}) \quad (4.35)$$

where \hat{S} is the shear operator. Using (4.33), f' can then be expanded in terms of cartesian Shapelets, and it is found that unlensed and lensed coefficients are related by

$$f'_n = (\delta_{nm} + \gamma_i S_{inm}) f_m \quad (4.36)$$

where

$$S_{inm} = \int_{\mathbb{R}} \int_{\mathbb{R}} B_n(\mathbf{x}; \beta) \hat{S}_i B_m(\mathbf{x}; \beta) d^2 x \quad (4.37)$$

is known as the ‘‘shear matrix’’. One can then form the following pair of shear estimators

$$\tilde{\Upsilon}_{1n} = \frac{f'_n - \langle f_n \rangle}{S_{1nm} \langle f_m \rangle} \quad n_1, n_2 \text{ even} \quad (4.38)$$

$$\tilde{\Upsilon}_{2n} = \frac{f'_n - \langle f_n \rangle}{S_{2nm} \langle f_m \rangle} \quad n_1, n_2 \text{ odd} \quad (4.39)$$

The angle brackets denote averaging over a large enough population of galaxies where the effective mean shear is zero. Combinations of estimators $\tilde{\Upsilon}_{in}$ can be used to construct high-level estimators. One example is the weighted estimator

$$\tilde{\Upsilon}_i = \frac{\sum_n w_{in} \tilde{\Upsilon}_{in}}{\sum_n w_{in}} \quad (4.40)$$

PSF modeling and correction

The goal is to obtain the deconvolve coefficients of a galaxy image and use them to form the shear estimators described by equations (4.38) and (4.39).

Convolution in the Shapelet formalism The convolution product function h of two functions f and g having respective scales α , β and γ is

$$h(\mathbf{x}) = f(\mathbf{x}) \star g(\mathbf{x}) = \int \int f(\mathbf{x} - \mathbf{x}') g(\mathbf{x}') d^2 x \quad (4.41)$$

As shown in Refregier (2003), the convolved coefficients h_n can be expressed in terms of the unconvolved coefficients f_n and g_n by

$$h_n = \sum_{ml} C_{nml} f_m g_l \quad (4.42)$$

Where $C_{nml} = C_{nml}(\alpha, \beta, \gamma)$ is the 2D ‘‘convolution tensor’’, which can be written in terms of a product of 1D convolution tensors $C_{nml}(\alpha, \beta, \gamma)$ as

$$C_{nml}(\alpha, \beta, \gamma) = C_{n_1 m_1 l_1}(\alpha, \beta, \gamma) C_{n_2 m_2 l_2}(\alpha, \beta, \gamma) \quad (4.43)$$

where

$$C_{nml}(\alpha, \beta, \gamma) = \sqrt{2\pi} (-1)^n i^{n+m+l} B_{nml}^{(3)}(\alpha^{-1}, \beta^{-1}, \gamma^{-1}) \quad (4.44)$$

with

$$\begin{aligned} B_{nml}^{(3)}(a_1, a_2, a_3) &= \int_{\mathbb{R}} B_l(x, a_1) B_m(x, a_2) B_n(x, a_3) dx \\ &= v \left[2^{l+m+n-1} \sqrt{\pi} l! m! n! a_1 a_2 a_3 \right] L_{lmn} \left(\sqrt{2} \frac{v}{a_1}, \sqrt{2} \frac{v}{a_2}, \sqrt{2} \frac{v}{a_3} \right) \end{aligned} \quad (4.45)$$

and $v = a_1^{-2} + a_2^{-2} + a_3^{-2}$, the expression for L_{lmn} being given by recurrence by

$$L_{l+1,m,n} = 2l(a^2 - 1) L_{l-1,m,n} + 2mab L_{l,m-1,n} + 2nac L_{l,m,n-1} \quad L_{0,0,0} = 1 \quad (4.46)$$

and similarly for $L_{l,m+1,n}$ and $L_{l,m,n+1}$.

PSF correction approaches Two approaches have been used for PSF correction:

- Straight inversion of the convolution matrix
- Convolution and fitting of a PSF model

The most intuitive technique is to extract the original unconvolved coefficients through matrix inversion (Refrégier & Bacon 2003). Equation (4.42) can be expressed as

$$h_n = \sum_m P_{nm} f_m \quad (4.47)$$

having defined the so-called “PSF matrix” as

$$P_{nm} = \sum_l C_{nml} g_l \quad (4.48)$$

Inverting the PSF matrix then gives the unconvolved coefficients f_m , i.e.

$$f_m = P_{nm}^{-1} h_n \quad (4.49)$$

This procedure assumes the matrix P_{nm} is invertible, but unfortunately this is not the case in common situations: high-order modes with high frequency oscillations are usually strongly altered by convolution and the PSF matrix typically only includes small values for these high-order modes. As a result, P_{nm} may not be invertible. One can make it invertible but at the cost of only keeping low enough modes. This amounts to eliminate from the reconstruction all relevant information encoded within high-order modes. Another drawback is that inversion algorithms are often numerically unstable. Melchior et al. (2009) claim, however, they have succeeded in developing a deconvolution method that overcomes these problems.

Instead the following method is preferred, as it only involves a convolution operation (not a deconvolution) and no matrix inversion (Kuijken 1999; Massey & Refregier 2005):

1. The observed galaxy image is decomposed into a set of basis function (here Shapelet functions) and a model of unconvolved galaxy is constructed.
2. A model convolution kernel is defined as well (e.g. from stars) and then decomposed into basis function the same way.
3. The model galaxy image obtained in (1) is then convolved with the model kernel of (2) until the convolution product model \star PSF best fits the observed galaxy image. This process yields the basis coefficients of the galaxy prior to convolution.
4. An approximation of the unconvolved image is then made by series expanding the coefficients obtained in (3) with the basis function obtained in (1).

Noise reduction

No provision for noise reduction is built into the Shapelet formalism. Noise is a serious issue with Shapelet-based methods: they are in most cases able to model shape information very well (although see Melchior et al. (2010)) but this turns against them because also faithfully reproduce noise patterns in images with low signal to noise ratio (Melchior et al. 2009). One way to reduce this "overfitting" is to reduce the order of expansion but this comes at the price of a lower accuracy.

Strength

- Flexibility and accuracy in analytically describing shapes
- The decomposition approach provides a way to analyze and manipulate an image with great accuracy. Operations such as pixelation, convolution and shear can be expressed in terms of Shapelets. The effect of shear can be measured on different basis coefficients which allows, in theory a more precise estimation. Usual information such as centroid location, central moments to any order and flux can be derived.
- Shapelets also provide a solution to the PSF interpolation problem: the PSF can be

modeled as Shapelets. The corresponding coefficients can then be interpolated at a new position and the PSF reconstructed using these new coefficients. This scheme has been successfully applied to several weak lensing cluster studies (Jee et al. 2005a,b, 2006, 2007b; Bergé et al. 2008; Romano et al. 2010). However, it has been argued (Jee et al. 2007a; Melchior et al. 2010) that even a high-order Shapelet-based PSF model is unable to reproduce extended PSF features (such as its wings) and that the flexibility of the model makes it vulnerable to pixelation and noise. So, although the level of residual errors after Shapelet decomposition appears low enough for cluster analysis, it may prove too high for precision cosmic shear measurement.

- Shapelets can be simply expressed and easily manipulated in Fourier space.

Weaknesses

- Sensitivity to noise (overfitting) as previously explained: Shapelets tend to reproduce noise patterns in data with low signal to noise ratio. Unless noise is reduced by some other technique, the only way to address this seems to reduce the order of expansion and chose a scale that is not too fine-grained. But this goes against accuracy.
- Another issue lies in the optimal choice of the scale parameter β and the order of expansion n_{\max} . Shapelets implementations usually determine n_{\max} by some significance measure of the model (Massey & Refregier 2005; Melchior et al. 2007) or fix n_{\max} at a value which seems reasonable to capture the general features of the shape (Refregier & Bacon 2003; Kuijken 2006).
- Melchior et al. (2010) have questioned the ability of the Shapelet method to provide weak-lensing measurements for all types of observable galaxies with an accuracy demanded by upcoming missions and surveys. They have found in particular that highly-elliptical galaxy shapes cannot be accurately modeled within the circular Shapelet basis system and are biased towards less elongated shapes.
- The shapelet method is known to be slow compared to other image analysis techniques.

4.4.5 Bayesian shear estimation with lensfit

General approach

The description of lensfit given here is mostly based on the papers from (Miller et al. 2007; Kitching et al. 2008). For the latest enhancements to the methods, refer to Miller et al. (2013).

Not unlike KSB/KSB+, the idea behind the lensfit method is to quantify the effect of shear on galaxy shapes from the measurement of ellipticities. However, lensfit differs from KSB/KSB+ in important respects. Firstly, it uses the definition of ellipticity (4.11) and the relation between unlensed and lensed ellipticity given by (4.14). It is assumed that ϵ is a good estimator of ellipticity e , so that (4.14) yields, for $|\mathbf{g}| < 1$,

$$\mathbf{e} = \frac{\mathbf{e}^{src} + \mathbf{g}}{1 + \mathbf{g}^* \mathbf{e}^{src}} \quad (4.50)$$

where \mathbf{e}^{src} denotes the intrinsic ellipticity and the symbol $*$ complex conjugation. The method also relies on $\langle \epsilon \rangle \approx \langle \mathbf{e}^{src} \rangle \approx \mathbf{0}$ for a large enough sample averaging and uses the shear estimator in ϵ given by (4.17).

4.4. A closer look at some shear measurement methods

Secondly, and more specifically, lensfit attempts to measure $\langle \mathbf{e} \rangle$ by adopting a Bayesian approach. So, instead of calculating the expectation value of ellipticity over a population of \mathcal{N} galaxies with probability distribution in ellipticity $f(\mathbf{e})$ as

$$\langle \mathbf{e} \rangle = \int \mathbf{e} f(\mathbf{e}) d\mathbf{e} \quad (4.51)$$

the application of the Bayesian formalism gives

$$\langle \mathbf{e} \rangle = \frac{1}{\mathcal{N}} \sum_i \int \mathbf{e} p_i(\mathbf{e} | \mathbf{y}_i) d\mathbf{e} = \frac{1}{\mathcal{N}} \int \mathbf{e} \sum_i p_i(\mathbf{e} | \mathbf{y}_i) d\mathbf{e} \quad (4.52)$$

In the above expression, the vector \mathbf{y}_i contains the pixel values for the surface brightness distribution of an individual galaxy and

$$p_i(\mathbf{e} | \mathbf{y}_i) = \frac{\mathcal{P}(\mathbf{e}) \mathcal{L}(\mathbf{y}_i | \mathbf{e})}{\int \mathcal{P}(\mathbf{e}) \mathcal{L}(\mathbf{y}_i | \mathbf{e}) d\mathbf{e}} \quad (4.53)$$

is the posterior probability in ellipticity. In that expression,

$$\mathcal{P}(\mathbf{e}) = \left\langle \frac{1}{\mathcal{N}} \sum_i p_i(\mathbf{e} | \mathbf{y}_i) \right\rangle \quad (4.54)$$

is the prior probability distribution of intrinsic ellipticities and $\mathcal{L}(\mathbf{y}_i | \mathbf{e})$ is the likelihood of obtaining \mathbf{y}_i given the intrinsic (unlensed) ellipticity \mathbf{e} of galaxy i .

Starting with a prior that is a good representation of the intrinsic distribution of ellipticities should produce an unbiased estimated posterior probability distribution, from which the shear can be deduced. Remains to evaluate the prior $\mathcal{P}(\mathbf{e})$ and the likelihood $\mathcal{L}(\mathbf{y}_i | \mathbf{e})$.

Finding the prior

The correct prior cannot be known in advance and a prior that contains a zero shear is used as a starting point. The assumption of a zero shear is wrong, however, and a correcting factor of the form $\partial \langle \mathbf{e} \rangle_i / \partial \mathbf{g}$, called the “shear sensitivity” must be applied to correct the expectation values of ellipticity (4.51) for individual galaxies. The Bayesian shear estimator

$$\hat{\mathbf{g}} = \frac{\sum_i^n \langle \mathbf{e} \rangle_i}{\sum_i^n |\partial \langle \mathbf{e} \rangle_i / \partial \mathbf{g}|} \quad (4.55)$$

is therefore used instead of (4.17). The $\hat{\mathbf{g}}$ value for an individual galaxy should lie in the range $0 < \partial \langle \mathbf{e} \rangle_i / \partial \mathbf{g} \leq 1$ and for a measurement completely dominated by noise, $\partial \langle \mathbf{e} \rangle_i / \partial \mathbf{g} \approx 0$.

To first order

$$\frac{\partial \langle \mathbf{e} \rangle_i}{\partial \mathbf{g}} \simeq 1 - \frac{\int (\langle \mathbf{e} \rangle - \mathbf{e} \mathcal{L}(\mathbf{e}) \frac{\partial \mathcal{P}(\mathbf{e})}{\partial \mathbf{e}} d\mathbf{e})}{\int \mathcal{P}(\mathbf{e}) \mathcal{L}(\mathbf{e}) d\mathbf{e}} \quad (4.56)$$

which gives an estimate of $\hat{\mathbf{g}}$. The prior $\mathcal{P}(\mathbf{e})$ in (4.56) is evaluated using an iterative method based on equation (4.53)

$$\mathcal{P}(\mathbf{e})_{i+1} = \left\langle \frac{1}{\mathcal{N}} \sum_i p_i(\mathbf{e} | \mathbf{y}_i) \right\rangle \quad (4.57)$$

that is repeated over i iterations over the \mathcal{N} galaxies of the population. After each step, the prior $\mathcal{P}(\mathbf{e})_{i+1}$ on the left-hand side should become closer to the true prior.

In practice, lensfit assumes for the prior a functional of the form

$$\mathcal{P}(\mathbf{e}) = \mathcal{P}(e_1, e_2) = A \cos\left(\frac{|\mathbf{e}| \pi}{2}\right) \exp\left[-\left(\frac{2|\mathbf{e}|}{B(1+|\mathbf{e}|^D)}\right)^C\right] \quad (4.58)$$

whose free parameters B , C , D are fitted by (4.57). The prior is always normalized and the value of the parameter A is fixed by normalization. The cosine factor ensures the prior goes to zero as $|\mathbf{e}|$ comes closer to 1.

Finding the likelihood

The likelihood is found by fitting a de Vaucouleurs profile to each galaxy image¹. This choice is justified by arguing that, for faint galaxies, de Vaucouleurs and exponential profiles are indistinguishable. The model depends on six free parameters: positions x and y , ellipticity components e_1 and e_2 , surface brightness and a scale factor. By working in Fourier space, the brightness and positions can be marginalized over analytically and the radius, numerically. What is left is a likelihood as a function of ellipticity, which can be inserted in equation (4.56) to calculate the shear estimator (4.55). Fast Fourier Transforms allow to calculate the likelihood for an individual galaxy in about 1 second on a 1 GHz CPU.

PSF modeling and correction

In lensfit, the PSF is modeled by stacking star images. The data for each star are sub-sampled onto a 50-times finer pixel grid using sinc function interpolation. The stars are coaligned and then downsampled to the original pixel sampling. A galaxy model is then convolved with the PSF model obtained earlier and then fitted to the data from observed galaxies.

Noise reduction

The method does not contain any noise reduction feature. A denoising scheme must be applied on the data prior to running the methods.

¹In recent versions of the code a sum of Sérsic functions is used instead to model a combination of bulge and disk

4.5. PSF interpolation for weak lensing analysis

Rank	Group Name	Method Name	Submission Date	Q	Sigma Sys
1	EPFL LASTRO	B-Splines	Aug. 25, 2011, 3:17 p.m.	13.3	7.52602E-05
2	EPFL LASTRO	IDW	July 18, 2011, 12:38 p.m.	13.2	7.59258E-05
3	EPFL LASTRO	RBF	Aug. 15, 2011, 4:42 p.m.	12.7	7.86296E-05
4	EPFL LASTRO	RBF-thin	Aug. 16, 2011, 4:33 p.m.	12.6	7.92756E-05
5	EPFL LASTRO	IDW	June 23, 2011, noon	8.7	0.000114747
6	EPFL LASTRO	IDW	June 2, 2011, 7:07 p.m.	7.2	0.000138215
7	EPFL LASTRO	Kriging	June 3, 2011, 4:13 p.m.	7.2	0.000138215
8	Purdue	Gaussianlets	July 19, 2011, 11:32 p.m.	4.1	0.000245255
9	EPFL LASTRO	IDW Stk	Aug. 25, 2011, 3:17 p.m.	4.0	0.000249888
10	AstrOmatic	PSFEx 3.10 baseline	Sept. 1, 2011, 4:40 p.m.	4.0	0.000252947
11	UPenn/USM	PSFEx	April 28, 2011, 4:45 p.m.	3.7	0.000268701
12	U. Penn	Shapelets	Sept. 1, 2011, 7:27 p.m.	3.5	0.000287593
13	Purdue	PCA+kriging	July 6, 2011, 9:34 p.m.	2.9	0.000342539
14	Purdue	PAC+kriging	July 20, 2011, 2:46 p.m.	2.1	0.000476479
15	AstrOmatic	PSFEx 3.10 tuned lo-mid	Sept. 2, 2011, 3:25 p.m.	1.9	0.00052613
16	AstrOmatic	PSFEx 3.10 baseline scaled	Sept. 2, 2011, 4:34 p.m.	1.9	0.00052613
17	AstrOmatic	PSFEx 3.10 tuned lo-hi	Sept. 2, 2011, 10:20 a.m.	1.9	0.000533332
18	AstrOmatic	PSFEx 3.10 tuned mid-hi	Sept. 2, 2011, 2:02 p.m.	1.8	0.000545185
19	InfEd	MoffatGP	Sept. 1, 2011, 4:39 p.m.	1.2	0.000800598
20	GREAT10		Dec. 7, 2010, 11:15 a.m.	1.0	0.00104465

Figure 4.8: The final leaderboard of the Star Challenge, as displayed on the GREAT10 web site just after the deadline. The six methods, B-Splines, IDW, RBF, RBF-thin, Kriging and IDW-Stk were developed by the author and are described in Gentile et al. (2013). See also Kitching et al. (2012c).

Assessment

the lensFIT method did not participate explicitly in the STEP programs, but, subsequently tested on the same data, it showed good performance according to Miller et al. (2007); Kitching et al. (2008). It performed relatively well in the GREAT08 challenge, respectively finishing in fourth and third rank in the leaderboards for the low-noise and real-noise image data sets (Bridle et al. 2010). On the other hand, although lensfit did initially compete in the GREAT10 challenge, its results were not included of the final leaderboard. It would have been interesting to see its level of performance compared to the other methods. Recently, a pipeline that uses the lensfit shear measurement algorithm has been applied to the CFHTLS Lensing survey (CFHTLenS) (Miller et al. 2013). The authors have claimed the lensfit has been significantly improved in the process. The method has certainly gained in maturity and possibly in accuracy, but it is difficult to assess its real level of performance compared to other shear measurement schemes.

4.5 PSF interpolation for weak lensing analysis

We mentioned PSF interpolation in Sect. 4.1.2 as one significant source of systematic errors in weak lensing surveys. The importance of this issue for next-generation surveys has only recently been acknowledged, as illustrated by the inclusion of a PSF interpolation challenge — the Star Challenge — in GREAT10 (see Sect. 4.2.2).

The author participated in the Star Challenge, presenting six PSF interpolation schemes. One

of them, the B-Splines method, won the Star Challenge and four methods (IDW, RBF, RBF-thin and Kriging) took the next four ranks. Fig. 4.8 shows the Star Challenge leaderboard at the close of the challenge. Refer to the Star Challenge results paper from Kitching et al. (2012c) for the full details of the results.

The Gentile et al. (2013) paper, reproduced below for convenience, provides a detailed review of the subject, a description of winning interpolation schemes and a thorough analysis of the Star Challenge results. The paper also includes a PSF-model independent assessment of several interpolation techniques, including the traditionally-used polynomial fitting technique.

So far, almost all cosmic shear surveys have been using simple PSF polynomial interpolation techniques. But the shortcoming of these interpolators have been pointed out by several authors (e.g., Hoekstra et al. 2004; Jarvis et al. 2004; Van Waerbeke et al. 2002b, 2005; Jee & Tyson 2011) and we have indeed shown the limitations of polynomials in our paper.

One of the findings of our analysis is that so-called “local” interpolation schemes were more accurate and more resilient to turbulence when run on the Star Challenge simulated data. One interpolator in particular, based on radial basis functions (RBF), proved the most accurate overall. It would be interesting to see if all this remains true on real data. Two aspects in particular would need to be explored: (1) the behavior of PSF interpolators on space-based diffraction-limited PSF fields which feature more complicated models, and (2) the influence of more realistic models of turbulence. The more realistic simulations of the forthcoming GREAT3 (Mandelbaum et al. 2013) may certainly help in this respect.

Interpolating point spread function anisotropy

M. Gentile, F. Courbin, and G. Meylan

Laboratoire d'astrophysique, École Polytechnique Fédérale de Lausanne (EPFL), Observatoire de Sauvigny, 1290 Versoix, Switzerland
e-mail: marc.gentile@epfl.ch

Received 3 June 2012 / Accepted 19 September 2012

ABSTRACT

Planned wide-field weak lensing surveys are expected to reduce the statistical errors on the shear field to unprecedented levels. In contrast, systematic errors like those induced by the convolution with the point spread function (PSF) will not benefit from that scaling effect and will require very accurate modeling and correction. While numerous methods have been devised to carry out the PSF correction itself, modeling of the PSF shape and its spatial variations across the instrument field of view has, so far, attracted much less attention. This step is nevertheless crucial because the PSF is only known at star positions while the correction has to be performed at any position on the sky. A reliable interpolation scheme is therefore mandatory and a popular approach has been to use low-order bivariate polynomials. In the present paper, we evaluate four other classical spatial interpolation methods based on splines (B-splines), inverse distance weighting (IDW), radial basis functions (RBF) and ordinary Kriging (OK). These methods are tested on the Star-challenge part of the GRavitational Lensing Accuracy Testing 2010 (GREAT10) simulated data and are compared with the classical polynomial fitting (Polyfit). In all our methods we model the PSF using a single Moffat profile and we interpolate the fitted parameters at a set of required positions. This allowed us to win the Star-challenge of GREAT10, with the B-splines method. However, we also test all our interpolation methods independently of the way the PSF is modeled, by interpolating the GREAT10 star fields themselves (i.e., the PSF parameters are known exactly at star positions). We find in that case RBF to be the clear winner, closely followed by the other local methods, IDW and OK. The global methods, Polyfit and B-splines, are largely behind, especially in fields with (ground-based) turbulent PSFs. In fields with non-turbulent PSFs, all interpolators reach a variance on PSF systematics σ_{sys}^2 better than the 1×10^{-7} upper bound expected by future space-based surveys, with the local interpolators performing better than the global ones.

Key words. gravitational lensing: weak – methods: data analysis

1. Introduction

The convolution of galaxy images with a point spread function (PSF) is among the primary sources of systematic error in weak lensing measurement. The isotropic part of the PSF kernel makes the galaxy shape appear rounder, while the anisotropic part introduces an artificial shear effect that may be confused with the genuine shear lensing signal.

To tackle these issues, various PSF correction methods have been proposed (Kaiser et al. 1995; Luppino & Kaiser 1997; Hoekstra et al. 1998; Kaiser 2000; Bernstein & Jarvis 2002; Hirata & Seljak 2003; Refregier & Bacon 2003) and some of them implemented as part of shear measurement pipelines (Heymans et al. 2006; Massey et al. 2007; Bridle et al. 2010). However, these correction schemes do not have built-in solutions for addressing another problem: the spatial variation of the PSF across the instrument field of view that may arise, for instance, from imperfect telescope guidance, optical aberrations or atmospheric distortions.

A non-constant PSF field implies the PSF is no longer accurately known at galaxy positions and must then be estimated for the accurate shape measurement of galaxies. Bivariate polynomials, typically used as interpolators for this purpose, have in several cases been found unable to reproduce sparse, multi-scale or quickly varying PSF anisotropy patterns (Hoekstra 2004; Jarvis & Jain 2004; Van Waerbeke et al. 2002, 2005; Jee & Tyson 2011).

This raises the question of whether there exists alternative PSF models and interpolation schemes better suited for PSF estimation than those used so far. Indeed, it seems important to improve this particular aspect of PSF modeling in the perspective of future space-based missions such as Euclid or advanced ground-based telescopes like the LSST (Jee & Tyson 2011).

Only recently has the PSF variation problem begun to be taken seriously with, notably, the advent of the GRavitational Lensing Accuracy Testing 2010 (GREAT10) Star Challenge, one of the two GREAT10 challenges (Kitching et al., in prep.). The Star Challenge images have been designed to simulate a variety of typical position-varying PSF anisotropy patterns and competing PSF interpolation methods were judged on their ability to reconstruct the true PSF field at asked, non-star positions.

The Star Challenge gave us the opportunity to evaluate a number of alternative schemes suitable for the interpolation of realistic, spatially-varying PSF fields. The objective of this paper is twofold: (1) to describe our approach for tackling the problems raised by the Star Challenge and to discuss our results; (2) to perform a comparative analysis of the different interpolation methods after applying them on the Star Challenge simulations.

Our paper is thus organized as follows. We begin by reviewing the most commonly used PSF representation and interpolation schemes in Sect. 2 and continue with an overview of the interpolation schemes mentioned above in Sect. 3. We then describe our PSF estimation pipeline and analyze our results in Sects. 4 and 5. Lastly, in Sect. 6, we measure the respective accuracy of



Fig. 1. Interpolating a spatially-varying PSF field. The illustrated field is a subset of an actual GREAT10 Star Challenge PSF field.

all methods based on the solutions made available after completion of the challenge and discuss the merits of each method. We conclude in Sect. 7.

2. An overview of existing PSF interpolation schemes

Before correcting galaxies in the image for a spatially-varying PSF field, every shear measurement pipeline has, in one way or another, to interpolate the PSF between the stars, as illustrated in Fig. 1. The way this is best achieved depends essentially on the PSF model used and on the PSF interpolation algorithm. The PSF model defines which features of the PSF are to be represented, which also determines on which quantities spatial interpolation is performed. The role of the interpolation scheme, on the other hand, is to apply a prediction algorithm to find the best estimates for those quantities.

In the KSB method Kaiser et al. (1995) and its KSB+ variant (Luppino & Kaiser 1997; Hoekstra et al. 1998), the relevant features of the PSF model are its ellipticity and size, which are estimated from the second-order geometrical moments of the PSF image. The main idea behind the PSF correction scheme is that the PSF distortion on a galaxy image can be well described by a small but highly anisotropic kernel q , convolved with a large, circular seeing disk. To find the appropriate q for galaxies, the values of q^* at star positions (and sometimes the so-called “smear” and “shear” polarization tensors P^{sm^*} and P^{sh^*}) are interpolated across the image. For doing so, the typical procedure is to fit a second or third-order bivariate polynomial function.

Exactly which quantity is interpolated and which order is used for the polynomial depends on the KSB+ implementations. See e.g. Heymans et al. (2006, Appendix A), Massey et al. (2007) and recently published studies using KSB+ (Hoekstra et al. 1998; Clowe & Schneider 2002; Heymans et al. 2005; Hettterscheidt et al. 2007; Paulin-Henriksson et al. 2007; Fu et al. 2008; Umetsu et al. 2010).

A model representing a PSF as only a size and first-order deviation from circularity certainly appears quite restrictive. One can instead look for an extensive, but compact description of the PSF image, better suited to operations like noise filtering or deconvolution. A natural approach is to characterize the full PSF as a compact, complete set of orthogonal basis functions provided in analytical form, each basis being associated with a particular feature of the image (shape, frequency range, etc.). Ideally, this would not only simplify galaxy deconvolution from the PSF but also allow to better model the spatial variation of the PSF across the field of view.

Bernstein & Jarvis (2002) and Refregier (2003); Refregier & Bacon (2003); Massey & Refregier (2005) have proposed PSF expansions based on the eigenfunctions of the two-dimensional quantum harmonic oscillator, expressed in terms of Gauss-Laguerre orthogonal polynomials (Abramowitz & Stegun 1965). These functions can be interpreted as perturbations around a circular or elliptical Gaussian. The effect of a given operation (such as shear or convolution), on an image can then be traced through its contribution on each coefficient in the basis function expansion. For instance, the second-order $f_{2,2}$ coefficient of a Shapelet is the ellipticity estimator based on the Gaussian-weighted quadrupole moments used in KSB.

Modeling the PSF variation patterns with Shapelets typically involves the following steps: stars are expanded in terms of Shapelet basis functions and the expansion coefficients for each of the basis functions are fitted with a third or fourth-order polynomial. The interpolated values of the Shapelet coefficients are then used to reconstruct the PSF at galaxy positions.

This scheme has been successfully applied to several weak lensing cluster studies (Jee et al. 2005a,b, 2006, 2007b; Bergé et al. 2008; Romano et al. 2010). However, it has been argued (Jee et al. 2007a; Melchior et al. 2010) that even a high-order Shapelet-based PSF model is unable to reproduce extended PSF features (such as its wings) and that the flexibility of the model makes it vulnerable to pixelation and noise. So, although the level of residual errors after Shapelets decomposition appears low enough for cluster analysis, it may prove too high for precision cosmic shear measurement.

Actually, it is not clear if there exists any set of basis functions expressed in analytical form that is capable of accurately describing all the signal frequencies contained in the PSF. An alternative approach is to decompose the PSF in terms of basis functions directly derived from the data through Principal Component Analysis (PCA), as pioneered by Lauer (2002), Lupton et al. (2001). This approach is supposed to yield a set of basis function, the so-called “Principal Components”, optimized for a particular data configuration and sorted according to how much they contribute to the description of the data.

In practice, two main procedures have been experimented that essentially depend on the type data where PCA is applied. Jarvis & Jain (2004) and Schrabback et al. (2010) fit selected components of the PSF (e.g. ellipticity or KSB anisotropy kernel) across all image exposures with a two-dimensional polynomial of order 3 or 4. PCA analysis is performed on the coefficients of the polynomial, which allows the large-scale variations of the PSF in each exposure to be expressed as a weighted sum of a small set of principal components. A further, higher-order polynomial fit is then conducted on each exposure to capture more detailed features of the PSF.

On the other hand, and more recently, Jee et al. (2007a), Nakajima et al. (2009) and Jee & Tyson (2011) experimented a different procedure for modeling the variation of the *Hubble* Space telescope (HST) ACS camera and a simulated Large Synoptic Survey Telescope (LSST) PSF. Instead of applying PCA on polynomial coefficients, they perform a PCA decomposition on the star images themselves into a basis made of the most discriminating star building blocks. Each star can then be expanded in terms of these “eigenPSFs” and the spatial variation of their coefficients in that basis is modeled with a bivariate polynomial.

Regardless of the procedure used, the PCA scheme proves superior to wavelets and Shapelet for reproducing smaller-scale features in the PSF variation pattern, thanks to improved PSF modeling and the use of higher-order polynomials. In the case

of [Jarvis & Jain \(2004\)](#), applying PCA across all exposures allowed to compensate for the small number of stars available per exposure. Moreover, PCA is not tied to any specific PSF model.

It should be noted, however, that at least two factors may limit the performance of PCA in practical weak lensing applications: the first is that the PCA algorithm is only able to capture linear relationships in the data and thus may fail to reproduce some types of high-frequency variation patterns; the other is that PCA misses the components of the PSF pattern that are random and uncorrelated, such as those arising from atmospheric turbulence. How serious these limitations prove to be and how they can be overcome need to be investigated further (e.g. [Jain et al. 2006](#); [Schrabback et al. 2010](#)).

All the above methods attempt to model PSF variation patterns in an empirical way by the application of some mathematical formalism. It may, on the contrary be more beneficial to understand which physical phenomena determine the structure of the PSF patterns and, once done, seek appropriate models for reproducing them ([Jee et al. 2007a](#); [Stabenau et al. 2007](#); [Jee & Tyson 2011](#)). The PSF of the HST ACS camera, for instance, has been studied extensively and in some cases, the physical origin of some of the patterns clearly identified. [Jee et al. \(2007a\)](#) and [Jee & Tyson \(2011\)](#) could relate the primary principal component to changes in telescope focus caused by constraints on the secondary mirror supporting structure and the “thermal breathing” of the telescope.

In fact, various combined effects make the PSF vary spatially or over time. Some patterns are linked to the behavior of the optical system of the telescope or the detectors. Others are related to mechanical or thermal effects that make the telescope move slightly during an observation. For ground-based instruments, refraction in the atmosphere and turbulence induce further PSF distortion.

Incorporating such a wide diversity of effects into a PSF variation model is not an easy task. However, according to [Jarvis et al. \(2008\)](#), models of low-order optical aberrations such as focus and astigmatism can reproduce 90% of the PSF anisotropy patterns found in real observation data. If so, physically-motivated models could provide an alternative or a complement to purely empirical methods such as PCA.

3. Looking for better PSF interpolation schemes

The analysis of commonly used PSF interpolation schemes in the previous section has shown that the range of PSF interpolation algorithms is actually quite restricted: almost always the quantities used to characterize the PSF are fitted using a bivariate polynomial function.

But it is important to acknowledge there may exist alternative interpolation schemes that would prove more effective for that purpose than polynomial fitting. Beyond this, it is essential to recognize the goal here is not to only interpolate changes in the PSF but also to perform a *spatial* interpolation of such changes.

Interpolation (e.g. [Press et al. 2007](#)) is commonly understood as the process of estimating of values at location where no sample is available, based on values measured at sample locations. *Spatial interpolation* differs from regular interpolation in that it can take into account and potentially exploit spatial relationships in the data. In particular, it is often the case that points close together in space are more likely to be similar than points further apart. In other words, points may be spatially autocorrelated, at least locally. Most spatial interpolation methods attempt to make use of such information to improve their estimates.

After a critical review of polynomial fitting, we consider and discuss alternative spatial interpolation schemes for modeling PSF variation patterns.

3.1. A critical view of polynomial fitting

In the context of spatial interpolation, fitting polynomial functions of the spatial coordinate $\mathbf{x} = (x_i, y_i)$ to the sampled $z(\mathbf{x})$ values of interest by ordinary least squares regression (OLS) is known as “Trend Surface Analysis” (TSA). The fitting process thus consists in minimizing the sum of squares for $(\hat{z}(\mathbf{x}) - z(\mathbf{x}))$, assuming the data can be modeled as a surface of the form

$$\hat{z}(\mathbf{x}) = \sum_{r+s \leq p} b_{rs} x^r y^s \quad (1)$$

The integer p is the order of the trend surface (and the order of the underlying polynomial). Finding the b_i coefficients is a standard problem in multiple regression and can be computed with standard statistical packages.

In the literature reviewed from the previous section, authors often justify their choice of polynomial fitting by arguing the PSF varies in a smooth manner over the image. Indeed trend surfaces are well suited to modeling broad features in the data with a smooth polynomial surface, commonly of order 2 or 3.

However, PSF variation patterns result from a variety of physical effects and even though polynomials may adequately reproduce the smoothest variations, there may exist several other types of patterns that a low-order polynomial function cannot capture. Polynomials are also quite poor at handling discontinuities or abrupt changes in the data. This concerns particularly sharp discontinuities across chip gaps and rapid changes often found near the corners of the image.

An illustrative example of the shortcomings just described was the detection of a suspicious non-zero B-mode cosmic shear signal in the VIRMOS-DESCART survey ([Van Waerbeke et al. 2001, 2002](#)). After investigation ([Hoekstra 2004](#); [Van Waerbeke et al. 2005](#)), the small scale component of the signal was traced to the PSF interpolation scheme: the second-order polynomial function was unable to reproduce the rapid change in PSF anisotropy at the edges of the images. In fact, one of the main limitations of polynomials when used for interpolating PSF images in weak lensing studies lie in their inability to reproduce variations on scales smaller than the typical inter-stellar distance on the plane of the sky (often $\lesssim 1$ arcmin at high galactic latitude).

Unfortunately there are no satisfactory solutions to these shortcomings. Increasing the order of the polynomial function does not help as it leads to oscillations while attempting to capture smaller-scale or rapidly-varying features. The $z(\mathbf{x})$ values may reach extremely (and unnaturally) small or large values near the edge or just outside the area covered by the data. Such extreme values can also create problems in calculations.

One way to alleviate such problems is to pack more densely the interpolating points closer to the boundaries, but this may not be easy to achieve in practice. [Hoekstra \(2004\)](#) and [Van Waerbeke et al. \(2005\)](#) also obtained good results with an interpolator made of a polynomial function to model large-scale changes combined with a rational function to deal with small-scale variations. It is not clear, however, if this scheme can be safely applied on different data and this may require a significant amount of fine tuning.

In addition to the issues just mentioned, local effects in one part of the image may influence the fit of the whole regression

Table 1. Least squares polynomial fitting/trend surface: Pros and cons.

Least squares polynomial fitting	
Pros	Simple and intuitive Fast to compute
Cons	Usually only able to capture broad features (underfitting) Increasing the order of polynomials does not improve and generally degrades accuracy (overfitting) High-order polynomials generate numerical issues (rounding errors, overflow, etc.) High sensitivity to outliers and fitting errors Local changes propagate to the whole polynomial surface No estimation of interpolation errors (deterministic)

surface, which makes trend surfaces very sensitive to outliers, clustering effects or observable errors in the $z(\mathbf{x})$. Finally, OLS regression implicitly assumes the $z(\mathbf{x})$ are normally distributed with uncorrelated residuals. These assumptions do not hold true when spatial dependence exists in the data.

Actually, the fact that trend surfaces tend to ignore any spatial correlation or small-scale variations can turn into an advantage to remove broad features of the data prior to using some other, finer-grained interpolator. Indeed, we saw in Sect. 1 that [Jarvis & Jain \(2004\)](#) took advantage of this feature in their PCA-based interpolation scheme.

Most of the aforementioned limitations are rooted in the use of standard polynomials. One possible way out is to abandon trend surfaces altogether and use piecewise polynomials instead (especially Chebyshev polynomials), splines ([de Boor 1978](#); [Dierckx 1995](#); [Schumaker 2007](#); [Prenter 2008](#)) or alternative schemes that do not involve polynomials. Table 1 recalls the main advantages and disadvantages of polynomial fitting.

3.2. Toward alternative PSF interpolation methods

Having pointed out some important shortcomings of polynomial regression, it seems legitimate to look for alternative classes of interpolators. It is however, probably illusory to look for an ideal interpolation scheme that can describe equally well any kind of PSF variation structure. For instance the patterns of variation in a turbulent PSF are very different from those found in a diffraction-limited PSF. It is therefore probably more useful to identify which class of interpolators should be preferably used for a particular type of PSF pattern.

It is also key to realize that one does not need to reconstruct the entire PSF field: one only has to infer the PSF at specific galaxy positions based on its knowledge at sample star positions. This implies that the class of interpolation schemes applicable to the PSF variation problem is not restricted to surface fitting algorithms such as polynomial fitting, but also encompasses interpolation algorithms acting on scattered data.

Such data may also be considered as a partial realization of some stochastic process. In such case, it becomes possible to quantify the uncertainty associated with interpolated values and the corresponding interpolation method is referred to as a method for *spatial prediction*. In this article we will neglect this distinction and use the generic term “spatial interpolation”.

In fact, there are quite a few interpolation schemes that can be applied to model PSF changes. Over the years a large number of interpolation methods have been developed in many disciplines and with various objectives in mind. Spatial interpolators are usually classified according to their range (*local* versus *global*), the amount of smoothing (*exact* versus *approximate*)

Table 2. Spatial interpolation methods reviewed in this article.

Interpolation method	Scope	Exactness	Model
Polynomial fitting	global	approximate	deterministic
Basis splines	global	approximate ¹	deterministic
Inverse distance weighting	local	exact ²	deterministic
Radial basis function	local	exact ³	deterministic
Ordinary Kriging	local	exact ⁴	stochastic

Notes. ⁽¹⁾ Can be made exact by disabling smoothing. ⁽²⁾ Smoothing possible with specific algorithms. ⁽³⁾ Some Kriging algorithms are approximate.

and whether they consider the data as a realization of some random process (*stochastic* versus *deterministic*).

A *global* method makes use of all available observations in the region of interest (e.g. the image of a whole portion of the sky) to derive the estimated value at the target point whereas a *local* method only considers observations found within some small neighborhood around the target point. Thus, global methods may be preferable to capture the general trend in the data, whereas local methods may better capture the local or short-range variations and exploit spatial relationships in the data ([Burrough & McDonnell 1998](#)). A trend surface is an example of global estimator.

An interpolation methods that produces an estimate that is the same as the observed value at a sampled point is called an *exact* method. On the contrary a method is *approximate* if its predicted value at the point differs from its known value: some amount of smoothing is involved for avoiding sharp peaks or troughs in the resulting fitted surface.

Lastly, a *stochastic* (also called *geostatistical*) interpolator incorporates the concept of randomness and yields both an estimated value (the deterministic part) and an associated error (the stochastic part, e.g. an estimated variance). On the other hand, a *deterministic* method does not provide any assessment of the error made on the interpolated value.

Table 2 contains the list of spatial interpolation methods covered in this article along with their classification.

Nearly all methods of spatial interpolation share the following general spatial prediction formula

$$\hat{z}(\mathbf{x}_0) = \sum_{i=1}^N \lambda_i z(\mathbf{x}_i) \quad (2)$$

where \mathbf{x}_0 is a target point where the value should be estimated, the $z(\mathbf{x}_i)$ are the locations where an observation is available and the λ_i are the weights assigned to individual observations. N represents the number of points involved in the estimation (see Fig. 2 for an illustration). Each interpolation method has its own algorithm for estimating the weights λ_i . All the interpolation methods evaluated in this article except splines, follow Eq. (2).

We now review several widely used interpolation schemes that can be applied to the PSF interpolation problem: polynomial splines, inverse distance weighting (IDW), radial basis functions (RBF) and Kriging. In the remaining sections, we test these interpolation methods using the GREAT10 Star Challenge simulated data.

3.3. Spline interpolation

A (polynomial) univariate *spline* or degree p (order $p+1$) is made of a set of polynomial pieces, joined together such that pieces

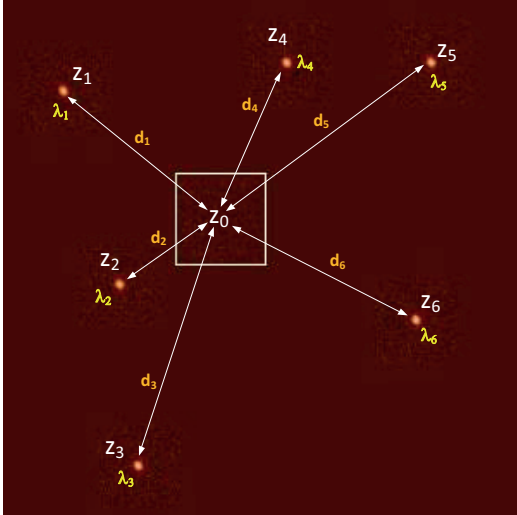


Fig. 2. An illustration of local interpolation between a set of neighboring observations $Z(x_i)$ at distances d_i from a target location x_0 . In this example, a set of weights λ_i is assigned to each of the $Z(x_i)$, as in Eq. (2).

and their derivatives at junction points (*knots*) are continuous up to degree $p - 1$ (de Boor 1978; Dierckx 1995; Schumaker 2007; Prenter 2008).

When it comes to modeling two-dimensional spatially varying PSF attributes across an image, we are more specifically interested in bivariate polynomial splines. A function $s(x, y)$ defined on a domain $[a, b] \times [c, d]$ with respective, strictly increasing knot sequences λ_i , $i = 0, 1, \dots, g + 1$ ($\lambda_0 = a, \lambda_{g+1} = b$) in the x direction and μ_j , $j = 0, 1, \dots, h + 1$ ($\mu_0 = c, \mu_{h+1} = d$) in the y direction is called a bivariate (tensor product) spline function of degree $k > 0$ (order $k + 1$) in x and $l > 0$ (order $l + 1$) in y if the following two conditions are satisfied:

1. on each subregion $\mathcal{D}_{i,j} = [\lambda_i, \lambda_{i+1}] \times [\mu_j, \mu_{j+1}]$, $s(x, y)$ is given by a polynomial of degree k in x and l in y

$$s(x, y) \in \mathcal{P}_k \otimes \mathcal{P}_l \quad i = 0, 1, \dots, g; j = 0, 1, \dots, h;$$

2. The function $s(x, y)$ and all its partial derivatives are continuous on $\mathcal{D}_{i,j}$

$$\frac{\partial^{i+j} s(x, y)}{\partial x^i \partial y^j} \in C(\mathcal{D}_{i,j}) \quad i = 0, 1, \dots, k - 1; j = 0, 1, \dots, l - 1.$$

We saw earlier that polynomial fitting suffers in particular from two serious drawbacks. One of these is that individual observations can exert an influence, in unexpected ways, on different parts of the interpolating surface. The other is the tendency of the interpolation surface to wiggle without control as soon as one increases the degree of the polynomial to try to obtain a closer fit.

Polynomial splines solve these problems in two ways. First, a spline is not made of a single “global” polynomial but of a set of “local” polynomial pieces. This design confines the influence of individual observations within the area covered by the enclosing polynomial piece. In most applications, a specific type of spline is preferred, the so-called “Basis spline” (*B-spline*), built from as a linear combination of basis polynomial functions

called *B-splines*

$$s(x, y) = \sum_{i=-k}^g \sum_{j=-l}^h c_{i,j} N_{i,k+1}(x) M_{j,l+1}(y)$$

where $N_{i,k+1}(x)$ and $M_{j,l+1}(y)$ are B-splines defined on the λ and μ knot sequences respectively. B-splines are popular for their computational efficiency, e.g. with the algorithms of Cox (Cox 1972) or de Boor (de Boor 1972). For a formal definition of the B-spline basis see e.g. de Boor (1978); Dierckx (1995); Prenter (2008).

The second issue is solved by the ability to control the smoothness of the spline. The example of polynomial fitting shows that a good fit to the data is not the one and only goal in surface fitting; another, and conflicting, goal is to obtain an estimate that does not display spurious fluctuations. A successful interpolation is, actually, a tradeoff between goodness of fit (fidelity to the data) and roughness (or “wiggleness”) of fit: a good balance between these two criteria will allow the approximation to not pick up too much noise (overfitting) while avoiding signal loss (underfitting).

There is an extensive literature on spline interpolation and many algorithms and variants have been developed since their invention in the 1960s. Still, one can divide spline interpolation algorithms into two main families: those based on the so-called *constructive* approach, where the form of the spline function is specified in advance and the estimation problem is reduced to the determination of a discrete set of parameters; and those that follow a *variational* approach, where the approximation function is not known a priori, but follows from the solution of a variational problem, which can often be interpreted as the minimization of potential energy. We outline both approaches below.

Variational approach of spline interpolation

The variational approach (Wahba 1990; Green & Silverman 1994) consists in minimizing the functional

$$S(f, \alpha) = \sum_{i=1}^N \|z(s_i) - f(s_i)\|^2 + \alpha \int_{\mathcal{D}} \{f^{(m)}\}^2 ds_i \quad (3)$$

where the bivariate spline function f is fitted to the $z(s_i)$, $i = 0, \dots, N$ set of points in the region \mathcal{D} where the approximation is to be made. It can be shown (e.g. Green & Silverman 1994) that the solution is a natural spline, that is, a spline whose second and third derivatives are zero at the boundaries. Splines obtained in such a way as known in the literature as *smoothing splines*. The parameter m represents the order of the derivative of f and $\alpha \geq 0$ is a smoothing parameter controlling the tradeoff between fidelity to the data and roughness of the spline approximation.

1. As $\alpha \rightarrow 0$ (no smoothing), the left-hand side least squares estimate term dominates the roughness term on the right-hand side and the spline function attempts to match every single observation point (oscillating as required).
2. As $\alpha \rightarrow \infty$ (infinite smoothing), the roughness penalty term on the right-hand side becomes paramount and the estimate converges to a least squares estimate at the risk of underfitting the data.

The most popular variational spline interpolation scheme is that based on the *thin-plate spline* (TPS; Duchon 1976; Meinguet 1979; Wahba & Wendelberger 1980; Wahba 1990; Hutchinson 1995). The TPS interpolating spline is obtained by

minimizing an energy function of the form (3)

$$S(f, \alpha) = \sum_{i=1}^N \|z(s_i) - f(s_i)\|^2 + \alpha J_m(g) \, ds_i \quad (4)$$

The most common choice of m is 2 with J_2 of the form

$$J_2(g) = \int_{\mathcal{D}} \left\{ \left(\frac{\partial^2 g}{\partial x^2} \right)^2 + 2 \left(\frac{\partial^2 g}{\partial x \partial y} \right)^2 + \left(\frac{\partial^2 g}{\partial y^2} \right)^2 \right\} dx \, dy \quad (5)$$

where the roughness function $g(x, y)$ is given by

$$g(s) = a_0 + a_1 x + a_2 y + \sum_1^N \lambda_i \phi(s - s_i) \quad (6)$$

ϕ being the RBF: $\Phi(x, y) = d_i^2 \ln(d_i)$ with Euclidean distance $d_i = \sqrt{(x - x_i)^2 + (y - y_i)^2}$. The λ_i are weighting factors.

Constructive approach of spline interpolation

Interpolating splines obtained through such a scheme are often referred to as *least squares splines* (Dierckx 1980, 1995; Hayes & Halliday 1994). For such splines, goodness of fit is measured through a least squares criterion, as in the variational approach, but smoothing is implemented in a different way: in the variational solution, the number and positions of knots are not varied, and the approximating spline is obtained by minimizing an energy function. On the other hand, in the constructive approach, one still tries to find the smoothest spline that is also closest to the observation points. But this is achieved by optimizing the number and placement of the knots and finding the corresponding coefficients c in the B-Spline basis. This is measured by a so-called *smoothing norm* $G(c)$. Thus, the approximating spline arises as the minimization of

$$S(f, \alpha) = \sum_{i=1}^N \|z(s_i) - f(s_i)\|^2 + \alpha G(c) \quad (7)$$

using the same notation as in (3). An example of knot placement strategy is to increase the number of knots (i.e. reduce the inter-knot distance) in areas where the surface to fit varies faster or more abruptly. By the way, we note that minimization is not obtained by increasing the degree of the spline (which is kept low, typically 3).

Whatever the approach followed for obtaining a suitable interpolating spline, spline interpolation is essentially *global*, *approximate* and *deterministic*, as it involves all available observations points, makes use of smoothing and does not provide any estimation on interpolation errors. The interpolation can however be made exact by setting the smoothing coefficient to zero. Also, for smoothing splines (variational approach) a technique called *generalized cross-validation* (GCV; Craven & Wahba 1978; Wahba 1990; Hutchinson & Gessler 1994) allows to automatically choose, in expression (4), suitable parameters for α and m for minimizing cross-validation residuals. Otherwise, one can always use standard cross-validation or Jackknifing to optimize the choice of input parameters (see Sect. 4.3).

The most frequently used splines for interpolation are cubic splines, which are made of polynomials pieces of degree at most 3 that are twice continuously differentiable. Experience has shown that in most applications, using splines of higher degree seldom yields any advantage. As we saw earlier, splines avoid the pitfalls of polynomial fitting while being much more flexible,

Table 3. Spline interpolation: Pros and cons.

Spline interpolation	
Pros	Able to capture both broad and detailed features The tradeoff between goodness and roughness of fit can be adjusted through smoothing
Cons	Overall smoothness may still be too high Keep a tendency to oscillate No estimation of interpolation errors in most algorithms Potentially less efficient to compute than local interpolation algorithms

which allows them, despite their low degree, to capture finer-grained details. The method assumes the existence of measurement errors in the data and those can be handled by adjusting the amount of smoothing.

On the minus side, cubic or higher degree splines are sometimes criticized for producing an interpolation that is “too smooth”. They also keep a tendency to oscillate (although this can be controlled unlike with standard polynomials). In addition, the final spline estimate is influenced by the number and placement of knots, which confers some arbitrariness to the method, depending on the approach and algorithm used. This can be a problem since there is, in general, no built-in mechanism for quantifying interpolation errors. Lastly, spline interpolation is a global method and performance may suffer on large datasets. A summary of the main strengths and weaknesses of spline interpolation is given in Table 3.

3.4. Inverse distance weighting

Inverse distance weighting (IDW; Shepard 1968) is one of the oldest spatial interpolation method but also one of the most commonly used. The estimated value $\hat{z}(x_0)$ at a target point x is given by Eq. (2) where the weights λ_i are of the form:

$$\lambda_i = \frac{1}{d^\beta(x_0, x_i)} / \sum_{i=1}^N \frac{1}{d^\beta(x_0, x_i)} \quad \beta \geq 0 \quad \sum_{i=1}^N \lambda_i = 1. \quad (8)$$

In the above expression, $d(x_0, x_i)$ is the distance between points x_0 and x_i , β is a power parameter and N is the number of points found in some neighborhood around the target point x_0 . Scaling the weights λ_i so that they sum to unity ensures the estimation is unbiased.

The rationale behind this formula is that data points near the target points carry a larger weight than those further away. The weighting power β determines how fast the weights tend to zero as the distance $d(x_0, x_i)$ increases. That is, as β is increased, the predictions become more similar to the closest observations and peaks in the interpolation surface becomes sharper. In this sense, the β parameter controls the degree of smoothing desired in the interpolation.

Power parameters between 1 and 4 are typically chosen and the most popular choice is $\beta = 2$, which gives the inverse-distance-squared interpolator. IDW is referred to as “moving average” when $\beta = 0$ and “linear interpolation” when $\beta = 1$.

For a more detailed discussion on the effect of the power parameter β , see e.g. Laslett et al. (1987); Burrough (1988); Brus et al. (1996); Collins & Bolstad (1996). Another way to control the smoothness of the interpolation is to vary the size of the neighborhood: increasing N yields greater smoothing.

Table 4. Inverse distance weighting: Pros and cons.

Inverse distance weighting	
Pros	Simple and intuitive Fast to compute
Cons	Choice of interpolation parameters empirical The interpolation is always exact (no smoothing) Sensitivity to outliers and sampling configuration (clustered and isolated points) No estimation of interpolation errors (deterministic)

IDW is a *local* interpolation technique because the estimation at \mathbf{x}_0 is based solely on observations points located in the neighboring region around \mathbf{x}_0 and because the influence of points further away decreases rapidly for $\beta > 0$. It is also forced to be *exact* by design since the expression for λ_i in Eq. (8) reaches the indeterminate form ∞/∞ when the estimation takes place at the point \mathbf{x}_0 itself. IDW is further labeled as *deterministic* because the estimation algorithm relies purely on geometry (distances) and does not provide any estimate on the error made.

IDW is popular for its simplicity, computational speed and ability to work on scattered data. The method also has a number of drawbacks. One is that the choice of the β parameter and the neighborhood size and shape are arbitrary, although techniques such as cross-validation or jackknifing can provide hints for tuning these parameters (see Sect. 4.3). Another is that there exists no underlying statistical model for measuring uncertainty in the predictions. Further, the results of the method are sensitive to outliers and influenced by the way observations have been sampled. In particular, the presence of clustering can bias the estimation since in such cases clustered points and isolated points at similar but opposite distances will carry about the same weights. A common feature of IDW-generated interpolation surfaces is the presence of spikes or pits around observation points since isolated points have a marked influence on the prediction in their vicinity.

The original Shepard algorithm has been enhanced by several authors to address some of the shortcomings listed above. See in particular Renka (1988), Tomczak (1998) and Lukaszzyk (2004). One frequent extension consists in explicitly introducing a smoothing factor s into Eq. (8), which then becomes

$$\lambda_i = \frac{1}{(d(\mathbf{x}_0, \mathbf{x}_i) + s)^\beta} \bigg/ \sum_{i=1}^N \frac{1}{(d(\mathbf{x}_0, \mathbf{x}_i) + s)^\beta} \quad (9)$$

with values of s typically chosen between 1 and 5. Table 4 summarizes the main pros and cons of inverse distance weighting.

3.5. Interpolation with radial basis functions

We just described IDW, a simple form of interpolation on scattered data where the weighting power ascribed to a set neighboring point \mathbf{x}_i from some point \mathbf{x} only depends on an inverse squared distance function.

We now describe a similar, but more versatile form of interpolation where the distance function is more general and expressed in terms of a RBF (Buhmann 2003; Press et al. 2007). A RBF function, or *kernel* ϕ is a real-valued function where the value evaluated at some point \mathbf{x}_0 only depends on the radial distance between \mathbf{x}_0 and a set of points \mathbf{x}_i , so that $\phi(\mathbf{x}_0 - \mathbf{x}_i) = \phi(\|\mathbf{x}_0 - \mathbf{x}_i\|)$. The norm usually represents the Euclidean distance but other types of distance functions are also possible.

Table 5. Most popular RBF kernels.

RBF kernel $\phi(r)$	Expression
Multiquadric	$\sqrt{1 + (\epsilon r)^2}$
Inverse multiquadric	$1/[1 + (\epsilon r)^2]$
Gaussian	$\exp[-(\epsilon r)^2]$
Thin-plate	$r^2 \ln(r)$
Linear	r
Cubic	r^3

The idea behind RBF interpolation is to consider that the influence of each observation on its surrounding is the same in all direction and well described by a RBF kernel. The interpolated value at a point \mathbf{x}_0 is a weighted linear combination of RBF evaluated on points located within a given neighborhood of size N according to the expression

$$\hat{z}(\mathbf{x}_0) = \sum_{i=1}^N \lambda_i z(\mathbf{x}_i) = \sum_{i=1}^N \lambda_i \phi(\|\mathbf{x}_0 - \mathbf{x}_i\|). \quad (10)$$

The weights are determined by imposing that the interpolation be exact at all neighboring points \mathbf{x}_i , which entails the resolution of a linear system of N equations with N unknown weighting factors λ_i . In some cases, it is necessary to add a low-degree polynomial $P_k(\mathbf{x})$ of degree k to account for a trend in $z(\mathbf{x})$ and ensure positive-definiteness of the solution. Expression (10) is then transformed into

$$\hat{z}(\mathbf{x}_0) = P_k(\mathbf{x}_0) + \sum_{i=1}^N \lambda_i \phi(\|\mathbf{x}_0 - \mathbf{x}_i\|). \quad (11)$$

Sometimes, an interpolation scheme based on a *normalized RBF* (NRBF) of the form

$$\hat{z}(\mathbf{x}_0) = \sum_{i=1}^N \lambda_i \phi(\|\mathbf{x}_0 - \mathbf{x}_i\|) \bigg/ \sum_{i=1}^N \phi(\|\mathbf{x}_0 - \mathbf{x}_i\|) \quad (12)$$

is preferred to (10), although no significant evidence for superior performance has been found.

The actual behavior and accuracy of RBF interpolation closely depends on how well the ϕ kernel matches the spatial distribution of the data. The most frequently used RBF kernels are listed in Table 5, where $r = \|\mathbf{x} - \mathbf{x}_i\|$ and the quantity ϵ is the so-called *shape parameter*. The required conditions for ϕ to be a suitable RBF kernel have been given by Micchelli (1986) but the choice of the most adequate kernel for a problem at hand is often empirical.

The shape parameter ϵ contained in the multiquadric, inverse multiquadric and Gaussian kernels influences the shape of the kernel function and controls the tradeoff between fitting accuracy and numerical stability. A small shape parameter produces the most accurate results, but is always associated with a poorly conditioned interpolation matrix. Despite the research work of e.g. Hardy (1990), Foley (1994) and Rippa (1999), finding the most suitable shape parameter is often a matter of trial and error. A rule of thumb is to set ϵ to approximately the mean distance to the nearest neighbor.

RBF interpolation based on the *multiquadric* (MQ) kernel $\sqrt{1 + (\epsilon r)^2}$ is the most common. It was first introduced by Hardy (1971) as a “superpositioning of quadric surfaces” for solving a problem in cartography. In its review of interpolation methods on

Table 6. Radial basis functions for interpolation: Pros and cons.

Radial basis functions	
Pros	Flexibility, thanks to various choice of kernel functions Relatively fast (local method), but computational speed depends on the kernel function
Cons	Choice of kernel functions and interpolation parameters empirical The interpolation is always exact (no smoothing) Sensitivity to outliers and sampling configuration (clustered and isolated points) No estimation of interpolation errors (deterministic)

scattered data, Franke (1982) highlighted the good performance of the MQ kernel, which has, since then proven highly successful in many disciplines (Hardy 1990).

RBF interpolation is fundamentally a *local, exact* and *deterministic* method. There are, however, algorithms that allow to introduce smoothing to better handle noise and measurement errors in the data. The method can prove highly accurate but this really depends on the affinity between the data and the kernel function used. Also, because predictions are exact, RBF functions can be locally sensitive to outliers. As for other deterministic methods like splines or IDW, the optimal set of parameters are most often determined by cross-validation or Jackknifing (see Sect. 4.3). Table 6 recapitulates the favorable and less favorable aspects of interpolation based on RBFs.

3.6. Kriging

Kriging is a spatial prediction technique initially created in the early 1950's by mining engineer Daniel G. Krige (Krige 1951) with the intent of improving ore reserve estimation in South Africa. But it was essentially the mathematician and geologist Georges Matheron who put Krige's work a firm theoretical basis and developed most of the modern Kriging formalism (Matheron 1962, 1963).

Following Matheron's work, the method has spread from mining to disciplines such as hydrology, meteorology or medicine, which triggered the creation of several Kriging variants. It is thus more accurate to refer to Kriging as a family of spatial prediction techniques instead of a single method. It is also essential to understand that Kriging constitutes a general method of interpolation that is in principle applicable to any discipline, such as astronomy.

The following textbooks provide a good introduction to the subject: Journel & Huijbregts (1978); Isaaks & Srivastava (1989); Cressie (1991); Deutsch & Journel (1997); Goovaerts (1997); Chilès & Delfiner (1999); Wackernagel (2003); Waller & Gotway (2004); Webster & Oliver (2007).

Like most of the local interpolation methods described so far in this article, Kriging makes use of the weighted sum (2) to estimate the value at a given location based on nearby observations. But instead of computing weights based on geometrical distances only, Kriging also takes into account the *spatial correlation* existing in the data. It does so by treating observed values $z(\mathbf{x})$ as *random variables* $Z(\mathbf{x})$ varying according to a spatial *random process*¹. In fact, Kriging assumes the underlying process has a form of second-order stationarity called

¹ Also called *random function* or *stochastic process*.

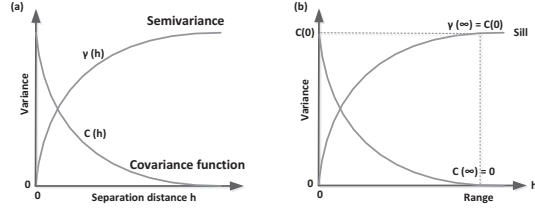


Fig. 3. a) Typical variogram $\gamma(\mathbf{h})$ and its equivalent covariance function $C(\mathbf{h})$: if the data has some sort of spatial autocorrelation, nearby (small h) $Z(\mathbf{x})$ observed values will be more similar than more distant $Z(\mathbf{x})$ values (larger h); b) as the separation distance h grows, the quantity $Z(\mathbf{x} + \mathbf{h}) - Z(\mathbf{x})$ in expression (16) will tend to increase on average, but less and less as the influence of $Z(\mathbf{h})$ on $Z(\mathbf{x} + \mathbf{h})$ weakens; at some threshold distance h , called the *range*, the increase in variance becomes negligible and the asymptotical variance value is known as the *sill*

intrinsic stationarity. Second-order stationarity is traditionally defined as follows:

1. The mathematical expectation $E(Z(\mathbf{x}))$ exists and does not depend on \mathbf{x}

$$E[Z(\mathbf{x})] = m, \quad \forall \mathbf{x}. \quad (13)$$

2. For each pair of random variable $\{Z(\mathbf{x}), Z(\mathbf{x} + \mathbf{h})\}$, the covariance exists and only depends on the separation vector $\mathbf{h} = \mathbf{x}_j - \mathbf{x}_i$,

$$C(\mathbf{h}) = E\{[Z(\mathbf{x} + \mathbf{h}) - m][Z(\mathbf{x}) - m]\}, \quad \forall \mathbf{x}. \quad (14)$$

Kriging's *intrinsic stationarity* (Matheron 1963, 1965) is a slightly weaker form of second-order stationarity where the difference $Z(\mathbf{x} + \mathbf{h}) - Z(\mathbf{x})$ is treated as the stationary variable instead of $Z(\mathbf{x})$:

$$1. E[Z(\mathbf{x} + \mathbf{h}) - Z(\mathbf{x})] = 0, \quad \forall \mathbf{x} \quad (15)$$

$$2. \text{Var}[Z(\mathbf{x} + \mathbf{h}) - Z(\mathbf{x})] = E\{[Z(\mathbf{x} + \mathbf{h}) - Z(\mathbf{x})]^2\} = 2\gamma(\mathbf{h}). \quad (16)$$

The function $\gamma(\mathbf{h})$ is called *semivariance* and its graph *semivariogram* or simply *variogram*.

One reason for preferring intrinsic stationarity over secondary stationarity is that semivariance remains valid under a wider range of circumstances. When covariance exists, both stationarities are related through

$$\gamma(\mathbf{h}) = C(0) - C(\mathbf{h}), \quad C(0) = \text{Var}[Z(\mathbf{x})], \quad (17)$$

Figure 3 shows a typical variogram along with its equivalent covariance function.

Over the years about a dozen Kriging variants have been developed. We will concentrate here on *ordinary Kriging* (OK), which is, by far, the most widely used. The description of other forms of Kriging can be found in the literature given at the beginning of this section.

ordinary Kriging is a *local, exact* and *stochastic* method. The set of $Z(\mathbf{x})$ is assumed to be an intrinsically stationary random process of the form

$$Z(\mathbf{x}) = m + \epsilon(\mathbf{x}). \quad (18)$$

The quantity $\epsilon(\mathbf{x})$ is a random component drawn from a probability distribution with mean zero and variogram $\gamma(\mathbf{h})$ given by (16). The mean $m = E[Z(\mathbf{x})]$ is assumed constant because

Table 7. Authorized Kriging theoretical variogram models.

Model	Expression	
Pure nugget	$\gamma(h) = 0$	$h = 0$
	$\gamma(h) = c_0$	$c_0 \geq 0$ $h > 0$
Spherical	$\gamma(h) = c_0 + c \left\{ \frac{3h}{2a} - \frac{1}{2} \left(\frac{h}{a} \right)^3 \right\}$	$h \leq a$
	$\gamma(h) = c_0 + c$	$h > a$
Exponential	$\gamma(h) = c_0 + c \left\{ 1 - \exp \left(-\frac{h}{a} \right) \right\}$	
Gaussian	$\gamma(h) = c_0 + c \left\{ 1 - \exp \left(-\frac{h^2}{a^2} \right) \right\}$	
Power	$\gamma(h) = c_0 + b h^p$	$b \geq 0, 0 \leq p < 2$

Notes. The models in this table correspond to purely isotropic Kriging. More elaborate formulas exist for correcting geometrical anisotropy through the rescaling or rotation of coordinate axes along the direction of major spatial continuity. In the above expressions, $c_0 = \lim_{h \rightarrow 0} \gamma(h)$ is the so-called *nugget* constant that represents measurement errors or indicates a spatially discontinuous process. The quantities $(c_0 + c)$ and a respectively represent the variogram *sill* and *range*. The *pure nugget* model corresponds to absence of spatial correlation.

of (15), but remains *unknown*. The ordinary Kriging predictor is given by the weighted sum

$$\hat{Z}(\mathbf{x}_0) = \sum_{i=1}^N \lambda_i Z(\mathbf{x}_i) \quad (19)$$

where the weights λ_i are obtained by minimizing the so-called *Kriging variance*

$$\sigma^2(\mathbf{x}_0) = \text{Var} \left[\hat{Z}(\mathbf{x}_0) - Z(\mathbf{x}_0) \right] = E \left\{ \left[\hat{Z}(\mathbf{x}_0) - Z(\mathbf{x}_0) \right]^2 \right\} \quad (20)$$

subject to the unbiasedness condition

$$E \left[\hat{Z}(\mathbf{x}_0) - Z(\mathbf{x}_0) \right] = 0 = \sum_{i=1}^N \lambda_i E[z(\mathbf{x}_i)] - m. \quad (21)$$

The resulting system of $N + 1$ equations in $N + 1$ unknowns λ_i is known as the *ordinary Kriging equations*. It is often expressed in matrix form as $\mathbf{A}\boldsymbol{\lambda} = \mathbf{b}$ with

$$\mathbf{A} = \begin{bmatrix} \gamma(\mathbf{x}_1, \mathbf{x}_1) & \gamma(\mathbf{x}_1, \mathbf{x}_2) & \cdots & \gamma(\mathbf{x}_1, \mathbf{x}_N) & 1 \\ \gamma(\mathbf{x}_2, \mathbf{x}_1) & \gamma(\mathbf{x}_2, \mathbf{x}_2) & \cdots & \gamma(\mathbf{x}_2, \mathbf{x}_N) & 1 \\ \vdots & \vdots & \ddots & \vdots & \vdots \\ \gamma(\mathbf{x}_N, \mathbf{x}_1) & \gamma(\mathbf{x}_N, \mathbf{x}_2) & \cdots & \gamma(\mathbf{x}_N, \mathbf{x}_N) & 1 \\ 1 & 1 & \cdots & 1 & 0 \end{bmatrix} \quad (22)$$

$$\boldsymbol{\lambda}^T = \left[\lambda_1 \ \lambda_2 \ \cdots \ \lambda_N \ \mu \right] \quad \sum_{i=1}^N \lambda_i = 1$$

$$\mathbf{b}^T = \left[\gamma(\mathbf{x}_1, \mathbf{x}_0) \ \gamma(\mathbf{x}_2, \mathbf{x}_0) \ \cdots \ \gamma(\mathbf{x}_N, \mathbf{x}_0) \ 1 \right].$$

The weights λ_i , along with the Lagrange multiplier μ , are obtained by inverting the \mathbf{A} matrix

$$\boldsymbol{\lambda} = \mathbf{A}^{-1} \mathbf{b}. \quad (23)$$

The main interpolation steps with ordinary Kriging can now be articulated:

1. Construct an experimental variogram by computing the experimental semivariance $\hat{\gamma}(\mathbf{h})$ for a range of separation distances $\|\mathbf{h}\|$.

Table 8. Kriging interpolation: Pros and cons.

Kriging	
Pros	Predictions based on a spatial statistical analysis of the data
	Best linear unbiased estimator (BLUE)
	Many forms of Kriging available, applicable to various data configurations
	Automatically accounts for clustering and screening effects; remains efficient in conditions of sparse data
Cons	Can take into account variation bias toward specific directions (anisotropy)
	Able to quantify interpolation errors (Kriging variance)
	Overall complexity
	Requires care when modeling spatial correlation structures
	Assumptions of intrinsic stationarity may not be valid (drift) and be handled through an appropriate Kriging variant
	Most Kriging variants are exact (no smoothing)
	Kriging is more computationally intensive than other local methods

2. Fit the experimental variogram against an authorized variogram model. The mathematical expressions for the most common authorized *theoretical variogram* models are summarized in Table 7. After completion of this step, the $\gamma(\mathbf{x}_i, \mathbf{x}_j)$ value at any separation vector $\mathbf{h} = \mathbf{x}_j - \mathbf{x}_i$ can be calculated and used to compute the \mathbf{A} matrix (22).
3. Calculate interpolated values: derive the Kriging weights λ_i for each point of interest \mathbf{x}_0 by solving Eq. (23) and obtain the Kriging estimate at \mathbf{x}_0 by substituting in (19).

Most of the strengths of Kriging interpolation stem from the use of semivariance instead of pure geometrical distances. This feature allows Kriging to remain efficient in condition of sparse data and to be less affected by clustering and screening effects than other methods.

In addition, as a true stochastic method, Kriging interpolation provides a way of directly quantifying the uncertainty in its predictions in the form of the Kriging variance specified in Eq. (20).

The sophistication of Kriging, on the other hand, may also be considered as one of its disadvantages. A thorough preliminary analysis of the data is required or at least strongly recommended prior to applying the technique (e.g. Tukey 1977). This can prove complex and time consuming.

One should also bear in mind that Kriging is more computationally intensive than the other local interpolation methods described in this article. The strong and weaker points of Kriging interpolation are highlighted in Table 8.

4. Applying spatial interpolation schemes on the GREAT10 Star Challenge data

In 2011, we participated in the GREAT10 Star Challenge competition (Kitching et al., in prep.), which allowed us to evaluate the performance of the interpolation schemes described above: those based on splines, IDW, RBF and ordinary Kriging. To our knowledge, the only reference to a similar work in the field of astronomy is that of Bergé et al. (2012).

The GREAT10 Star Challenge ran from December 2010 to September 2011 as an open, blind competition. As illustrated in Fig. 4, the data consisted in 26 datasets of 50 PSF fields, each field containing between 500 and 2000 simulated star images and featuring specific patterns of variation. The stars

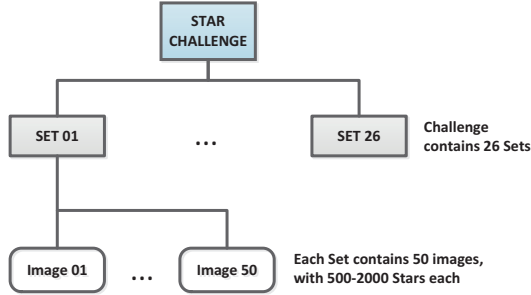


Fig. 4. Star Challenge simulated data.

images were supplied as non-overlapping, randomly-scattered 48×48 pixels postage stamps, altered by Gaussian noise.

After completion of the challenge, it was revealed the stars had either a Moffat (Moffat 1969) or pseudo-Airy (Born & Wolf 1999; Kuijken 2008) profile, with a telescope component model from Jarvis et al. (2008). Depending on the sets, specific additional effects, such as Kolmogorov turbulence, were also incorporated.

The challenge itself was to predict the PSF at 1000 requested positions in each of the 1300 PSF fields (see Fig. 1).

4.1. Which model for the PSF?

The first important step to make was to choose an appropriate model for the PSF. Indeed, before selecting a particular PSF interpolator, one has to decide on which type of data that interpolator will operate.

Essentially three PSF modeling approaches have been explored in the literature:

1. PSF as a combination of basis functions;
2. PSF left in pixel form;
3. PSF expressed in functional form.

To help choosing the right model for the data at hand, useful guidance is provided by the notions of complexity and sparsity, recently put forward by (Paulin-Henriksson et al. 2008, 2009). The complexity of a model is characterized by the amount of information required to represent the underlying PSF image, which can be expressed as the number of degrees of freedom (DoF) present in the model. The more sophisticated the model the greater the number of its DoF. Sparsity, on the other hand, is meant to describe how efficiently a model can represent the actual PSF with a limited number of DoF, that is, with a simple model.

The simulated star images looked relatively simple and we decided that the right level of sparsity could be achieved with PSF in functional form (the third option). We then assumed that the most likely PSF profile used to create the stars was either Airy or Moffat. We opted for an elliptically symmetric Moffat function for its simplicity and because the stars did not show significant diffraction spikes. Each star was thus assumed to have a light intensity distribution of the form:

$$I(\xi) = I_0 \left[1 + \left(\frac{\xi}{a} \right)^2 \right]^{-\beta}, \quad \xi = \sqrt{(x' - x_c)^2 + \frac{(y' - y_c)^2}{q^2}}.$$

In the above expression, I_0 is the flux intensity at $\xi = 0$, ξ being the radius distance from the centroid (x_c, y_c) of the PSF to a

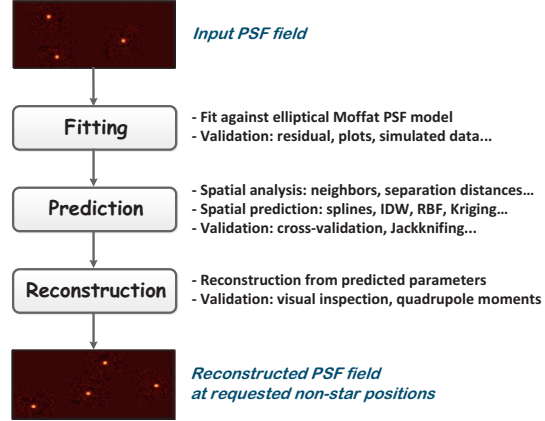


Fig. 5. The three-stage PSF prediction pipeline we used to compete in the Star Challenge. Elliptical Moffat profiles are fitted to the stars contained in the input Star Challenge PSF field; the model resulting parameters are then individually interpolated across the field at requested locations, using one of our PSF spatial interpolator. Lastly, the star images are reconstructed from the set of Moffat parameters predicted in the previous stage.

spatial coordinate

$$\begin{bmatrix} x' - x_c \\ y' - y_c \end{bmatrix} = \begin{bmatrix} \cos \phi & \sin \phi \\ -\sin \phi & \cos \phi \end{bmatrix} \begin{bmatrix} x - x_c \\ y - y_c \end{bmatrix}, \quad (24)$$

obtained after counterclockwise rotation through an angle ϕ with respect to the $(0, x)$ axis. The quantity $\alpha = FWHM [2^{1/\beta} - 1]^{-1/2}$ is the Moffat scale factor expressed in terms of the full width at half maximum (FWHM) of the PSF and the Moffat shape parameter β . Lastly, q is the ratio of the semi-minor axis b to the semi-major axis a of the isophote ellipse, given by $q = b/a = (1 - |e|)/(1 + |e|)$, with $|e| = \sqrt{e_1^2 + e_2^2}$, $e_1 = |e| \cos 2\phi$ and $e_2 = |e| \sin 2\phi$.

4.2. Our PSF prediction pipeline

The three-stage PSF prediction pipeline we used in the Star Challenge is sketched in Fig. 5. The purpose of the *fitting* stage is to produce a catalog of estimated FWHM and ellipticity values of the stars found at known spatial positions within the input Star Challenge PSF image.

In the *prediction* stage, that catalog is processed by an interpolation algorithm and a catalog is produced with estimated FWHM and ellipticities at new positions in the same image. Competitors were required to submit their results in the form of FITS Cube images (Kitching et al. 2011). In the *reconstruction* stage, each star in a PSF field is thus reconstructed using that format from the interpolated quantities predicted in the *prediction* stage. A more detailed description of the pipeline is given in Appendix A.

4.3. Cross-validation and Jackknifing

The Star Challenge was a *blind* competition. The true answers being unknown, it was essential to find ways to evaluate how far the actual results were from the truth. To assess the fitting

Table 9. Common diagnostic statistics for use with cross-validation and Jackknifing.

Statistics	Expression
Mean error	$ME = \frac{1}{n} \sum_{i=1}^n [Z(x_i) - Z(x_{[i]})]$
Mean squared error	$MSE = \frac{1}{n} \sum_{i=1}^n [Z(x_i) - Z(x_{[i]})]^2$
Mean absolute error	$MAE = \frac{1}{n} \sum_{i=1}^n \ Z(x_i) - Z(x_{[i]})\ $
Mean squared deviation ratio	$MSDR = \frac{1}{n} \sum_{i=1}^n \{[Z(x_i) - Z(x_{[i]})]^2 / \sigma_{[i]}^2\}$

accuracy in the first stage of the pipeline we could rely somewhat on the analysis of the residuals between observed and fitted star images. But when it came to evaluate prediction results, we had no such residuals to help us appraise the accuracy of the interpolation algorithm: we could only rely on the fitted observations $Z(x_i)$. The use of cross-validation and Jackknifing provided a satisfactory solution to this problem.

Cross-validation

Cross-validation (CV) is a resampling technique frequently used in the fields of machine learning and data mining to evaluate and compare the performance of predictive models (Stone 1974; Geisser 1975; Isaaks & Srivastava 1989; Browne 2000).

In the context of the Star Challenge, we used CV to both evaluate the performance of an interpolation method and tune the free parameters of the underlying interpolation models.

As explained earlier, the deterministic interpolation methods (IDW, RBF, splines) we tested in the competition did not provide any quantification of residual errors. The first three diagnostic statistics mentioned in Table 9 provided a good indication of the level of accuracy reached. This technique was useful for Kriging as well because we could directly compare the mean error (ME) and mean squared error (MSE) provided by CV: Kriging being an unbiased estimator, we expected ME to be nearly zero, the MSE to be close to the Kriging variance provided by Eq. (20) and the mean squared deviation ratio (MSDR) to be around unity.

CV also proved useful for tuning the free parameters of the models behind the interpolation schemes, as mentioned in Appendix A.2. For instance, for RBF interpolation, we could rapidly try and discard the cubic, quintic, Gaussian and inverse multiquadric kernel functions. Another example was the ability to find the best search neighborhood size for local distance-based interpolation methods.

Jackknifing

The Jackknifing resampling technique was first proposed by Quenouille (1956) and further developed by Tukey (1958). A classical review on that subject is that of Miller (1974). See also Efron (1982); Efron & Gong (1983); Davis (1987); Tomczak (1998) for more general discussions on the use of CV in connection to Jackknifing.

To Jackknife a Star Challenge PSF field image, we would typically split the set of input coordinates into two equally-sized sets of star locations, i.e. 1000 randomly-selected star centroid positions from a set of 2000, one used for input and one used for prediction. We would then interpolate the PSF of the prediction set based on the PSF of the input set.

Table 10. Final results obtained by the B-SPLINE, IDW, Kriging and RBF methods in the Star Challenge, sorted by decreasing P -factors.

Rank	PSF interpolation method	P	σ_{sys}^2
1	Basis spline (B-splines)	13.29	7.53×10^{-5}
2	Inverse distance weighting (IDW)	13.17	7.59×10^{-5}
3	Radial basis function (RBF)	12.72	7.86×10^{-5}
4	Radial basis function (RBF thin)	12.61	7.93×10^{-5}
5	Ordinary Kriging (OK)	7.23	1.38×10^{-4}

Notes. The B-splines method obtained the highest P -factor of the competition while the remaining four achieved the next highest scores.

5. Analyzing our GREAT10 Star Challenge results

5.1. Results on the Star Challenge data

The results obtained in the Star Challenge by the B-splines, IDW, Kriging, RBF and RBF-thin PSF interpolation schemes are shown in Table 10.

The B-splines method won the Star Challenge while the remaining four achieved the next highest scores of the competition.

The quantity P refers to the so-called P -factor, specified in Kitching et al. (in prep.). That P -factor is defined so as to measure the average variance over all images between the estimated and true values of two key PSF attributes: its size R and ellipticity modulus $e = |e|$, estimated using second brightness moments computed over the reconstructed PSF images. Since the GREAT10 simulated star images have either Moffat or Airy profiles, R is actually an estimator of the FWHM of the stars.

The σ_{sys}^2 quantity is related to the P -factor by $\sigma_{\text{sys}}^2 = 10^{-3}/P$ and represents a total residual variance in the measurement of the PSF. It approximates the corresponding metric specified in Amara & Réfrégier (2008); Paulin-Henriksson et al. (2008, 2009).

5.2. Performance metrics

In this article, we do not rely on the P -factor as a metric for assessing the performance of our methods, for the following reasons. Firstly, the P -factor is specific to the Star Challenge and is not mentioned anywhere else in the literature on PSF interpolation. Secondly, we are really interested in knowing the individual accuracy of ellipticity and size but P only appraises the combined performance of these quantities.

To assess the performance of an interpolator, we calculate instead the root mean squared error (RMSE) and standard error on the mean (SEM) of the residuals between true and calculated values of PSF ellipticity and size. As in Paulin-Henriksson et al. (2008); Kitching et al. (in prep.), we adopt the ellipticity modulus $e = (e_1^2 + e_2^2)^{1/2}$ and size squared R^2 as respective measures of ellipticity and size, and define the corresponding residuals as

$$\delta(e) = e_{\text{calc}} - e_{\text{true}}, \quad \delta(R^2) = R_{\text{calc}}^2 - R_{\text{true}}^2.$$

As regards PSF ellipticity, we adopt as performance metrics

$$E(e) = RMSE(\delta(e)/2), \quad \sigma(e) = SEM(\delta(e)/2)$$

while for PSF size, we evaluate

$$E(R^2) = RMSE(\delta(R^2))/\langle R_{\text{true}}^2 \rangle, \quad \sigma(R^2) = SEM(\delta(R^2))/\langle R_{\text{true}}^2 \rangle$$

Table 11. Average values of the performance metrics E and σ (see Sect. 5.2) over all sets, obtained by the B-SPLINE, IDW, Kriging and RBF methods in the Star Challenge.

Method	$E(e)$	$\sigma(e)$	$E(R^2)$	$\sigma(R^2)$
B-splines	2.03×10^{-2}	8.57×10^{-4}	1.90×10^{-1}	8.25×10^{-4}
IDW	2.04×10^{-2}	8.69×10^{-4}	1.92×10^{-1}	1.07×10^{-3}
RBF	2.26×10^{-2}	9.73×10^{-4}	1.98×10^{-1}	1.39×10^{-3}
Kriging	3.17×10^{-2}	1.26×10^{-3}	2.22×10^{-1}	2.18×10^{-3}

Table 12. Performance metrics used in this article.

PSF attribute	Metrics
PSF ellipticity	$E(e) = \sqrt{\langle (e_{\text{calc}} - e_{\text{true}})^2 \rangle} / 2$ $\sigma(e) = \text{stdev}(e_{\text{calc}} - e_{\text{true}}) / \sqrt{2} / \sqrt{N}$
PSF size	$E(R^2) = \sqrt{\langle (R_{\text{calc}}^2 - R_{\text{true}}^2)^2 \rangle} / (R_{\text{true}}^2)$ $\sigma(R^2) = \text{stdev}(R_{\text{calc}}^2 - R_{\text{true}}^2) / (R_{\text{true}}^2) / \sqrt{N}$

Notes. The angle brackets $\langle \rangle$ and stdev denote averages and standard deviation. These statistics are calculated over the $N = 1000$ stars in each of the 50 images of each set.

where the angle brackets $\langle \rangle$ and stdev denote averaging. The factor 2 in the expressions of $E(e)$ and $\sigma(e)$ arises because ellipticity has two components. We calculate these metrics over the $N = 1000$ stars in each of the 50 images of each set.

The quantity E provides a measure of the global accuracy of the interpolator (bias and precision combined) while σ provides insights into the variance of the residuals. The exact expressions for these performance metrics are given in Table 12.

5.3. Analysis of the star challenge results

The performance metrics of B-splines, IDW, RBF and Kriging are given in Table 11. The results of RBF and RBF-thin being very close, we no longer distinguish these two interpolators in the remainder of this paper and only mention them collectively as RBF.

Since a detailed analysis of the Star Challenge results of B-splines, IDW, RBF and Kriging as already been performed in Kitching et al. (in prep.), a similar analysis would be redundant here. We do have, however, a couple of observations to make, based on the metrics in Tables 10 and 11.

We observe that the global σ_{sys}^2 variance of the most successful interpolation method is on the order of 10^{-4} . As demonstrated in Amara & Réfrégier (2008); Paulin-Henriksson et al. (2008) and confirmed by Kitching et al. (2009), future large surveys will need to constrain the total variance in the systematic errors to $\sigma_{\text{sys}}^2 < 10^{-7}$, which corresponds to $E(e) \lesssim 10^{-3}$ and $E(R^2) \lesssim 10^{-3}$. The Star Challenge results thus tend to suggest that a ~ 10 improvement in $E(e)$ and a ~ 100 improvement in $E(R^2)$ are still required for achieving that goal.

Secondly, since we have been using a three-stage pipeline as described in Sect. 4.2, each stage, fitting, interpolation and reconstruction, can potentially contribute to the final error in size and ellipticity. Investigations following the publication of the true size and ellipticity values after the end of the Star Challenge, have led us to conclude fitting was actually the main

Table 13. Average values of the performance metrics E and σ (see Sect. 5.2) over all sets, based on the true input ellipticities and sizes.

Method	$E(e)$	$\sigma(e)$	$E(R^2)$	$\sigma(R^2)$
RBF	1.73×10^{-2}	7.18×10^{-4}	4.58×10^{-3}	1.44×10^{-4}
IDW	1.78×10^{-2}	7.24×10^{-4}	9.25×10^{-3}	2.91×10^{-4}
Kriging	1.82×10^{-2}	7.09×10^{-4}	6.47×10^{-3}	2.03×10^{-4}
Polyfit	2.29×10^{-2}	7.52×10^{-4}	5.16×10^{-3}	1.62×10^{-4}
B-splines	2.33×10^{-2}	7.39×10^{-4}	6.45×10^{-3}	2.04×10^{-4}

performance limiting factor, not the interpolation or reconstruction process.

Also, the comparatively lower performance of Kriging is not related to the interpolation algorithm itself, but is actually due to an inadequate fitting setup, that was subsequently fixed for B-splines, IDW and RBF submissions.

As the main goal of this article is to assess the respective merits of the interpolation methods, we wish to eliminate all inaccuracies related to fitting. To achieve this, we use instead of our fitted ellipticity and FWHM estimates at known positions, the *true* input values, kindly supplied to us by the GREAT10 team. We interpolate these true input values at the expected target positions and then measure the error made by the interpolators. We present and analyze the corresponding results in the next section.

6. Comparing PSF spatial interpolation schemes

The results presented in this section are based on true FWHM and ellipticity values at known positions in the Star Challenge PSF images. We are thus confident that error statistics we obtained truly reflect the performance of the PSF interpolation methods and are not influenced in any way by inaccuracies due to the fitting of our PSF model or to the image reconstruction processes.

We compare below the respective performance of five PSF spatial interpolation schemes:

- The four interpolation schemes introduced in Sect. 3 that competed in the Star Challenge: B-splines, IDW, RBF and ordinary Kriging.
- An additional scheme, labeled *Polyfit*, which corresponds to a least-squares bivariate polynomial fit of the PSF, similar to that typically used in weak lensing studies (see Sect. 3.1).

The metric values reflecting the average accuracy E and error on the mean σ for these five interpolation schemes are given in Table 13.

6.1. Overall performance

The E and σ metrics on ellipticity and size after interpolation with all five methods are given in Table 13. These results lead to the following observations:

- If we compare Tables 13 and 12 we observe a ~ 100 -fold decrease of $E(R^2)$ for all interpolators. This confirms that the fitting of PSF sizes was the main limitation that prevented us from reaching better results in the Star Challenge. In comparison, the fitting of ellipticities was quite good.
- If we now concentrate on Table 13, we find that the RBF interpolation scheme based on the use of radial basis functions,

has the highest accuracy and smallest error of the mean, both on size and ellipticity. We also observe that $E(e) \sim 10^{-2}$ whereas $E(R^2) \sim 10^{-3}$. This is because these statistics are averages over 26 image sets with different characteristics (see Sect. 6.2). In reality, $E(e)$ varies between $\sim 10^{-2}$ and $\sim 10^{-4}$, whereas $E(R^2) \sim 10^{-3}$ regardless of the sets.

- If we consider $E(e)$ in particular, two groups emerge. The first one contains RBF, IDW and Kriging, with $E(e) \leq 1.8 \times 10^{-2}$. The interpolators of the second group, B-splines and Polyfit with $E(e) \geq 2.3 \times 10^{-2}$. We will see below that this is essentially due to the better accuracy of local interpolators on turbulent sets as regards ellipticity. If we focus on $E(R^2)$, the distinction between local and global interpolation schemes disappears. RBF and Polyfit stand out from the others with $E(R^2) \simeq 5 \times 10^{-3}$. We also note that the accuracy of IDW on size is worse by several order of magnitude.
- The errors on the mean $\sigma(e)$ and $\sigma(R^2)$ are on the order of 10^{-4} for all five schemes. As was observed for $E(e)$, we find that the local interpolators RBF, IDW and Kriging reach better $\sigma(e)$ values compared to global ones, B-splines and Polyfit. As for $\sigma(R^2)$, the best values are reached by RBF and Polyfit, similarly to what was found for $E(R^2)$.

6.2. Influence of PSF features simulated in the images

As explained in the Star Challenge result paper (Kitching et al., in prep.), the image sets were designed to simulate typical PSF features found in real astronomical images. Each set implements a unique combination of characteristics against which a method can be evaluated. All 50 images within a set share the same broad features, but differ in the way star positions, sizes and ellipticities are spatially distributed across the field.

The various PSF features tracked in the images are outlined below:

- *PSF model*: the fiducial PSF model includes a static and a dynamic component. The static component is based on a pseudo-Airy (Born & Wolf 1999; Kuijken 2008) or Moffat (Moffat 1969) functional form, depending on the set. The dynamic component made the ellipticity and size of individual stars vary spatially across the image of the PSF field.
- *Star size*: the images from most of the sets share the same “fiducial” 3-pixel FWHM, except sets 6, 14, 26 and sets 7, 15 whose images have respectively a FWHM of 1.5 and 6 pixels.
- *Masking*: sets 2, 10, 22 have a 4-fold symmetric mask denoted as “+” and sets 3, 11, 23 have a 6-fold mask symbolized by a “*”. Images from all other sets are unmasked.
- *Number of stars*: the majority of images contain 1000 stars. Sets 4, 12, 24 are denser, with 2000 stars, whereas sets 5, 13, 25 are sparser, with only 1500 stars.
- *Kolmogorov turbulence (KM)*: an attempt was made on sets 9 to 15, 17, 19 and 21 to simulate the effect of atmospheric turbulence by including a Kolmogorov spectrum in PSF ellipticity. See Heymans et al. (2012); Kitching et al. (in prep.) for the details. Figure 6 shows side by side a non-turbulent and a turbulent PSF.
- *Telescope effect*: a deterministic component was included in sets 17, 19 and 21 to reproduce effects from the telescope optics on the PSF ellipticity and size, essentially primary astigmatism, primary defocus and coma (Born & Wolf 1999), based on the model of Jarvis & Jain (2004).

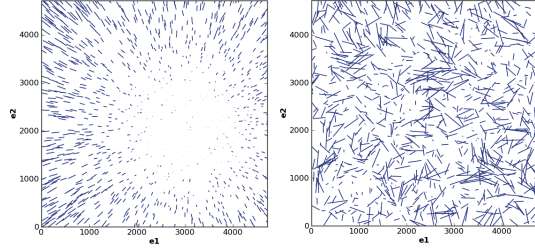


Fig. 6. A Star Challenge non-turbulent PSF (left) compared with a turbulent PSF (right). Each “whisker” represents the amplitude $|e|$ of the ellipticity of stars. The largest whisker in the left hand side image corresponds to an ellipticity of 0.16. The right hand side image has a maximum ellipticity of 0.37. The ellipticity plots have respectively been made from the first PSF field image of sets 8 and 14.

In order to determine how interpolation schemes are affected by the aforementioned PSF characteristics, we have computed for each of them the performance metrics per individual image sets. We have plotted the metrics $E(e)$ and $E(R^2)$ in Figs. 7 and 8. We analyze the results below.

- *Influence of turbulence*: the PSF feature that affects the interpolation methods the most is the presence of a Kolmogorov (KM) turbulence in ellipticity. Figure 6 illustrates how erratic the spatial variation pattern of ellipticity can become in the presence of KM turbulence. It is clear that a prediction algorithm faces a much more challenging task on turbulent images than on images with more regular PSF patterns. To highlight this, we have averaged in Tables 14 and 15 the metrics E and σ separately over turbulent and non-turbulent sets. Comparing these two tables shows that $E(e) \sim 10^{-4}$ and $\sigma(e) \sim 10^{-5}$ on non-turbulent sets, whereas $E(e) \sim 10^{-2}$ and $\sigma(e) \sim 10^{-3}$ on turbulent sets. This represents a ~ 100 -fold decrease in accuracy and error on the mean. This effect can also be seen on the plots of $E(e)$ in Figs. 7 for and 8.

We also observe that, on sets without a KM spectrum, all interpolators evaluated in this paper typically reach $\sigma_{\text{sys}}^2 \sim 10^{-8}$ already beyond the $\sim 10^{-7}$ goal of next-generation space-based weak lensing surveys. In contrast, sets with turbulent PSF do not match that requirement, with $\sigma_{\text{sys}}^2 \sim 10^{-6}$.

The similarities between $E(e)$ and $\sigma(e)$ values for RBF, IDW and Kriging in Table 15 suggest these methods behave more or less the same when confronted with turbulent ellipticities. To check this, we have compiled in Fig. 9 the true ellipticity pattern of turbulent set 9 along with the actual predictions of the same pattern by all five interpolators. The same metrics for Polyfit and B-splines show that these global methods are even more handicapped by the presence of a KM spectrum.

Turbulence also makes the spatial distribution of the FWHM less predictable and the methods are affected to various degrees: RBF, IDW, Polyfit and B-Spline are little influenced with similar $E(R^2)$ and $\sigma(R^2)$ values in Tables 14 and 15 and on the corresponding plots in Figs. 7 and 8. The only one really impacted is Kriging.

- *Influence of star density*: following the discussion of Sect. 3.2, we expect the local interpolation methods to be more accurate than global ones on images with higher star density but see their performance degrade on sparser star fields. Such local interpolators base their predictions on

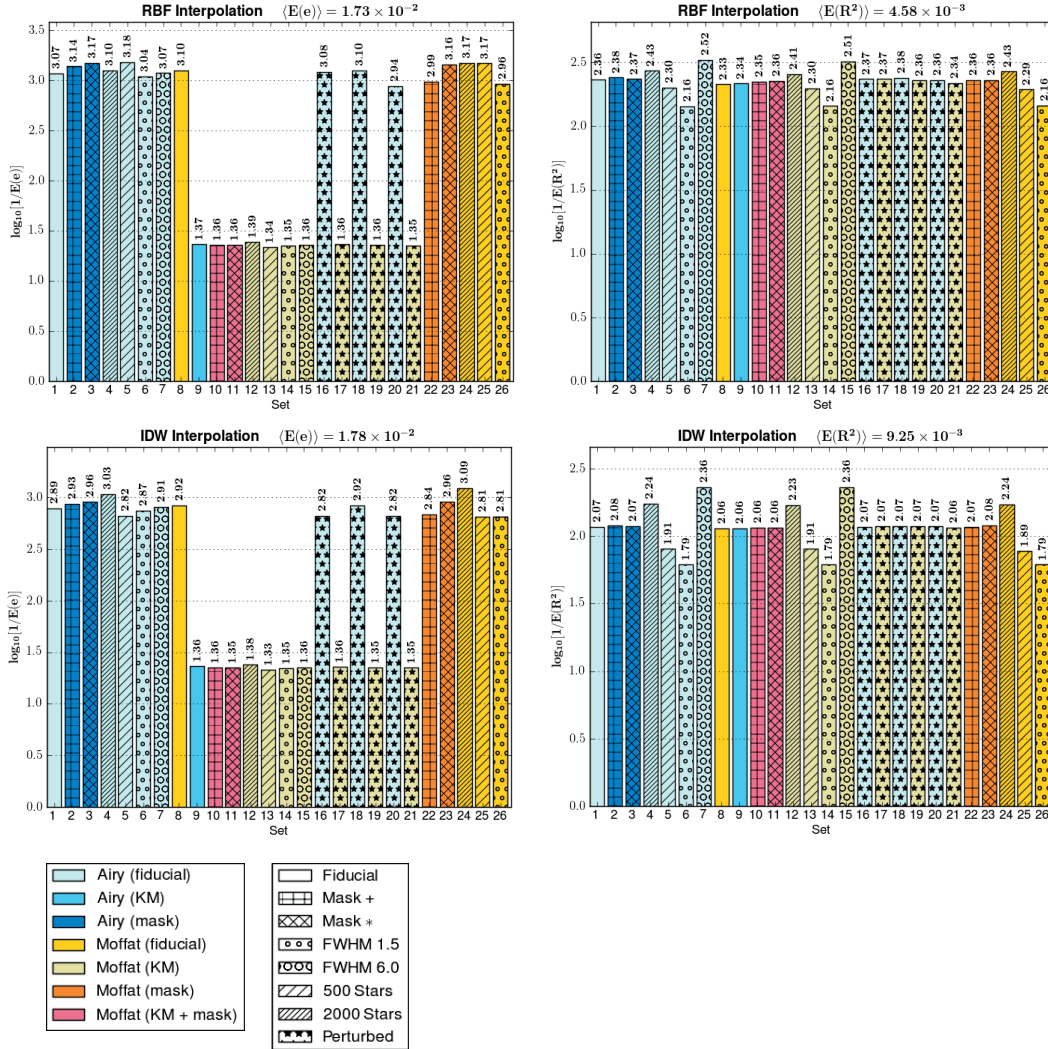


Fig. 7. Accuracy per set for the RBF and IDW interpolation methods. Sets with pseudo-Airy and Moffat are respectively colored in different shades of blue and orange, as specified in the legend at the bottom left of the figure. The various patterns contained in the left hand-side legend indicate the types of physical PSF features simulated in the images. The values on the bars correspond to $\log_{10}(1/E(e))$ and $\log_{10}(1/E(R^2))$ depending on the quantity plotted, so the taller the bar the greater the corresponding accuracy.

observations found in local neighborhoods and should therefore be in position to take advantage of any additional available. On the other hand, they should suffer comparatively more from insufficient sampling when the data is too sparse. This is indeed what we observe in the IDW plot Fig. 7, but the conclusion is less clear regarding RBF and Kriging: these schemes are indeed more accurate on denser sets when it comes to estimate the FWHM but the reverse is seen concerning ellipticities (plots Figs. 7 and 8). This is mostly noticeable on non-turbulent sets and may be caused by some overfitting taking place on denser ellipticity fields. This phenomenon does not occur on FWHM possibly because the

FWHM spatial distribution is generally smoother than that of ellipticities in the Star Challenge dataset.

We also expect the global interpolators B-splines and Polyfit to be little affected by difference in star density, since such schemes attempt to find a regression surface that takes all available data into account but at the same time minimize the overall bias through the least squares criterion. Such a surface tends to smooth out small-scale variations, mostly capturing broad features in the image. The corresponding predictions may become less accurate but, on the other hand, remain little influenced by sampling differences. This is exactly what we find in the plots of Polyfit and B-splines Fig. 8.

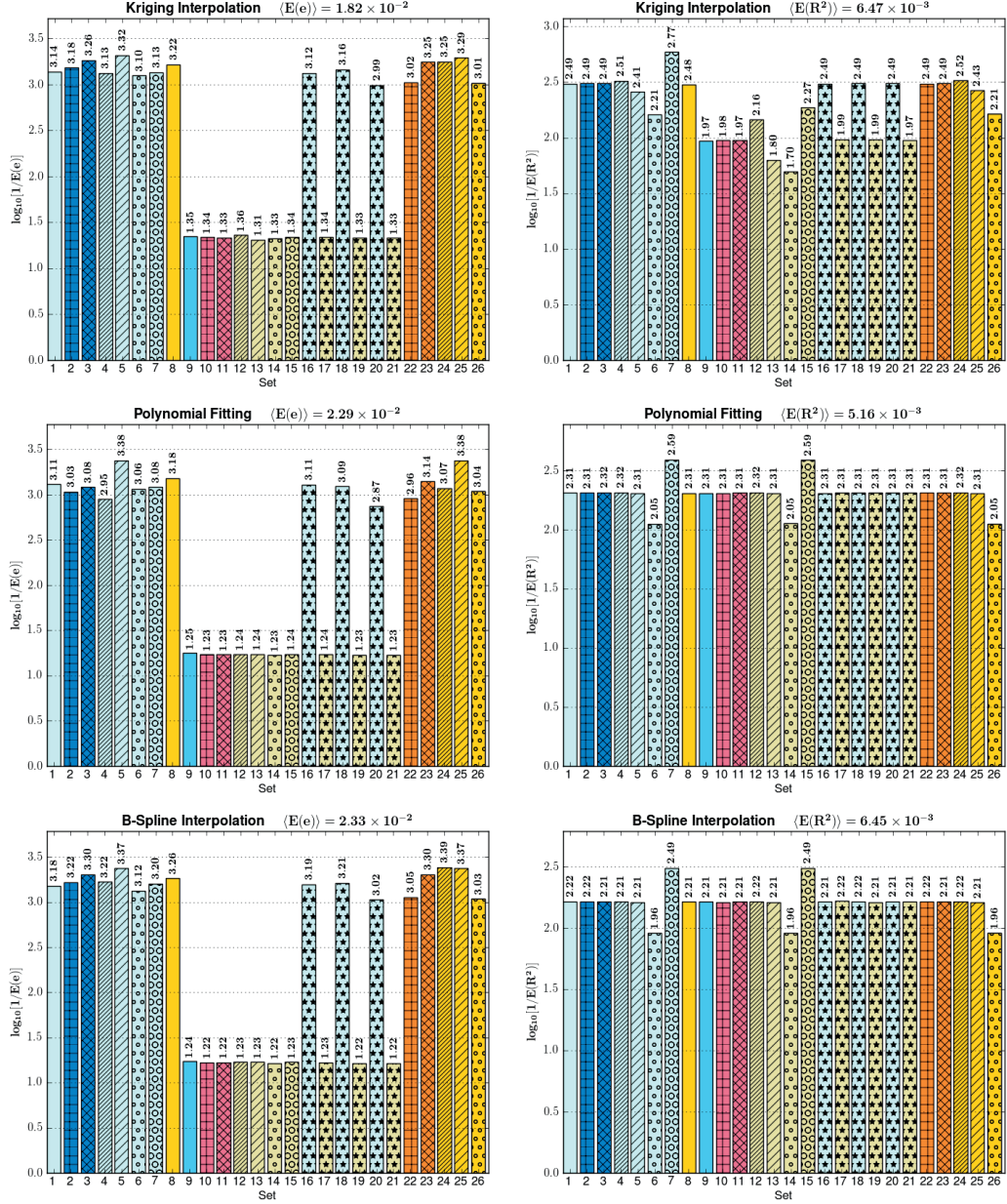


Fig. 8. Accuracy per set for Kriging, polynomial fitting and B-splines. The legend is the same as that used in Fig. 7. The values on the bars correspond to $\log_{10}(1/E(e))$ and $\log_{10}(1/E(R^2))$ depending on the quantity plotted, so the taller the bar the greater the corresponding accuracy.

The smoothness of the prediction surfaces of Polyfit and B-splines compared to that of local interpolators is clearly noticeable in Fig. 9.

- *Influence of the PSF model and size, masking and telescope effects:* although some interpolators do better than others

on a particular PSF models, each individual scheme perform equally well on Moffat and Airy images. This can be seen, for example, on fiducial sets 1 and 8 where the error statistics on Moffat or Airy sets are almost identical for a given method. The same can be said of the influence

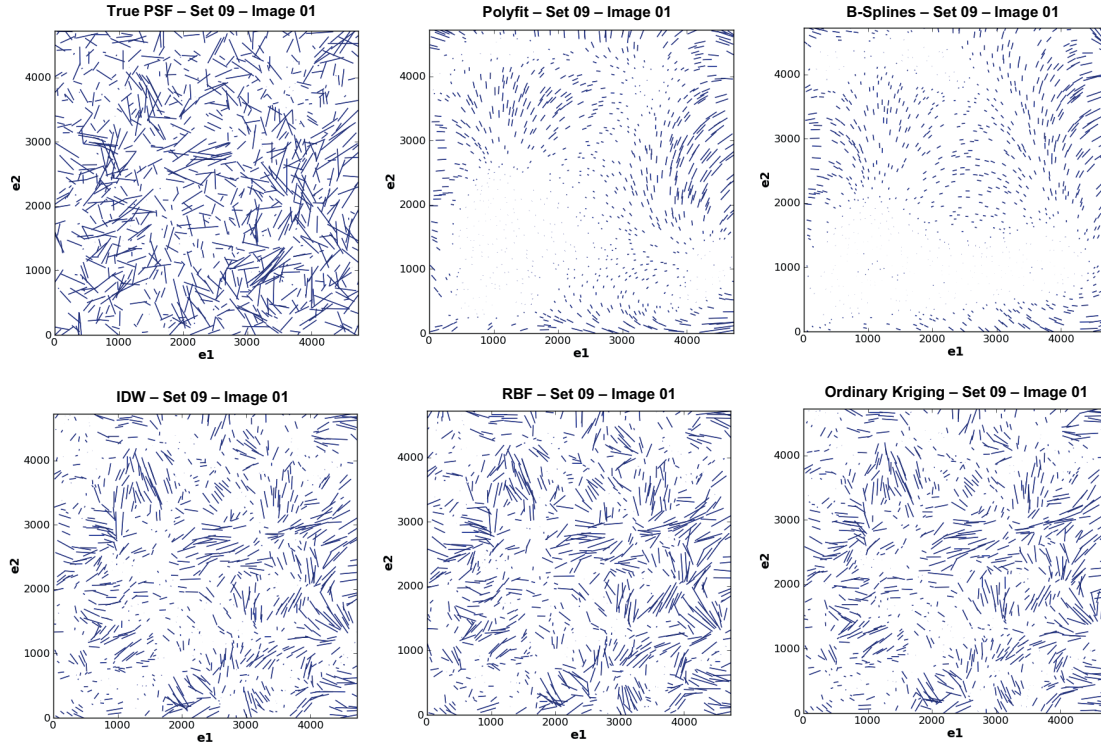


Fig. 9. An illustration of how the various interpolation methods studied in this article handled a turbulent PSF, which in this case is the first image of set 9. The true ellipticities are plotted on the upper-left corner of the figure and the remaining plots show the predictions of each method. The largest whisker in the upper-left corner plot corresponds to an ellipticity of 0.38.

Table 14. Non-turbulent sets: average values of E and σ .

Method	$E(e)$	$\sigma(e)$	$E(R^2)$	$\sigma(R^2)$
RBF	8.26×10^{-4}	3.60×10^{-5}	4.59×10^{-3}	1.45×10^{-4}
IDW	1.28×10^{-3}	5.67×10^{-5}	9.37×10^{-3}	2.95×10^{-4}
Kriging	7.06×10^{-4}	3.16×10^{-5}	3.57×10^{-3}	1.13×10^{-4}
Polyfit	8.37×10^{-4}	3.73×10^{-5}	5.23×10^{-3}	1.64×10^{-4}
B-splines	6.28×10^{-4}	2.80×10^{-5}	6.53×10^{-3}	2.06×10^{-4}

Table 15. Turbulent sets: average values of E and σ .

Method	$E(e)$	$\sigma(e)$	$E(R^2)$	$\sigma(R^2)$
RBF	4.36×10^{-2}	1.81×10^{-3}	4.57×10^{-3}	1.44×10^{-4}
IDW	4.42×10^{-2}	1.79×10^{-3}	9.05×10^{-3}	2.85×10^{-4}
Kriging	4.61×10^{-2}	1.79×10^{-3}	1.11×10^{-2}	3.49×10^{-4}
Polyfit	5.82×10^{-2}	1.89×10^{-3}	5.04×10^{-3}	1.58×10^{-4}
B-splines	5.97×10^{-2}	1.88×10^{-3}	6.31×10^{-3}	1.99×10^{-4}

of FWHM, masking and telescope effects. We also observe star size to have a negligible impact on $E(e)$ for all methods, but we clearly see that $E(R^2)$ significantly increases (resp. decreases) for star fields with smaller (resp. larger) FWHM. Finally, all methods reach a slightly higher accuracy on masked images, especially with 6-fold masks.

6.3. Results from individual interpolation methods

– *Interpolation with radial basis functions (RBF)*: as shown in our previous discussion, the RBF interpolation scheme is the overall winner of our evaluation. According to our benchmarks, ellipticity patterns were best estimated by a *linear kernel* function, whereas a *thin-plate kernel* was more effective on FWHM values. A neighborhood size between 30 and

40 stars was used. Refer to Sect. 3.5 and Table 5 for a description of RBF interpolation and the definitions of these kernels. That combination of linear and thin-plate kernels yields very competitive error statistics on both turbulent and non-turbulent sets: Tables 14 and 15 as well as plots Fig. 7 show RBF is the most accurate on turbulent sets whereas its results on non-turbulent sets are the second best behind ordinary Kriging. The possibility of selecting the most suitable kernel for a given PSF patterns is a very attractive feature of RBF interpolation.

– *Inverse distance weighted interpolation (IDW)*: the IDW methods (see Sect. 3.4) obtains the second best average $E(e)$ behind RBF over all sets as seen in Table 13. It does so thanks to very competitive $E(e)$ results on turbulent sets, just behind RBF (Table 15). But IDW's estimates of the FWHM

on non-turbulent sets are by far the worst of all five interpolation algorithms, both on ellipticity and size (Table 14). As found in Sect. 6.2, IDW looks quite sensitive to variations in star density. In fact, we observe that IDW underperforms on star fields with low-density and smaller FWHM (sets 5, 6, 13, 14, 25, 26). We were unable to find a setup that significantly improves that level of accuracy, which suggests the method has difficulty coping with such constraints in density and size. All in all, IDW performs quite well overall, knowing it is based on a very simple interpolation algorithm, with fewer adjustable parameters than RBF or ordinary Kriging (see Sect. 3.4).

- *Interpolation with ordinary Kriging (OK)*: despite its reputation of best interpolator on spatially-scattered data, ordinary Kriging, introduced in Sect. 3.6, arrives only third behind RBF and IDW when considering error statistics in Table 13. As seen in shown in Table 14 and plots Fig. 8, Kriging’s estimates on non-perturbed sets are the best of all five methods. But this cannot compensate for its relatively poor performance on estimating the FWHM on turbulent sets, as shown in the value of $E(R^2)$ in Table 15. The reason for this is probably related to the significant spatial drift of the FWHM values across the image. The condition of intrinsic stationarity required by ordinary Kriging is no longer fulfilled in some areas, especially near the edges of the image. As a result, we were forced to reduce the size of the search neighborhood over which the Kriging weights are calculated, which leads to a loss in accuracy in the corresponding regions. Kriging variants with ability to correct such a drift, like Universal Kriging, would probably achieve better results. Also, our implementation of Kriging for the Star Challenge assumes spatial isotropy, even though experimental variograms for ellipticity on non-turbulent sets also show evidence of geometric anisotropy. A more sophisticated implementation could have corrected these effects by rescaling and rotating coordinate axes along the direction of maximum spatial continuity.
- *Polynomial fitting (Polyfit)*: the results of Polyfit are of particular interest since polynomial fitting is currently the method of choice for modeling spatial variations of a PSF in lensing studies (see Sects. 2 and 3.1). polynomial fitting performs relatively well on non-turbulent sets with $E(e)$ and $E(R^2)$ statistics fairly close to those of RBF (Table 14). However, the corresponding statistics on turbulent sets are significantly worse than those achieved by local methods, as seen in Table 15. This confirms the conclusion of Sect. 3.1 whereby polynomials have difficulty coping with small or rapid variations found in a PSF pattern. Low-degree polynomials generally produce satisfactory result but tend to underfit the data, which leads to suboptimal accuracy. The resulting interpolation surfaces are characteristically smooth, as clearly observed in the Polyfit plot of Fig. 9. The Star Challenge images without KM power spectrum are smooth enough for Polyfit to approach the accuracy of RBF and ordinary Kriging. These results were obtained with a fifth-degree polynomial, higher degrees degrading the fit.
- *Interpolation with basis splines (B-splines)*: polynomial splines are generally considered superior for interpolation than simple polynomials as explained in Sect. 3.3, and we would have expected B-splines to achieve better results than Polyfit on the Star Challenge data. But this is not reflected in the averaged results from Tables 13. The level of accuracy reached by both interpolators is nevertheless of the same order.

As seen in Table 14 and plots Fig. 8, the ellipticity estimates from B-splines are superior to those of Polyfit on non-turbulent sets and of similar accuracy on turbulent ones. This tends to confirm the better ability of splines to capture small-scale and rapid variations in the data than polynomials. The results show, however, errors $E(R^2)$ on the FWHM much larger for B-splines than for Polyfit, which explains the relative lower performance compared to Polyfit. The FWHM spatial distribution being overall quite smooth in the Star Challenge images, this result suggests polynomials may be better suited than splines for modeling smoothly-varying patterns of variation. Combining both schemes may also be worth investigating.

7. Conclusions

The GREAT10 Star Challenge gave us the opportunity to evaluate several interpolation methods on spatially-varying PSF fields:

- Two global, approximate and deterministic spatial interpolation schemes: polynomial fitting (Polyfit) and basis splines (B-splines).
- Two local, exact and deterministic techniques relying on inverse distance weighting (IDW) and radial basis functions (RBF).
- An implementation of ordinary Kriging, a local, exact and stochastic spatial prediction method, frequently used in Geostatistics and environmental sciences.

We used a three-stage PSF estimation pipeline, which we described in Sect. 4.2 and Appendix A. Elliptical Moffat profiles were fitted to the stars contained in each Star Challenge image and then estimated and reconstructed at new positions in the same image using one of the five interpolation schemes listed above.

That approach proved quite successful since it allowed us to win the GREAT10 Star Challenge. We were, however, disappointed by the relatively high σ_{sys}^2 values reached, on the order of 10^{-4} , i.e., still far from the $\sigma_{\text{sys}}^2 \lesssim 10^{-7}$ target demanded by future large weak lensing surveys. The lack of accuracy could be traced to the suboptimal fitting of Airy PSF profiles by our pipeline and not to a deficiency in the PSF interpolation methods. However, this issue made it difficult to unambiguously conclude on the level of accuracy of individual interpolation algorithms, which is the main objective of this article.

In order to measure errors purely due to interpolation and only these, we used the true input ellipticity and FWHM catalog for the input Star Challenge images instead of our fitted estimates for these quantities. We also chose new metrics, better suited than the P -factor for assessing estimates on ellipticity and size. The results are summarized in Tables 13–15 along with the corresponding plots in Figs. 7 and 8. We highlight our main conclusions below.

- Table 13 shows the overall $E(e)$ and $E(R^2)$ errors to be on the order of 10^{-2} and 10^{-3} respectively. Figure 14, however indicates that $E(e) \sim 10^{-4}$ and $E(R^2) \sim 10^{-3}$ on images devoid of Kolmogorov turbulence, to be compared with the $E(e) \lesssim 10^{-3}$ and $E(R^2) \lesssim 10^{-3}$ estimated requirements of future next-generation surveys. Although the Star Challenge PSF fields lack realism in certain aspects, this suggests that the best methods, RBF, IDW and OK, may already be suitable for space-based surveys where turbulence is absent.

- All interpolation methods see their accuracy drastically degraded in images where atmospheric turbulence effects have been simulated, with $E(e)$ and $E(R^2)$ errors increased by a factor of ~ 100 . The better performance on turbulent images of RBF, IDW and OK compared to Polyfit and B-splines in the GREAT10 Star Challenge, suggests local methods may be able to better cope with turbulence than global ones. We note, however, that these results are only valid for the specific turbulence model used in the simulations and would have to be confirmed on real data.
- After turbulence, the factors influencing results the most are the density of stars and their size. As far as density is concerned, local methods are more impacted than global ones and generally improve their estimates on denser sets much more than global methods. A similar conclusion is reached concerning local methods as far as PSF size is concerned. However, the results suggest both global and local methods have difficulty coping with objects smaller than the fiducial FWHM of 3 pixels. Among all methods, IDW suffered the most from sparse star fields with small FWHM.
- The RBF interpolator proved the most accurate, reaching the best results on both turbulent and non-turbulent sets. The use of kernel functions brings additional versatility compared to a simpler interpolator like IDW, while avoiding the complexity of Kriging. The selection of the most suitable kernel function and associated parameters can be greatly simplified by the use of cross-validation or Jackknifing. These techniques, as shown in Sect. 4.3, can prove very helpful to tune the runtime parameters of an interpolation schemes and evaluate the accuracy of its results.
- Despite its simplicity, the IDW interpolation method obtained better than expected results, outperforming polynomials and splines in the simulations. Fast and easy to tune, it could potentially constitute a simple alternative/complement to polynomials before trying more elaborate interpolation schemes such as Kriging or RBF.
- Ordinary Kriging is, in our opinion, potentially the most accurate method as shown especially by its results on non-turbulent images. However, the FWHM spatial distributions in the Star Challenge have a significant spatial drift that the standard ordinary Kriging algorithm is unable to correct. Another Kriging variant such as Universal Kriging would possibly have proved more accurate. It remains that Kriging, because of its sophistication, is more difficult and time consuming to operate than the other interpolators we evaluated.
- Overall, our analysis of the Star Challenge results suggests local interpolators should be preferred over global ones based on splines and polynomials. However, one should bear in mind that (1) these results are based on simulated data where star images are isolated, bright enough and well sampled; (2) the spatial variation of the PSF as simulated in GREAT10 may tend to favor local interpolators over global ones. We strongly believe, nevertheless, that local interpolation schemes for PSF interpolation have the potential to improve the accuracy of existing and future ground-based lensing surveys and deserve to be investigated further.

Acknowledgements. We thank Tom Kitching for his help and especially for providing us with the true input ellipticity and FWHM catalog of the Star Challenge PSF images. We also acknowledge support from the International Space Science Institute (ISSI) in Bern, where some of this research has been discussed. This work is supported by the Swiss National Science Foundation (SNSF).

Appendix A: Our PSF prediction pipeline (PSFPP)

A.1. Overview

The PSF prediction pipeline used in the Star Challenge is outlined in Fig. 5. A PSF field is fed into the pipeline and goes through three processing stages:

1. *Fitting* stage: the Moffat PSF model described in Sect. 4.1 is fitted to each star at known position (x_c, y_c) in the PSF field image. A catalog is produced, containing a set of fitted parameters $\{(x_c, y_c); (e_1, e_2); \phi, (\alpha, \beta)\}$ for each star. Instead of an out-the-box minimizer, we employ a custom minimizer we developed at the EPFL Laboratory of astrophysics and well suited to fitting faint and noisy images like those frequently found in weak lensing. The minimizer uses an “adaptive cyclic coordinate descent algorithm” that find a local minimum with the lowest χ^2 of the residuals. That same minimizer has also been used in the version of the *gfit* shear measurement method that competed in the GREAT10 Galaxy Challenge (Kitching et al. 2012). The star images processed by the minimizer are 16×16 -pixel cutouts instead of the original 48×48 -pixel postage stamps.
2. *Prediction* stage:
 - First, an analysis of the spatial distribution of each parameter across the image is performed. In particular, all separation distances between stars are recorded in the form of *KD-trees* (Bentley 1975) for efficiently finding the nearest neighboring stars located within a given separation distance $\|h\|$.
 - Second, a spatial prediction scheme is applied to estimate the values $Z'_p(x'_i, y'_i)$ of the parameter p at asked locations (x'_i, y'_i) , given the fitted parameter values $Z_p(x_i, y_i)$ obtained in the previous stage. One of the four methods described in Sect. 3 is applied here.
3. *Reconstruction* stage: All stars in a PSF field are reconstructed based on the elliptical Moffat model described in Sect. 4.1, but using the parameters predicted for that star during the *Prediction* stage.

A.2. Pipeline implementation and configuration

The pipeline code is written in Python, a programming language known for its power, flexibility and short development cycle. The usual standard Python libraries are used, notably: NumPy, SciPy, PyFITS and matplotlib. SciPy is the standard scientific library for Python. Most of its functions are thin Python wrappers on top of fortran, C and C++ functions. SciPy takes advantage of installed optimized libraries such as LAPACK (Linear Algebra PACKage) library (Anderson et al. 1990). We employ the cross-validation and Jackknifing resampling techniques (see Sect. 4.3) to tune the run-time parameters for the interpolation schemes and evaluate the accuracy of the results. We highlight below a few aspects related to the implementation of the methods.

- IDW: the code for Inverse Distance Weighted interpolation is written in Python, based on Eq. (2) with weighting factors specified by (8). The free parameters are the power factor β and the neighborhood size N (see Sect. 3.4). A configuration with $\beta = 2$, with $5 \leq N \leq 15$ depending on the density of stars in images gives the best results according to our tests.
- RBF: we use the `rbf()` interpolation function available in the *SciPy interpolate* module. The number of parameters to tune is greater compared to IDW: a kernel function chosen among those listed in Table 5; the neighborhood search size

- N ; a shape parameter ϵ for the *multiquadric*, *inverse multiquadric* and *Gaussian* kernels; and a last parameter for controlling the smoothness of the interpolation (see Sect. 3.5). Only the *linear*, *thin-plate* and *multiquadric* kernels gave stable enough predictions. Choosing $25 \leq N \leq 30$ and disabling smoothing (i.e. use exact interpolation) yielded the best cross-validation and Jackknifing results for the chosen kernels.
- splines: we have selected the `bisplrep()` and `bisplev()` bivariate B-spline interpolation functions provided by the SciPy `interpolate` module. These functions are Python wrappers on top of the fortran FITPACK package (Dierckx 1995). The underlying algorithms follow the *constructive* approach for spline interpolation described in Sect. 3.3 and are specified in Dierckx (1980). The main parameters affecting the interpolation are the degree p of the spline, the number of knots N and a smoothing factor s . We have fixed p to 3 but let the algorithm automatically set N and s .
 - Kriging: we have used our own custom-developed Python code of ordinary Kriging (see Sect. 3.6). The Kriging used in the Star Challenge and in this article is isotropic and does not implement any spatial anisotropy or drift correction scheme. The accuracy of the ordinary Kriging interpolation scheme was influenced by the following set of parameters:
 - The interpolation range, i.e. the range in pixels used for interpolation. Depending on the images, we chose a circular area with a radius between 700 and 1000 pixels from the center of the 4800×4800 PSF field.
 - Lag distance h in pixels. We used values in the range $100 \leq h \leq 300$ depending on the image and the PSF model parameter to estimate.
 - The number of observations N in Eq. (19) to include in the neighborhood: we used $5 \leq N \leq 20$ depending on the image star density.
 - Tolerance distance Δh (pixels) and angle $\Delta \theta$ considered when locating neighboring observations. As a rule of thumb, we selected $\Delta h \approx h/2$ and $\Delta \theta = 22.5^\circ$.
 - A theoretical variogram model such as those listed in Table 7. The experimental variograms were fitted using the *Levenberg-Marquardt* least-squares `leastsq` routine from the SciPy `optimize` module. The program dynamically selected the theoretical variogram models and parameters that produced the best fit.
 - The Polyfit code is based on the `leastsq()` function from the SciPy `optimize` Python module. A least-squares fit to a bivariate polynomial of degree 5 gave the best estimates.

References

- Abramowitz, M., & Stegun, I. A. 1965, Handbook of Mathematical Functions, 1st edn., Dover books on mathematics (Dover Publications)
- Amara, A., & Réfrégier, A. 2008, MNRAS, 391, 228
- Anderson, E., Bai, Z., Dongarra, J., et al. 1990, in Proc. 1990 ACM/IEEE conference on Supercomputing, Supercomputing '90 (Los Alamitos, CA, USA: IEEE Computer Society Press), 2
- Bentley, J. L. 1975, Commun. ACM, 18, 509
- Bergé, J., Pacaud, F., Réfrégier, A., et al. 2008, MNRAS, 385, 695
- Bergé, J., Price, S., Amara, A., & Rhodes, J. 2012, MNRAS, 419, 2356
- Bernstein, G. M., & Jarvis, M. 2002, AJ, 123, 583
- Born, M., & Wolf, E. 1999, Principles of Optics: Electromagnetic Theory of Propagation, Interference and Diffraction of Light, ed. C. U. Press, Vol. 7th Edition (Cambridge University Press), 986
- Bridle, S., Balan, S. T., Bethge, M., et al. 2010, MNRAS, 405, 2044
- Browne, M. 2000, J. Math. Psychol., 44, 108
- Brus, D. J., Gruijter, J. J. D., Marsman, B. A., et al. 1996, Environmetrics, 7, 1
- Buhmann, M. D. 2003, Radial basis functions: theory and implementations (Cambridge University Press), 12, 274
- Burrough, P. 1988, Principles of geographical information systems for land resources assessment, Monographs on soil and resources survey (Oxford University Press)
- Burrough, P., & McDonnell, R. 1998, Principles of geographical information systems, Spatial information systems and geostatistics (Oxford University Press)
- Chilès, J., & Delfiner, P. 1999, Geostatistics: modeling spatial uncertainty, Wiley series in probability and statistics (Wiley)
- Clowe, D., & Schneider, P. 2002, A&A, 395, 385
- Collins, F. C., & Bolstad, P. V. 1996, A Comparison of Spatial Interpolation Techniques in Temperature Estimation (USA: NCGIA – National Center for Geographic Information and Analysis)
- Cox, M. G. 1972, IMA J. Appl. Math., 10, 134
- Craven, P., & Wahba, G. 1978, Numerische Mathematik, 31, 377
- Cressie, N. 1991, Statistics for spatial data, Wiley series in probability and mathematical statistics: Applied probability and statistics (J. Wiley)
- Davis, B. M. 1987, Mathematical Geology, 19, 241
- de Boor, C. 1972, J. Approximation Theory, 6, 50, collection of articles dedicated to J. L. Walsh on his 75th birthday, V (Proc. Internat. Conf. Approximation Theory, Related Topics and their Applications, Univ. Maryland, College Park, Md., 1970)
- de Boor, C. 1978, A Practical Guide to Splines (Springer-Verlag Berlin and Heidelberg GmbH & Co. K)
- Deutsch, C. V., & Journé, A. 1997, GSLIB: geostatistical software library and user's guide, Applied Geostatistics (Oxford University Press)
- Dierckx, P. 1980, An algorithm for surface fitting with spline functions (Katholieke Univ. Leuven)
- Dierckx, P. 1995, Curve and surface fitting with splines, Monographs on numerical analysis (Clarendon Press)
- Duchon, J. 1976, RAIRO Analyse numérique, 10, 1
- Efron, B. 1982, The Jackknife, the Bootstrap and Other Resampling Plans, ed. S. I. A. M.Editors (Society for Industrial and Applied Mathematics), 38, 92
- Efron, B., & Gong, G. 1983, Am. Stat., 37, 36
- Foley, T. A. 1994, J. Appl. Sci. Comput., 1, 51
- Franke, R. 1982, Mathematics of Computation, 38, 181
- Fu, L., Semboloni, E., Hoekstra, H., et al. 2008, A&A, 479, 9
- Geisser, S. 1975, J. Am. Stat. Assoc., 70, 320
- Goovaerts, P. 1997, Geostatistics for natural resources evaluation, Applied geostatistics series (Oxford University Press)
- Green, P., & Silverman, B. 1994, Nonparametric regression and generalized linear models: a roughness penalty approach, Monographs on statistics and applied probability (Chapman & Hall)
- Hardy, R. L. 1971, J. Geophys. Res., 76, 1905
- Hardy, R. L. 1990, Computers Mathematics with Applications, 19, 163
- Hayes, J. G., & Halliday, J. 1994, Teaching Mathematics and its Applications, 14, 89
- Hettterscheidt, M., Simon, P., Schirmer, M., et al. 2007, A&A, 468, 859
- Heymans, C., Brown, M. L., Barden, M., et al. 2005, MNRAS, 361, 160
- Heymans, C., Van Waerbeke, L., Bacon, D., et al. 2006, MNRAS, 368, 1323
- Heymans, C., Rowe, B., Hoekstra, H., et al. 2012, MNRAS, 421, 381
- Hirata, C., & Seljak, U. 2003, MNRAS, 343, 459
- Hoekstra, H. 2004, MNRAS, 347, 1337
- Hoekstra, H., Franx, M., Kuijken, K., & Squires, G. 1998, ApJ, 504, 636
- Hutchinson, M. F. 1995, International journal of geographical information systems, 9, 385
- Hutchinson, M., & Gessler, P. 1994, Geoderma, 62, 45
- Isaaks, E. H., & Srivastava, R. 1989, Applied geostatistics (Oxford University Press)
- Jain, B., Jarvis, M., & Bernstein, G. 2006, J. Cosmology Astropart. Phys., 2, 1
- Jarvis, M., & Jain, B. 2004, unpublished [arXiv:0412234]
- Jarvis, M., Schechter, P., & Jain, B. 2008, PASP submitted [arXiv:0810.0027]
- Jee, M. J., & Tyson, J. A. 2011, PASP, 123, 596
- Jee, M. J., White, R. L., Benítez, N., et al. 2005a, ApJ, 618, 46
- Jee, M. J., White, R. L., Ford, H. C., et al. 2005b [arXiv:0508044]
- Jee, M. J., White, R. L., Ford, H. C., et al. 2006, ApJ, 642, 720
- Jee, M. J., Blakeslee, J. P., Sirianni, M., et al. 2007a, PASP, 119, 1403
- Jee, M. J., Ford, H. C., Illingworth, G. D., et al. 2007b, ApJ, 661, 728
- Journé, A., & Huijbregts, C. 1978, Mining geostatistics (Academic Press)
- Kaiser, N. 2000, ApJ, 537, 555
- Kaiser, N., Squires, G., & Broadhurst, T. 1995, ApJ, 449, 460
- Kitching, T. D., Amara, A., Abdalla, F. B., Joachimi, B., & Réfrégier, A. 2009, MNRAS, 399, 2107
- Kitching, T., Amara, A., Gill, M., et al. 2011, Ann. Appl. Stat., 5, 2231
- Kitching, T. D., Balan, S. T., Bridle, S., et al. 2012, MNRAS, 423, 3163
- Krige, D. G. 1951, J. Chem. Metall. Mining Soc. of South Africa, 52, 119
- Kuijken, K. 2008, A&A, 482, 1053

- Laslett, G. M., McBratney, A. B., Pahl, P. J., & Hutchinson, M. F. 1987, *J. Soil Sci.*, 38, 325
- Lauer, T. 2002, in *SPIE Conf. Ser.* 4847, eds. J.-L. Starck, & F. D. Murtagh, 167
- Lukaszyk, S. 2004, *Computational Mechanics*, 33, 299
- Luppino, G. A., & Kaiser, N. 1997, *ApJ*, 475, 20
- Lupton, R., Gunn, J. E., Ivezić, Z., et al. 2001, in *Astronomical Data Analysis Software and Systems X*, eds. F. R. Harnden Jr., F. A. Primini, & H. E. Payne, *ASP Conf. Ser.*, 238, 269
- Massey, R., & Refregier, A. 2005, *MNRAS*, 363, 197
- Massey, R., Heymans, C., Bergé, J., et al. 2007, *MNRAS*, 376, 13
- Matheron, G. 1962, *Traité de Géostatistiques Appliquées*, Tome I., Vol. 14 (Editions Technip)
- Matheron, G. 1963, *Economic Geology*, 58, 1246
- Matheron, G. 1965, *Les variables régionalisées et leur estimation*, Paris
- Meinguet, J. 1979, *ZAMP*, 30, 292
- Melchior, P., Böhnert, A., Lombardi, M., & Bartelmann, M. 2010, *A&A*, 510, A75
- Micchelli, C. A. 1986, *Constructive Approximation*, 2, 11
- Miller, R. G. 1974, *Biometrika*, 61, 1
- Moffat, A. F. J. 1969, *A&A*, 3, 455
- Nakajima, R., Bernstein, G. M., Fadely, R., Keeton, C. R., & Schrabback, T. 2009, *ApJ*, 697, 1793
- Paulin-Henriksson, S., Antonuccio-Delogu, V., Haines, C. P., et al. 2007, *A&A*, 467, 427
- Paulin-Henriksson, S., Amara, A., Voigt, L., Refregier, A., & Bridle, S. L. 2008, *A&A*, 484, 67
- Paulin-Henriksson, S., Refregier, A., & Amara, A. 2009, *A&A*, 500, 647
- Prenter, P. 2008, *Splines and Variational Methods* (Dover Publications)
- Press, W. H., Teukolsky, S. A., Vetterling, W. T., & Flannery, B. P. 2007, *Numerical Recipes, The Art of Scientific Computing*, 3rd edn. (Cambridge University Press)
- Quenouille, M. H. 1956, *Biometrika*, 43, 353
- Refregier, A. 2003, *MNRAS*, 338, 35
- Refregier, A., & Bacon, D. 2003, *MNRAS*, 338, 48
- Renka, R. J. 1988, *ACM Trans. Math. Softw.*, 14, 139
- Rippa, S. 1999, *Adv. Comp. Math.*, 11, 193
- Romano, A., Fu, L., Giordano, F., et al. 2010, *A&A*, 514, A88
- Schrabback, T., Hartlap, J., Joachimi, B., et al. 2010, *A&A*, 516, A63
- Schumaker, L. 2007, *Spline functions: basic theory*, Cambridge mathematical library (Cambridge University Press)
- Shepard, D. 1968, in *ACM '68: Proc. 1968 23rd ACM national conference* (New York, NY, USA: ACM), 517
- Stabenau, H. F., Jain, B., Bernstein, G., & Lampton, M. 2007, *ArXiv e-prints*
- Stone, M. 1974, *J. Roy. Stat. Soc. Ser. B Methodol.*, 36, 111
- Tomczak, M. 1998, *J. Geog. Inf. Dec. Anal.*, 2, 18
- Tukey, J. 1977, *Exploratory data analysis*, Addison-Wesley series in behavioral sciences (Addison-Wesley Pub. Co.)
- Tukey, J. W. 1958, *Bias and confidence in not-quite large samples*
- Umetsu, K., Medezinski, E., Broadhurst, T., et al. 2010, *ApJ*, 714, 1470
- Van Waerbeke, L., Mellier, Y., Radovich, M., et al. 2001, *A&A*, 374, 757
- Van Waerbeke, L., Mellier, Y., Pelló, R., et al. 2002, *A&A*, 393, 369
- Van Waerbeke, L., Mellier, Y., & Hoekstra, H. 2005, *A&A*, 429, 75
- Wackernagel, H. 2003, *Multivariate geostatistics: an introduction with applications* (Springer)
- Wahba, G. 1990, *Spline models for observational data*, CBMS-NSF regional conference series in applied mathematics (Society for Industrial and Applied Mathematics)
- Wahba, G., & Wendelberger, J. 1980, *Monthly Weather Rev.*, 108, 1122
- Waller, L., & Gotway, C. 2004, *Applied spatial statistics for public health data*, Wiley series in probability and statistics (John Wiley & Sons)
- Webster, R., & Oliver, M. 2007, *Geostatistics for environmental scientists*, Statistics in practice (Wiley)

4.6 A denoising scheme for weak lensing

As discussed in Sect. 4.1.2, the most valuable galaxy images for weak lensing analysis are also the faintest, which are often the noisiest ones. It is thus of interest to look for noise correction techniques capable of improving the signal-to-noise ratio () of such images while preserving the shape information that encodes the shear signal. In fact, any kind of shear measurement algorithm can potentially improve its accuracy in this way. Moreover, a good denoising scheme also allows to process galaxy images which otherwise would not be usable for weak lensing analysis.

The author, in collaboration with Dr. G. Nurbaeva, Dr. F. Courbin and Prof. G. Meylan, explored the applicability to weak lensing images of three popular denoising schemes: median filtering (e.g., Arce 2005), Wiener filtering (Wiener 1949) and discrete wavelet transform (DWT) with Bayes thresholding. We tested these algorithms on synthetic data with known ellipticities and the same characteristics as the GREAT08 datasets, varying S/N, resolution and sampling. We also evaluated the same algorithms on the actual low-noise and high-noise GREAT08 datasets (Bridle et al. 2009, 2010). We measured the effectiveness of these algorithms in eliminating noise while preserving ellipticities by running the KSB+ code developed by Catherine Heymans and Ludovic Van Waerbeke (Heymans et al. 2006). The results are discussed in the Nurbaeva et al. (2011) paper, included below as part of this thesis.

While performing this research we discovered that an algorithm combining DWT and Wiener, which we called “DWT-Wiener”, significantly improved the accuracy of shape measurement on our datasets. The corresponding results are also included in our paper. The DWT-Wiener scheme has been since tested in the GREAT10 Galaxy Challenge by several shear measurement methods developed at the laboratory of astrophysics of EPFL: *gfit* Gentile et al. (2012), MegaLUT (Tewes et al. 2012) and TVNN (Nurbaeva et al. 2013). In all cases, significant improvements in accuracy were obtained. An analysis of the effect of the application of DWT-Wiener on accuracy and bias by *gfit* in GREAT10 is also included in Gentile et al. (2012). We will soon release the code of DWT-Wiener to the image processing and astronomical communities.

We refer the reader to the article below for further details on this study.

On the effect of image denoising on galaxy shape measurements

G. Nurbaeva, F. Courbin, M. Gentile, and G. Meylan

Laboratoire d'astrophysique, École Polytechnique Fédérale de Lausanne (EPFL), Observatoire de Sauvigny, 1290 Versoix, Switzerland

Received 21 January 2011 / Accepted 24 April 2011

ABSTRACT

Weak gravitational lensing is a very sensitive way of measuring cosmological parameters, including dark energy, and of testing current theories of gravitation. In practice, this requires exquisite measurement of the shapes of billions of galaxies over large areas of the sky, as may be obtained with the EUCLID and WFIRST satellites. For a given survey depth, applying image denoising to the data both improves the accuracy of the shape measurements and increases the number density of galaxies with a measurable shape. We perform simple tests of three different denoising techniques, using synthetic data. We propose a new and simple denoising method, based on wavelet decomposition of the data and a Wiener filtering of the resulting wavelet coefficients. When applied to the GREAT08 challenge dataset, this technique allows us to improve the quality factor of the measurement (Q ; GREAT08 definition), by up to a factor of two. We demonstrate that the typical pixel size of the EUCLID optical channel will allow us to use image denoising.

Key words. methods: data analysis – techniques: image processing – gravitational lensing: weak – dark energy – cosmological parameters – methods: statistical

1. Introduction

The observed accelerated expansion of the Universe (Riess et al. 1998; Perlmutter et al. 1999) can currently be explained by either the existence of a repulsive force associated with so-called “dark energy”, or an erroneous description of gravity by General Relativity on large spatial scales (for a review, see Frieman et al. 2008). Both explanations have profound implications for our understanding of cosmology and physics in general and are the main motivations of future large cosmological surveys. These surveys, such as the ESA EUCLID satellite project (Réfrégier et al. 2010) combine several complementary cosmological probes to constrain the cosmological parameters, including the dark energy equation of state parameter $w(z)$ and its evolution with redshift.

The main cosmological probe to be employed by EUCLID is weak gravitational lensing, also known as cosmic shear. The observational signature of cosmic shear is an apparent distortion of the image of distant galaxies under the influence of gravitational lensing by a foreground potential well. The exact way in which the galaxies are distorted is very sensitive to the dark matter and dark energy distributions in the foreground large-scale structures, hence providing an efficient tool for cosmological measurements. While the first detections of cosmic shear are already a decade old and were performed on data with relatively limited field of view and depth (Bacon et al. 2000; van Waerbeke et al. 2000; Wittman et al. 2000), the use of cosmic shear in terms of cosmological applications requires a major space survey. However, the effectiveness of the method in constraining cosmology relies on image processing techniques that measure the shapes of individual galaxies in the most accurate possible way. These techniques must provide solutions to the four following problems: (i) the degradations caused by the dominating Poisson noise; (ii) the sampling adopted to represent the data; (iii) the convolution by the instrumental point spread function (PSF) and its possible variations across the field

of view; and (iv) the measurement of the cosmic shear itself and its power spectrum from all the galaxy shape measurements, i.e., billions of galaxies.

The techniques currently in use to measure cosmic shear are sufficient to detect it and even sometimes to reconstruct the 3D mass map of large-scale structures (e.g., Massey et al. 2007a) but it is estimated that a tenfold improvement in the precision of galaxy shape measurements is needed to place stringent constraints on cosmological models. Thanks to both the STEP programs (Heymans et al. 2006; Massey et al. 2007b) and the GREAT08¹ challenge (Bridle et al. 2010), the lensing community has made excellent progress toward meeting this goal. However, even the most successful shear measurement methods see their accuracy decrease significantly under high noise conditions. It is therefore of interest to develop suitable denoising techniques that are capable of solving the difficult problem of removing noise without compromising the fragile shear signal.

In the present work, we focus on the effects of denoising and pixelisation on shape measurement. Both are closely connected since the spatial frequencies contained in the galaxy images change with the adopted pixel size, but not the noise frequency. Moreover, for a given exposure time, changing the pixel size affects the signal-to-noise ratio (SNR) of the data.

For this reason, it is important to explore the large parameter space of the problem and to weight the relative impacts of different samplings and $SNRs$ on the shear measurement. To investigate this problem, we use sets of synthetic galaxies with known ellipticities, for different resolutions and samplings spanning a range of observational setups. Using these data, as well as a subset of the GREAT08 data (Bridle et al. 2010), we test the performance of three popular denoising algorithms: median filtering, Wiener filtering, and discrete wavelet transform (DWT). We also propose a new denoising method based on a combination of wavelet transform and Wiener filtering.

¹ <http://www.greatchallenges.info/>

2. Methods

2.1. Median filter

The median filter is a nonlinear denoising technique widely used in digital image processing. Apart from its simplicity, median filtering has two important properties: firstly, it is particularly effective for images corrupted by Poisson noise and secondly, it preserves edges in images.

A median filter works by sliding a box of given size (3×3 pixels in our case) over the image, replacing the central value by the median of its neighboring pixels (Arce 2005; Arias-Castro & Donoho 2009).

2.2. Wiener filter

The Wiener filter uses a least mean squares filtering algorithm (Wiener 1949) based on a stochastic framework that minimizes the mean square error in the noise. The Wiener filter has become a classical signal smoothing technique and is widely used in signal processing (Khiredine et al. 2007; Press et al. 2007). In our study, we use the following simplified algorithm.

If we define I to be the input brightness of the pixel of the noisy image, the output brightness I_{wiener} of the denoised pixel is then given by

$$I_{\text{wiener}} = \begin{cases} I(1 - \sigma_n^2/\sigma_w^2), & \sigma_w^2 \geq \sigma_n^2, \\ 0, & \sigma_w^2 < \sigma_n^2, \end{cases} \quad (1)$$

where σ_n is the estimated mean standard deviation of the noise in the image and σ_w^2 is an average variance in the pixel values calculated in a local window of 3×3 pixels.

The algorithm implemented in this work uses the scientific libraries (SciPy community 2010) available with the Python programming language.

2.3. Discret wavelet transform (DWT)

Wavelet analysis is an efficient and fast computational technique widely used for data compression and noise reduction (Bruce et al. 1996). In our study, we apply the 2D discrete wavelet transform (DWT). Denoising in wavelet space involves three steps: (i) linear forward wavelet decomposition, (ii) shrinkage of wavelet coefficients, and (iii) linear inverse wavelet reconstruction.

As the basis function we adopt the Haar wavelet, which is orthogonal and computationally simple. The latter property is of primary importance to preserving shape invariance.

The Haar wavelet is defined by two basic functions: a scaling function ϕ and a wavelet function, called the mother wavelet ψ . The set of basic functions for the 1D case is given by

$$\begin{cases} \phi_i^j(x) = \phi(2^{k-j}x - i) \\ \psi_i^j(x) = \psi(2^{k-j}x - i), \end{cases} \quad i = 0, 1, 2, \dots, N-1 \quad (2)$$

where $N = 2^k - j$ is the number of wavelet coefficients, which also defines the size of the subband of a given decomposition level j , where k is the coarsest level. The scaling function and the mother wavelet are defined as follows:

$$\phi(x) = \begin{cases} 1, & 0 \leq x < 1 \\ 0, & \text{otherwise} \end{cases} \quad \psi(x) = \begin{cases} 1, & 0 \leq x < 1/2 \\ -1, & 1/2 \leq x < 1 \\ 0, & \text{otherwise.} \end{cases} \quad (3)$$

To decompose a two-dimensional image, the coefficients are obtained by multiplying the one-dimensional scaling and the

wavelet functions both in the horizontal and vertical directions. For each resolution level, the image is divided into four images of coefficients, called subbands. The first, often labeled *LL* (low-low), contains the main (low)-frequency features of the signal. The three others are dominated by the noise in the horizontal direction, *HL* (high-low), vertical direction, *LH* (low-high), and diagonal direction, *HH* (high-high). Iterating the described scheme (Eq. (2)), one can obtain an image sequence with a cascading structure as illustrated in Fig. 2.

The most important part of the DWT denoising technique is the wavelet shrinkage, which drives the efficiency of denoising. The wavelet shrinkage is applied to the subbands associated with the noise: *HL*, *LH*, and *HH*. The classical way to suppress the noise by shrinking the wavelet coefficients is to apply a threshold to the wavelet coefficients. There are two types of thresholding algorithms: soft and hard thresholding. For a given value of the threshold T , hard thresholding sets all coefficients less than T to zero. For the soft thresholding, T is subtracted from all coefficients greater than T (see e.g., Vetterli & Kovacevic 1995).

2.3.1. Bayes thresholding

The wavelet shrinkage step depends heavily on the choice of the thresholding scheme. Popular thresholding methods include Stein's unbiased risk estimate (SURE; Donoho & Johnstone 1994) and universal thresholding (Donoho & Johnstone 1995), the latter depending on image size. A more efficient thresholding scheme is the Bayes wavelet threshold proposed by Chang (2000), which uses a different threshold level for each of the three *HL*, *LH*, and *HH* noise subbands. This adaptive threshold, T_{Bayes} , is computed to be

$$T_{\text{Bayes}} = \frac{\sigma_n^2}{\sigma_x}, \quad (4)$$

where σ_x is the standard deviation in the noiseless coefficients in a given subband, which can be estimated as

$$\sigma_x = \sqrt{\max(\sigma_y^2 - \sigma_n^2, 0)}, \quad (5)$$

where σ_y^2 is the variance in the coefficients in a subband. If $\sigma_x = 0$ then T_{Bayes} diverges to infinity, meaning that all coefficients in the corresponding subband must be set to zero.

2.3.2. Combined DWT-Wiener filter: a new thresholding scheme

The DWT-Bayes thresholding gives good results for general-purpose imaging of relatively small dynamical range. However, it is quickly limited when dealing with astronomical images where the intensity levels vary sharply on spatial scales in the order of the PSF size. Standard thresholding, where T is the same across each wavelet subband, degrades galaxy shapes with steep intensity profiles, especially when images are critically sampled. This is simply because the light profile between two neighboring pixels is much steeper than the estimated noise per pixel, σ_n . The resulting denoised image is therefore too smooth in rather flat areas such as the image background, and too noisy in areas of larger dynamical range, i.e., where galaxies lie. This has a significant effect on the shape measurement accuracy.

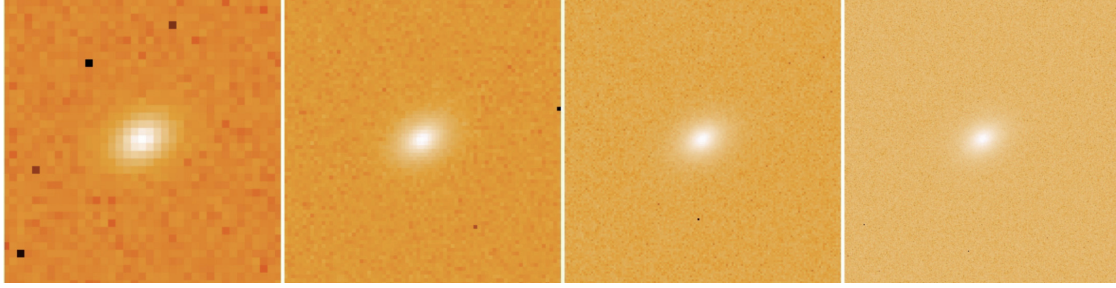


Fig. 1. Artificial galaxies of different resolutions. From left to right the stamp size is 40, 80, 160 and 320 pixels on a side, corresponding to a mean *SNR* per pixel of 1.5, 0.75, 0.37 and 0.19, respectively. The first two samplings on the left correspond to the “realistic sampling” and the “small sampling” cases, respectively (see text).

For this reason, we propose a simple and effective method that combines the Haar DWT and the classical Wiener algorithms in the following way:

1. we decompose the image and calculate the HL_j , LH_j , and HH_j subbands of wavelet coefficients for all resolution levels $j = 1, 2, \dots, k$, where k is the coarsest level;
2. we then modify the wavelet subbands HL_j , LH_j , and HH_j using the kernel Wiener algorithm (Eq. (1));
3. we finally apply the inverse DWT to the modified wavelet coefficient to reconstruct the denoised image.

In other words, we apply the Wiener method to the wavelet coefficients rather than to the data pixels themselves. We show in the following that, for images of faint and small galaxies, this simple method not only conserves the shape of the galaxies, but also improves their measurement.

3. Synthetic data

We use a set of 10 000 simulated galaxies in order to (i) test the effect of the different denoising techniques on the shape measurement and (ii) estimate how this behavior depends on the sampling and the *SNR* of the data. Each galaxy is represented by a Sersic profile of known ellipticity and Sersic index. This profile is sampled on five different grids of pixels. In doing this, we keep the size of the galaxy fixed on the plane of the sky.

Our finest sampling has galaxies with a full-width-half-maximum of $FWHM = 17.3$ pixels. Each of the 10 000 galaxy images is represented on a stamp of 320×320 pixels. We then degrade the sampling by a factor of two, four times in a row, to produce galaxy images with $FWHM \sim 17, 9, 5, 3$ pixels, which correspond, respectively, to image sizes of 320, 160, 80, and 40 pixels on a side.

We then add Poisson noise to the simulated data, assuming that the data are sky-dominated, i.e. to a good approximation the amplitude of the noise is the same for all pixels across the galaxy image. We generate noisy images that mimic those of the GREAT08 challenge (Bridle et al. 2010) with a standard deviation set to the value of $\sigma_n = 1000$ for all pixels. Before adding the noise, we scale the galaxy images so that we probe a range of realistic *SNR*. In the rest of the paper, we refer to the mean *SNR* per pixel, i.e.,

$$SNR = \sum_{j=1}^N \frac{I_j}{N \times \sigma_n}, \quad (6)$$

where I_j is the image value at pixel j and N is the total number of pixels in the image. Since the exposure time is limited in real sky surveys, improving the sampling of the data is done to the cost of a lower *SNR* per pixel. All our simulated images are computed for a fixed integration time.

We use four different samplings, characterized by the typical $FWHM$ of the simulated galaxies. The first two samplings have $FWHM \sim 3$ and 5 pixels which are typical values for a space mission such as EUCLID. In the following, we refer to these as “real sampling” data. We also use two smaller samplings of $FWHM \sim 9$ and 17 pixels. We refer to these as “small sampling” data. Figure 1 give examples of simulated images for the same realization of a galaxy. Our simulations span the *SNR* range between 0.05 to 4.0.

For reference, the *SNR* of the GREAT08 challenge data range from 0.68 to 2.6 in the “low noise” dataset and from 0.003 to 0.38 for the high noise dataset. The $FWHM$ of the galaxies in GREAT08 varies from 1.1 to 14.5 pixels.

4. Results and discussion

4.1. Denoising efficiency for synthetic galaxies

Using the set of 10 000 artificial galaxies described in Sect. 3, we test the performance of the four methods under different *SNR* and sampling conditions. Examples of denoised images are shown in Fig. 3, where it is immediately seen that the four methods behave very differently.

The median filtering has a kernel size of 3×3 pixels. As a consequence, when the sampling changes, the spatial frequencies removed by the filter change with respect to the ones contained in the galaxy. When the sampling becomes coarse enough, the frequencies removed by the filter are close to those contained in the galaxy. This is seen in Fig. 3, where the size of the granulation in the noise becomes larger as the pixel size becomes larger (right column of the figure). For this reason, the performance of the median filtering are expected to degrade quickly in cases of coarse sampling.

The Wiener filter is a low-pass filter, which translates in Fig. 3 into a strong “flattening” of the sky noise but almost no denoising of the galaxy itself. The wavelet method is fully local and adaptive, explaining the patchy aspect of the galaxy in Fig. 3: low frequency signals are represented using a limited number of coefficients and a high frequency requires more coefficients

Finally, we show the results of both DWT-Wiener and DWT-Bayes methods. As explained earlier, the standard DWT-Bayes thresholding is not effective in removing noise from high

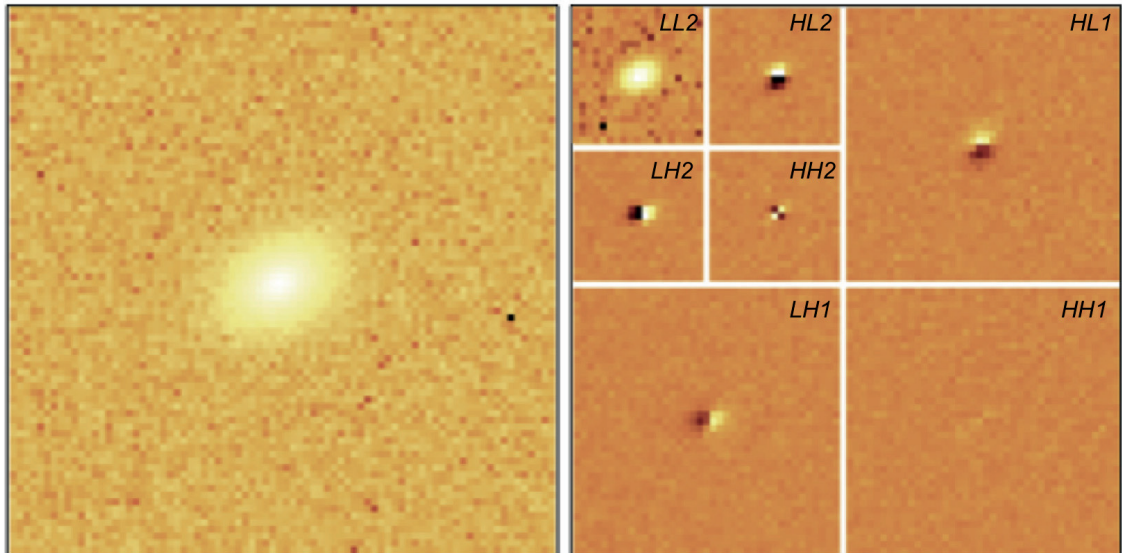


Fig. 2. DWT decomposition of the galaxy image, with Poisson noise. *Left:* original galaxy image. *Right:* two consecutive resolution levels, as explained in Sect. 2.3.

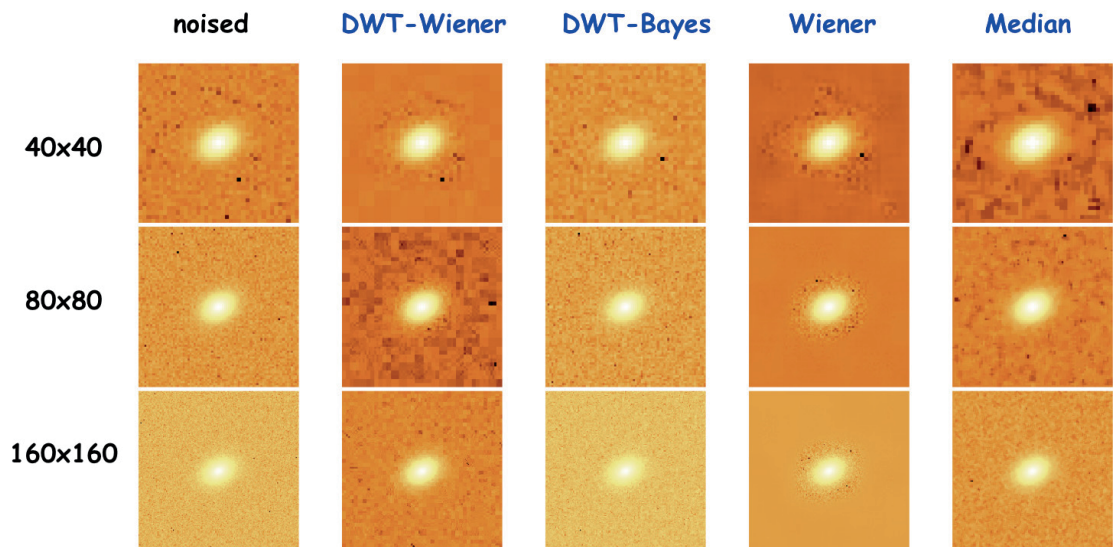


Fig. 3. Examples of different denoising methods, using simulated data with three different samplings.

dynamical range data such as astronomical images. In the particular case of galaxy images, using a fixed threshold for all the wavelet subbands tends to degrade the galaxy shape in areas where the difference in brightness between neighboring pixels is much higher than the standard deviation of the Poisson noise. In other words, the threshold is too high for the image background, leading to an excessive smoothing, whereas the same threshold proves too small for the high intensity pixels of the galaxy image.

This phenomenon is clearly visible in the image denoised with the DWT-Bayes threshold (middle column of Fig. 3), where the results of the denoising process leaves the original image almost unchanged. This is unfortunate because preserving the original intensity profile of the galaxy is essential for the accuracy of the measurement of its shape. Removing noise effectively while preserving the galaxy shape requires a very delicate denoising approach.

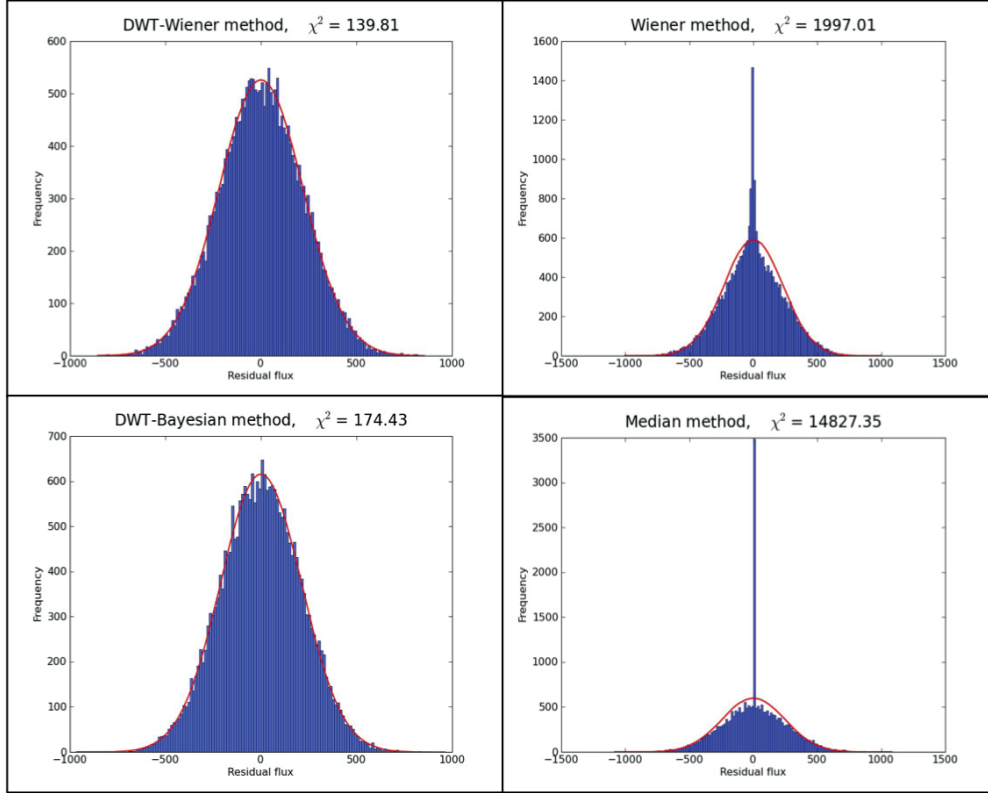


Fig. 4. Effect of the four denoising methods on the noise properties of the original data. Each panel shows the normalized histograms of residual images, i.e., the difference between the original noisy data and the denoised data. The red line shows the best-fit Gaussian. In each case, the χ^2 of the fit is indicated. The mean SNR in the image selected to compute the histogram is $SNR = 0.38$.

The DWT-Wiener method proposed in this paper removes noise according to the local gradient of luminosity, resulting in a more adaptive and local denoising process than DWT-Bayes. The advantage of DWT-Wiener in comparison to the classical Wiener filter is that DWT-Wiener is applied to high-frequency subbands coefficients only, which are those associated with noise, thus preserving the low frequency subband that contains the main features of the signal.

The effect of the four methods on the noise properties of the original data is seen more quantitatively in Fig. 4. In this figure, we choose a galaxy realization with a $SNR = 0.38$ and sampling of $FWHM = 5$ pixels (realistic sampling). We then compute the difference between the original noisy image and the denoised image, as obtained from the four methods and plot histograms of these distributions in Fig. 4. A method that does not affect the noise properties of the original data should ideally yield a perfectly Gaussian histogram. Only the two local denoising methods using wavelets possess this important property.

For each denoising method, we thus compute the χ^2 statistics of its normalized histogram as (Press et al. 2007)

$$\chi^2 = \sum_i \frac{(N_i - n_i)^2}{n_i}, \quad (7)$$

where N_i is the number of pixels observed in the i th bin, and n_i is the number for an expected Gaussian distribution.

Our new DWT-Wiener method has the smallest χ^2 , which indicates that its residuals represent the best fit to a normal distribution. We now test the performance of the four methods on the sets of 10 000 simulated galaxies described in Sect. 3, without considering the effect of convolution by the PSF. This is done by directly comparing the ellipticity measured for the galaxies before and after denoising. Using 10 000 galaxies ensures that an ellipticity measurement is accurate to 1%, which is sufficient for our purposes. In this work, the galaxy ellipticity $e = e_1 + ie_2$ was estimated as

$$e = \frac{Q_{11} - Q_{22} + 2iQ_{12}}{Q_{11} + Q_{22}}, \quad (8)$$

where Q_{mn} , ($m, n \in \{1, 2\}$) are the second-order quadrupole moments of the galaxy surface brightness (Bartelmann & Schneider 2001).

We define the accuracy of each of the denoising methods as the inverse of the root mean square deviation (RMSD)

$$RMSD = \sqrt{\frac{1}{N} \sum_1^N (e_i - e_i^*)^2}, \quad (9)$$

where e_i and e_i^* denote estimated and true galaxy ellipticities, respectively.

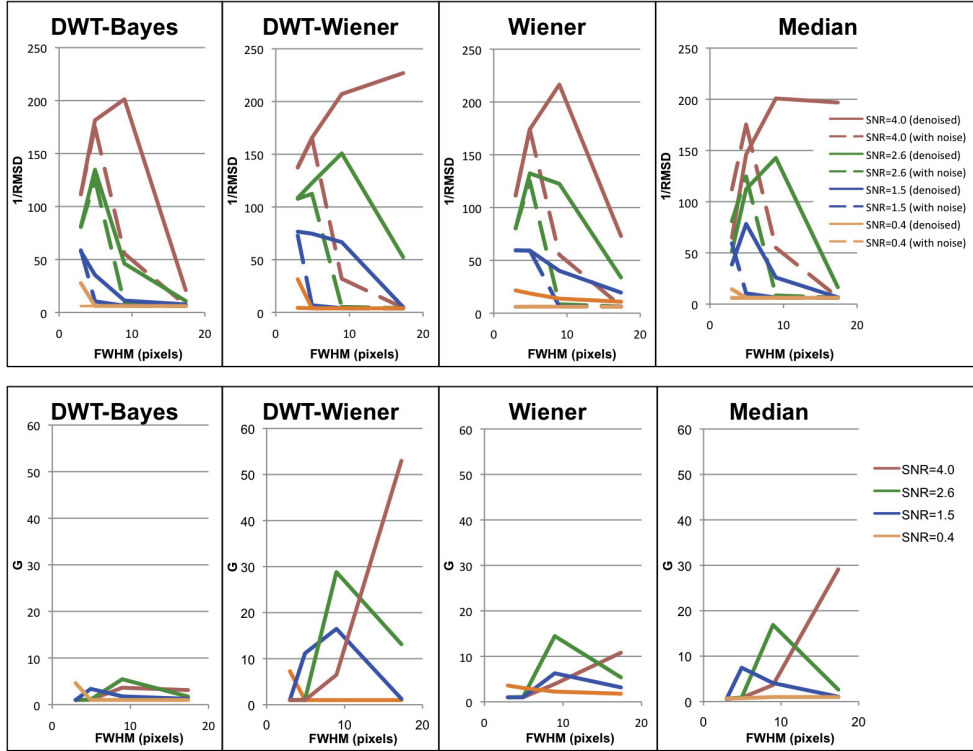


Fig. 5. *Top panels:* accuracy, $1/RMSD$, of the shape measurement using the four denoising methods (solid curves). The dashed curves show for comparison the results obtained with the data before denoising. In each panel, the color code indicates different noise levels. *Bottom panels:* gain ratio, G , for the four denoising methods. The curves are the ratio of the solid to dashed curves shown in the top panels.

To evaluate the effectiveness of the denoising methods in providing improved measurement over the original data, we also define a gain ratio, G , as the ratio of the shape measurement error using the noisy data, to the same quantity using the denoised data

$$G = \frac{RMSD_{\text{original}}}{RMSD_{\text{denoised}}}. \quad (10)$$

The results are summarized in Table 1 and Fig. 5. With no big surprise, all methods lead to high accuracy measurements as soon as excellent sampling and high SNR are available. However, when the SNR decreases, the performance of all methods drops sharply. This means that there is no reason to improve the sampling indefinitely without compensating for an increased SNR , i.e., exposure time. This also means that the interest in denoising exceeds the improvement for poor SNR data. Performances improve with high SNR data (red curves in Fig. 5, hence showing that denoising is as important for well exposed galaxies as for galaxies barely measurable in the original data.

In coarse sampling conditions, the median filter degrades shape measurement instead of improving it. This is illustrated in Fig. 5 by the dashed curves systematically being above the solid ones. In Table 1, the gain ratio factor, ξ , is indeed lower than 1. This is because the frequencies removed by the median filter cannot be easily controlled and depend on the size of the objects with respect to the size of the median kernel. This makes the

Table 1. Gain ratio (G ; see text) for the four denoising methods under different SNR and sampling conditions.

SNR	Stamp size	$FWHM$ galaxies	Median	Wiener	DWT Bayes	DWT Wiener
4.00	40	2.99	0.58	1.00	1.00	1.01
2.00	80	4.92	0.83	1.00	1.04	1.01
1.00	160	8.96	3.65	3.91	3.62	6.49
0.50	320	17.30	29.10	10.80	3.12	52.98
2.60	40	2.99	0.64	1.00	1.01	1.01
1.30	80	4.92	0.90	1.06	1.08	1.10
0.65	160	8.96	16.87	14.47	5.45	28.81
0.33	320	17.30	2.63	5.40	1.73	13.15
1.50	40	2.99	0.65	1.00	0.98	1.05
0.75	80	4.92	7.45	1.00	3.38	11.17
0.38	160	8.96	4.08	6.28	1.77	16.48
0.19	320	17.30	1.07	3.18	1.24	1.28
0.40	40	2.99	0.69	3.59	2.67	7.28
0.20	80	4.92	0.74	3.05	0.31	1.01
0.10	160	8.96	1.00	2.25	0.99	1.00
0.05	320	17.30	1.00	1.79	1.00	1.00

Notes. The SNR is per pixel (Eq. (6)).

use of the median filter very hazardous in general, in spite of its good performance in small sampling conditions. A similar trend is found for the Wiener filter in realistic sampling conditions,

Table 2. Q factor for KSB deconvolution for 15 galaxy sets of GREAT08 low noise-blind (LNBL) and 100 sets of GREAT08 real noise-blind (RNBL).

Dataset	α	Original	DWT-Bayes denoising	DWT-Wiener denoising
LNBL (Low-Noise)	0.01	32.37	32.29	32.37
	0.05	32.37	32.36	32.79
	0.10	32.37	32.37	61.53
	0.50	32.37	32.21	60.13
	1.00	32.37	31.60	75.70
RNBL (Real-Noise)	0.01	11.54	11.32	11.51
	0.05	11.54	11.32	11.54
	0.10	11.54	11.55	15.94
	0.50	11.54	11.55	15.12
	1.00	11.54	3.34	4.67

although it is not so pronounced. The best gain factors are usually achieved with the DWT-Wiener method.

Finally, for each method there exists an optimal sampling where the gain factor is maximum. For realistic sampling and SNR conditions (blue and orange lines in Fig. 5, this sampling is about $FWHM \sim 9$ pixels. By realistic conditions, we mean conditions similar to those in the GREAT08 challenge, i.e., data quality mimicking that of the EUCLID satellite in terms of sampling and SNR.

4.2. Denoising of the GREAT08 challenge dataset

The goal of the previous section was to test the effect of both denoising and sampling on the quality of the shape measurement of galaxies, in the absence of other numerical or instrumental disturbances. For this reason, the convolution of the galaxy images by the instrumental PSF is not included.

We now test the two most effective denoising methods, i.e., the DWT-Bayes and the DWT-Wiener, against the additional effect of PSF deconvolution and centroid shifts. This requires the use of a shape measurement method. For the sake of simplicity, we choose the KSB algorithm (Kaiser 1995) with the code developed by Catherine Heymans and Ludovic Van Waerbeke (Heymans et al. 2006), which is widely used, public, and efficient in terms of computing time. In addition, it does not rely on any fit of an arbitrary galaxy profile to the data.

The GREAT08 challenge dataset is ideal for carrying out our test in both low noise and real noise conditions. For this purpose, we use the whole low noise-blind (LNBL) dataset and a subset of 100 frames of the real noise-blind (RNBL) dataset (see the GREAT08 handbook for more detail, Bridle et al. 2009). The total number of galaxies used is therefore 15 000 in low noise and 100 000 in real noise conditions.

The PSF convolution, which modifies the effect of the noise on the galaxy shape measurement, makes it necessary to control the effect of denoising, prior to the shape measurements itself. We therefore introduce a “denoising strength” that allows us to fine-tune the amount of denoising of the data. In practice, we replace the noise mean standard deviation, σ_n , in Eqs. (1), (4), and (5), with a fractional mean standard deviation $\alpha\sigma_n$, where $0 < \alpha \leq 1.0$.

We run the KSB method on the denoised GREAT08 data using three denoising strengths $\alpha = \{0.01, 0.05, 0.1, 0.5, 1.0\}$. The results are summarized in Table. 2, where the quality factor, Q , is defined as in Bridle et al. (2010). High values of Q indicate good

shape measurements. As a sanity check, we run the KSB algorithm on the original noisy data as well and check that we obtain the same quality factors as in Bridle et al. (2010), i.e., $Q = 32.37$ in low noise and $Q = 11.54$ in real noise conditions.

The main result is that the DWT-Bayes method does not improve the quality factor and even degrades the shape measurement if full denoising ($\alpha = 1.0$) is used. The DWT-Wiener method improves the Q factor by a factor of almost two in low noise conditions and by 35% in real noise conditions. Interestingly, we note that full denoising may degrade the results. One may instead apply partial denoising ($\alpha = 0.1$), which allows us to achieve a significant gain in quality factor without any significant risk of corrupting the data.

5. Conclusions

We have tested four different image denoising techniques on synthetic data of faint and small galaxies and we evaluate their effect on the shape measurement of galaxies in view of weak lensing studies. We have compared the performance of the algorithms for a range of SNR and sampling conditions.

We found that simple median and Wiener filtering degrades the quality of the galaxy shape measurement unless very fine sampling is used. Local denoising methods such as wavelet filtering (DWT-Bayes) preserve the shape of galaxies in fine sampling condition but not for coarser sampling. However, a simple modification of the thresholding scheme of the wavelet method allows us to improve the SNR of the data and the quality of the shape measurement. This new method, DWT-Wiener, consists of applying Wiener filtering to the wavelet coefficients rather than to the data themselves.

The DWT-Wiener method is tested on the GREAT08 challenge data in low noise and real noise conditions, showing an improvement of up to a factor of two (on the quality factor Q) over the shape measurement using the original, noisy, data.

Finally, we have shown that for a fixed SNR there exist an optimal sampling of the galaxy images. For the typical SNR expected in weak lensing space surveys, this sampling is about $FWHM \sim 9$ pixels. Satellites such as EUCLID or WFIRST will have a typical pixel scale of $0.1''$, allowing us to observe typical $z = 1-2$ galaxies with almost this optimal sampling. This lends considerable hope to significantly improving future weak lensing measurements with image denoising.

Acknowledgements. The authors would like to thank C. Heyman and L. van Waerbeke for their KSB method code. The authors are also grateful to Malte Tewes for fruitful discussion. This work is supported by the Swiss National Science Foundation (SNSF).

References

- Arce, G. R. 2005, *Nonlinear Signal Processing: A Statistical Approach* (New Jersey USA: Wiley)
- Arias-Castro, E., & Donoho, D. L. 2009, *Ann. Statist.*, 37, 1772
- Bacon, D. J., Réfrégier, A. R., & Ellis, R. S. 2000, *MNRAS*, 318, 625
- Bartelmann, M., & Schneider, P. M. 2001, *Phys. Rep.*, 340, 291
- Bridle, S., Shawe-Taylor, J., & Amara, A. 2009, *Ann. App. Statist.*, 3, 6
- Bridle, S., Balan, S. T., Bethge, M., et al. 2010, *MNRAS*, 405, 2044
- Bruce, A., Donoho, D., & Gao, H. 1996, *Wavelet Analysis*, *IEEE Spectrum*, 33, 26
- Chang, S. G., Yu, B., & Vetterli, M. 2000, *IEEE Trans. Image Process.*, 9, 1532
- Daubchies, I. 1992, *Ten Lectures on Wavelets*, Society for Industrial and Applied Mathematics
- Donoho, D. L., & Johnstone, I. M. 1994, *Biometrika*, 81, 425

- Donoho, D. L., & Johnstone, I. M. 1995, *J. Stat. Assoc.*, 90, 1200
- Frieman, J. A., Turner, M. S., & Huterer, D. 2008, *ARA&A*, 46, 385
- Gonzalez, R. C., & Woods R. E. 1992, *Digital Image Processing* (Addison-Wesley)
- Haar Zur, A. 1910, *Math. Ann.*, 69, 331
- Heymans, C., Van Waerbeke, L., Bacon, D., et al. 2006, *MNRAS*, 368, 1323
- Howell Steve, B. 2006, *Handbook of CCD Astronomy* (Cambridge University Press)
- Kaiser, N., Squires, G., & Broadhurst, T. 1995, *ApJ*, 449, 460
- Khireddine, A., Benmahammed, K., & Puech, W. 2007, *Adv. Eng. Software*, 38, 513
- Mallat, S. 1989, *IEEE Trans. Pattern Anal. Mach. Intell.*, 11, 674
- Massey, R., Rhodes, J., Ellis, R., et al. 2007a, *Nature*, 445, 286
- Massey, R., Heymans, C., Bergé, J., et al. 2007b, *MNRAS*, 376, 13
- Meyer, Y. 1990, *Ondelettes et operateurs*, I. *Ondelettes* (Paris: Hermann)
- Perlmutter, S., Aldering, G., Goldhaber, G., et al. 1999, *ApJ*, 517, 565
- Press, W. H., Flannery, B. P., Teukolsky, S. A., & Vetterling, W. T. 2007, *Numerical Recipes, The Art of Scientific Computing*, 3rd edn. (Cambridge University Press)
- Réfrégier, A., Amara, A., Kitching, T. D., et al. 2010 [[arXiv:1001.0061](https://arxiv.org/abs/1001.0061)]
- Riess, A. G., Filippenko, A. V., Challis, P., et al. 1998, *AJ*, 116, 1009
- SciPy community 2010, *SciPy Reference Guide Release*, Release 0.9.0.dev6641 docs.scipy.org/doc/scipy/scipy-ref.pdf
- Vetterli, M., & Kovacevic, J. 1995, *Wavelets and Subband Coding*, Englewood Cliffs (NJ: Prentice Hall)
- Van Waerbeke, L., Mellier, Y., Erben, T., et al. 2000, *A&A*, 358, 30
- Wiener, N. 1949, *Extrapolation, Interpolation, and Smoothing of Stationary Time Series* (New York: Wiley)
- Wittman, D. M., Tyson, J. A., Kirkman, D., Dell'Antonio, I., & Bernstein, G. 2000, *Nature*, 405, 143

5 Conclusion

In Chapter 2, we have shown that the standard Λ CDM cosmological model provides an excellent phenomenological description of the Universe but hardly any explanation of what dark matter and dark energy really are. A number of potential extensions to standard cosmology have been proposed, but the corresponding theoretical models cannot be tested until significantly more accurate measurements become available.

In Chapter 3, we have also explained how weak lensing as a tool can be used to place very tight constraints on cosmology. We have shown in particular how powerful this technique is for probing the elusive dark energy. The weak lensing framework itself seems now very well capable of delivering the required constraints on the theory of structure formation and the properties of dark energy. Finding out if dark energy really is the cosmological constant or is instead the manifestation of new physics like a modified gravity law or exotic scalar fields, seems within reach. Promising extensions have even been recently added in the form of three-dimensional cosmic shear analysis or higher-order statistical tools.

Despite these advances, a number of challenges of observational nature remain before weak lensing as a cosmological probe can realize its full potential. The main limiting factor has long been the small sky area covered by cosmic shear surveys that reduced the accuracy of their predictions. But recent surveys have already begun addressing this issue and planned large-scale ground and space-based surveys like LSST and EUCLID will reduce its impact even further. Such surveys will also capture with high accuracy the redshift data required for cosmic shear analysis.

The real challenge now instead seems to reside in the area of shear measurement. The ambitious science goals of EUCLID-like surveys will not be fulfilled unless shear measurement data are measured with the required accuracy. We have explored in Chapter 4 the main difficulties involved and showed these are not trivial to overcome. Realizing this and worried by significant discrepancies found between cosmic shear results, the weak lensing community has reacted by launching initiatives such as the STEP programs and GREAT08/10 challenges to assess the accuracy of available shear measurement methods and foster the development of new algorithms. It was further recognized shear measurement could also benefit from contributions of experts from a wider community, especially from the domains of image processing, data analysis and machine learning. These challenges have shown steady progress in terms of accuracy and bias reduction. We have presented in this context the main contributions of the author published in Gentile et al. (2012, 2013). The GREAT10 results have indeed shown the

Chapter 5. Conclusion

best performing methods, which included the author's *gfit*, are able to match the requirements of advanced surveys like KIDS, HSC or DES. The apparition of machine learning algorithms in shear measurement is also quite promising. Nevertheless it is estimated a tenfold improvement in accuracy is still needed to observationally discriminate between dark energy models with different equations of state or gravitational physics.

The inaccuracies of shear measurement methods critically depend not only on the quality of shear measurement algorithms but also on the effectiveness of PSF correction and interpolation techniques. The study we have conducted in Gentile et al. (2013) has highlighted the current lack of maturity of the PSF correction & interpolation schemes but also explored new promising possibilities. Now is possibly the time to include in the next editions of the GREAT series of challenge more realistic models of PSF (as was initially done in STEP) in preparation of LSST and EUCLID. The forthcoming GREAT3 Challenge (Mandelbaum et al. 2013) is moving in that direction. Taking into account color information in images is also likely to pose new conceptual and technical challenges but also to offer new perspectives. It is also worth exploring new denoising schemes well suited to the specific need of weak lensing such as the wavelet-based algorithm proposed in Nurbaeva et al. (2011). A good denoising algorithm can significantly improve the overall effectiveness of shear measurement, independently of the shear measurement scheme used.

There is good hope that the steady progress made so far and the dedication of the weak lensing community will make this endeavor successful.

A Appendix

A.1 Gravitational lensing magnification and shear

A.1.1 Inverse magnification transformation $\partial\boldsymbol{\beta}/\partial\boldsymbol{\theta}$

As seen in Sect. 3.1, the inverse magnification transformation from image to source $\boldsymbol{\theta} \rightarrow \boldsymbol{\beta}$ is described to first order by the Jacobian matrix

$$\mathcal{A}(\boldsymbol{\theta}) = \begin{pmatrix} 1 - \kappa - \gamma_1 & \epsilon - \gamma_2 \\ -\gamma_2 & 1 - \kappa + \gamma_1 \end{pmatrix} \quad (\text{A.1})$$

where κ and $|\boldsymbol{\gamma}| = \sqrt{\gamma_1^2 + \gamma_2^2}$ are the convergence and shear respectively.

Eigenvalues and eigenvectors

The \mathcal{A} matrix is symmetric, so one expects two real eigenvalues, which two associated orthogonal eigenvectors. The characteristic equation is given by

$$\det(\mathcal{A} - \lambda\mathcal{I}) = 0 \quad (\text{A.2})$$

where \mathcal{I} is the identity matrix and λ one of the eigenvalues, with

$$\begin{aligned} \det(\mathcal{A} - \lambda\mathcal{I}) &= (1 - \kappa - \gamma_1 - \lambda)(1 - \kappa + \gamma_1 - \lambda) - \gamma_2^2 \\ &= (1 - \kappa - \lambda)^2 - |\boldsymbol{\gamma}|^2 \\ &= (1 - \kappa - \lambda - |\boldsymbol{\gamma}|)(1 - \kappa - \lambda + |\boldsymbol{\gamma}|) \end{aligned}$$

Equation (A.2) thus yields the two real eigenvalues

$$\lambda_- = 1 - \kappa - |\boldsymbol{\gamma}| \quad (\text{A.3})$$

$$\lambda_+ = 1 - \kappa + |\boldsymbol{\gamma}| \quad (\lambda_- < \lambda_+) \quad (\text{A.4})$$

The Eigenvectors of \mathcal{A} are given by

$$(\mathcal{A} - \lambda\mathcal{I})\boldsymbol{\theta} = \mathbf{0} \quad (\text{A.5})$$

Appendix A. Appendix

For $\lambda = \lambda_-$, one obtains

$$(1 - \kappa - \gamma_1 - \lambda_-) \theta_1 - \gamma_2 \theta_2 = 0 \quad (\text{A.6a})$$

$$-\gamma_2 \theta_1 + (1 - \kappa + \gamma_1 - \lambda_-) \theta_2 = 0 \quad (\text{A.6b})$$

Since

$$1 - \kappa - \gamma_1 - \lambda_- = 1 - \kappa - \gamma_1 - 1 + \kappa + |\boldsymbol{\gamma}| = -\gamma_1 + |\boldsymbol{\gamma}|$$

$$1 - \kappa + \gamma_1 - \lambda_- = 1 - \kappa + \gamma_1 - 1 + \kappa + |\boldsymbol{\gamma}| = \gamma_1 + |\boldsymbol{\gamma}|$$

equations (A.6a) and (A.6a) reduce to

$$(-\gamma_1 + |\boldsymbol{\gamma}|) \theta_1 - \gamma_2 \theta_2 = 0 \quad (\text{A.7a})$$

$$-\gamma_2 \theta_1 + (\gamma_1 + |\boldsymbol{\gamma}|) \theta_2 = 0 \quad (\text{A.7b})$$

A unit eigenvector \mathbf{U}_- for λ_- is therefore

$$\mathbf{U}_- = \frac{1}{\eta_1} \begin{pmatrix} \gamma_1 + |\boldsymbol{\gamma}| \\ \gamma_2 \end{pmatrix} = \frac{1}{\eta_1} \begin{pmatrix} \frac{\gamma_2}{|\boldsymbol{\gamma}| - \gamma_1} \\ 1 \end{pmatrix} = \frac{1}{\eta_1} \begin{pmatrix} 1 \\ \frac{|\boldsymbol{\gamma}| - \gamma_1}{\gamma_2} \end{pmatrix} \quad (\text{A.8})$$

where

$$\eta_1 = \sqrt{\gamma_2^2 + (|\boldsymbol{\gamma}| + \gamma_1)^2} = \sqrt{2|\boldsymbol{\gamma}|(|\boldsymbol{\gamma}| + \gamma_1)} \quad (\text{A.9})$$

For $\lambda = \lambda_+$

$$(1 - \kappa - \gamma_1 - \lambda_+) \theta_1 - \gamma_2 \theta_2 = 0 \quad (\text{A.10a})$$

$$-\gamma_2 \theta_1 + (1 - \kappa + \gamma_1 - \lambda_+) \theta_2 = 0 \quad (\text{A.10b})$$

Since

$$1 - \kappa - \gamma_1 - \lambda_+ = 1 - \kappa - \gamma_1 - 1 + \kappa - |\boldsymbol{\gamma}| = -\gamma_1 - |\boldsymbol{\gamma}| \quad (\text{A.11})$$

$$1 - \kappa + \gamma_1 - \lambda_+ = 1 - \kappa + \gamma_1 - 1 + \kappa - |\boldsymbol{\gamma}| = \gamma_1 - |\boldsymbol{\gamma}| \quad (\text{A.12})$$

equations (A.10a) and (A.10b) reduce to

$$(-\gamma_1 - |\boldsymbol{\gamma}|) \theta_1 - \gamma_2 \theta_2 = 0 \quad (\text{A.13a})$$

$$-\gamma_2 \theta_1 + (\gamma_1 - |\boldsymbol{\gamma}|) \theta_2 = 0 \quad (\text{A.13b})$$

A unit eigenvector \mathbf{U}_+ for λ_+ is

$$\mathbf{U}_+ = \frac{1}{\eta_2} \begin{pmatrix} \gamma_1 - |\boldsymbol{\gamma}| \\ \gamma_2 \end{pmatrix} = \frac{1}{\eta_2} \begin{pmatrix} -\frac{\gamma_2}{\gamma_1 + |\boldsymbol{\gamma}|} \\ 1 \end{pmatrix} = \frac{1}{\eta_2} \begin{pmatrix} 1 \\ -\frac{\gamma_1 + |\boldsymbol{\gamma}|}{\gamma_2} \end{pmatrix} \quad (\text{A.14})$$

where

$$\eta_2 = \sqrt{\gamma_2^2 + (|\boldsymbol{\gamma}| - \gamma_1)^2} = \sqrt{2|\boldsymbol{\gamma}|(|\boldsymbol{\gamma}| - \gamma_1)} \quad (\text{A.15})$$

So defined, the eigenvectors \mathbf{U}_- and \mathbf{U}_+ are orthonormal, verifying

$$\begin{aligned} \mathbf{U}_- \cdot \mathbf{U}_+ &= \frac{1}{\eta_1 \eta_2} [\gamma_1^2 + \gamma_2^2 - |\boldsymbol{\gamma}|^2] = 0 \\ \mathbf{U}_- \cdot \mathbf{U}_- &= \frac{1}{\eta_1^2} [\gamma_2^2 + (\gamma_1 + |\boldsymbol{\gamma}|)^2] = \frac{1}{\eta_1^2} (2|\boldsymbol{\gamma}|^2 + 2|\boldsymbol{\gamma}| \gamma_1) = 1 \\ \mathbf{U}_+ \cdot \mathbf{U}_+ &= \frac{1}{\eta_2^2} [\gamma_2^2 + (\gamma_1 - |\boldsymbol{\gamma}|)^2] = \frac{1}{\eta_2^2} (2|\boldsymbol{\gamma}|^2 - 2|\boldsymbol{\gamma}| \gamma_1) = 1 \end{aligned}$$

The diagonalisation of \mathcal{A} produces the diagonal matrix $\mathcal{D}_{\mathcal{A}}$ made of eigenvalues λ_- and λ_+

$$\mathcal{D}_{\mathcal{A}} = \begin{pmatrix} \lambda_- & 0 \\ 0 & \lambda_+ \end{pmatrix} = \begin{pmatrix} 1 - \kappa - |\boldsymbol{\gamma}| & 0 \\ 0 & 1 - \kappa + |\boldsymbol{\gamma}| \end{pmatrix} \quad (\text{A.16})$$

which shows that the effect of the transformation is to stretch by a factor $\lambda_+ = 1 - \kappa + |\boldsymbol{\gamma}|$ in the \mathbf{U}_+ direction and to compress by a factor $\lambda_- = 1 - \kappa - |\boldsymbol{\gamma}|$ in the \mathbf{U}_- direction.

Indeed, the diagonal matrix $\mathcal{D}_{\mathcal{A}}$ can be decomposed in eigenspace (v_1, v_2) as

$$\mathcal{D}_{\mathcal{A}} = (1 - \kappa) \begin{pmatrix} 1 & 0 \\ 0 & 1 \end{pmatrix} - |\boldsymbol{\gamma}| \begin{pmatrix} 1 & 0 \\ 0 & -1 \end{pmatrix} = (1 - \kappa) \mathcal{I} - |\boldsymbol{\gamma}| \mathcal{S} \quad (\text{A.17})$$

where \mathcal{S} represents a reflection about the \mathbf{U}_- axis in the (β_1, β_2) plane (see Fig. A.1).

The $(1 - \kappa) \mathcal{I}$ component describes a compression by a factor $(1 - \kappa)$ in the \mathbf{U}_- and \mathbf{U}_+ directions. The matrix $-\mathcal{S}$ describes a reflection about the \mathbf{U}_+ axis and therefore the component $-|\boldsymbol{\gamma}| \mathcal{S}$ describes a compression by a factor $|\boldsymbol{\gamma}|$ in the \mathbf{U}_- direction and a stretch of the same factor in the \mathbf{U}_+ direction. Both effects combine to produce a distortion by an factor $\lambda_- = 1 - \kappa - |\boldsymbol{\gamma}|$ in the \mathbf{U}_- direction and by a factor $\lambda_+ = 1 - \kappa + |\boldsymbol{\gamma}|$ in the \mathbf{U}_+ direction.

If applied to a circular image of radius R , these effects will result in an ellipse with semi-major and semi-minor axis a' and b' respectively given by:

$$a' = R \lambda_+ = R(1 - \kappa + |\boldsymbol{\gamma}|) \quad (\text{A.18})$$

$$b' = R \lambda_- = R(1 - \kappa - |\boldsymbol{\gamma}|) \quad (\text{A.19})$$

These effects, applied to a circular image of radius R are illustrated in Fig. A.1.

In the particular case of $\gamma_1 = 0$ or $\gamma_2 = 0$:

$$\begin{aligned} \gamma_1 = 0, \quad \lambda_- = 1 - \kappa - \gamma_2, \quad \lambda_+ = 1 - \kappa + \gamma_2, \quad \mathbf{U}_- = \begin{pmatrix} 1 \\ 1 \end{pmatrix}, \quad \mathbf{U}_+ = \begin{pmatrix} 1 \\ -1 \end{pmatrix} \\ \gamma_2 = 0, \quad \lambda_- = 1 - \kappa - \gamma_1, \quad \lambda_+ = 1 - \kappa + \gamma_1, \quad \mathbf{U}_- = \begin{pmatrix} 1 \\ 0 \end{pmatrix}, \quad \mathbf{U}_+ = \begin{pmatrix} 0 \\ 1 \end{pmatrix} \end{aligned}$$

Therefore, the effect of γ_2 alone is to compress by a factor $\lambda_- = 1 - \kappa - \gamma_2$ along the first diagonal

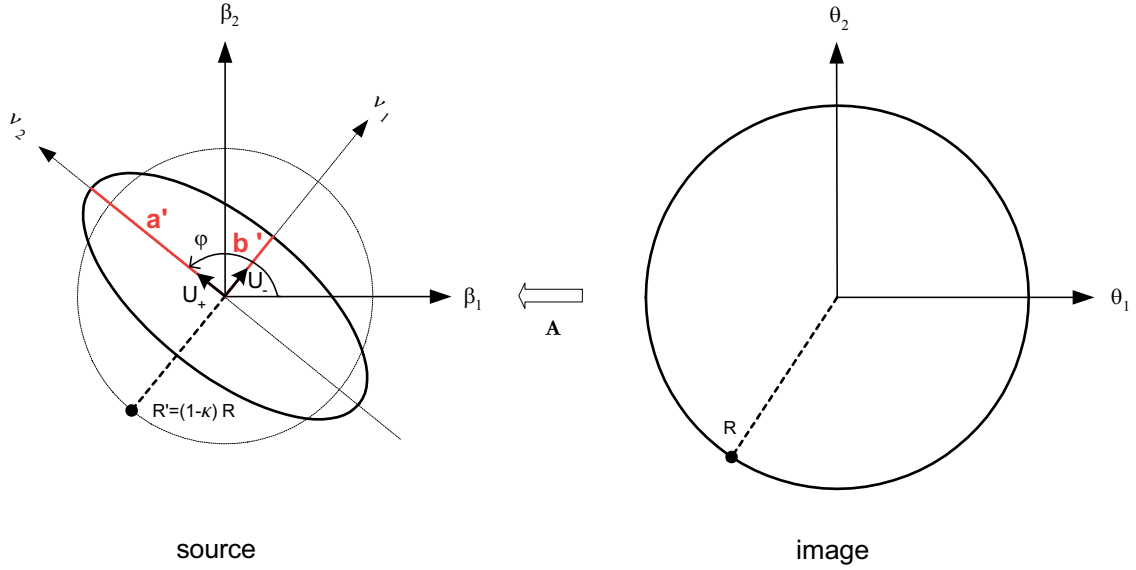


Figure A.1: Geometrical effects of the transformation $\boldsymbol{\theta} \rightarrow \boldsymbol{\beta}$ described by the \mathcal{A} matrix.

($\varphi = \pi/4$) and stretch by a factor $\lambda_+ = 1 - \kappa + \gamma_2$ along the second diagonal ($\varphi = -\pi/4$); whereas γ_1 alone causes a compression by a factor $\lambda_- = 1 - \kappa - \gamma_1$ along the θ_1 axis and a stretch by a factor $\lambda_+ = 1 - \kappa + \gamma_1$ along the θ_2 axis. The further a point lies from an eigenvector, the greater the compression/stretch effect is.

Representation in Polar coordinates

The angle φ between the semi-major axis in the \mathbf{U}_+ directions and the β_1 axis can be obtained from equation (A.13a) or (A.13b). One obtains

$$\tan(\varphi) = \frac{\theta_2}{\theta_1} = -\frac{\gamma_1 + |\boldsymbol{r}|}{\gamma_2} \quad (\text{A.20})$$

so that

$$\varphi = \arctan\left(-\frac{\gamma_1 + |\boldsymbol{r}|}{\gamma_2}\right) + k\pi = \frac{1}{2} \arctan\left(\frac{\gamma_2}{\gamma_1}\right) + k\pi \quad (k \in \mathbb{Z}) \quad (\text{A.21})$$

Further

$$\sin \varphi = -\frac{\gamma_1 + |\boldsymbol{r}|}{\sqrt{2|\boldsymbol{r}|(|\boldsymbol{r}| + \gamma_1)}} = -\frac{\gamma_1 + |\boldsymbol{r}|}{\eta_1} = -\frac{\sqrt{\gamma_1 + |\boldsymbol{r}|}}{\sqrt{2|\boldsymbol{r}|}} \quad (\text{A.22})$$

$$\cos \varphi = \frac{\gamma_2}{\sqrt{2|\boldsymbol{r}|(|\boldsymbol{r}| + \gamma_1)}} = \frac{\gamma_2}{\eta_1} \quad (\text{A.23})$$

The diagonal matrix \mathcal{D}_A given in (A.16) can be expressed as

$$\mathcal{D}_A = \mathcal{P}^{-1} \mathcal{A} \mathcal{P}$$

where the columns of \mathcal{P} are made of the eigenvector \mathbf{U}_- and \mathbf{U}_+ .

Because \mathcal{A} is symmetric, $\mathcal{P}^{-1} = \mathcal{P}^T$ and we also note $\det(\mathcal{P}) = 1$. Thus \mathcal{P} actually represents the anticlockwise rotation \mathcal{R}_φ in the (β_1, β_2) plane, generated by the diagonalisation transformation, with

$$\mathcal{R}_\varphi = \begin{pmatrix} \cos \varphi & -\sin \varphi \\ \sin \varphi & \cos \varphi \end{pmatrix} \quad (\text{A.24})$$

Thus

$$\mathcal{D}_A = \mathcal{R}_\varphi^{-1} \mathcal{A} \mathcal{R}_\varphi \Leftrightarrow \mathcal{R}_\varphi \mathcal{D}_A \mathcal{R}_\varphi^{-1} = \mathcal{R}_\varphi (\mathcal{R}_\varphi^{-1} \mathcal{A} \mathcal{R}_\varphi) \mathcal{R}_\varphi^{-1}$$

that is

$$\mathcal{A} = \mathcal{R}_\varphi \mathcal{D}_A \mathcal{R}_\varphi^{-1} = \mathcal{R}_\varphi \mathcal{D}_A \mathcal{R}_\varphi^T \quad (\text{A.25})$$

Equation (A.25) then gives

$$\begin{aligned} \mathcal{A} &= \mathcal{R}_\varphi [(1 - \kappa) \mathcal{I} - |\boldsymbol{\gamma}| \mathcal{S}] \mathcal{R}_\varphi^T \\ &= (1 - \kappa) \mathcal{R}_\varphi \mathcal{R}_\varphi^T - |\boldsymbol{\gamma}| \mathcal{R}_\varphi \mathcal{S} \mathcal{R}_\varphi^T \\ &= (1 - \kappa) \mathcal{I} - |\boldsymbol{\gamma}| \mathcal{R}_\varphi \mathcal{S} \mathcal{R}_\varphi^T \end{aligned} \quad (\text{A.26})$$

with

$$\begin{aligned} \mathcal{R}_\varphi \mathcal{S} \mathcal{R}_\varphi^T &= \begin{pmatrix} \cos \varphi & -\sin \varphi \\ \sin \varphi & \cos \varphi \end{pmatrix} \begin{pmatrix} 1 & 0 \\ 0 & -1 \end{pmatrix} \begin{pmatrix} \cos \varphi & \sin \varphi \\ -\sin \varphi & \cos \varphi \end{pmatrix} \\ &= \begin{pmatrix} \cos \varphi & \sin \varphi \\ -\sin \varphi & -\cos \varphi \end{pmatrix} \begin{pmatrix} \cos \varphi & \sin \varphi \\ -\sin \varphi & \cos \varphi \end{pmatrix} \\ &= \begin{pmatrix} \cos^2 \varphi - \sin^2 \varphi & 2 \sin \varphi \cos \varphi \\ 2 \sin \varphi \cos \varphi & -[\cos^2 \varphi - \sin^2 \varphi] \end{pmatrix} \\ &= \begin{pmatrix} \cos 2\varphi & \sin 2\varphi \\ \sin 2\varphi & -\cos 2\varphi \end{pmatrix} \end{aligned} \quad (\text{A.27})$$

Using equation (A.26), \mathcal{A} can therefore be expressed as

$$\mathcal{A} = (1 - \kappa) \begin{pmatrix} 1 & 0 \\ 0 & 1 \end{pmatrix} - |\boldsymbol{\gamma}| \begin{pmatrix} \cos 2\varphi & \sin 2\varphi \\ \sin 2\varphi & -\cos 2\varphi \end{pmatrix} = (1 - \kappa) \mathcal{I} - |\boldsymbol{\gamma}| \mathcal{S}_\varphi \quad (\text{A.28})$$

The matrix \mathcal{S}_φ is the representation of the reflexion matrix \mathcal{S} in polar coordinates in the (β_1, β_2) coordinate system.

Appendix A. Appendix

Comparing (A.28) with (A.1), one finds that the shear has components

$$\gamma_1 = |\boldsymbol{\gamma}| \cos 2\varphi \quad (\text{A.29})$$

$$\gamma_2 = |\boldsymbol{\gamma}| \sin 2\varphi \quad (\text{A.30})$$

and is thus invariant under a rotation of angle π radians.

A.1.2 Magnification transformation $\partial\boldsymbol{\theta}/\partial\boldsymbol{\beta}$

The Magnification matrix \mathcal{M} of the transformation $\boldsymbol{\beta} \rightarrow \boldsymbol{\theta}$ from source to image is

$$\mathcal{M}(\boldsymbol{\theta}) = \mathcal{A}^{-1}(\boldsymbol{\theta}) = \mu \begin{pmatrix} 1 - \kappa + \gamma_1 & \gamma_2 \\ \gamma_2 & 1 - \kappa - \gamma_1 \end{pmatrix} \quad (\text{A.31})$$

with

$$\mu = \det(\mathcal{A}^{-1}) = \frac{1}{\det(\mathcal{A})} = \mu^2 \det(\mathcal{M}) = \frac{1}{(1 - \kappa)^2 - |\boldsymbol{\gamma}|^2}, \quad \mu \geq 1 \quad (\text{A.32})$$

Magnification factor μ

Let two vectors \mathbf{X} and \mathbf{W} in the source plane and their respective images \mathbf{Y} and \mathbf{Z} through the transformation $\mathcal{M} = \mathcal{A}^{-1}$. The areas spanned by these vectors is given by the norm of their cross product, which is also of the determinant of the matrix they form

$$\|\mathbf{X} \times \mathbf{W}\| = X_i W_j = X_1 W_1 - X_2 W_2 = \det \begin{pmatrix} X_1 & W_1 \\ X_2 & W_2 \end{pmatrix} \quad (\text{A.33})$$

$$\|\mathbf{Y} \times \mathbf{Z}\| = Y_i Z_j = Y_1 Z_1 - Y_2 Z_2 = \det \begin{pmatrix} Y_1 & Z_1 \\ Y_2 & Z_2 \end{pmatrix} \quad (\text{A.34})$$

The lensing relations between source and image

$$\mathbf{X} = \mathcal{A} \mathbf{Y} \quad (\text{A.35})$$

$$\mathbf{W} = \mathcal{A} \mathbf{Z} \quad (\text{A.36})$$

translate to

$$\|\mathbf{X} \times \mathbf{W}\| = \|(\mathcal{A} \mathbf{Y}) \times (\mathcal{A} \mathbf{Z})\| \quad (\text{A.37})$$

Working through the matrix and vector components yields

$$\|\mathbf{X} \times \mathbf{W}\| = \det(\mathcal{A}) \|\mathbf{Y} \times \mathbf{Z}\| \quad (\text{A.38})$$

so that¹

$$\|\mathbf{Y} \times \mathbf{Z}\| = \frac{1}{\det(\mathcal{A})} \|\mathbf{X} \times \mathbf{W}\| = \det(\mathcal{A}^{-1}) \|\mathbf{X} \times \mathbf{W}\| = \mu \|\mathbf{X} \times \mathbf{W}\| \quad (\text{A.39})$$

The magnification factor μ is thus given by equation (A.32).

Eigenvalues and eigenvectors

The eigenvalues are solutions of the characteristic equation

$$\det(\mathcal{M} - \Lambda \mathcal{I}) = 0 \quad (\text{A.40})$$

where \mathcal{I} is the identity matrix and Λ one of the eigenvalues.

$$\begin{aligned} \det(\mathcal{M} - \Lambda \mathcal{I}) &= [\mu(1 - \kappa + \gamma_1) - \Lambda] [\mu(1 - \kappa - \gamma_1) - \Lambda] - \mu^2 \gamma_2^2 \\ &= [\mu(1 - \kappa) - \Lambda]^2 - \mu^2 |\boldsymbol{\gamma}|^2 \\ &= \mu^2 (1 - \kappa - \Lambda - |\boldsymbol{\gamma}|) (1 - \kappa - \Lambda + |\boldsymbol{\gamma}|) \end{aligned} \quad (\text{A.41})$$

Equation (A.2) thus yields the two real eigenvalues

$$\Lambda_- = \mu (1 - \kappa - |\boldsymbol{\gamma}|) = \mu \lambda_- = \frac{1}{1 - \kappa + |\boldsymbol{\gamma}|} = \frac{1}{\lambda_+} \quad (\text{A.42})$$

$$\Lambda_+ = \mu (1 - \kappa + |\boldsymbol{\gamma}|) = \mu \lambda_+ = \frac{1}{1 - \kappa - |\boldsymbol{\gamma}|} = \frac{1}{\lambda_-} \quad (\Lambda_- < \Lambda_+) \quad (\text{A.43})$$

This makes sense, since \mathcal{M} is the inverse matrix of \mathcal{A} which implies the eigenvalues of \mathcal{M} are also the inverse of the eigenvalues of \mathcal{A} .

The Eigenvectors of \mathcal{M} are given by

$$(\mathcal{M} - \Lambda \mathcal{I}) \boldsymbol{\beta} = \mathbf{0} \quad (\text{A.44})$$

For $\Lambda = \Lambda_-$, one obtains

$$[\mu(1 - \kappa + \gamma_1) - \Lambda_-] \beta_1 + \mu \gamma_2 \beta_2 = 0 \quad (\text{A.45})$$

$$\mu \gamma_2 \beta_1 + [\mu(1 - \kappa - \gamma_1) - \Lambda_-] \beta_2 = 0 \quad (\text{A.46})$$

Since

$$\begin{aligned} \mu(1 - \kappa + \gamma_1) - \Lambda_- &= \mu [1 - \kappa + \gamma_1 - (1 - \kappa - |\boldsymbol{\gamma}|)] = \mu(\gamma_1 + |\boldsymbol{\gamma}|) \\ \mu(1 - \kappa - \gamma_1) - \Lambda_- &= \mu [1 - \kappa - \gamma_1 - (1 - \kappa - |\boldsymbol{\gamma}|)] = \mu(-\gamma_1 + |\boldsymbol{\gamma}|) \end{aligned}$$

¹This relation holds for any matrix \mathcal{A} , not only for the Jacobian matrix of lensing.

Appendix A. Appendix

equations (A.45) and (A.46) yield

$$(\gamma_1 + |\boldsymbol{\gamma}|) \beta_1 + \gamma_2 \beta_2 = 0 \quad (\text{A.47a})$$

$$\gamma_2 \beta_1 + (-\gamma_1 + |\boldsymbol{\gamma}|) \beta_2 = 0 \quad (\text{A.47b})$$

A unit eigenvector is

$$\mathbf{V}_- = \frac{1}{\eta_2} \begin{pmatrix} \gamma_1 - |\boldsymbol{\gamma}| \\ \gamma_2 \end{pmatrix} = \mathbf{U}_+ = \frac{1}{\eta_2} \begin{pmatrix} -\frac{\gamma_2}{\gamma_1 + |\boldsymbol{\gamma}|} \\ 1 \end{pmatrix} = \frac{1}{\eta_2} \begin{pmatrix} 1 \\ -\frac{\gamma_1 + |\boldsymbol{\gamma}|}{\gamma_2} \end{pmatrix} \quad (\text{A.48})$$

For $\Lambda = \Lambda_+$, one gets

$$[\mu(1 - \kappa + \gamma_1) - \Lambda_+] \beta_1 + \mu\gamma_2 \beta_2 = 0 \quad (\text{A.49})$$

$$\mu\gamma_2 \beta_1 + [\mu(1 - \kappa - \gamma_1) - \Lambda_+] \beta_2 = 0 \quad (\text{A.50})$$

Since

$$\mu(1 - \kappa + \gamma_1) - \Lambda_+ = \mu [1 - \kappa + \gamma_1 - (1 - \kappa + |\boldsymbol{\gamma}|)] = \mu(\gamma_1 - |\boldsymbol{\gamma}|)$$

$$\mu(1 - \kappa - \gamma_1) - \Lambda_+ = \mu [1 - \kappa - \gamma_1 - (1 - \kappa + |\boldsymbol{\gamma}|)] = \mu(-\gamma_1 - |\boldsymbol{\gamma}|)$$

equations (A.49) and (A.50) yield

$$(\gamma_1 - |\boldsymbol{\gamma}|) \beta_1 + \gamma_2 \beta_2 = 0 \quad (\text{A.51})$$

$$\gamma_2 \beta_1 - (\gamma_1 + |\boldsymbol{\gamma}|) \beta_2 = 0 \quad (\text{A.52})$$

One can choose the unit eigenvector

$$\mathbf{V}_+ = \frac{1}{\eta_1} \begin{pmatrix} \gamma_1 + |\boldsymbol{\gamma}| \\ \gamma_2 \end{pmatrix} = \mathbf{U}_- = \frac{1}{\eta_1} \begin{pmatrix} \frac{\gamma_2}{|\boldsymbol{\gamma}| - \gamma_1} \\ 1 \end{pmatrix} = \frac{1}{\eta_1} \begin{pmatrix} 1 \\ \frac{|\boldsymbol{\gamma}| - \gamma_1}{\gamma_2} \end{pmatrix} \quad (\text{A.53})$$

The chosen eigenvectors \mathbf{V}_1 and \mathbf{V}_2 are orthonormal, verifying

$$\mathbf{V}_- \cdot \mathbf{V}_+ = \mathbf{U}_+ \cdot \mathbf{U}_- = \frac{1}{\eta_1 \eta_2} (\gamma_2^2 + \gamma_1^2 - |\boldsymbol{\gamma}|^2) = 0 \quad (\text{A.54})$$

$$\mathbf{V}_- \cdot \mathbf{V}_- = \mathbf{U}_+ \cdot \mathbf{U}_+ = \frac{1}{\eta_2^2} [\gamma_2^2 + (\gamma_1 - |\boldsymbol{\gamma}|)^2] = \frac{1}{\eta_2^2} (2|\boldsymbol{\gamma}|^2 - 2|\boldsymbol{\gamma}|\gamma_1) = 1$$

$$\mathbf{V}_+ \cdot \mathbf{V}_+ = \mathbf{U}_- \cdot \mathbf{U}_- = \frac{1}{\eta_1^2} [\gamma_2^2 + (|\boldsymbol{\gamma}| + \gamma_1)^2] = \frac{1}{\eta_1^2} (2|\boldsymbol{\gamma}|^2 + 2|\boldsymbol{\gamma}|\gamma_1) = 1$$

The diagonalisation of \mathcal{M} produces the diagonal matrix $\mathcal{D}_{\mathcal{M}}$ made of eigenvalues Λ_- and Λ_+

$$\mathcal{D}_{\mathcal{M}} = \begin{pmatrix} \Lambda_+ & 0 \\ 0 & \Lambda_- \end{pmatrix} = \mu \begin{pmatrix} 1 - \kappa + |\boldsymbol{\gamma}| & 0 \\ 0 & 1 - \kappa - |\boldsymbol{\gamma}| \end{pmatrix} \quad (\text{A.55})$$

which shows that the effect of the transformation is to stretch by a factor $\Lambda_+ = 1 - \kappa + |\boldsymbol{\gamma}|$ in the \mathbf{V}_+ direction and to compress by a factor $\Lambda_- = 1 - \kappa - |\boldsymbol{\gamma}|$ in the \mathbf{V}_- direction.

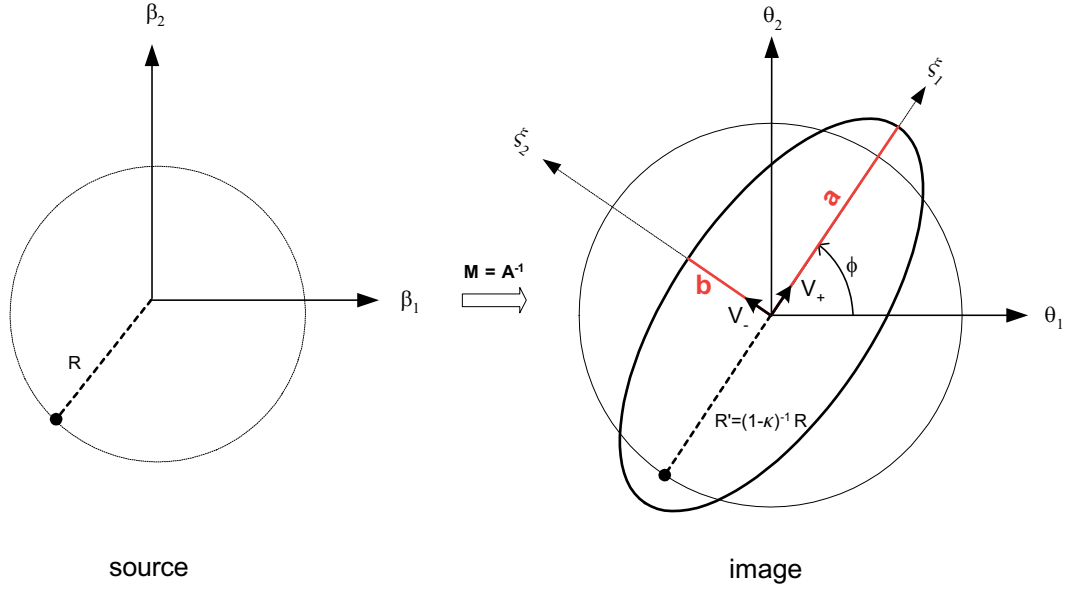


Figure A.2: Geometrical effects of the transformation $\boldsymbol{\beta} \rightarrow \boldsymbol{\theta}$ described by the \mathcal{M} matrix.

In analogy with the inverse magnification transformation, the diagonal matrix $\mathcal{D}_{\mathcal{M}}$ can be decomposed in eigenspace (ξ_1, ξ_2) as

$$\mathcal{D}_{\mathcal{M}} = \mu(1 - \kappa) \begin{pmatrix} 1 & 0 \\ 0 & 1 \end{pmatrix} + \mu |\boldsymbol{\gamma}| \begin{pmatrix} 1 & 0 \\ 0 & -1 \end{pmatrix} = \mu(1 - \kappa) \mathcal{I} + \mu |\boldsymbol{\gamma}| \mathcal{S} \quad (\text{A.56})$$

where \mathcal{S} represents a reflection about the V_+ axis in the (θ_1, θ_2) plane (see Fig. A.2). The $\mu(1 - \kappa) \mathcal{I}$ component describes a stretch by a factor $\mu(1 - \kappa)$ in the V_- and V_+ directions. The component $\mu |\boldsymbol{\gamma}| \mathcal{S}$ describes a compression by a factor $-\mu |\boldsymbol{\gamma}|$ in the V_- direction and a stretch by a factor $\mu |\boldsymbol{\gamma}|$ in the V_+ direction. Both effects combine to produce a distortion by a factor $\Lambda_- = (1 - \kappa - |\boldsymbol{\gamma}|)^{-1}$ in the V_- direction and by a factor $\Lambda_+ = (1 - \kappa + |\boldsymbol{\gamma}|)^{-1}$ in the V_+ direction.

If applied to a circular source of radius R , these effects will result in an ellipse with semi-major and semi-minor axis a and b respectively given by:

$$a = R' \Lambda_+ = \mu R (1 - \kappa + |\boldsymbol{\gamma}|) = \mu a' = \frac{R}{1 - \kappa - |\boldsymbol{\gamma}|} \quad (\text{A.57})$$

$$b = R' \Lambda_- = \mu R (1 - \kappa - |\boldsymbol{\gamma}|) = \mu b' = \frac{R}{1 - \kappa + |\boldsymbol{\gamma}|} \quad (\text{A.58})$$

These effects, applied to a circular source of radius R are illustrated in Fig. A.2.

Appendix A. Appendix

In the particular case of $\gamma_1 = 0$ or $\gamma_2 = 0$:

$$\begin{aligned} \gamma_1 = 0, \quad \Lambda_- = \mu(1 - \kappa - \gamma_2), \quad \Lambda_+ = \mu(1 - \kappa + \gamma_2), \quad \mathbf{V}_- = \begin{pmatrix} 1 \\ -1 \end{pmatrix}, \quad \mathbf{V}_+ = \begin{pmatrix} 1 \\ 1 \end{pmatrix} \\ \gamma_2 = 0, \quad \Lambda_- = \mu(1 - \kappa - \gamma_1), \quad \Lambda_+ = \mu(1 - \kappa + \gamma_1), \quad \mathbf{V}_- = \begin{pmatrix} 0 \\ 1 \end{pmatrix}, \quad \mathbf{V}_+ = \begin{pmatrix} 1 \\ 0 \end{pmatrix} \end{aligned}$$

Therefore, the effect of γ_2 alone is to stretch by a factor $\Lambda_+ = \mu(1 - \kappa + \gamma_2)$ along the first diagonal ($\phi = \pi/4$) and compress by a factor $\Lambda_- = \mu(1 - \kappa - \gamma_2)$ along the second diagonal ($\phi = -\pi/4$); whereas γ_1 alone causes a stretch by a factor $\Lambda_+ = 1 - \kappa + \gamma_1$ along the β_1 axis and a compression by a factor $\Lambda_- = 1 - \kappa - \gamma_1$ along the β_2 axis. The further a point lies from a eigenvector, the greater the compression/stretch effect is.

Representation in Polar coordinates

The angle ϕ between the semi-major axis in the \mathbf{V}_+ directions and the θ_1 axis can be obtained from equation (A.49) or (A.50). One obtains

$$\tan \phi = \frac{\beta_2}{\beta_1} = \frac{|\boldsymbol{\gamma}| - \gamma_1}{\gamma_2} = \frac{\gamma_2}{|\boldsymbol{\gamma}| + \gamma_1} \quad (\text{A.59})$$

so that

$$\phi = \arctan\left(\frac{|\boldsymbol{\gamma}| - \gamma_1}{\gamma_2}\right) + k\pi = \frac{1}{2} \arctan\left(\frac{\gamma_2}{\gamma_1}\right) + k\pi \quad (k \in \mathbb{Z}) \quad (\text{A.60})$$

Further

$$\sin \phi = \frac{|\boldsymbol{\gamma}| - \gamma_1}{\sqrt{2|\boldsymbol{\gamma}|(|\boldsymbol{\gamma}| - \gamma_1)}} = \frac{|\boldsymbol{\gamma}| - \gamma_1}{\eta^2} = \frac{\sqrt{|\boldsymbol{\gamma}| - \gamma_1}}{\sqrt{2|\boldsymbol{\gamma}|}} \quad (\text{A.61})$$

$$\cos \phi = \frac{\gamma_2}{\sqrt{2|\boldsymbol{\gamma}|(|\boldsymbol{\gamma}| - \gamma_1)}} = \frac{\gamma_2}{\eta^2} \quad (\text{A.62})$$

As in A.1.1, the diagonal matrix (A.55) can be expressed as

$$\mathcal{D} = \mathcal{R}_\phi^{-1} \mathcal{M} \mathcal{R}_\phi \Leftrightarrow \mathcal{R}_\phi \mathcal{D} \mathcal{R}_\phi^{-1} = \mathcal{R}_\phi (\mathcal{R}_\phi^{-1} \mathcal{M} \mathcal{R}_\phi) \mathcal{R}_\phi^{-1} \quad (\text{A.63})$$

that is

$$\mathcal{M} = \mathcal{R}_\phi \mathcal{D} \mathcal{R}_\phi^{-1} = \mathcal{R}_\phi \mathcal{D} \mathcal{R}_\phi^T \quad (\text{A.64})$$

Using (A.56), one obtains

$$\begin{aligned} \mathcal{M} &= \mathcal{R}_\phi [\mu(1 - \kappa) \mathcal{I} + \mu |\boldsymbol{\gamma}| \mathcal{S}] \mathcal{R}_\phi^T \\ &= \mu(1 - \kappa) \mathcal{R}_\phi \mathcal{R}_\phi^T + \mu |\boldsymbol{\gamma}| \mathcal{R}_\phi \mathcal{S} \mathcal{R}_\phi^T \\ &= \mu \left[(1 - \kappa) \mathcal{I} + |\boldsymbol{\gamma}| \mathcal{R}_\phi \mathcal{S} \mathcal{R}_\phi^T \right] \end{aligned} \quad (\text{A.65})$$

with

$$\mathcal{R}_\phi \mathcal{S} \mathcal{R}_\phi^T = \begin{pmatrix} \cos 2\phi & \sin 2\phi \\ \sin 2\phi & -\cos 2\phi \end{pmatrix} \quad (\text{A.66})$$

as in A.1.1. Using equation(A.66), \mathcal{M} can therefore be expressed as

$$\mathcal{M} = \mu(1 - \kappa) \begin{pmatrix} 1 & 0 \\ 0 & 1 \end{pmatrix} + \mu |\boldsymbol{\gamma}| \begin{pmatrix} \cos 2\phi & \sin 2\phi \\ \sin 2\phi & -\cos 2\phi \end{pmatrix} = \mu(1 - \kappa) \mathcal{I} + \mu |\boldsymbol{\gamma}| \mathcal{S}_\phi \quad (\text{A.67})$$

The shear has components

$$\gamma_1 = |\boldsymbol{\gamma}| \cos(2\phi) \quad (\text{A.68})$$

$$\gamma_2 = |\boldsymbol{\gamma}| \sin(2\phi) \quad (\text{A.69})$$

and is thus invariant under a rotation of angle π radians. One can also check this by using (A.59) with the identity

$$\tan 2\alpha = \frac{2 \tan \alpha}{1 - \tan^2 \alpha} \quad (\text{A.70})$$

which gives

$$\tan 2\phi = \frac{2}{1 - \left(\frac{|\boldsymbol{\gamma}| - \gamma_1}{\gamma_2}\right)^2} \frac{|\boldsymbol{\gamma}| - \gamma_1}{\gamma_2} = \frac{2\gamma_2 (|\boldsymbol{\gamma}| - \gamma_1)}{-2\gamma_1^2 + 2\gamma_1 |\boldsymbol{\gamma}|} = \frac{2\gamma_2 (|\boldsymbol{\gamma}| - \gamma_1)}{-2\gamma_1 (\gamma_1 - |\boldsymbol{\gamma}|)} = \frac{\gamma_2}{\gamma_1} \quad (\text{A.71})$$

A.2 Complex ellipticity χ

The second brightness moments of lensed and unlensed sources are respectively given by (4.3) and (4.6)

$$Q = (Q_{ij}) = \frac{\int w_I [I(\boldsymbol{\theta})] I(\boldsymbol{\theta}) (\theta_i - \bar{\theta}_i) (\theta_j - \bar{\theta}_j) d^2\theta}{\int w_I [I(\boldsymbol{\theta})] I(\boldsymbol{\theta}) d^2\theta} \quad i, j \in \{1, 2\} \quad (\text{A.72})$$

$$Q^{src} = (Q_{ij}^{src}) = \frac{\int w_I [I_{src}(\boldsymbol{\beta})] I_{src}(\boldsymbol{\beta}) (\beta_i - \bar{\beta}_i) (\beta_j - \bar{\beta}_j) d^2\beta}{\int w_I [I_{src}(\boldsymbol{\beta})] I_{src}(\boldsymbol{\beta}) d^2\beta} \quad i, j \in \{1, 2\} \quad (\text{A.73})$$

where the centroid $\bar{\boldsymbol{\theta}}$ has been defined by (4.4).

Gravitational lensing conserves surface brightness, so if $I_{src}(\boldsymbol{\beta})$ is the surface brightness in the source plane, the observed surface brightness distribution $I(\boldsymbol{\theta})$ in the lens plane is

$$I = I(\boldsymbol{\theta}) = I_{src} [\boldsymbol{\beta}(\boldsymbol{\theta})] \quad (\text{A.74})$$

Appendix A. Appendix

Hence

$$\beta_i = (\mathcal{A}\boldsymbol{\theta})_i = \sum_k \mathcal{A}_{ik} \theta_k \quad i, k \in \{1, 2\} \quad (\text{A.75})$$

and

$$d^2\beta = \det(\mathcal{A}) d^2\theta \quad (\text{A.76})$$

where

$$\mathcal{A} = \begin{pmatrix} 1 - \kappa - \gamma_1 & -\gamma_2 \\ -\gamma_2 & 1 - \kappa + \gamma_1 \end{pmatrix} \quad (\text{A.77})$$

and

$$\mathcal{M} = \mathcal{A}^{-1} = \mu \begin{pmatrix} 1 - \kappa + \gamma_1 & \gamma_2 \\ \gamma_2 & 1 - \kappa - \gamma_1 \end{pmatrix} \quad \mu = \frac{1}{(1 - \kappa)^2 - |\boldsymbol{\gamma}|^2} \quad (\text{A.78})$$

In the following, we assume without loss of generality that the Q_{ij} components of matrix (A.72) are evaluated at the centroid of the lensed image, that is $\bar{\theta}_i = 0$.

One commonly-used definition of ellipticity in weak lensing is

$$\boldsymbol{\chi} = \chi_1 + i\chi_2 = \frac{Q_{11} - Q_{22}}{T} + i \frac{2Q_{12}}{T} \quad T = Q_{11} + Q_{22} \quad (\text{A.79})$$

$$Q_{ij} = \frac{\int w I(\boldsymbol{\theta}) \theta_j \theta_j d^2\theta}{\int w I(\boldsymbol{\theta}) d^2\theta} \quad (\text{A.80})$$

so that:

$$Q_{11} = \frac{\int w I(\boldsymbol{\theta}) \theta_1 \theta_1 d^2\theta}{\int w I(\boldsymbol{\theta}) d^2\theta} \quad Q_{22} = \frac{\int w I(\boldsymbol{\theta}) \theta_2 \theta_2 d^2\theta}{\int w I(\boldsymbol{\theta}) d^2\theta} \quad (\text{A.81})$$

$$Q_{12} = Q_{21} = \frac{\int w I(\boldsymbol{\theta}) \theta_1 \theta_2 d^2\theta}{\int w I(\boldsymbol{\theta}) d^2\theta} \quad (\text{A.82})$$

An simple expression for $\boldsymbol{\chi}$ can be obtained, assuming the source is circular and variations of convergence and shear are negligible across the galaxy image.

A.2.1 Expression for χ_1

Using (A.72) and (A.76), one can relate the quadrupole moment of image and source as

$$\begin{aligned}
 Q_{ij} &= \frac{\int w I(\boldsymbol{\theta}) \theta_i \theta_j d^2 \boldsymbol{\theta}}{\int w I(\boldsymbol{\theta}) d^2 \boldsymbol{\theta}} \\
 &= \frac{\int w I_{src}(\boldsymbol{\beta}) \frac{1}{\det(\mathcal{A})} \sum_k \mathcal{A}_{ik}^{-1} \beta_k \sum_l \mathcal{A}_{jl}^{-1} \beta_l d^2 \boldsymbol{\beta}}{\int w I_{src}(\boldsymbol{\beta}) \frac{1}{\det(\mathcal{A})} d^2 \boldsymbol{\beta}} \\
 &= \frac{\int w I_{src}(\boldsymbol{\beta}) \sum_k \mathcal{A}_{ik}^{-1} \beta_k \sum_l \mathcal{A}_{jl}^{-1} \beta_l d^2 \boldsymbol{\beta}}{\int w I_{src}(\boldsymbol{\beta}) d^2 \boldsymbol{\beta}}
 \end{aligned} \tag{A.83}$$

Hence

$$\begin{aligned}
 Q_{11} &= \frac{\int w I(\boldsymbol{\theta}) \theta_1 \theta_1 d^2 \boldsymbol{\theta}}{\int w I_{src}(\boldsymbol{\beta}) d^2 \boldsymbol{\beta}} \\
 &= \frac{1}{\int w I_{src}(\boldsymbol{\beta}) d^2 \boldsymbol{\beta}} \int w I_{src}(\boldsymbol{\beta}) \sum_k \mathcal{A}_{1k}^{-1} \beta_k \sum_l \mathcal{A}_{1l}^{-1} \beta_l d^2 \boldsymbol{\beta} \\
 Q_{22} &= \frac{\int w I(\boldsymbol{\theta}) \theta_2 \theta_2 d^2 \boldsymbol{\theta}}{\int w I_{src}(\boldsymbol{\beta}) d^2 \boldsymbol{\beta}} \\
 &= \frac{1}{\int w I_{src}(\boldsymbol{\beta}) d^2 \boldsymbol{\beta}} \int w I_{src}(\boldsymbol{\beta}) \sum_k \mathcal{A}_{2k}^{-1} \beta_k \sum_l \mathcal{A}_{2l}^{-1} \beta_l d^2 \boldsymbol{\beta}
 \end{aligned} \tag{A.84}$$

$$\begin{aligned}
 \chi_1 &= \frac{Q_{11} - Q_{22}}{Q_{11} + Q_{22}} = \frac{\int w I_{src}(\boldsymbol{\beta}) d^2 \boldsymbol{\beta} \int \left(\sum_k \mathcal{A}_{1k}^{-1} \beta_k \sum_l \mathcal{A}_{1l}^{-1} \beta_l - \sum_k \mathcal{A}_{2k}^{-1} \beta_k \sum_l \mathcal{A}_{2l}^{-1} \beta_l \right) w I_{src}(\boldsymbol{\beta}) d^2 \boldsymbol{\beta}}{\int w I_{src}(\boldsymbol{\beta}) d^2 \boldsymbol{\beta} \int \left(\sum_k \mathcal{A}_{1k}^{-1} \beta_k \sum_l \mathcal{A}_{1l}^{-1} \beta_l + \sum_k \mathcal{A}_{2k}^{-1} \beta_k \sum_l \mathcal{A}_{2l}^{-1} \beta_l \right) w I_{src}(\boldsymbol{\beta}) d^2 \boldsymbol{\beta}} \\
 &= \frac{\sum_k \sum_l \left[\int (\mathcal{A}_{1k}^{-1} \mathcal{A}_{1l}^{-1} - \mathcal{A}_{2k}^{-1} \mathcal{A}_{2l}^{-1}) \beta_k \beta_l w I_{src}(\boldsymbol{\beta}) d\beta_k d\beta_l \right]}{\sum_k \sum_l \left[\int (\mathcal{A}_{1k}^{-1} \mathcal{A}_{1l}^{-1} + \mathcal{A}_{2k}^{-1} \mathcal{A}_{2l}^{-1}) \beta_k \beta_l w I_{src}(\boldsymbol{\beta}) d\beta_k d\beta_l \right]}
 \end{aligned} \tag{A.85}$$

Appendix A. Appendix

Neglecting the variation of convergence and shear on β across the galaxy image, the \mathcal{A}_{1k}^{-1} can be considered constant and the equation becomes

$$\chi_1 = \frac{\sum_k \sum_l \left[(\mathcal{A}_{1k}^{-1} \mathcal{A}_{1l}^{-1} - \mathcal{A}_{2k}^{-1} \mathcal{A}_{2l}^{-1}) \int w I_{src}(\boldsymbol{\beta}) \beta_k \beta_l d\beta_k d\beta_l \right]}{\sum_k \sum_l \left[(\mathcal{A}_{1k}^{-1} \mathcal{A}_{1l}^{-1} + \mathcal{A}_{2k}^{-1} \mathcal{A}_{2l}^{-1}) \int w I_{src}(\boldsymbol{\beta}) \beta_k \beta_l d\beta_k d\beta_l \right]} \quad (\text{A.86})$$

The integral $\int w I_{src}(\boldsymbol{\beta}) \beta_k \beta_l d\beta_k d\beta_l$ vanishes over a circular source unless $k = l$, so the above equation reduces to

$$\begin{aligned} \chi_1 &= \frac{\sum_k \sum_l (\mathcal{A}_{1k}^{-1} \mathcal{A}_{1k}^{-1} - \mathcal{A}_{2k}^{-1} \mathcal{A}_{2l}^{-1}) \delta_{kl}}{\sum_k \sum_l (\mathcal{A}_{1k}^{-1} \mathcal{A}_{1l}^{-1} + \mathcal{A}_{2k}^{-1} \mathcal{A}_{2l}^{-1}) \delta_{kl}} \\ &= \frac{(\mathcal{A}_{11}^{-1})^2 - (\mathcal{A}_{22}^{-1})^2}{(\mathcal{A}_{11}^{-1})^2 + (\mathcal{A}_{22}^{-1})^2 + 2(\mathcal{A}_{12}^{-1})^2} \end{aligned} \quad (\text{A.87})$$

Substituting the expression for the \mathcal{A}_{ij}^{-1} coefficients from (A.78) yields

$$\begin{aligned} \chi_1 &= \frac{\mu^2 (1 - \kappa + \gamma_1)^2 - \mu^2 (1 - \kappa - \gamma_1)^2}{\mu^2 (1 - \kappa + \gamma_1)^2 + \mu^2 (1 - \kappa - \gamma_1)^2 + 2\mu^2 \gamma_2^2} \\ &= \frac{4\gamma_1 (1 - \kappa)}{2(1 - \kappa)^2 + 2\mu^2 |\boldsymbol{\gamma}|^2} \end{aligned} \quad (\text{A.88})$$

$$= \frac{2\gamma_1 (1 - \kappa)}{(1 - \kappa)^2 + |\boldsymbol{\gamma}|^2} \quad (\text{A.89})$$

This can also be expressed as

$$\chi_1 = 2\gamma_1 \frac{\lambda_- + \lambda_+}{\lambda_-^2 + \lambda_+^2}$$

where

$$\lambda_{\pm} = 1 - \kappa \pm |\boldsymbol{\gamma}|, \quad (\lambda_- < \lambda_+)$$

are the eigenvalues of \mathcal{A} .

A.2.2 Expression for χ_2

Starting from

$$Q_{12} = Q_{21} = \frac{\int w I(\boldsymbol{\theta}) \theta_1 \theta_2 d^2\boldsymbol{\theta}}{\int w I_{src}(\boldsymbol{\beta}) d^2\boldsymbol{\beta}} \quad (\text{A.90})$$

and using (A.72) with (A.76), the second ellipticity component reads

$$\begin{aligned}
 \chi_2 &= \frac{2Q_{12}}{Q_{11} + Q_{22}} = 2 \frac{\int w I_{src}(\boldsymbol{\beta}) d^2 \boldsymbol{\beta} \int w I_{src}(\boldsymbol{\beta}) \sum_k \mathcal{A}_{1k}^{-1} \beta_k \sum_l \mathcal{A}_{2l}^{-1} \beta_l d^2 \boldsymbol{\beta}}{\int w I_{src}(\boldsymbol{\beta}) d^2 \boldsymbol{\beta} \int \left(\sum_k \mathcal{A}_{1k}^{-1} \beta_k \sum_l \mathcal{A}_{1l}^{-1} \beta_l + \sum_k \mathcal{A}_{2k}^{-1} \beta_k \sum_l \mathcal{A}_{2l}^{-1} \beta_l \right) w I_{src}(\boldsymbol{\beta}) d^2 \boldsymbol{\beta}} \\
 &= 2 \frac{\int w I_{src}(\boldsymbol{\beta}) \sum_k \mathcal{A}_{1k}^{-1} \beta_k \sum_l \mathcal{A}_{2l}^{-1} \beta_l d^2 \boldsymbol{\beta}}{\int \left(\sum_k \mathcal{A}_{1k}^{-1} \beta_k \sum_l \mathcal{A}_{1l}^{-1} \beta_l + \sum_k \mathcal{A}_{2k}^{-1} \beta_k \sum_l \mathcal{A}_{2l}^{-1} \beta_l \right) w I_{src}(\boldsymbol{\beta}) d^2 \boldsymbol{\beta}} \\
 &= 2 \frac{\sum_k \sum_l \left[\int \mathcal{A}_{1k}^{-1} \mathcal{A}_{2l}^{-1} \beta_k \beta_l w I_{src}(\boldsymbol{\beta}) d\beta_k d\beta_l \right]}{\sum_k \sum_l \left[\int (\mathcal{A}_{1k}^{-1} \mathcal{A}_{1l}^{-1} + \mathcal{A}_{2k}^{-1} \mathcal{A}_{2l}^{-1}) \beta_k \beta_l w I_{src}(\boldsymbol{\beta}) d\beta_k d\beta_l \right]} \tag{A.91}
 \end{aligned}$$

Making the same assumptions as before, this reduces to

$$\begin{aligned}
 \chi_2 &= 2 \frac{\sum_k \sum_l \left[\mathcal{A}_{1k}^{-1} \mathcal{A}_{2l}^{-1} \int \beta_k \beta_l w I_{src}(\boldsymbol{\beta}) d\beta_k d\beta_l \right]}{\sum_k \sum_l \left[(\mathcal{A}_{1k}^{-1} \mathcal{A}_{1l}^{-1} + \mathcal{A}_{2k}^{-1} \mathcal{A}_{2l}^{-1}) \int \beta_k \beta_l w I_{src}(\boldsymbol{\beta}) d\beta_k d\beta_l \right]} \\
 &= 2 \frac{\sum_k \sum_l \mathcal{A}_{1k}^{-1} \mathcal{A}_{2l}^{-1} \delta_{kl}}{\sum_k \sum_l (\mathcal{A}_{1k}^{-1} \mathcal{A}_{1l}^{-1} + \mathcal{A}_{2k}^{-1} \mathcal{A}_{2l}^{-1}) \delta_{kl}} \\
 &= 2 \frac{\mathcal{A}_{11}^{-1} \mathcal{A}_{21}^{-1} + \mathcal{A}_{12}^{-1} \mathcal{A}_{22}^{-1}}{(\mathcal{A}_{11}^{-1})^2 + (\mathcal{A}_{22}^{-1})^2 + 2(\mathcal{A}_{12}^{-1})^2} \quad \text{with } \mathcal{A}_{21}^{-1} = \mathcal{A}_{12}^{-1} \tag{A.92}
 \end{aligned}$$

$$= 2 \frac{\mathcal{A}_{12}^{-1} (\mathcal{A}_{11}^{-1} + \mathcal{A}_{22}^{-1})}{(\mathcal{A}_{11}^{-1})^2 + (\mathcal{A}_{22}^{-1})^2 + 2(\mathcal{A}_{12}^{-1})^2} \tag{A.93}$$

Substituting the expression for the \mathcal{A}_{ij}^{-1} coefficients from (A.78)

$$\begin{aligned}
 \chi_2 &= 2 \frac{2\mu^2 \gamma_2 (1 - \kappa)}{2\mu^2 (1 - \kappa)^2 + 2\mu^2 |\boldsymbol{\gamma}|^2} \\
 &= \frac{2\gamma_2 (1 - \kappa)}{(1 - \kappa)^2 + |\boldsymbol{\gamma}|^2} \\
 &= 2\gamma_2 \frac{\lambda_- + \lambda_+}{\lambda_-^2 + \lambda_+^2} \tag{A.94}
 \end{aligned}$$

The ellipticity χ thus reads

$$\begin{aligned}
 \chi &= \frac{2\gamma_1(1-\kappa)}{(1-\kappa)^2 + |\boldsymbol{\gamma}|^2} + i \frac{2\gamma_2(1-\kappa)}{(1-\kappa)^2 + |\boldsymbol{\gamma}|^2} \\
 &= \frac{2(1-\kappa)}{(1-\kappa)^2 + |\boldsymbol{\gamma}|^2} (\gamma_1 + i\gamma_2) \\
 &= \frac{2(1-\kappa)}{(1-\kappa)^2 + |\boldsymbol{\gamma}|^2} \boldsymbol{\gamma} \quad \text{with } \boldsymbol{\gamma} = \gamma_1 + i\gamma_2 \\
 &= \frac{2(1-\kappa)}{(1-\kappa)^2 + |\boldsymbol{\gamma}|^2} |\boldsymbol{\gamma}| e^{2i\phi}
 \end{aligned} \tag{A.95}$$

Therefore one can define

$$\begin{aligned}
 |\chi| &= \frac{2(1-\kappa)}{(1-\kappa)^2 + |\boldsymbol{\gamma}|^2} |\boldsymbol{\gamma}| \\
 &= \frac{\lambda_+^2 - \lambda_-^2}{\lambda_+^2 + \lambda_-^2} = \frac{\Lambda_+^2 - \Lambda_-^2}{\Lambda_+^2 + \Lambda_-^2} = \frac{\Sigma_+ - \Sigma_-}{\Sigma_+ + \Sigma_-}
 \end{aligned} \tag{A.96}$$

where λ_+ , Λ_{\pm} and Σ_{\pm} are the respective eigenvalues of \mathcal{A} , $\mathcal{M} = \mathcal{A}^{-1}$ and Q respectively (see Sects. A.1.1 and A.1.2).

$$\lambda_{\pm} = 1 - \kappa \pm |\boldsymbol{\gamma}| \quad \Lambda_{\pm} = \mu (1 - \kappa \pm |\boldsymbol{\gamma}|) = \frac{1}{\lambda_{\mp}} \quad \Sigma_{\pm} = \Lambda_{\pm}^2$$

and write

$$\boldsymbol{\chi} = |\chi| e^{2i\phi} \tag{A.97}$$

Substituting (A.3), (A.4), (A.18, A.19) into (A.97) yields

$$\boldsymbol{\chi} = \frac{a^2 - b^2}{a^2 + b^2} e^{2i\phi} \tag{A.98}$$

An equivalent form in terms of reduced shear $|\mathbf{g}| = \frac{|\boldsymbol{\gamma}|}{1-\kappa}$ is

$$\boldsymbol{\chi} = \frac{2}{(1-\kappa)^2 |\mathbf{g}| (1 + |\mathbf{g}|^2)} e^{2i\phi} \tag{A.99}$$

A.3 Explicit expression of the image (Q_{ij}) matrix

From Sects. A.2.2 and A.2.2, one obtains the expressions for the individual moments

$$Q_{11} + Q_{22} = 2\mu^2 \left[(1-\kappa)^2 + |\boldsymbol{\gamma}|^2 \right] \quad Q_{11} - Q_{22} = 4\mu^2 \gamma_1 (1-\kappa) \tag{A.100}$$

$$\begin{aligned}
 Q_{12} &= Q_{21} = 2\mu^2 \gamma_2 (1 - \kappa) \\
 &= 2\mu(1 - \kappa) \mu \gamma_2 \\
 &= 2 \frac{\mathcal{M}_{11} + \mathcal{M}_{22}}{2} \mathcal{M}_{12} \\
 &= (\mathcal{M}_{11} + \mathcal{M}_{22}) \mathcal{M}_{12} = (\mathcal{M}_{11} + \mathcal{M}_{22}) \mathcal{M}_{21}
 \end{aligned}$$

where \mathcal{M} is the magnification matrix with expression

$$\mathcal{M} = \mathcal{A}^{-1} = \mu \begin{pmatrix} 1 - \kappa + \gamma_1 & \gamma_2 \\ \gamma_2 & 1 - \kappa - \gamma_1 \end{pmatrix} \quad (\text{A.101})$$

and μ is the magnification factor

$$\mu = \frac{1}{(1 - \kappa)^2 - |\boldsymbol{\gamma}|^2} \quad (\text{A.102})$$

Hence

$$\begin{aligned}
 2Q_{11} &= 2\mu^2 \left[(1 - \kappa)^2 + |\boldsymbol{\gamma}|^2 \right] + 4\mu^2 \gamma_1 (1 - \kappa) \\
 &= 2\mu^2 \left[(1 - \kappa)^2 + |\boldsymbol{\gamma}|^2 + 2\gamma_1 (1 - \kappa) \right]
 \end{aligned} \quad (\text{A.103})$$

so that

$$\begin{aligned}
 Q_{11} &= \mu^2 \left[(1 - \kappa)^2 + |\boldsymbol{\gamma}|^2 + 2\gamma_1 (1 - \kappa) \right] \\
 &= \mu^2 \left[(1 - \kappa)^2 + 2\gamma_1 (1 - \kappa) \right] + |\boldsymbol{\gamma}|^2 - \gamma_1^2 \\
 &= \mu^2 \left[(1 - \kappa + \gamma_1)^2 + |\boldsymbol{\gamma}|^2 - \gamma_1^2 \right] \\
 &= \mu^2 \left[(1 - \kappa + \gamma_1)^2 + \gamma_2^2 \right] \\
 &= (\mathcal{M}_{11})^2 + (\mathcal{M}_{12})^2
 \end{aligned} \quad (\text{A.104})$$

The same way

$$2Q_{22} = 2\mu^2 \left[(1 - \kappa)^2 + |\boldsymbol{\gamma}|^2 \right] - 4\mu^2 \gamma_1 (1 - \kappa) \quad (\text{A.105})$$

$$= 2\mu^2 \left[(1 - \kappa)^2 + |\boldsymbol{\gamma}|^2 - 2\gamma_1 (1 - \kappa) \right] \quad (\text{A.106})$$

Therefore

$$\begin{aligned}
 Q_{22} &= \mu^2 \left[(1 - \kappa)^2 + |\boldsymbol{\gamma}|^2 - 2\gamma_1 (1 - \kappa) \right] \\
 &= \mu^2 \left[(1 - \kappa)^2 - 2\gamma_1 (1 - \kappa) \right] + |\boldsymbol{\gamma}|^2 - \gamma_1^2 \\
 &= \mu^2 \left[(1 - \kappa - \gamma_1)^2 + \gamma_2^2 \right] \\
 &= (\mathcal{M}_{22})^2 + (\mathcal{M}_{21})^2
 \end{aligned} \quad (\text{A.107})$$

To summarise

$$Q_{11} = \mu^2 \left[(1 - \kappa + \gamma_1)^2 + \gamma_2^2 \right] = (\mathcal{M}_{11})^2 + (\mathcal{M}_{12})^2 \quad (\text{A.108})$$

$$Q_{22} = \mu^2 \left[(1 - \kappa - \gamma_1)^2 + \gamma_2^2 \right] = (\mathcal{M}_{22})^2 + (\mathcal{M}_{21})^2 \quad (\text{A.109})$$

$$Q_{12} = Q_{21} = 2\mu^2 (1 - \kappa) \gamma_2 = (\mathcal{M}_{11} + \mathcal{M}_{22}) \mathcal{M}_{12} = (\mathcal{M}_{11} + \mathcal{M}_{22}) \mathcal{M}_{21} \quad (\text{A.110})$$

It follows that the quadrupole moment matrix reads

$$(Q_{ij}) = \mu^2 \begin{pmatrix} (1 - \kappa + \gamma_1)^2 + \gamma_2^2 & 2(1 - \kappa) \gamma_2 \\ 2(1 - \kappa) \gamma_2 & (1 - \kappa - \gamma_1)^2 + \gamma_2^2 \end{pmatrix} \quad (\text{A.111})$$

$$= \begin{pmatrix} (\mathcal{M}_{11})^2 + (\mathcal{M}_{12})^2 & (\mathcal{M}_{11} + \mathcal{M}_{22}) \mathcal{M}_{12} \\ (\mathcal{M}_{11} + \mathcal{M}_{22}) \mathcal{M}_{21} & (\mathcal{M}_{22})^2 + (\mathcal{M}_{21})^2 \end{pmatrix} \quad (\text{A.112})$$

A.4 Eigenvalues of the image (Q_{ij}) matrix

A.4.1 First Derivation

The characteristic equation of the (Q_{ij}) matrix is given by

$$\det \begin{pmatrix} Q_{11} - \Sigma & Q_{12} \\ Q_{21} & Q_{22} - \Sigma \end{pmatrix} = 0 \Leftrightarrow (Q_{11} - \Sigma)(Q_{22} - \Sigma) - Q_{21}Q_{12} = 0 \quad (\text{A.113})$$

where Σ represents a eigenvalue of (Q_{ij}) . We expect the matrix to be symmetric, thus $Q_{21} = Q_{21}$ and the equation becomes

$$\Sigma^2 - \Sigma(Q_{11} + Q_{22}) + Q_{11}Q_{22} - Q_{12}^2 = 0 \quad (\text{A.114})$$

$$\Sigma^2 - 2\mu^2 \Sigma \left[(1 - \kappa)^2 + |\boldsymbol{r}|^2 \right] + \mu^4 \left\{ [(1 - \kappa) - |\boldsymbol{r}|]^2 [(1 - \kappa) + |\boldsymbol{r}|]^2 \right\} = 0 \quad (\text{A.115})$$

where the magnification factor μ is given by (A.102). The discriminant is

$$\begin{aligned} \Delta' &= \mu^4 \left[(1 - \kappa)^2 + |\boldsymbol{r}|^2 \right]^2 - \mu^4 \left\{ [(1 - \kappa) - |\boldsymbol{r}|]^2 [(1 - \kappa) + |\boldsymbol{r}|]^2 \right\} \\ &= \mu^4 \left[(1 - \kappa)^2 + |\boldsymbol{r}|^2 + [(1 - \kappa) - |\boldsymbol{r}|] [(1 - \kappa) + |\boldsymbol{r}|] \right] \left[(1 - \kappa)^2 + |\boldsymbol{r}|^2 - [(1 - \kappa) - |\boldsymbol{r}|] [(1 - \kappa) + |\boldsymbol{r}|] \right] \\ &= \mu^4 \left[(1 - \kappa)^2 + |\boldsymbol{r}|^2 + (1 - \kappa)^2 - |\boldsymbol{r}|^2 \right] \left[(1 - \kappa)^2 + |\boldsymbol{r}|^2 - (1 - \kappa)^2 + |\boldsymbol{r}|^2 \right] \\ &= \mu^4 [2(1 - \kappa)^2] [2|\boldsymbol{r}|^2] \\ &= 4\mu^4 (1 - \kappa)^2 |\boldsymbol{r}|^2 > 0 \end{aligned} \quad (\text{A.116})$$

Which gives the two real positive eigenvalues

$$\begin{aligned}\Sigma_- &= \mu^2 \left[(1-\kappa)^2 + |\gamma|^2 \right] - 2\mu^2(1-\kappa)|\gamma| \\ &= \mu^2 \left[1-\kappa - |\gamma| \right]^2 \\ &= \mu^2 \lambda_-^2 = \Lambda_-^2\end{aligned}\tag{A.117}$$

$$\begin{aligned}\Sigma_+ &= \mu^2 \left[(1-\kappa)^2 + |\gamma|^2 \right] + 2\mu^2(1-\kappa)|\gamma| \\ &= \mu^2 \left[1-\kappa + |\gamma| \right]^2 \\ &= \mu^2 \lambda_+^2 = \Lambda_+^2\end{aligned}\tag{A.118}$$

A.4.2 Second Derivation

The diagonal matrix \mathcal{D}_Q to be found is assumed to be of the form

$$\mathcal{D}_Q = \begin{pmatrix} \Sigma_+ & 0 \\ 0 & \Sigma_- \end{pmatrix}\tag{A.119}$$

and the following expression holds

$$Q = \mathcal{R}_\phi \mathcal{D}_Q \mathcal{R}_\phi^{-1}$$

where

$$\mathcal{R}_\phi = \begin{pmatrix} \cos \phi & -\sin \phi \\ \sin \phi & \cos \phi \end{pmatrix}\tag{A.120}$$

represents the anticlockwise rotation R_ϕ in the image plane, generated by the diagonalisation transformation.

$$\begin{aligned}Q &= \mathcal{R}_\phi \mathcal{D}_Q \mathcal{R}_\phi^{-1} = \begin{pmatrix} \cos \phi & -\sin \phi \\ \sin \phi & \cos \phi \end{pmatrix} \begin{pmatrix} \Sigma_+ & 0 \\ 0 & \Sigma_- \end{pmatrix} \begin{pmatrix} \cos \phi & \sin \phi \\ -\sin \phi & \cos \phi \end{pmatrix} \\ &= \begin{pmatrix} \Sigma_+ \cos \phi & -\Sigma_- \sin \phi \\ \Sigma_+ \sin \phi & \Sigma_- \cos \phi \end{pmatrix} \begin{pmatrix} \cos \phi & \sin \phi \\ -\sin \phi & \cos \phi \end{pmatrix} \\ &= \begin{pmatrix} \Sigma_+ \cos^2 \phi + \Sigma_- \sin^2 \phi & \cos \phi \sin \phi (\Sigma_- - \Sigma_+) \\ \cos \phi \sin \phi (\Sigma_- - \Sigma_+) & \Sigma_+ \sin^2 \phi + \Sigma_- \cos^2 \phi \end{pmatrix} \\ &= \begin{pmatrix} \Sigma_+ + \sin^2 \phi (\Sigma_- - \Sigma_+) & \cos \phi \sin \phi (\Sigma_+ - \Sigma_-) \\ \cos \phi \sin \phi (\Sigma_+ - \Sigma_-) & \Sigma_- + \sin^2 \phi (\Sigma_+ - \Sigma_-) \end{pmatrix}\end{aligned}\tag{A.121}$$

Using

$$\sin \phi = \frac{|\mathbf{r}| - \gamma_1}{\sqrt{2|\mathbf{r}|(|\mathbf{r}| - \gamma_1)}} = \frac{|\mathbf{r}| - \gamma_1}{\eta^2} = \frac{\sqrt{|\mathbf{r}| - \gamma_1}}{\sqrt{2|\mathbf{r}|}} \quad (\text{A.122})$$

$$\cos \phi = \frac{\gamma_2}{\sqrt{2|\mathbf{r}|(|\mathbf{r}| - \gamma_1)}} = \frac{\gamma_2}{\eta^2} \quad (\text{A.123})$$

one derives

$$\sin \phi \cos \phi = \frac{\gamma_2}{2|\mathbf{r}|} \quad \sin^2 \phi = \frac{|\mathbf{r}| - \gamma_1}{2|\mathbf{r}|} \quad \cos^2 \phi = \frac{\gamma_2^2}{2|\mathbf{r}|(|\mathbf{r}| - \gamma_1)}$$

Comparing with the Q_{ij} coefficients

$$Q_{12} = Q_{21} = 2\mu^2(1 - \kappa)\gamma_2 = \frac{\gamma_2}{2|\mathbf{r}|}(\Sigma_+ - \Sigma_-) \quad (\text{A.124})$$

$$Q_{11} = \mu^2 \left[(1 - \kappa)^2 + |\mathbf{r}|^2 + 2\gamma_1(1 - \kappa) \right] = \Sigma_+ + \frac{|\mathbf{r}| - \gamma_1}{2|\mathbf{r}|}(\Sigma_- - \Sigma_+) \quad (\text{A.125})$$

$$Q_{22} = \mu^2 \left[(1 - \kappa)^2 + |\mathbf{r}|^2 - 2\gamma_1(1 - \kappa) \right] = \Sigma_- + \frac{|\mathbf{r}| - \gamma_1}{2|\mathbf{r}|}(\Sigma_+ - \Sigma_-) \quad (\text{A.126})$$

one finds

$$(\Sigma_+ - \Sigma_-) = 4\mu^2(1 - \kappa)|\mathbf{r}| \quad (\text{A.127})$$

$$\begin{aligned} \Sigma_+ &= \mu^2 \left[(1 - \kappa)^2 + |\mathbf{r}|^2 + 2\gamma_1(1 - \kappa) \right] + \frac{|\mathbf{r}| - \gamma_1}{2|\mathbf{r}|} 4\mu^2(1 - \kappa)|\mathbf{r}| \\ &= \mu^2 \left[(1 - \kappa)^2 + |\mathbf{r}|^2 + 2\gamma_1(1 - \kappa) + 2(|\mathbf{r}| - \gamma_1)(1 - \kappa) \right] \\ &= \mu^2 \left[(1 - \kappa)^2 + |\mathbf{r}|^2 + 2|\mathbf{r}|(1 - \kappa) \right] \\ &= \mu^2 \left[(1 - \kappa) + |\mathbf{r}| \right]^2 \\ &= \mu^2 \lambda_+^2 \end{aligned} \quad (\text{A.128})$$

$$= \Lambda_+^2 \quad (\text{A.129})$$

A.5. Representation of the image (Q_{ij}) matrix in Polar coordinates

$$\begin{aligned}
\Sigma_- &= \mu^2 \left[(1-\kappa)^2 + |\boldsymbol{\gamma}|^2 - 2\gamma_1(1-\kappa) \right] - \frac{|\boldsymbol{\gamma}| - \gamma_1}{2|\boldsymbol{\gamma}|} 4\mu^2(1-\kappa)|\boldsymbol{\gamma}| \\
&= \mu^2 \left[(1-\kappa)^2 + |\boldsymbol{\gamma}|^2 - 2\gamma_1(1-\kappa) - 2(|\boldsymbol{\gamma}| - \gamma_1)(1-\kappa) \right] \\
&= \mu^2 \left[(1-\kappa)^2 + |\boldsymbol{\gamma}|^2 - 2|\boldsymbol{\gamma}|(1-\kappa) \right] \\
&= \mu^2 [(1-\kappa) - |\boldsymbol{\gamma}|]^2 \\
&= \mu^2 \lambda_-^2 && \text{(A.130)} \\
&= \Lambda_-^2 && \text{(A.131)}
\end{aligned}$$

A.4.3 Expression in terms of the “shape parameters” Σ and $\Delta\Sigma$

These eigenvalues can also be conveniently expressed in terms of the shape parameters Σ and $\Delta\Sigma$ (Kochanek 1990) as

$$\Sigma_+ = \Sigma + \Delta\Sigma \quad \Sigma_- = \Sigma - \Delta\Sigma \quad \text{(A.132)}$$

where

$$\Sigma = \frac{\Sigma_+ + \Sigma_-}{2} = \mu^2 \left[(1-\kappa)^2 + |\boldsymbol{\gamma}|^2 \right] \quad \Delta\Sigma = \frac{\Sigma_+ - \Sigma_-}{2} = 2\mu^2(1-\kappa)|\boldsymbol{\gamma}| \quad \text{(A.133)}$$

The shape parameters Σ and $\Delta\Sigma$ respectively describes estimate the size of the galaxy and the deviation of its shape from circularity.

Equation (A.98) also yields

$$|\boldsymbol{\chi}| = \frac{\Delta\Sigma}{\Sigma} = \frac{a^2 - b^2}{a^2 + b^2} = \frac{\lambda^2 - \lambda'^2}{\lambda^2 + \lambda'^2} = \frac{\Lambda^2 - \Lambda'^2}{\Lambda^2 + \Lambda'^2} \quad \text{(A.134)}$$

A.5 Representation of the image (Q_{ij}) matrix in Polar coordinates

The diagonal matrix \mathcal{D}_Q of Q reads

$$\mathcal{D}_Q = \begin{pmatrix} \Sigma_+ & 0 \\ 0 & \Sigma_- \end{pmatrix} = \mu^2 \begin{pmatrix} [1-\kappa + |\boldsymbol{\gamma}|]^2 & 0 \\ 0 & [1-\kappa - |\boldsymbol{\gamma}|]^2 \end{pmatrix} = \begin{pmatrix} \Sigma + \Delta\Sigma & 0 \\ 0 & \Sigma - \Delta\Sigma \end{pmatrix} \quad \text{(A.135)}$$

or

$$\mathcal{D}_Q = \Sigma \begin{pmatrix} 1 & 0 \\ 0 & 1 \end{pmatrix} + \Delta\Sigma \begin{pmatrix} 1 & 0 \\ 0 & -1 \end{pmatrix} = \Sigma \mathcal{I} + \Delta\Sigma \mathcal{S} \quad \text{(A.136)}$$

\mathcal{D}_Q can be expressed as

$$\mathcal{D}_Q = \mathcal{R}_\phi^{-1} Q \mathcal{R}_\phi \quad \text{(A.137)}$$

where

$$\mathcal{R}_\phi = \begin{pmatrix} \cos \phi & -\sin \phi \\ \sin \phi & \cos \phi \end{pmatrix} \quad \text{(A.138)}$$

Appendix A. Appendix

describes the anticlockwise rotation R_ϕ in the image plane, generated by the diagonalization transformation. Thus

$$Q = \mathcal{R}_\phi D_Q \mathcal{R}_\phi^{-1} \quad (\text{A.139})$$

or

$$\begin{aligned} Q &= \mathcal{R}_\phi [\Sigma \mathcal{I} + \Delta \Sigma \mathcal{S}] \mathcal{R}_\phi^{-1} \\ &= \Sigma \mathcal{R}_\phi \mathcal{I} \mathcal{R}_\phi^{-1} + \Delta \Sigma \mathcal{R}_\phi \mathcal{S} \mathcal{R}_\phi^{-1} \\ &= \Sigma \mathcal{I} + \Delta \Sigma \mathcal{S}_\phi \end{aligned} \quad (\text{A.140})$$

where the reflection matrix \mathcal{S}_ϕ is

$$\begin{aligned} \mathcal{S}_\phi &= \mathcal{R}_\phi \mathcal{S} \mathcal{R}_\phi^T = \begin{pmatrix} \cos \phi & -\sin \phi \\ \sin \phi & \cos \phi \end{pmatrix} \begin{pmatrix} 1 & 0 \\ 0 & -1 \end{pmatrix} \begin{pmatrix} \cos \phi & \sin \phi \\ -\sin \phi & \cos \phi \end{pmatrix} \\ &= \begin{pmatrix} \cos 2\phi & \sin 2\phi \\ \sin 2\phi & -\cos 2\phi \end{pmatrix} \end{aligned} \quad (\text{A.141})$$

It follows from (A.140) that an expression for the matrix Q in terms of the phase angle ϕ and the shape parameters Σ and $\Delta \Sigma$ is ϕ is

$$Q = \Sigma \mathcal{I} + \Delta \Sigma \mathcal{S}_\phi \quad (\text{A.142})$$

$$\begin{aligned} &= \Sigma \begin{pmatrix} 1 & 0 \\ 0 & 1 \end{pmatrix} + \Delta \Sigma \begin{pmatrix} \cos 2\phi & \sin 2\phi \\ \sin 2\phi & -\cos 2\phi \end{pmatrix} \quad (\text{A.143}) \\ &= \mu^2 \left[(1-\kappa)^2 + |\gamma|^2 \right] \begin{pmatrix} 1 & 0 \\ 0 & 1 \end{pmatrix} + 2\mu^2 (1-\kappa) |\gamma| \begin{pmatrix} \cos 2\phi & \sin 2\phi \\ \sin 2\phi & -\cos 2\phi \end{pmatrix} \\ &= \mu^2 \begin{pmatrix} (1-\kappa + |\gamma|)^2 + 2(1-\kappa) |\gamma| \cos 2\phi & 2(1-\kappa) |\gamma| \sin 2\phi \\ 2(1-\kappa) |\gamma| \sin 2\phi & (1-\kappa)^2 + |\gamma|^2 - 2(1-\kappa) |\gamma| \cos 2\phi \end{pmatrix} \end{aligned}$$

With

$$\begin{aligned} \det Q &= \mu^2 \left[\left[(1-\kappa)^2 + |\gamma|^2 \right]^2 - 4(1-\kappa)^2 |\gamma|^2 \right] \\ &= \frac{\left[(1-\kappa)^2 - |\gamma|^2 \right]^2}{\left[(1-\kappa)^2 + |\gamma|^2 \right]^2} = 1 \end{aligned} \quad (\text{A.144})$$

The distortion characterized by the matrix Q is thus area-preserving. Second-order brightness moments characterize the elliptical area formed by distorting a circularly symmetric distribution of points along two orthogonal directions while preserving the total area of that distribution.

Bibliography

- Abdalla, M. C. B., Nojiri, S., & Odintsov, S. D. 2005, *Classical and Quantum Gravity*, 22, L35
- Abramowitz, M. & Stegun, I. A. 1965, *Handbook of Mathematical Functions*, 1st edn., Dover books on mathematics (Dover Publications)
- Adams, W. S. 1908, *ApJ*, 27, 45
- Ade, P. A. R., Aghanim, N., Armitage-Caplan, C., et al. 2013a, *ArXiv e-prints*
- Ade, P. A. R., Aghanim, N., Armitage-Caplan, C., et al. 2013b, *ArXiv e-prints*
- Afonso, C., Albert, J. N., Andersen, J., et al. 2003, *A&A*, 400, 951
- Alam, U., Sahni, V., Deep Saini, T., & Starobinsky, A. A. 2004, *MNRAS*, 354, 275
- Albrecht, A., Bernstein, G., Cahn, R., et al. 2006, *ArXiv Astrophysics e-prints*
- Albrecht, A. & Steinhardt, P. J. 1982, *Physical Review Letters*, 48, 1220
- Alcock, C., Akerlof, C. W., Allsman, R. A., et al. 1993, *Nature*, 365, 621
- Alpher, R. A., Bethe, H., & Gamow, G. 1948, *Phys. Rev.*, 73, 803
- Alpher, R. A., Follin, J. W., & Herman, R. C. 1953, *Physical Review*, 92, 1347
- Alpher, R. A. & Herman, R. 1948, *Nature*, 162, 774
- Alpher, R. A. & Herman, R. C. 1949, *Phys. Rev.*, 75, 1089
- Amendola, L. & Tsujikawa, S. 2010, *Dark Energy: Theory and Observations*, *Dark Energy: Theory and Observations* (Cambridge University Press)
- Anderson, L., Aubourg, E., Bailey, S., et al. 2012, *MNRAS*, 427, 3435
- Arce, G. 2005, *Nonlinear Signal Processing: A Statistical Approach* (Wiley)
- Armendariz-Picon, C., Mukhanov, V., & Steinhardt, P. J. 2000, *Physical Review Letters*, 85, 4438
- Astier, P., Guy, J., Regnault, N., et al. 2006, *A&A*, 447, 31
- Babul, A. & Lee, M. H. 1991, *MNRAS*, 250, 407
- Bacon, D. J., Massey, R. J., Refregier, A. R., & Ellis, R. S. 2003, *MNRAS*, 344, 673

Bibliography

- Bacon, D. J., Refregier, A. R., & Ellis, R. S. 2000, *Monthly Notices of the Royal Astronomical Society*, 318, 625
- Bacon, D. J., Taylor, A. N., Brown, M. L., et al. 2005, *MNRAS*, 363, 723
- Bahcall, J., Piran, T., & Weinberg, S. 2004, *Dark Matter in the Universe: Second Edition* (World Scientific Publishing Company)
- Bahcall, N. A., Lubin, L. M., & Dorman, V. 1995, *ApJ*, 447, L81
- Bartelmann, M., Narayan, R., Seitz, S., & Schneider, P. 1996, *ApJ*, 464, L115
- Bartelmann, M. & Schneider, P. 1999, *A&A*, 345, 17
- Bartelmann, M. & Schneider, P. 2001, *Phys. Rep.*, 340, 291
- Baum, W. A. 1962, in *IAU Symposium, Vol. 15, Problems of Extra-Galactic Research*, ed. G. C. McVittie, 390
- Baumann, D. 2009, *ArXiv e-prints*
- Bellagamba, F., Meneghetti, M., Moscardini, L., & Bolzonella, M. 2012, *MNRAS*, 422, 553
- Benítez, N. 2000, *ApJ*, 536, 571
- Benjamin, J., Heymans, C., Semboloni, E., et al. 2007, *MNRAS*, 381, 702
- Benjamin, J., Van Waerbeke, L., Heymans, C., et al. 2012, *ArXiv e-prints*
- Bennett, C. L., Bay, M., Halpern, M., et al. 2003a, *ApJ*, 583, 1
- Bennett, C. L., Halpern, M., Hinshaw, G., et al. 2003b, *ApJS*, 148, 1
- Bennett, C. L., Larson, D., Weiland, J. L., et al. 2012, *ArXiv e-prints*
- Bergé, J., Pacaud, F., Réfrégier, A., et al. 2008, *MNRAS*, 385, 695
- Bernardeau, F., Mellier, Y., & van Waerbeke, L. 2002, *A&A*, 389, L28
- Bernardeau, F., van Waerbeke, L., & Mellier, Y. 1997, *A&A*, 322, 1
- Bernstein, G. & Jain, B. 2004, *ApJ*, 600, 17
- Bernstein, G. M. & Jarvis, M. 2002, *AJ*, 123, 583
- Bertone, G. 2010, *Particle Dark Matter : Observations, Models and Searches* (Cambridge University Press)
- Blandford, R. & Narayan, R. 1986, *ApJ*, 310, 568
- Blandford, R. D., Saust, A. B., Brainerd, T. G., & Villumsen, J. V. 1991, *MNRAS*, 251, 600
- Blumenthal, G. R., Faber, S. M., Primack, J. R., & Rees, M. J. 1984, *Nature*, 311, 517
- Bond, J. R. & Efstathiou, G. 1984, *ApJ*, 285, L45

- Bond, J. R., Efstathiou, G., & Tegmark, M. 1997, MNRAS, 291, L33
- Bond, J. R. & Szalay, A. S. 1983, ApJ, 274, 443
- Bosma, A. 1978, PhD thesis, PhD Thesis, Groningen Univ., (1978)
- Boughn, S. & Crittenden, R. 2004, Nature, 427, 45
- Bridle, S., Balan, S. T., Bethge, M., et al. 2010, MNRAS, 405, 2044
- Bridle, S., Shawe-Taylor, J., Amara, A., et al. 2009, Annals of Applied Statistics, 3, 6
- Bridle, S. L., Kneib, J.-P., Bardeau, S., & Gull, S. F. 2002, in The Shapes of Galaxies and their Dark Halos, ed. P. Natarajan, 38–46
- Broadhurst, T. J., Taylor, A. N., & Peacock, J. A. 1995, ApJ, 438, 49
- Brown, M. L., Taylor, A. N., Bacon, D. J., et al. 2003, MNRAS, 341, 100
- Burke, W. L. 1981, ApJ, 244, L1
- Caldwell, R. R. 2002, Physics Letters B, 545, 23
- Capozziello, S., Carloni, S., & Troisi, A. 2003, ArXiv Astrophysics e-prints
- Carroll, S. M., Duvvuri, V., Trodden, M., & Turner, M. S. 2004, Phys. Rev. D, 70, 043528
- Carroll, S. M., Hoffman, M., & Trodden, M. 2003, Phys. Rev. D, 68, 023509
- Chang, C., Kahn, S. M., Jernigan, J. G., et al. 2013, MNRAS, 428, 2695
- Chang, K. & Refsdal, S. 1979, Nature, 282, 561
- Charbonnel, C. 2002, Nature, 415, 27
- Chevallier, M. & Polarski, D. 2001, International Journal of Modern Physics D, 10, 213
- Chiba, T. 2006, Phys. Rev. D, 73, 063501
- Chiba, T., Okabe, T., & Yamaguchi, M. 2000, Phys. Rev. D, 62, 023511
- Cline, J. M., Jeon, S., & Moore, G. D. 2004, Phys. Rev. D, 70, 043543
- Clowe, D., Bradač, M., Gonzalez, A. H., et al. 2006, ApJ, 648, L109
- Clowe, D. & Schneider, P. 2002, A&A, 395, 385
- Colless, M., Peterson, B. A., Jackson, C., et al. 2003, ArXiv Astrophysics e-prints
- Conley, A., Guy, J., Sullivan, M., et al. 2011, ApJS, 192, 1
- Contaldi, C. R., Hoekstra, H., & Lewis, A. 2003, Physical Review Letters, 90, 221303
- Copeland, E. J. 2007, in American Institute of Physics Conference Series, Vol. 957, Particles, Strings, and Cosmology-PASCOS 2007, ed. A. Rajantie, C. Contaldi, P. Dauncey, & H. Stoica, 21–29

Bibliography

- Copi, C. J., Schramm, D. N., & Turner, M. S. 1995, *ApJ*, 455, L95
- Courbin, F. & Minniti, D., eds. 2002, *Lecture Notes in Physics*, Berlin Springer Verlag, Vol. 608, *Gravitational Lensing: An Astrophysical Tool*
- Crittenden, R. G., Natarajan, P., Pen, U.-L., & Theuns, T. 2002, *ApJ*, 568, 20
- Dahle, H., Kaiser, N., Irgens, R. J., Lilje, P. B., & Maddox, S. J. 2002, *ApJS*, 139, 313
- de Bernardis, P., Ade, P. A. R., Bock, J. J., et al. 2002, *ApJ*, 564, 559
- de Bernardis, P., Ade, P. A. R., Bock, J. J., et al. 2000, *Nature*, 404, 955
- de Jong, J. T. A., Verdoes Kleijn, G. A., Kuijken, K. H., & Valentijn, E. A. 2012, *Experimental Astronomy*, 34
- de Sitter, W. 1916a, *MNRAS*, 76, 699
- de Sitter, W. 1916b, *MNRAS*, 77, 155
- de Sitter, W. 1917, *MNRAS*, 78, 3
- de Sitter, W. 1930, *The Observatory*, 53, 33
- de Sitter, W. 1931, *Naturwissenschaften*, 19, 365
- Dekel, A. 1994, *ARA&A*, 32, 371
- Diemand, J., Zemp, M., Moore, B., Stadel, J., & Carollo, C. M. 2005, *MNRAS*, 364, 665
- Dodelson, S. 2003, *Modern Cosmology*, Academic Press (Academic Press)
- Dodelson, S., Shapiro, C., & White, M. 2006, *Phys. Rev. D*, 73, 023009
- Doroshkevich, A. G., Khlopov, M. I., Sunyaev, R. A., Szalay, A. S., & Zeldovich, Y. B. 1981, *Annals of the New York Academy of Sciences*, 375, 32
- Drees, M. & Gerbier, G. 2012, *ArXiv e-prints*
- Drell, P. S., Loredo, T. J., & Wasserman, I. 2000, *ApJ*, 530, 593
- Dupé, F.-X., Rassat, A., Starck, J.-L., & Fadili, M. J. 2011, *A&A*, 534, A51
- Dvali, G., Gabadadze, G., & Porrati, M. 2000, *Physics Letters B*, 485, 208
- Dyson, F. W., Eddington, A. S., & Davidson, C. 1920, *Royal Society of London Philosophical Transactions Series A*, 220, 291
- Eddington, A. S. 1930, *MNRAS*, 90, 668
- Eddington, A. S. 1931, *Nature*, 127, 447
- Efstathiou, G., Moody, S., Peacock, J. A., et al. 2002, *MNRAS*, 330, L29
- Efstathiou, G. & Silk, J. 1983, *Fund. Cosmic Phys.*, 9, 1

- Einasto, J., Kaasik, A., & Saar, E. 1974, *Nature*, 250, 309
- Einstein, A. 1915, *Sitzungsberichte der Preussischen Akademie der Wissenschaften zu Berlin*, 844
- Einstein, A. 1917, *Sitzungsberichte der Königlich Preußischen Akademie der Wissenschaften (Berlin)*, Seite 142-152., 142
- Einstein, A. 1922, *Zeitschrift für Physik*, 11, 326
- Einstein, A. 1923, *Zeitschrift für Physik*, 16, 228
- Einstein, A. 1931, *Sitzungsber. Preuss. Akad. Wiss.*, 142, 235
- Einstein, A. 1936, *Science*, 84, 506
- Einstein, A. & de Sitter, W. 1932, *Proceedings of the National Academy of Science*, 18, 213
- Eisenstein, D. J. & Hu, W. 1998, *ApJ*, 496, 605
- Eke, V. R., Cole, S., & Frenk, C. S. 1996, *MNRAS*, 282, 263
- Erben, T., Hildebrandt, H., Miller, L., et al. 2012, *ArXiv e-prints*
- Faber, S. M. & Gallagher, J. S. 1979, *Annual Review of Astronomy and Astrophysics*, 17, 135
- Fall, S. M. & Efstathiou, G. 1980, *MNRAS*, 193, 189
- Feng, J. L. 2005, *Annals of Physics*, 315, 2
- Filippenko, A. V. 2001, *PASP*, 113, 1441
- Fischer, P., Bernstein, G., Rhee, G., & Tyson, J. A. 1997, *AJ*, 113, 521
- Fisher, R. A. 1935, *Journal of the Royal Statistical Society*, 98, 39
- Forman, W. & Jones, C. 1982, *ARA&A*, 20, 547
- Fort, B. & Mellier, Y. 1994, *A&A Rev.*, 5, 239
- Fort, B., Prieur, J. L., Mathez, G., Mellier, Y., & Soucail, G. 1988, *A&A*, 200, L17
- Freedman, W. L., Madore, B. F., Gibson, B. K., et al. 2001, *ApJ*, 553, 47
- Friedmann, A. 1922, *Zeitschrift für Physik*, 10, 377
- Friedmann, A. 1924, *Zeitschrift für Physik*, 21, 326
- Friedmann, A. 1999a, *General Relativity and Gravitation*, 31, 1991
- Friedmann, A. 1999b, *General Relativity and Gravitation*, 31, 2001
- Frieman, J. & Dark Energy Survey Collaboration. 2013, in *American Astronomical Society Meeting Abstracts*, Vol. 221, *American Astronomical Society Meeting Abstracts*
- Frieman, J. A., Bassett, B., Becker, A., et al. 2008, *AJ*, 135, 338

Bibliography

- Fu, L., Semboloni, E., Hoekstra, H., et al. 2008, *A&A*, 479, 9
- Gentile, M., Courbin, F., & Meylan, G. 2012, ArXiv e-prints
- Gentile, M., Courbin, F., & Meylan, G. 2013, *A&A*, 549, A1
- González-Díaz, P. 2003, *Phys. Rev. D*, 68, 021303
- Goullioud, R., Content, D. A., Kuan, G. M., et al. 2012, in *Society of Photo-Optical Instrumentation Engineers (SPIE) Conference Series*, Vol. 8442, *Society of Photo-Optical Instrumentation Engineers (SPIE) Conference Series*
- Gray, M. E., Taylor, A. N., Meisenheimer, K., et al. 2002, *ApJ*, 568, 141
- Gregory, P. 2005, *Bayesian Logical Data Analysis for the Physical Sciences: A Comparative Approach with Mathematica® Support* (Cambridge University Press)
- Gunn, J. E. 1967, *ApJ*, 150, 737
- Guth, A. 1997, *The Inflationary Universe: The Quest for a New Theory of Cosmic Origins*, *Helix books* (Perseus Books Group)
- Guth, A. H. 1981, *Phys. Rev. D*, 23, 347
- Hamilton, A. J. S., Kumar, P., Lu, E., & Matthews, A. 1991, *ApJ*, 374, L1
- Hamuy, M., Phillips, M. M., Suntzeff, N. B., et al. 1996, *AJ*, 112, 2391
- Harrison, E. R. 1970, *Phys. Rev. D*, 1, 2726
- Hawking, S. & Ellis, G. 1975, *The Large Scale Structure of Space-Time*, *Cambridge Monographs on Mathematical Physics* (Cambridge University Press)
- Heavens, A. 2003, *MNRAS*, 343, 1327
- Heavens, A. 2011, in *American Astronomical Society Meeting Abstracts*, 113.10
- Heavens, A. F., Kitching, T. D., & Taylor, A. N. 2006, *MNRAS*, 373, 105
- Heckmann, O. 1932, *Veroeffentlichungen der Universitaets-Sternwarte zu Goettingen*, 2, 180
- Henry, J. P., Evrard, A. E., Hoekstra, H., Babul, A., & Mahdavi, A. 2009, *ApJ*, 691, 1307
- Hetterscheidt, M., Simon, P., Schirmer, M., et al. 2007, *A&A*, 468, 859
- Hewitt, J. N., Turner, E. L., Burke, B. F., Lawrence, C. R., & Bennett, C. L. 1987, in *13th Texas Symposium on Relativistic Astrophysics*, ed. M. P. Ulmer, 317–320
- Heymans, C., Van Waerbeke, L., Bacon, D., et al. 2006, *MNRAS*, 368, 1323
- Heymans, C., Van Waerbeke, L., Miller, L., et al. 2012, *MNRAS*, 427, 146
- High, F. W., High, J., Massey, R., & Ellis, R. 2007, *PASP*, 119, 1295
- Hilbert, S., Hartlap, J., White, S. D. M., & Schneider, P. 2009, *A&A*, 499, 31

- Hildebrandt, H., Arnouts, S., Capak, P., et al. 2010, *A&A*, 523, A31
- Hinshaw, G., Larson, D., Komatsu, E., et al. 2012, *ArXiv e-prints*
- Hirata, C. & Seljak, U. 2003, *MNRAS*, 343, 459
- Hoekstra, H., Franx, M., Kuijken, K., & Squires, G. 1998, *ApJ*, 504, 636
- Hoekstra, H. & Jain, B. 2008, *Annual Review of Nuclear and Particle Science*, 58, 99
- Hoekstra, H., Mellier, Y., van Waerbeke, L., et al. 2006, *ApJ*, 647, 116
- Hoekstra, H., Yee, H. K. C., & Gladders, M. D. 2004, in *IAU Symposium, Vol. 220, Dark Matter in Galaxies*, ed. S. Ryder, D. Pisano, M. Walker, & K. Freeman, 439
- Hoekstra, H., Yee, H. K. C., Gladders, M. D., et al. 2002, *ApJ*, 572, 55
- Hopfield, J. 1982, *Proc.Nat.Acad.Sci.*, 79, 2554
- Hoyle, F. 1948, *MNRAS*, 108, 372
- Hu, W. 1999, *ApJ*, 522, L21
- Hu, W. 2002a, *Phys. Rev. D*, 66, 083515
- Hu, W. 2002b, *Phys. Rev. D*, 65, 023003
- Hu, W. & Jain, B. 2004, *Phys. Rev. D*, 70, 043009
- Hu, W. & Sugiyama, N. 1996, *ApJ*, 471, 542
- Hu, W. & Tegmark, M. 1999, *ApJ*, 514, L65
- Hubble, E. 1929a, *Proceedings of the National Academy of Science*, 15, 168
- Hubble, E. & Humason, M. L. 1931, *ApJ*, 74, 43
- Hubble, E. P. 1929b, *ApJ*, 69, 103
- Humason, M. L. 1931, *ApJ*, 74, 35
- Huterer, D. 2002, *Phys. Rev. D*, 65, 063001
- Huterer, D. 2010, *General Relativity and Gravitation*, 42, 2177
- Ilbert, O., Arnouts, S., McCracken, H. J., et al. 2006, *A&A*, 457, 841
- Jain, B., Mo, H. J., & White, S. D. M. 1995, *MNRAS*, 276, L25
- Jain, B. & Seljak, U. 1997, *ApJ*, 484, 560
- Jain, B. & Taylor, A. 2003, *Physical Review Letters*, 91, 141302
- Jaroszynski, M., Park, C., Paczynski, B., & Gott, III, J. R. 1990, *ApJ*, 365, 22
- Jarvis, M., Bernstein, G., & Jain, B. 2004, *MNRAS*, 352, 338

Bibliography

- Jarvis, M., Bernstein, G. M., Fischer, P., et al. 2003, *AJ*, 125, 1014
- Jarvis, M., Jain, B., Bernstein, G., & Dolney, D. 2006, *ApJ*, 644, 71
- Jauzac, M., Jullo, E., Kneib, J.-P., et al. 2012, *MNRAS*, 426, 3369
- Jeans, J. H. 1928, *Astronomy and cosmogony*
- Jee, M. J., Blakeslee, J. P., Sirianni, M., et al. 2007a, *PASP*, 119, 1403
- Jee, M. J., Ford, H. C., Illingworth, G. D., et al. 2007b, *ApJ*, 661, 728
- Jee, M. J. & Tyson, J. A. 2011, *PASP*, 123, 596
- Jee, M. J., White, R. L., Benítez, N., et al. 2005a, *ApJ*, 618, 46
- Jee, M. J., White, R. L., Ford, H. C., et al. 2005b, *ArXiv Astrophysics e-prints*
- Jee, M. J., White, R. L., Ford, H. C., et al. 2006, *ApJ*, 642, 720
- Kaiser, N. 1992, *ApJ*, 388, 272
- Kaiser, N. 1994, in *Clusters of Galaxies*, ed. F. Durret, A. Mazure, & J. Tran Thanh Van, 269
- Kaiser, N. 1998, *ApJ*, 498, 26
- Kaiser, N. & Squires, G. 1993, *ApJ*, 404, 441
- Kaiser, N., Squires, G., & Broadhurst, T. 1995, *ApJ*, 449, 460
- Kaiser, N., Wilson, G., & Luppino, G. A. 2000, *ArXiv Astrophysics e-prints*
- Kapteyn, J. C. 1922, *ApJ*, 55, 302
- Katz, N. & Gunn, J. E. 1991, *ApJ*, 377, 365
- Kauffmann, G., White, S. D. M., & Guiderdoni, B. 1993, *MNRAS*, 264, 201
- Kessler, R., Becker, A. C., Cinabro, D., et al. 2009, *ApJS*, 185, 32
- Kilbinger, M. & Schneider, P. 2005, *A&A*, 442, 69
- Kitching, T., Balan, S., Bernstein, G., et al. 2010, *ArXiv e-prints*
- Kitching, T. D., Balan, S. T., Bridle, S., et al. 2012a, *MNRAS*, 423, 3163
- Kitching, T. D., Heavens, A. F., & Miller, L. 2011, *MNRAS*, 413, 2923
- Kitching, T. D., Heavens, A. F., Taylor, A. N., et al. 2007, *MNRAS*, 376, 771
- Kitching, T. D., Miller, L., Heymans, C. E., van Waerbeke, L., & Heavens, A. F. 2008, *MNRAS*, 390, 149
- Kitching, T. D., Rhodes, J., Heymans, C., et al. 2012b, *ArXiv e-prints*
- Kitching, T. D., Rowe, B., Gill, M., et al. 2012c, *ArXiv e-prints*

- Klypin, A., Kravtsov, A. V., Valenzuela, O., & Prada, F. 1999, *ApJ*, 522, 82
- Knop, R. A., Aldering, G., Amanullah, R., et al. 2003, *ApJ*, 598, 102
- Kochanek, C. S. 1990, *MNRAS*, 247, 135
- Koo, D. C. 1985, *AJ*, 90, 418
- Koo, D. C. 1999, in *Astronomical Society of the Pacific Conference Series*, Vol. 191, *Photometric Redshifts and the Detection of High Redshift Galaxies*, ed. R. Weymann, L. Storrie-Lombardi, M. Sawicki, & R. Brunner, 3
- Kowalski, M., Rubin, D., Aldering, G., et al. 2008, *ApJ*, 686, 749
- Krauss, L. M. & Turner, M. S. 1995, *General Relativity and Gravitation*, 27, 1137
- Kristian, J. & Sachs, R. K. 1966, *ApJ*, 143, 379
- Krumm, N. & Salpeter, E. E. 1976, *ApJ*, 208, L7
- Kuijken, K. 1999, *A&A*, 352, 355
- Kuijken, K. 2006, *A&A*, 456, 827
- Laureijs, R., Amiaux, J., Arduini, S., et al. 2011, *ArXiv e-prints*
- Leibundgut, B. 2002, *Computer Physics Communications*, 147, 459
- Lemaître, A. G. 1931a, *Nature*, 128, 704
- Lemaître, A. G. 1931b, *MNRAS*, 91, 483
- Lemaître, A. G. 1931c, *Nature*, 127, 706
- Lemaître, G. 1925, *Journal of Mathematics and Physics*, 4, 188
- Lemaître, G. 1927, *Annales de la Societe Scietifique de Bruxelles*, 47, 49
- Liddle, A. & Lyth, D. 2000, *Cosmological Inflation and Large-Scale Structure* (Cambridge University Press)
- Lima, J. A. S., Zanchin, V., & Brandenberger, R. 1997, *MNRAS*, 291, L1
- Limber, D. N. 1953, *ApJ*, 117, 134
- Linde, A. D. 1982a, *Physics Letters B*, 108, 389
- Linde, A. D. 1982b, *Physics Letters B*, 116, 335
- Linder, E. V. 2003, *Physical Review Letters*, 90, 091301
- Linder, E. V. & Jenkins, A. 2003, *MNRAS*, 346, 573
- Livio, M. 2004, *The Dark Universe*
- LSST Science Collaboration, Abell, P. A., Allison, J., et al. 2009, *ArXiv e-prints*

Bibliography

- Lue, A. 2006, *Phys. Rep.*, 423, 1
- Luppino, G. A. & Kaiser, N. 1997, *ApJ*, 475, 20
- Malquarti, M., Copeland, E. J., Liddle, A. R., & Trodden, M. 2003, *Phys. Rev. D*, 67, 123503
- Mandelbaum, R., Rowe, B., & GREAT3 Collaboration. 2013, in *American Astronomical Society Meeting Abstracts*, Vol. 221, American Astronomical Society Meeting Abstracts, 341.05
- Maoli, R., Van Waerbeke, L., Mellier, Y., et al. 2001, *A&A*, 368, 766
- Margoniner, V. E., Lubin, L. M., Wittman, D. M., & Squires, G. K. 2005, *AJ*, 129, 20
- Massey, R., Heymans, C., Bergé, J., et al. 2007a, *MNRAS*, 376, 13
- Massey, R. & Refregier, A. 2005, *MNRAS*, 363, 197
- Massey, R., Refregier, A., & Bacon, D. 2005, in *IAU Symposium*, Vol. 225, *Gravitational Lensing Impact on Cosmology*, ed. Y. Mellier & G. Meylan, 31–36
- Massey, R., Rhodes, J., Leauthaud, A., et al. 2007b, *ApJS*, 172, 239
- Mateo, M. L. 1998, *ARA&A*, 36, 435
- Mathews, G. J., Kajino, T., & Shima, T. 2005, *Phys. Rev. D*, 71, 021302
- Mathews, W. G. 1978, *The Astrophysical Journal*, 219, 413
- Melchior, P., Andrae, R., Maturi, M., & Bartelmann, M. 2009, *A&A*, 493, 727
- Melchior, P., Böhnert, A., Lombardi, M., & Bartelmann, M. 2010, *A&A*, 510, A75
- Melchior, P., Meneghetti, M., & Bartelmann, M. 2007, *A&A*, 463, 1215
- Mellier, Y. & Fort, B. 1997, in *The Early Universe with the VLT.*, ed. J. Bergeron, 189
- Meszáros, P. 1974, *A&A*, 37, 225
- Miknaitis, G., Pignata, G., Rest, A., et al. 2007, *ApJ*, 666, 674
- Miller, L., Heymans, C., Kitching, T. D., et al. 2013, *MNRAS*, 532
- Miller, L., Kitching, T. D., Heymans, C., Heavens, A. F., & van Waerbeke, L. 2007, *MNRAS*, 382, 315
- Milne, E. A. 1935, *Relativity, gravitation and world-structure*
- Miralda-Escude, J. 1991a, *ApJ*, 370, 1
- Miralda-Escude, J. 1991b, *ApJ*, 380, 1
- Mitchell, J. L., Keeton, C. R., Frieman, J. A., & Sheth, R. K. 2005, *ApJ*, 622, 81
- Mo, H., van den Bosch, F., & White, S. 2010, *Galaxy Formation and Evolution*, *Galaxy Formation and Evolution* (Cambridge University Press)

- Moore, B., Ghigna, S., Governato, F., et al. 1999, *ApJ*, 524, L19
- Mukhanov, S. 2007, *Journal of Physics A Mathematical General*, 40, 6561
- Mukhanov, V. 2005, *Physical Foundations of Cosmology* (Cambridge University Press)
- Munshi, D., Valageas, P., van Waerbeke, L., & Heavens, A. 2008, *Phys. Rep.*, 462, 67
- Munshi, D. & Wang, Y. 2003, *ApJ*, 583, 566
- Nakajima, R. & Bernstein, G. 2007, *AJ*, 133, 1763
- Narayan, R. & Bartelmann, M. 1996, *ArXiv Astrophysics e-prints*
- Navarro, J. F., Frenk, C. S., & White, S. D. M. 1997, *ApJ*, 490, 493
- Navarro, J. F., Hayashi, E., Power, C., et al. 2004, *MNRAS*, 349, 1039
- Navarro, J. F. & White, S. D. M. 1994, *MNRAS*, 267, 401
- Nojiri, S. & Odintsov, S. D. 2006, *ArXiv High Energy Physics - Theory e-prints*
- Norgaard-Nielsen, H. U., Hansen, L., Jorgensen, H. E., et al. 1989, *Nature*, 339, 523
- Nurbaeva, G., Courbin, F., Gentile, M., & Meylan, G. 2011, *A&A*, 531, A144
- Nurbaeva, G., Tewes, M., Courbin, F., & Meylan, G. 2013, *A&A submitted*
- Ödman, C. J., Melchiorri, A., Hobson, M. P., & Lasenby, A. N. 2003, *Phys. Rev. D*, 67, 083511
- Oh, S.-H., de Blok, W. J. G., Brinks, E., Walter, F., & Kennicutt, Jr., R. C. 2011, *AJ*, 141, 193
- Olive, K. A. & Steigman, G. 1995, *ApJS*, 97, 49
- Oort, J. H. 1932, *Bull. Astron. Inst. Netherlands*, 6, 249
- Ostriker, J. P. & Peebles, P. J. E. 1973, *ApJ*, 186, 467
- Ostriker, J. P., Peebles, P. J. E., & Yahil, A. 1974, *ApJ*, 193, L1
- Ostriker, J. P. & Steinhardt, P. J. 1995, *Nature*, 377, 600
- Paczynski, B. 1996, *ARA&A*, 34, 419
- Paraficz, D. & Hjorth, J. 2010, *ApJ*, 712, 1378
- Peacock, J. 1998, *Cosmological Physics*, Cambridge Astrophysics Series (Cambridge University Press)
- Peacock, J. A., Cole, S., Norberg, P., et al. 2001, *Nature*, 410, 169
- Peacock, J. A. & Dodds, S. J. 1996, *MNRAS*, 280, L19
- Peebles, P. J. E. 1966, *ApJ*, 146, 542
- Peebles, P. J. E. & Yu, J. T. 1970, *ApJ*, 162, 815

Bibliography

- Peiris, H. V., Komatsu, E., Verde, L., et al. 2003, *ApJS*, 148, 213
- Pen, U.-L. 2000, *ApJ*, 534, L19
- Pen, U.-L., Lu, T., van Waerbeke, L., & Mellier, Y. 2003, *MNRAS*, 346, 994
- Penzias, A. A. & Wilson, R. W. 1965, *ApJ*, 142, 419
- Perlmutter, S., Aldering, G., Della Valle, M., et al. 1998, *Nature*, 392, 311
- Perlmutter, S., Aldering, G., Goldhaber, G., et al. 1999, *ApJ*, 517, 565
- Perlmutter, S., Gabi, S., Goldhaber, G., et al. 1997, *ApJ*, 483, 565
- Peter, A. H. G. 2012, *ArXiv e-prints*
- Pires, S., Starck, J.-L., & Refregier, A. 2010, *IEEE Signal Processing Magazine*, 27, 76
- Pritchett, C. J. & SNLS Collaboration. 2005, in *Astronomical Society of the Pacific Conference Series*, Vol. 339, *Observing Dark Energy*, ed. S. C. Wolff & T. R. Lauer, 60
- Pryke, C., Halverson, N. W., Leitch, E. M., et al. 2002, *ApJ*, 568, 46
- Puschell, J. J., Owen, F. N., & Laing, R. A. 1982, *ApJ*, 257, L57
- Randall, L. & Sundrum, R. 1999, *Physical Review Letters*, 83, 4690
- Rees, M. J. & Ostriker, J. P. 1977, *MNRAS*, 179, 541
- Refregier, A. 2003a, *MNRAS*, 338, 35
- Refregier, A. 2003b, *ARA&A*, 41, 645
- Refregier, A. & Bacon, D. 2003, *MNRAS*, 338, 48
- Refsdal, S. 1964a, *MNRAS*, 128, 307
- Refsdal, S. 1964b, *MNRAS*, 128, 295
- Rendall, A. D. 2006, *Classical and Quantum Gravity*, 23, 1557
- Riess, A. G., Filippenko, A. V., Challis, P., et al. 1998, *AJ*, 116, 1009
- Riess, A. G., Macri, L., Casertano, S., et al. 2011, *ApJ*, 730, 119
- Riess, A. G., Strolger, A. L.-G., Casertano, S., et al. 2007, *ApJ*, 659, 98
- Riess, A. G., Strolger, L.-G., Tonry, J., et al. 2004, *ApJ*, 607, 665
- Roberts, M. S. & Whitehurst, R. N. 1975, *ApJ*, 201, 327
- Robertson, H. P. 1929, *Proceedings of the National Academy of Science*, 15, 822
- Robertson, H. P. 1933, *Reviews of Modern Physics*, 5, 62
- Robertson, H. P. 1935, *ApJ*, 82, 284

- Robertson, H. P. 1936a, *ApJ*, 83, 187
- Robertson, H. P. 1936b, *ApJ*, 83, 257
- Rogstad, D. H. & Shostak, G. S. 1972, *ApJ*, 176, 315
- Romano, A., Fu, L., Giordano, E., et al. 2010, *A&A*, 514, A88
- Rozo, E., Wechsler, R. H., Rykoff, E. S., et al. 2010, *ApJ*, 708, 645
- Rubiño-Martin, J. A., ReboYou need not be afraid of phantom energylo, R., Carreira, P., et al. 2003, *MNRAS*, 341, 1084
- Rubin, V. C. & Ford, Jr., W. K. 1970, *ApJ*, 159, 379
- Rubin, V. C., Ford, W. K. J., & . Thonnard, N. 1980, *ApJ*, 238, 471
- Rubin, V. C., Thonnard, N., & Ford, Jr., W. K. 1978, *ApJ*, 225, L107
- Scherrer, R. J. 2005, *Phys. Rev. D*, 71, 063519
- Schindler, S., Binggeli, B., & Böhringer, H. 1999, *A&A*, 343, 420
- Schmidt, B. P., Suntzeff, N. B., Phillips, M. M., et al. 1998, *ApJ*, 507, 46
- Schneider, P. 1996, *MNRAS*, 283, 837
- Schneider, P., Ehlers, J., & Falco, E. E. 1992, *Gravitational Lenses*
- Schneider, P., Kochanek, C. S., Wambsganss, J., et al., eds. 2006, *Gravitational Lensing: Strong, Weak and Micro*
- Schneider, P. & Seitz, C. 1995, *A&A*, 294, 411
- Schneider, P., van Waerbeke, L., Jain, B., & Kruse, G. 1998, *MNRAS*, 296, 873
- Schneider, P., van Waerbeke, L., Kilbinger, M., & Mellier, Y. 2002a, *A&A*, 396, 1
- Schneider, P., van Waerbeke, L., & Mellier, Y. 2002b, *A&A*, 389, 729
- Schrabback, T., Hartlap, J., Joachimi, B., et al. 2010, *A&A*, 516, A63
- Schramm, D. N. & Turner, M. S. 1998, *Reviews of Modern Physics*, 70, 303
- Seitz, C. & Schneider, P. 1995, *A&A*, 297, 287
- Seitz, C. & Schneider, P. 1997, *A&A*, 318, 687
- Seljak, U. 1995, PhD thesis, MASSACHUSETTS INSTITUTE OF TECHNOLOGY.
- Semboloni, E., Mellier, Y., van Waerbeke, L., et al. 2006, *A&A*, 452, 51
- Sen, A. A. 2006, *J. Cosmology Astropart. Phys.*, 3, 10
- Sérsic, J. L. 1968, *Cordoba*

Bibliography

- Sheldon, E. S., Johnston, D. E., Frieman, J. A., et al. 2004, *AJ*, 127, 2544
- Simon, J. D. & Geha, M. 2007, *ApJ*, 670, 313
- Simon, P., King, L. J., & Schneider, P. 2004, *A&A*, 417, 873
- Slipher, V. M. 1913, *Lowell Observatory Bulletin*, 2, 56
- Slipher, V. M. 1915, *Popular Astronomy*, 23, 21
- Smith, R. 1982, *The Expanding Universe: Astronomy's "Great Debate," 1900-1931* (Cambridge University Press)
- Smith, R. E., Peacock, J. A., Jenkins, A., et al. 2003, *MNRAS*, 341, 1311
- Smoot, G. F., Bennett, C. L., Kogut, A., et al. 1992, *ApJ*, 396, L1
- Somerville, R. S. & Primack, J. R. 1999, *MNRAS*, 310, 1087
- Sotiriou, T. P. 2006, *Classical and Quantum Gravity*, 23, 1253
- Spano, M., Marcelin, M., Amram, P., et al. 2008, *MNRAS*, 383, 297
- Spergel, D. N., Verde, L., Peiris, H. V., et al. 2003, *ApJS*, 148, 175
- Springel, V., White, S. D. M., Jenkins, A., et al. 2005, *Nature*, 435, 629
- Springel, V., Yoshida, N., & White, S. D. M. 2001, *New A*, 6, 79
- Squires, G. & Kaiser, N. 1996, *ApJ*, 473, 65
- Stebbins, A. 1996, in *Bulletin of the American Astronomical Society*, Vol. 28, American Astronomical Society Meeting Abstracts, 1385
- Steigman, G. 2006, *International Journal of Modern Physics E*, 15, 1
- Steinhardt, P. J. 2003, *Royal Society of London Philosophical Transactions Series A*, 361, 2497
- Steinhardt, P. J., Wang, L., & Zlatev, I. 1999, *Phys. Rev. D*, 59, 123504
- Stuart, A., Ord, K., & Arnold, S. 2009, *Kendall's Advanced Theory of Statistics, Classical Inference and the Linear Model*, Kendall's library of statistics No. v. 2 (John Wiley & Sons)
- Sullivan, M., Guy, J., Conley, A., et al. 2011, *ApJ*, 737, 102
- Sullivan, M. & Supernova Legacy Survey Collaboration. 2005, in *Bulletin of the American Astronomical Society*, Vol. 37, American Astronomical Society Meeting Abstracts #206, 503
- Sunyaev, R. A. 1978, in *IAU Symposium*, Vol. 79, *Large Scale Structures in the Universe*, ed. M. S. Longair & J. Einasto, 393–402
- Suzuki, N., Rubin, D., Lidman, C., et al. 2012, *ApJ*, 746, 85
- Swaters, R. A., Madore, B. F., van den Bosch, F. C., & Balcells, M. 2003, *ApJ*, 583, 732

- Takada, M. & Jain, B. 2003, MNRAS, 344, 857
- Tauber, J. A., Mandolesi, N., Puget, J.-L., et al. 2010a, A&A, 520, A1
- Tauber, J. A., Norgaard-Nielsen, H. U., Ade, P. A. R., et al. 2010b, A&A, 520, A2
- Taylor, A. N. 2001, ArXiv Astrophysics e-prints
- Tegmark, M., Blanton, M. R., Strauss, M. A., et al. 2004a, ApJ, 606, 702
- Tegmark, M., Strauss, M. A., Blanton, M. R., et al. 2004b, Phys. Rev. D, 69, 103501
- Tegmark, M., Taylor, A. N., & Heavens, A. F. 1997, ApJ, 480, 22
- Tewes, M., Cantale, N., Courbin, F., Kitching, T., & Meylan, G. 2012, A&A, 544, A8
- Tolman, R. C. 1934, Relativity, Thermodynamics, and Cosmology
- Trodden, M. 2006, in CMB and Physics of the Early Universe
- Turner, E. L. 1990, ApJ, 365, L43
- Turner, E. L. & Ostriker, J. P. 1977, ApJ, 217, 24
- Turner, E. L., Ostriker, J. P., & Gott, III, J. R. 1984, ApJ, 284, 1
- Turner, M. S. 1991, Physica Scripta Volume T, 36, 167
- Turnshek, D. A., Lupie, O. L., Rao, S. M., Espey, B. R., & Sirola, C. J. 1997, The Astrophysical Journal, 485, 100
- Tyson, J. A., Wenk, R. A., & Valdes, F. 1990, ApJ, 349, L1
- Tytler, D., O'Meara, J. M., Suzuki, N., & Lubin, D. 2001, in Particle Physics and the Universe, ed. L. Bergström, C. Fransson, & P. Carlson, 12–31
- Umetsu, K. 2010, ArXiv e-prints
- van Waerbeke, L., Bernardeau, F., & Mellier, Y. 1999, A&A, 342, 15
- Van Waerbeke, L. & Mellier, Y. 2003, ArXiv Astrophysics e-prints
- Van Waerbeke, L., Mellier, Y., Erben, T., et al. 2000, A&A, 358, 30
- Van Waerbeke, L., Mellier, Y., & Hoekstra, H. 2005, A&A, 429, 75
- Van Waerbeke, L., Mellier, Y., Pelló, R., et al. 2002a, A&A, 393, 369
- Van Waerbeke, L., Mellier, Y., Pelló, R., et al. 2002b, A&A, 393, 369
- Van Waerbeke, L., Mellier, Y., Radovich, M., et al. 2001, A&A, 374, 757
- van Waerbeke, L., Mellier, Y., Schneider, P., Fort, B., & Mathez, G. 1997, A&A, 317, 303
- Vegetti, S., Lagattuta, D. J., McKean, J. P., et al. 2012, Nature, 481, 341

Bibliography

- Viel, M., Haehnelt, M. G., & Springel, V. 2010, *J. Cosmology Astropart. Phys.*, 6, 15
- Villumsen, J. V. 1996, *MNRAS*, 281, 369
- Vollick, D. N. 2003, *Phys. Rev. D*, 68, 063510
- Wagoner, R. V., Fowler, W. A., & Hoyle, F. 1967, *ApJ*, 148, 3
- Walker, A. G. 1935, *MNRAS*, 95, 263
- Walsh, D., Carswell, R. F., & Weymann, R. J. 1979, *Nature*, 279, 381
- Wang, L. & Steinhardt, P. J. 1998, *ApJ*, 508, 483
- Wang, P. & Meng, X.-H. 2004, *ArXiv Astrophysics e-prints*
- Wechsler, R. H., Bullock, J. S., Primack, J. R., Kravtsov, A. V., & Dekel, A. 2002, *ApJ*, 568, 52
- Weinberg, S. 1989, *Reviews of Modern Physics*, 61, 1
- Weyl, H. 1923, *General Relativity and Gravitation*
- White, M. 2005, *Astroparticle Physics*, 23, 349
- White, S. D. M., Frenk, C. S., & Davis, M. 1983, *ApJ*, 274, L1
- White, S. D. M., Navarro, J. F., Evrard, A. E., & Frenk, C. S. 1993, *Nature*, 366, 429
- White, S. D. M. & Rees, M. J. 1978, *MNRAS*, 183, 341
- Wiener, N. 1949, *Extrapolation, Interpolation, and Smoothing of Stationary Time Series* (MIT Press)
- Wittman, D., Margoniner, V. E., Tyson, J. A., et al. 2003, *ApJ*, 597, 218
- Wittman, D. M., Tyson, J. A., Kirkman, D., Dell'Antonio, I., & Bernstein, G. 2000, *Nature*, 405, 143
- Wood-Vasey, W. M., Miknaitis, G., Stubbs, C. W., et al. 2007, *ApJ*, 666, 694
- Wu, X.-P. 1996, *Fund. Cosmic Phys.*, 17, 1
- Zeldovich, Y. 1967, *JETP Lett.*, 6, 316
- Zeldovich, Y. B. 1972, *MNRAS*, 160, 1P
- Zeldovich, Y. B., Einasto, J., & Shandarin, S. F. 1982, *Nature*, 300, 407
- Zeldovich, Y. B. & Novikov, I. D. 1983, *Relativistic astrophysics. Volume 2 - The structure and evolution of the universe / Revised and enlarged edition/*
- Zentner, A. R. & Bullock, J. S. 2002, *Phys. Rev. D*, 66, 043003
- Zuntz, J., Kacprzak, T., Voigt, L., et al. 2013, *ArXiv e-prints*
- Zwicky, F. 1933, *Helvetica Physica Acta*, 6, 110
- Zwicky, F. 1937a, *Phys. Rev.*, 51, 290
- Zwicky, F. 1937b, *ApJ*, 86, 217



Marc GENTILE

Avenue de Tivoli, 56
1007 Lausanne, Switzerland

French Nationality, C Swiss resident permit
Email : marc.gentile@epfl.ch
Tel : + 41 78 852 3284 (mobile, Suisse)

Education

- 2008 - 2013 : PhD thesis in Physics
Laboratoire d'astrophysique, Ecole Polytechnique Fédérale de Lausanne, Switzerland
"Weak Gravitational Lensing by large-scale structures : a tool for constraining cosmology"
- 2005 - 2006: Master in Science (MSc) en Astrophysics (with distinction), Queen Mary University of London, UK.
- 1984- 1987: ESLSCA (Ecole Supérieure Libre des Sciences Commerciales Appliquées) Business School, Paris, France

Languages

English

- Fluent (lived 5 years in London from 1997 to 2002 and 2005)
- Computer TOEFL, total score: 273, essay rating: 5 (obtained on 16/02/2004)
- Cambridge First Certificate, (2000), grade B
- London Chamber of Commerce spoken and written certificates (EFC, SEFIC), (1985)

Spanish

- Diploma de la 'Camara de Comercio de España', 1986 (commercial spanish)

Professional experience in computing

S&H Switzerland. Geneva, Switzerland, Architect / Senior Software Developer	February 2010 – Present
IRIS Integrated Risk management ag, Lausanne, Switzerland, Senior Software Developer	April 2007 – January 2010
SWX Swiss Exchange, Zürich, Switzerland, Technical Architect (6-month contract)	September. 2006 – March 2007
Interruption for studying for a MSc in Astrophysics at Queen Mary University, London, U.K.	September 2005 – August 2006
Sedona, Paris, Senior Software Engineer	August 2003 – August 2005
eFORCE France, Paris, eBusiness Technical Architect	December. 2001 – July 2003
eFORCE Europe Ltd, London, U.K., Senior Software Developer	June 2000 – November 2001
The Financial Times, London, Senior Software Engineer	October 1999 – May 2000
United Bank of Switzerland (UBS), London, U.K., Senior Software Engineer	July 1997 – September 1999
Chronopost, Paris, France, Software Engineer	March 1996 – June 1997
Elliott, Paris, France, Software Engineer	March 1995 – February 1996
Unilog, Paris, France, Software Engineer	April 1990 – February 1995

Prizes and awards

- Winner of the GRavitational lEnsing Accuracy Testing 2010 (GREAT10) Star Challenge in 2011
- Médaille de bronze de la Défense Nationale, obtained during my military service in the French army (1989)

Invited talks

- Kriging Interpolation: application to the GREAT10 Star Challenge*, 4 May 2011, Cosmology Meets Machine Learning and GREAT10 Workshop, University College of London (UCL), London, U.K.
- Some lessons learned from the GREAT10 Star Challenge*, 27 September 2011, Image Analysis Workshop, California Institute of Technology (CALTECH), Pasadena, USA 195
- PSF interpolation for Weak Lensing: learning from the GREAT10 Star Challenge*, 18 October 2012, First GREAT3 Working Meeting, Carnegie Mellon University, Pittsburgh, USA

Scientific publications

- "Interpolating point spread function anisotropy",
Gentile, M., Courbin, F., Meylan, G., 2013, *Astronomy & Astrophysics*, Vol. 549, astro-ph/1210.2696
- "A simple fitting method (*gfit*) for galaxy shape measurement in weak lensing surveys",
Gentile, M., Courbin, F., Meylan, G., 2012, astro-ph/1211.4847
- "Image Analysis for Cosmology: Results from the GREAT10 Star Challenge",
Kitching, T. D., Rowe, B., Gill, M., Heymans, C., Massey, R., Witherick, D., Courbin, F., Georgatzis, K., Gentile, M., Gruen, D., Kilbinger, M., Li, G. L., Mariglis, A. P., Meylan, G., Storkey, A., Xin, B., and 6 coauthors, 2012, submitted to *ApJS*, astro-ph/1210.1979
- "Image analysis for cosmology: results from the GREAT10 Galaxy Challenge",
Kitching, T. D., Balan, S. T., Bridle, S., Cantale, N., Courbin, F., Eifler, T., Gentile, M., Gill, M. S. S., Harmeling, S., Heymans, C., and 18 coauthors, 2012, *Monthly Notices of the Royal Astronomical Society*, Vol. 423, Issue 4, pp. 3163-3208, astro-ph/1202.5254
- "On the effect of image denoising on galaxy shape measurements",
Nurbaeva, G.; Courbin, F.; Gentile, M.; Meylan, G., 2011, *Astronomy & Astrophysics*, Volume 531, astro-ph/ 1106.0927
- "Gravitational Lensing Accuracy Testing 2010 (GREAT10) Challenge Handbook",
Kitching, T., Balan, S. T., Bernstein, G., Bethge, M., Bridle, S., Courbin, F., Gentile, M., Heavens, A., Hirsch, M., Hosseini, R., and 25 coauthors, 2010, *Annals of Applied Statistics*, Vol. 5, Issue. 3, pp. 2231-2263, astro-ph/1009.0779
- "Results of the GREAT08 Challenge: an image analysis competition for cosmological lensing",
Bridle, S., Balan, S. T., Bethge, M., Gentile, M., Harmeling, S., Heymans, C., Hirsch, M., Hosseini, R., Jarvis, M., Kirk, D., and 24 coauthors, 2010, *Monthly Notices of the Royal Astronomical Society*, Vol. 405, Issue 3, pp. 2044-2061, astro-ph/0908.0945

